Stellingen

1. Het bepalen van intrinsieke diffusiecoëfficiënten in zeolieten met behulp van membraanpermeatiemetingen dient men bij voorkeur met goed gedefinieerde éénkristallen te verrichten, terwijl dit bij het onderzoeken van het scheidend vermogen voor industriële toepassingen in beginsel niet noodzakelijk is. Om die reden hadden de twee onderzoeksgroepen die voor de eerste keer de permeatie door zeolietmembranen maten beter hun preparaten kunnen uitwisselen.

    D.L. Wernick, and E.J. Osterhuber, in: *Proc. 6th Int.Zeol.Conf.*, D. Olson, and A. Bisio (Eds), Butterworths, London, 1984, 122; A.R. Paravar, and D.T. Hayhurst, *ibid.*, 217.

2. De adsorptiegegevens voor methaan, kooldioxide en stikstof in silikaliet in verschillende artikelen van dezelfde auteur zijn niet consistent.

    L.V.C. Rees, *Stud.Surf.Sci.Catal.* 65 (1991) 61; L.V.C. Rees et al., in: *Zeolite Microporous Solids: Synthesis, Structure, and Reactivity*, Kluwer Academic Publishers, The Netherlands, 1992, 133.

3. In de vergelijking tussen de diffusiecoëfficiënt gemeten via adsorptiemetingen en de zelfdiffusiecoëfficiënt volgens de pfg NMR techniek, beide als functie van de deeltjesgrootte, is het schijnbaar minder duidelijke effect van het adsorptieproces op de diffusie in het geval van ethaan in zeoliet 5A ten opzichte van methaan in chabaziet slechts het gevolg van een aanzienlijk verschil in de maximale deeltjesgrootte.

    Figuren 22 en 23: M.F.M. Post, *Stud.Surf.Sci.Catal.* 58 (1991) 391.

4. De algemene veronderstelling dat scheurvorming in zeolietkristallen tijdens het uitbranden van zogenaamde 'template'-moleculen/ionen als gevolg van 'hot spots' plaatsvindt is op grond van waarnemingen met lichtmicroscopie onwaarschijnlijk. Bovendien zal het stoftransport van moleculaire zuurstof in de zeolietporiën gehinderd worden door de verwijdering van de verbrandingsproducten.

    dit proefschrift, Hoofdstuk 4 en 7.

5. Het niet opgeven van het permeatievolume sluit verificatie van de met de 'time lag' methode bepaalde diffusiecoëfficiënten met behulp van de 'quasi-steady-state' permeabiliteit uit.

    D.T. Hayhurst, and A.R. Paravar, *Zeolites*, 8 (1988) 27.

6. De toegankelijkheid van de sinusoïdale kanalen van zeoliet MFI voor p-xyleen bij temperaturen boven de fasenovergang orthorhombisch-monoklien dient nog te worden vastgesteld bij een voldoende hoge p-xyleen dampspanning.

D.H. Olson, G.T. Kokotailo, S.L. Lawton, and W.M. Maier, *J.Phys.Chem.*, 85 (1981) 2238; H. van Koningsveld, F. Tuinstra, J.C. Jansen, and H. van Bekkum, *Acta Cryst.*, B45 (1989) 423.

7. De beschrijving van de bereiding van zeolietmembranen zonder het vermelden van de kristalstructuur van de betrokken zeoliet is wellicht toelaatbaar in een octrooi, doch zeker niet in een wetenschappelijk artikel.

A. Ishikawa, T.H. Chiang, and F. Toda, *Chem.Comm.*, (1989) 764; S. Sakurada, N. Tagaya, T. Maeshima, and T. Isoda, Canadian Patent 1,235,684 (1988).

8. Het feit dat de beschrijving van diffusie in een systeem van samengeperste zeolietkristallieten in de vorm van een wafer met behulp van een standaardoplossing van de diffusievergelijking voldoet getuigt van een goed uitgevoerde keramische procesgang.

H. Karge, and W. Niessen, *Catal.Today*, 8 (1991) 451.

9. Door het combineren van licht- en electronenmicroscopie kan men een veel completer beeld verkrijgen van de natuur; de toepassing van dergelijke complementaire technieken moet in hoge mate bevorderd worden.

dit proefschrift, Hoofdstuk 3 en 4.

10. Het is te verwachten dat op het gebied van de integrale kwaliteitszorg de universiteiten uiteindelijk het bedrijfsleven zullen volgen.

11. De technische en medische voortbrengselen van het menselijk vernuft ontstijgen steeds vaker het bevattingsvermogen van de schepper, zodat de ontwikkeling van de mens de hoogste prioriteit verdient.

12. De complexiteit van de menselijke geest is van dien aard dat een studie psychologie een hoger intelligentieniveau van de student vereist dan de gemiddelde technische studie.

13. Terwijl bijzondere mensen zich gelukkig prijzen dat ze zo uniek zijn, kunnen gewone mensen zich slechts troosten met het feit dat ze niet de enige zijn.

Eduard Geus   27 april 1993

Preparation and Characterization of Composite Inorganic Zeolite Membranes with Molecular Sieve Properties

PROEFSCHRIFT

ter verkrijging van de graad van doctor

aan de Technische Universiteit Delft,

op gezag van de Rector Magnificus, prof. drs P.A. Schenck,

in het openbaar te verdedigen ten overstaan van

een commissie, aangewezen door het College van Dekanen

op dinsdag 27 april 1993 te 11.00 uur door

Eduard Geus

geboren te Sittard

scheikundig ingenieur
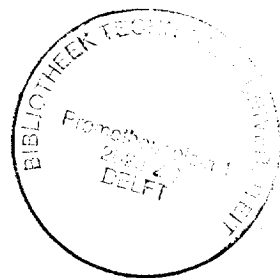
Dit proefschrift is goedgekeurd door de promotoren

Prof.dr.ir. H. van Bekkum

Prof.dr. J. Schoonman

Aan mijn ouders

Contents

1. General Introduction

Chapter 1

1.1 Membrane Technology

Industrial chemical conversions usually call for separation processes. Often the thermodynamic equilibrium is not completely on one side, which limits the conversion, or achievement of a high selectivity requires an excess of one of the reactants. After the reaction the product and the remaining reactants must be separated. Furthermore, by-products may have to be removed to meet the desired purity. Several separation processes are industrially utilized, such as distillation, crystallization, centrifugation, extraction, and adsorption.

During the past few decades, the use of membranes for separation on an industrial scale has increased substantially. The continuous operation with membranes is an obvious advantage, and for some separations the 'classical' techniques are energy demanding (e.g. solvent recovery), or non-selective. A membrane process makes use of the ability of some components in the mixture (feed) to pass more readily through the introduced barrier to the other side (permeate), whereas other components are left behind (retentate). The membrane field covers, however, a wide range of applications, and the membrane function can be based on different separation characteristics (Table 1).[1]

There are roughly three groups of membrane processes. Microfiltration (MF) and ultrafiltration (UF) utilize the size of the solute to separate particles by sieving, similar to well-known domestic coffee-filters and colanders. These membranes are, indeed, best referred to as filters. A number of separation processes is based on differences in affinity between feed components and the membrane material (resulting in different solubilities of components in the organic polymer membrane material), and/or a difference in mobility through the membrane phase. This group of membrane processes covers dialysis, reverse osmosis (RO), and gas separation and pervaporation. Finally, charged molecules may be separated from uncharged ones by anion or cation selective membranes (electrodialysis).

Membrane reactors offer the option to combine the chemical reaction and separation in one process, thus shifting the equilibrium to the desired side with a gain in yield and possibly in selectivity. Thus far, such processes are limited to relatively low temperatures, and the development of high-temperature membrane systems is still challenging.

Table 1   Membrane separation processes, adapted from Lonsdale[1]

	Permeate	Driving Force	Retentate
Microfiltration (MF)	Water and Dissolved Species	Pressure	Suspended Material
Ultrafiltration (UF)	Water and Salts	Pressure	Colloids and Macromolecules
Dialysis	Ions and Low-Molecular Weight Organics	Concentration	Suspended and Dissolved Material with Molecular Weight > 1000 g/mol
Reverse Osmosis (RO)	Water	Pressure	Virtually All Suspended and Dissolved Material
Gas Separation	Small Molecules (Gases and/or Vapours)	Pressure	Membrane-Impermeable Molecules
Pervaporation	Molecules in the Vapour Phase	Concentration	Molecules in the Liquid Phase
Electrodialysis	Ions	Voltage	Non-ionic and Macromolecular Species

1.2 Inorganic Membranes for Separation on a Molecular Level

Separation on a molecular level requires intimate contact between the permeating molecules and the membrane material. For polymer membranes two basically different approaches have been pursued to achieve highly selective membranes. First, there are dense organic polymer films, in which the permeating molecules are dissolved, whereas the non-dissolving molecules remain in the retentate phase. The permeation may then be characterized by a solution-diffusion model.[2] The other option is to make use of microporous films, although control of the pore size may only lead to Knudsen selectivity. With Knudsen selectivity the pores are sufficiently small to preclude bulk gas flow by molecular diffusion, and the permeability is inversely proportional to the square root of the molecular mass. The main

difference between both types of membranes is that for dense membranes the pores are created in a dynamical (and reversible) way as a result of the dissolving process. In microporous membranes the pores are present permanently, but the same solution-diffusion mechanism may be involved.[3]

The same distinction in porous and dense membranes can be made for inorganic membranes. As compared with organic polymers, only a few dense inorganic materials are available in which components from the feed can actually dissolve. Good examples are palladium (hydrogen) and silver (oxygen) films, while several solid ionic conductors are known as oxygen transporting membranes. For microporous inorganic membranes, on the other hand, the separation process may be conducted in various ways involving different types of molecules. In contrast to the above metal films, the microporous membranes generally have an asymmetric composite structure, in which the thin separative layer is strongly attached to a thicker and thus mechanically stronger macroporous support.

Inorganic or ceramic membranes have some great disadvantages over polymer membranes (e.g. brittleness, higher cost, and lower specific surface areas).[4] Therefore, the use of inorganic membranes is in principle restricted to applications in which polymer membranes cannot, or can only with difficulty, be applied. Under more severe conditions high-temperature stability (> 200°C) and resistance against extreme conditions (chemical stability over a wide range of pH levels, aggressive organic media) are required. It can be expected that the above superior properties of inorganic membranes will raise the life-time substantially.[4,5] Moreover, regeneration of the membranes by treatment at high temperatures will be possible.

In several review articles the use of inorganic membranes for combined separation and catalytic processes (membrane reactors) has been forwarded as the great potential application for this new type of membrane.[4-8] Some studies on catalytic membrane reactors have already been published, such as the dehydrogenation reactions over palladium-silver alloy films[9,10] or pure palladium foil,[11] platinum-modified Vycor glass membranes,[12] sol-gel membranes of metal oxides,[13] and silver or vanadia modified sol-gel membranes.[14] For low-temperature catalytic conversions (< 200°C) inert, polymer membranes are available, that may be combined with homogeneously catalyzed reactions in suitable solvents (e.g. heteropoly acids).[15]

1.3 Material Selection for Porous, Inorganic Gas Separation Membranes

Currently, and in particular on an industrial scale, the application of inorganic membranes suffers from several limitations:[4]

- Available only with small membrane surface areas
- Difficult to reproduce
- Examples of pore sizes < 0.5 μm scarce
- Highly expensive
- Not able to be effectively sealed into modules to be operated at temperatures above 250°C
- High surface reactivity

The high surface reactivity is commonly observed with inorganic (ceramic) membranes, since with pores within the nanometer range the material becomes more liable to phase or structural changes as the result of steam attack or of the operating temperature.[7] The sealing problem relates to the large mismatch in material properties of the ceramic membrane and the generally stainless steel housing. It has been claimed to remedy the material compatibility problems by application of multilayer sealings to moderate the differences in thermal expansion.[16]

Several well-known materials have been used as porous (often *amorphous*) inorganic membranes, such as oxidic (e.g. alumina and silica) ceramics, microporous carbons,[17-19] and non-oxide ceramics (e.g. carbides).[20] Leenaars has been one of the first to explore the sol-gel technique for the preparation of inorganic membranes by means of the dip-coating technique.[21] Many studies have now been published on the control of pore size by means of the sol-gel technique,[22-24] in which also other oxides have been included, such as titania and zirconia.[25] Unfortunately, such membranes often suffer from cracks formed during preparation, and the sol-gel technique generally leads to still slightly too large pore sizes. Therefore research has been directed to the modification of the internal surface of the

initially prepared sol-gel membranes or by the deposition of another layer.[5] Recent improvements of the permselectivity have been reported via the modification of γ-alumina films, for instance by magnesia,[26,27] and silica.[28]

The problem to achieve the desired pore diameter in a reproducible way is not restricted to the sol-gel membranes. Each newly prepared membrane material needs to be characterized in order to determine whether the desired pore size has resulted. Very different approaches have been reported, such as the deposition of pure silica layers via sputtering techniques,[29] and the anodizing of thin aluminium foils to prepare alumina films with straight, parallel cylinders with diameter smaller than 6 nm.[30] Mesoporous glass membranes (pore size > 2 nm) can be prepared via selective acid leaching of a solid phase after effecting a heat-induced phase segregation in the glass phase (e.g. Vycor glass).[31] Recently, the preparation of thin hollow fiber glass membranes has been reported with pore sizes within the micropore region.[32,33]

The above examples show that several materials may serve as the membrane material, being either directly deposited or formed via some precursor. Again referring to the above problems in the application of inorganic membranes for gas separation, it can be seen that *crystalline* molecular sieves such as zeolites by-pass two important limitations, viz. reproducibility and pore size. The advantages of zeolites as the membrane material are listed below:

- crystalline material (pores are well-defined by crystallography; yet the lattice exhibits some flexibility)
- large variety in zeolite types with different pore sizes and channel structures
- (thermo)stability (600-1100°C), other properties are generally known and often adjustable (polarity)
- catalytically active sites are often intrinsically present and/or can be introduced via well-known procedures
- much data on sorption and diffusion available

The first zeolite-based membranes consisted of zeolite-filled polymer sheets, in which zeolite crystals were incorporated to enhance the membrane performance of the polymer membrane.[34-37] The adsorption behaviour of the zeolite phase deviates from the dense polymer phase, which has been suggested to lead to more hindered permeation for the species weakly adsorbing within the zeolite phase (higher effective membrane thickness). The strongly adsorbing molecules, on the other hand, accumulate in the zeolite crystals, which may lead to higher fluxes (transport through the zeolite phase). It has been proposed to describe the permeation through these composite membranes by combined resistances connected in series and in parallel.[37,38]

The preparation of inorganic zeolite membranes was only reported in the early eighties, predominantly by H. Suzuki. In a first patent, an ultrathin (>1 nm) zeolite layer was envisaged as to minimize the resistance for flow through the micropores of the membrane.[39] This approach was later on abandoned as the formation of such a continuous ultrathin layer proved hard to accomplish. In a second patent fine zeolite crystals are injected into a porous support and subsequently hydrothermally treated.[40] A variety of approaches has been claimed afterwards, for instance by mixing a binder with zeolite crystallites to obtain an unsupported layer.[41,42] Most patents, however, refer to the direct growth of a zeolite layer on top of a macroporous support (in situ growth).[42-45] Recently, several research groups have reported the preparation of unsupported zeolite layers.[46-48]

1.4 Scope of the Thesis

This thesis describes the development of inorganic zeolite membranes for high-temperature applications. The membrane preparation has been based on two basically different approaches, that are schematically shown in Figure 1. In either approach the selected zeolite type is silicalite-1, the high-silica version of ZSM-5 (MFI-type; MFI is the three letter mnemonic 'Mobil Five' as proposed by the International Zeolite Association to denote the

framework of ZSM-5). Throughout this thesis the name silicalite will be used to denote all-silica MFI. Silicalite can be grown as large single crystals (up to a length of 500 μm), which facilitates the preparation procedure according to Figure 1a. The same zeolite has been selected for the continuous layer approach (Figure 1b).

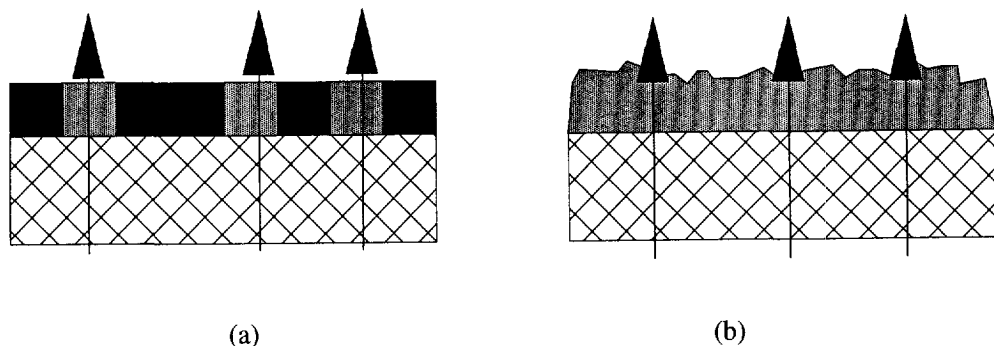(a)   (b)

Figure 1   Schematic representation of the two preparation approaches to an inorganic zeolite membrane: (a) large, oriented single crystals in a gas-tight matrix on a support, and (b) supported, randomly oriented (in situ grown) crystals. Passage sections are indicated by the arrows.

The crystallization of MFI-type zeolites is favourably performed with a template molecule, i.e. tetrapropyl ammonium (TPA) ion. It has to be investigated whether the removal of the template molecules from the framework (by thermal treatment) does not cause formation of cracks within the zeolite crystals. Obviously, such cracks (larger pores) are disastrous for a gas separation membrane. Another important aspect is the thermomechanical behaviour of the zeolite crystals within either membrane configuration. The thermal expansion and strength of the zeolite phase are of paramount importance for the membrane stability during high-temperature application and thermal cycling.

Due to the use of large crystals (as single crystals or a polycrystalline layer) the thickness of the membrane layers will be at least some 50 μm. As transport through micropores is expected to be a rather slow process, accurate data on the diffusion of different species within the zeolite crystals are essential. Moreover, the concomitant passage of two different

molecules within the narrow pores of zeolites may lead to a peculiar permeation behaviour for mixtures. Therefore both sorption and diffusion within separate zeolite (single) crystals, and permeation through prepared zeolite membranes (also of binary mixtures) are dealt with.

The field of membrane technology to which the inorganic (ceramic) membranes belong has been presented in *Chapter 1*. The selection of zeolites as the separating layer for separation on a molecular level has been explained, and the two different approaches for the preparation of zeolite membranes dealt with in this thesis have been introduced.

Chapter 2 discusses the synthesis of large high-silica ZSM-5 (MFI-type) crystals. These large crystals (up to a length of some 500 µm) initiated the preparation of composite membranes, consisting of oriented zeolite crystals on top of a macroporous support, embedded in a gas-tight matrix.

Instead of the use of separately prepared zeolite crystals, the membrane preparation may also be achieved by direct crystallization on a porous support (*Chapter 3*). The effect of the reactivity of aluminosilicate support materials in the hydrothermal synthesis of zeolites is discussed, and compared with more inert materials such as porous stainless steel. It is shown that the optimal membrane preparation is achieved by the direct growth of the zeolite layer in a preformed membrane module, thus avoiding the use of gas-tight sealants during installation of the membrane.

The removal of the template (TPA) from the MFI-framework by calcination in air (activation) is studied by light microscopy and microscope FTIR-spectroscopy in *Chapter 4*. For large MFI-type (single) crystals, the activation gives rise to the development of cracks, which is detrimental to the desired molecular sieve properties of the membrane. Furthermore, the thus far unknown thermomechanical properties of MFI (both as-synthesized and calcined) are studied by powder X-ray diffraction. The results serve to evaluate the thermomechanical stability of MFI-based membranes (*Chapter 5*), and to endeavour to establish a 'safe' calcination procedure for supported MFI-membranes. It

seems that calcination at 400°C in air is sufficient to fully activate the MFI-layer without the occurrence of cracks.

Knowledge on the adsorption and diffusion processes within zeolites is essential for a good interpretation of permeation measurements on zeolite membranes. For this reason, sorption and diffusion processes within one single zeolite (MFI) crystal are studied by microscope FTIR-spectroscopy (*Chapter 6*).

The permeation through zeolite membranes is discussed in *Chapter 7*. First, the mass transport through zeolites as membranes is considered from a step-wise permeation model. Based on purely intracrystalline diffusion, a mathematical model for permeation is proposed, in order to relate the observed permeation rates to the current theory. The permeation results for some prototype membranes are presented, and finally the molecular sieve properties of the MFI/stainless steel membranes in the high-temperature membrane module are demonstrated and discussed.

1.5 Literature

1. H.K. Lonsdale, *J.Membrane Sci.*, 10 (1982) 81.
2. H.K. Lonsdale, U. Merten, and R.L. Riley, *J.Appl.Polymer Sci.*, 9 (1965) 1341.
3. S.T. Hwang, and K. Kammermeier, *Membranes in Separations*, Techniques of Chemistry, Vol. 7, A. Weissberger (Ed.), Wiley-Interscience, 1975, 91.
4. J.N. Armor, *ChemTech*, (1992) 557.
5. A.J. Burggraaf, K. Keizer, R.S.A. de Lange, Z.A.E.P. Vroon, and V.T. Zaspalis, in: J.B. Higgins, R. von Ballmoos, and M.M.J. Treacy (Eds.), Proc.9th Int.Zeol.Conf., Butterworth-Heinemann, Stoneham, Massachusetts, 1992, in press.
6. H.P. Hsieh, *AIChE Symp.Ser.*, Vol. 85, 268 (1989) 53.
7. H.P. Hsieh, *Catal.Rev.-Sci.Eng.*, 33 (1991) 1.
8. J.N. Armor, *Appl.Catal.*, 49 (1989) 1.
9. B.J. Wood, *J.Catal.*, 11 (1968) 30.
10. S. Uemiya, T. Matsuda, and E. Kikuchi, *J.Membrane Sci.*, 56 (1991) 315.
11. R. Zhao, N. Itoh, and R. Govind, in: *Novel Materials in Heterogeneous Catalysis*, R.T.K. Baker, and L.L. Murrell, (Eds), ACS Symp.Ser. Vol. 437, ACS, Washington D.C., 1990, 216.
12. Y.M. Sun, and S.J. Khang, *Ind.Eng.Chem.Res.*, 27 (1988) 1136.
13. M.A. Anderson, F. Tiscareno-Lechuga, Q. Xu, and C.G. Hill, in: *Novel Materials in Heterogeneous Catalysis*, R.T.K. Baker, and L.L. Murrell, (Eds), ACS Symp.Ser. 437,

ACS, Washington D.C., 1990, 198.

14. V.T. Zaspalis, PhD Thesis, University of Twente, The Netherlands, 1990.
15. I.K. Song, and W.Y. Lee, *Catal.Lett.*, 9 (1991) 339.
16. F.M. Velterop, Dutch Patent Application 9,001,662 (1990).
17. J.E. Koresh, and A. Sofer, *Sepn.Sci.Techn.*, 18 (1983) 723.
18. J.E. Koresh, and A. Sofer, *J.Chem.Soc.Faraday Trans.*, 82 (1986) 2057.
19. M.B. Rao, S. Sircar, T.C. Golden, European Patent Application 428,052 A2 (1990) to Air Products and Chemicals, Inc.
20. A.B. Shelekhin, E.J. Grosgogeat, and S.T. Hwang, in: *Inorganic Membranes*, A.J. Burggraaf, J. Charpin, and L. Cot (Eds), Proc. 2nd Int.Conf. on Inorg.Membr., Key Eng.Mat. Vol. 61&62, Trans Tech Publ., 1991, 1.
21. A. Leenaars, PhD Thesis, Twente University, The Netherlands, 1984.
22. A. Larbot, J.P. Fabre, C. Guizard, and L. Cot, *J.Membrane Sci.*, 39 (1988) 203.
23. M.A. Anderson, M.J. Gieselmann, and Q. Xu, *J.Membrane Sci.*, 39 (1988) 243.
24. L.C. Klein, and N. Giszpenc, *Ceramic Bull.*, 69 (1990) 1821.
25. A. Larbot, J.P. Fabre, C. Guizard, L. Cot, and J. Gillot, *J.Am.Ceram.Soc.*, 72 (1989) 257.
26. R.J.R. Uhlhoorn, PhD Thesis, Twente University, The Netherlands, 1990.
27. K. Keizer, R.J.R. Uhlhoorn, and A.J. Burggraaf, *J.Membrane Sci.*, 39 (1988) 285.
28. R.S.A. de Lange, J.H.A. Hekkink, K. Keizer, A.J. Burggraaf, in: *Inorganic Membranes*, A.J. Burggraaf, J. Charpin, and L. Cot (Eds), Proc. 2nd Int.Conf. on Inorg.Membr., Key Eng.Mat. Vol. 61&62, Trans Tech Publ., 1991, 77.
29. W.F. Maier, M. Wiedorn, and H.O. Schramm, *Angew.Chem.*, 103 (1991) 1523.
30. Y.F. Chu, E. Ruckenstein, *J.Catal.*, 41 (1976) 384.
31. R. Schnabel, A. Hölzel, and K. Gotter, German Patent Appl. 2,462,567 A1 (1977) to Jenaer Glaswerk Schott.
32. J.J. Hammel, US Patent 4,853,001 (1989) to PPG Industries.
33. J.D. Way, and D.L. Roberts, *Sepn.Sci.Techn.*, 27 (1992) 29.
34. G. Christen, A. Fabre, and A. Faure, French Patent 7,003,548 (1971) to Rhone-Poulenc.
35. H.J.C. te Hennepe, M.H.V. Mulder, C.A. Smolders, D. Bargeman, and G.A.T. Schroeder, European Patent Appl. 254,758 (1986) to SETEC B.V.
36. E. Drioli, L. Nicolais, F. Perone, and M. Narkis, *J.Membrane Sci.*, 5 (1979) 349.
37. H.J.C. te Hennepe, PhD Thesis, Twente University, The Netherlands, (1988).
38. E.L. Cussler, *J.Membrane Sci.*, 52 (1990) 275.
39. H. Suzuki, European Patent Appl. 135,069 (1984).
40. H. Suzuki, European Patent Appl. 180,200 (1985).
41. G. Bellussi, F. Buonomo, A. Esposito, M.G. Clerici, U. Romano, European Patent Appl. 265,018 (1987) to Eniricerche.
42. K. Miyazaki, Japanese Patent 60,129,119 (1985) to Matsushita Denki Sangyo K.K.
43. S. Sakurada, N. Tagaya, T. Maeshima, and T. Isoda, Canadian Patent 1,235,684 (1988) to Toa Nenryo Kogyo K.K.
44. R. Schulten, and L. Lücke, German Patent Appl. 3,827,049 A1 (1990).

45. S.A.I. Barri, G.J. Bratton, and T. de Villiers Naylor, European Patent Appl. 481,660 A1 (1991) to British Petroleum.
46. (a) W.O. Haag, and J.G. Tsikoyiannis, US Patent 5,019,263 (1991) to Mobil Oil; (b) J.G. Tsikoyiannis, and W.O. Haag, *Zeolites*, 12 (1991) 126.
47. F. Crea, R. Aiello, A. Nastro, and J.B. Nagy, *Zeolites*, 11 (1991) 521.
48. T. Sano, Y. Kiyozumi, M. Kawamura, F. Mizukami, H. Takaya, T. Mouri, W. Inaoka, Y. Toida, M. Watanabe, and K. Toyoda, *Zeolites*, 11 (1991) 842.

2. Zeolite Synthesis and Zeolite Single Crystal Membranes

The step-wise preparation of inorganic zeolite membranes, based on separately synthesized large silicalite (MFI-type) crystals, is reported. An array of individual silicalite crystals is arranged as a monolayer on top of a macroporous support with the zeolite channels perpendicular to the surface of the support. In between the crystals a gas-tight ceramic matrix is deposited in order to ensure mass transport to proceed exclusively via the zeolite micropores. Various thin film techniques such as sol-gel, Chemical Vapour Deposition (CVD), and glazing techniques have been applied so as to achieve a selective deposition between the zeolite crystals, resulting in a two-step membrane preparation procedure.

2.1 Introduction

This chapter deals with the preparation of zeolite-based inorganic composite membranes as shown in Figure 1. The membrane consists of a monolayer of oriented zeolite crystals in a gas-tight inorganic matrix on a macroporous support.

gas tight matrix

zeolite crystals
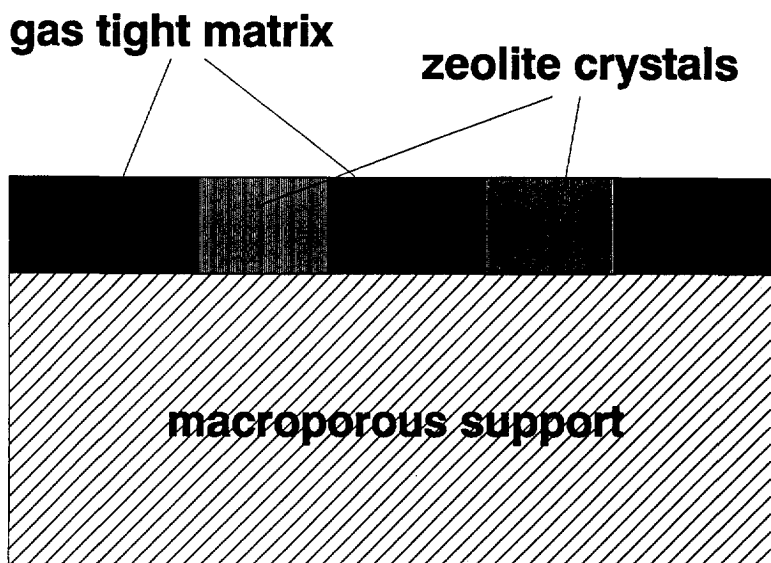
macroporous support

Figure 1   Schematic view of the composite zeolite single crystal membrane

The preparation involves three separate stages (cf. Figure 2): (I) synthesis of zeolite crystals of equal shape and size, (II) orientation and fixation of zeolite crystals on top of a macroporous or mesoporous support, and (III) deposition of a gas-tight matrix material, either selectively in between the zeolite crystals, or as a homogeneous film covering both the zeolite crystals and the macroporous support. Selective deposition of matrix material is favoured, because it does not require the subsequent removal of matrix material from the zeolite crystals by polishing or (plasma) etching as a final preparative step. In this chapter deposition techniques are presented aiming at a selective deposition in between the zeolite crystals.
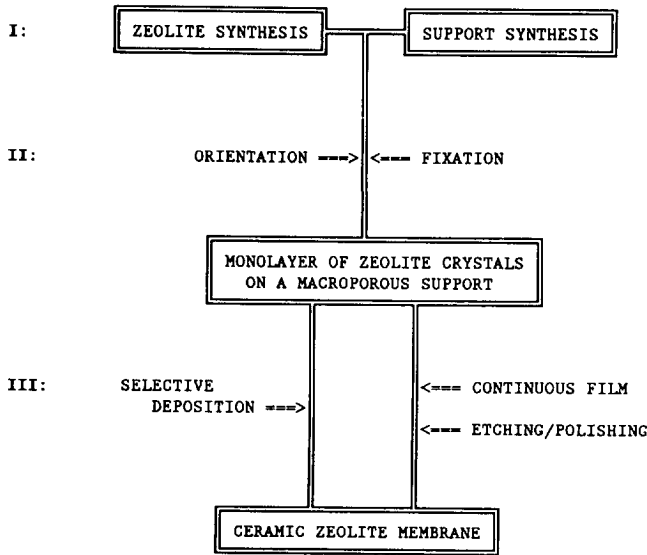
Figure 2   Overview of the preparative steps for composite zeolite membranes

2.2 Zeolite Synthesis

A substantial number of publications has been devoted to the synthesis of zeolites and related crystalline molecular sieves.[1-3] Parameters such as the Si/Al ratio, the mineralizing agent, the structure directing template molecules, and the incorporation of other atoms have been studied extensively. When the framework is based on other elements as with aluminium phosphates[4,5] or metal sulfides,[6] the general name of crystalline molecular sieves is used.

The synthesis of large single crystals has been pursued for specific studies such as X-ray diffraction (XRD) single crystal structure analysis,[7-9] adsorption and diffusion processes within several uniformly shaped crystals[10] or within one single crystal by microscope FTIR-spectroscopy (cf. chapter 6), and for the preparation of zeolite membranes.[11-13]

2.2.1 Pore Structure and Crystal Form

As the zeolite crystals are oriented on a basically flat surface, the pore structure, as related to the crystal morphology and form, is an essential parameter. Zeolites with a three dimensional pore system are in many cases regularly shaped as cubes (zeolite A, LTA) or octahedra (zeolite X and Y, FAU). With analcime (ANA) more crystal faces can be observed (cf. Figure 3). When the pore channels are only present in one or in two directions the crystal form is often elongated. Many zeolites with a one dimensional pore system ($AlPO_4$-5, AFI; zeolite L, LTL), or one main channel (mordenite, MOR; ferrierite, FER) crystallize as acicular particles with the pore direction parallel to the long axis of the crystal, requiring a unique orientation of the crystals on the support.

A special case is ZSM-5/silicalite (MFI). The crystal lattice contains straight [010] and sinusoidal [100] channels in the b- and a-direction, respectively, which are connected by intersections. Despite the two dimensional pore system, mass transport can also proceed in the [001] or c-direction, because the sinusoidal channels are oriented within the (010) plane. For this research silicalite (Si-rich ZSM-5) has been chosen as the starting zeolite material for a number of reasons: (i) relatively large crystals of equal shape and size can be synthesized in high quantities, (ii) the pore structure in connection with the highly controllable crystal form is optimal for the present membrane concept, and (iii) silicalite remains stable up to at least 900° C.[14] In Table 1 some chemical and physical properties of ZSM-5/silicalite are listed.
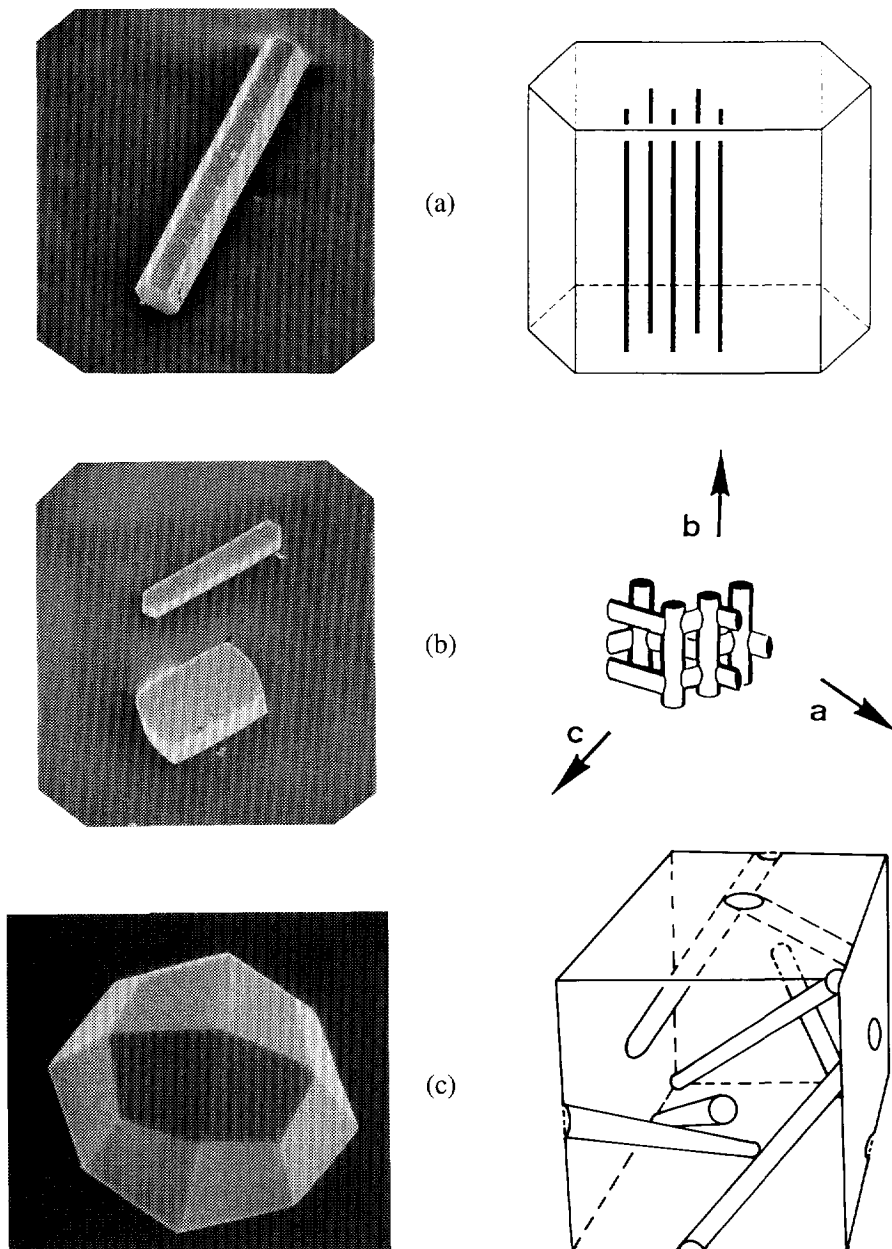
Figure 3   SEM-pictures of zeolite crystals with different dimensional pore systems
(a) 1-D: AFI, (b) 2-D: MFI, (c) 3-D: ANA

Table 1   Characteristics of the as-synthesized (TPA-ZSM-5)[7] and calcined
(H-ZSM-5)[8] silicalite/MFI-type framework

	TPA-ZSM-5	H-ZSM-5
Structure	orthorhombic	monoclinic
Space group	Pnma	$P2_1/n.1.1$
Lattice parameters (Å)		
a	20.022	19.879
b	19.899	20.107
c	13.383	13.369
ß		90.67°
Channel size (Å) (minimal-maximal)		
sinusoidal (a-direction; [100])	5.55-5.29	5.89-5.01
straight (b-direction; [010])	5.22-5.75	5.83-5.27
Density (g/cm^{-3})$^{\#}$	2.06	1.80
Micropore volume (cm^3/g) N_2-adsorption at 77 K	-	0.184
Adsorption volumes$^{\$}$ (molecules/u.c.) / (cm^3/g)		
methanol	-	0.193 / 27.6
n-butane	-	0.190 / 10.9
n-hexane	-	0.199 / 8.8
benzene	-	0.134 / 8.7

\#   theoretical values: TPA-ZSM-5 including 4 TPAOH molecules/unit cell (u.c.);
H-ZSM-5 for the anhydrous framework

\$ calculated from normal liquid densities at the adsorption temperature (room
temperature); data obtained from Flanigen et al.[14]

2.2.2 Synthesis of Large Silicalite Crystals

Argauer and Landolt reported the first crystallization of ZSM-5 in 1972.[15] Although several
other templates can be used, the tetrapropyl ammonium ion (TPA) is optimal to synthesize
large crystals with a broad spectrum of chemical compositions (i.e. other metal atoms
instead of Si). The position of TPA in the as-synthesized framework (at the intersections,

with the alkyl chains pointing towards the straight and sinusoidal channels) agrees with the structure-directing property of a template molecule. Synthesis procedures for the preparation of large MFI crystals are summarized in Table 2, which demonstrates the possible variation in the chemical composition of the synthesis mixture.

Table 2   Synthesis procedures for large MFI-type zeolites according to the literature

Reactants	Gel composition (molar ratio)	Conditions	Product length c-axis	Ref.
Ludox AS-40, NH$_3$, TPABr	100 SiO$_2$: 4.4 (TPA)$_2$O : 67 (NH$_4$)$_2$O : 830 H$_2$O	180°C 48 hours	prisms <35 μm	16
Ludox LS-30 NaOH, TPABr, NH$_4$CH$_3$COO	100 SiO$_2$: 2.5 (TPA)$_2$O : 7.8 Na$_2$O : 1380 H$_2$O (Si/NH$_4$CH$_3$COO = 9.5)	200°C 65 hours	90° inter-grown prisms or cubes 15 μm	17
Aerosil TT600, NaAlO$_2$, TPABr, NaOH	100 SiO$_2$: 4 Al$_2$O$_3$: 177 (TPA)$_2$O : 179 Na$_2$O : 16000 H$_2$O	187°C 240 hours	cubes 160 μm	18
Ludox AS-40, NaOH, TPABr	100 SiO$_2$: 2.6 (TPA)$_2$O : 2.25 Na$_2$O : 2830 H$_2$O	185°C 168 hours	prisms 400 μm	19
Ludox AS-40, NH$_3$, TPABr	100 SiO$_2$: 6.8 (TPA)$_2$O : 294 (NH$_4$)$_2$O : 1460 H$_2$O	180°C 96 hours	prisms 285 μm	20
Aerosil 130, NH$_4$HF$_2$, TPABr	100 SiO$_2$: 6 (TPA)$_2$O : 7.4 (NH$_4$)$_2$O : 3260 H$_2$O (Si/F = 3.4)	165°C 36 hours	prisms 800 μm	21
Ludox AS-40, TPAOH, NH$_3$, VO(H$_2$O)$_5$SO$_4$	100 SiO$_2$: 5.5(TPA)$_2$O : 5.5 (NH$_4$)$_2$O : 1200 H$_2$O (V/Si = 0.02)	180°C 72 hours	cubes 60 μm	22

When no aluminium is added to the synthesis mixture, crystals can be prepared which are larger as compared to the ZSM-5 synthesis.[19,20] The crystal growth history of the two well-

known crystal forms of MFI (elongated prism and cube) as shown in Figure 3b is very different. Elongated prisms are obtained from a dispersed low-density gel, whereas cube shaped crystals are formed from a dense silica gel phase due to the presence of trivalent cations, such as Al^{3+}, Fe^{3+}, or Cr^{3+} in the synthesis mixture.[23] Cube shaped crystals are considered to be single crystals, and are, therefore, used in XRD single crystal structure analysis.[7-9,18] MFI crystals show a tendency to form additional (100) crystal faces on the (010) face, which may be referred to as 90° intergrown crystals.[24] Thus, additional sinusoidal channels are introduced on the external zeolite surface.

In this work different procedures have been applied to synthesize large silicalite crystals (Table 3 and Figure 4). Prismatic shaped crystals are prepared from mixtures containing either hydroxide[16] or fluoride[17] ions as the mineralizing agent. In the presence of hydroxide the crystals are present together with a gel phase, that can be dissolved by alkaline treatment (70-80°C, 0.5 M NaOH). In the case of fluoride the silicalite crystals can be filtered from a clear solution, and are subsequently washed with water and then ethanol and dried under ambient conditions. For low fluoride concentrations additional (0kl) crystal faces are observed, and the particle size distribution is broader. In all cases intergrown material (still with a prismatic morphology) results besides separate prisms. The synthesized prismatic shaped crystals with the desired narrow particle size distribution are subsequently separated by ultrasonic sifting (ATM Sonic Sifter L3P) using sieve meshes of 38, 45, and 75 μm.

Large cube shaped single crystals have been prepared from dilute mixtures at a high pH,[18] but the crystalline product consists of cubic crystals of various sizes and more irregularly formed (intergrown) material. The crystals are obtained from a clear solution, and treated as described above. Ultrasonic sifting is not effective, and the crystals may be selected manually. Much smaller cube shaped crystals (VS-1) are prepared in large quantities by introducing vanadium in the synthesis mixture.[22] The crystallization proceeds from a dispersed silica gel, and requires also dissolution of the gel phase. With longer crystallization times the gel phase disappears, but then the crystals tend to be more intergrown. The optimized synthesis mixture results in almost exclusively non-intergrown cubes (Table 3; V-containing silicalite) with a very narrow crystal size distribution. Similar

to trivalent cations,[23] the presence of vanadium or rather vanadate ions (VO^{2+}) seems to change the nature of the dispersed silica gel phase, perhaps leading to the local formation of a high density gel from which crystallization proceeds. Also large 90° intergrown cubes can be formed (Figure 4c). For too high vanadium concentrations no MFI material is obtained.[22]

Table 3   Synthesis results for the preparation of large silicalite crystals

| Reactants[#]	Gel composition (molar ratio)	Conditions	Product/Remarks
Ludox AS-40, NH$_4$OH, TPABr	100 SiO$_2$: 4.7 (TPA)$_2$O : 68 (NH$_4$)$_2$O : 1888 H$_2$O	180°C 162 hours	Prisms; 35x30x180 μm + intergrown material
Aerosil 200, NaOH, TPABr	100 SiO$_2$: 112 (TPA)$_2$O : 112 Na$_2$O : 31000 H$_2$O	180°C 120 hours	Cubes: 200x120x350 μm + crystal aggregates
Aerosil 200, HF, TPABr, Pr$_3$N	100 SiO$_2$: 13 (TPA)$_2$O : 3400 H$_2$O (Si/F=0.95; H$_2$O/Pr$_3$N=16)	190°C 120 hours	Prisms: 35x25x140 μm + intergrown material
	100 SiO$_2$: 13 (TPA)$_2$O : 3200 H$_2$O (Si/F=1.2; H$_2$O/Pr$_3$N=15)	190°C 120 hours	Prisms: 50x35x200 μm additional (0kl) faces
Ludox AS-40, NH$_4$OH, TPAOH, VO(H$_2$O)$_5$SO$_4$	100 SiO$_2$: 6 (TPA)$_2$O : 3 (NH$_4$)$_2$O : 1650 H$_2$O (Si/V=48)	180°C 72 hours	Cubes: 35x15x60 μm uniform; (Si/V=117)
	100 SiO$_2$: 6 (TPA)$_2$O : 3 (NH$_4$)$_2$O : 1650 H$_2$O (Si/V=84)	180°C 96 hours	90° intergrown cubes: 100x90x150 μm uniform; (Si/V=125)

[#]   TPABr and TPAOH provided by CFZ, Zaltbommel, The Netherlands; Ludox AS-40 (Dupont); Aerosil 200 (Degussa); NH$_4$OH and NaOH (Baker); HF and Pr$_3$N (Merck); VO(H$_2$O)$_5$SO$_4$ (Janssen)

(a) _____ = 100 μm   (b) _____ = 80 μm

(c) _____ = 60 μm
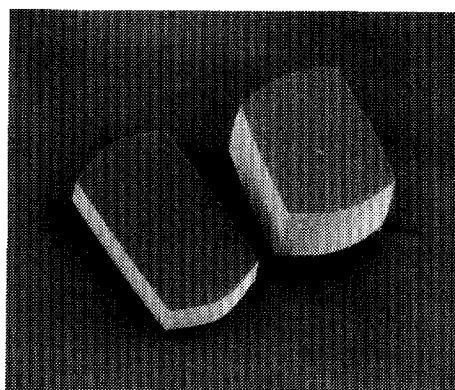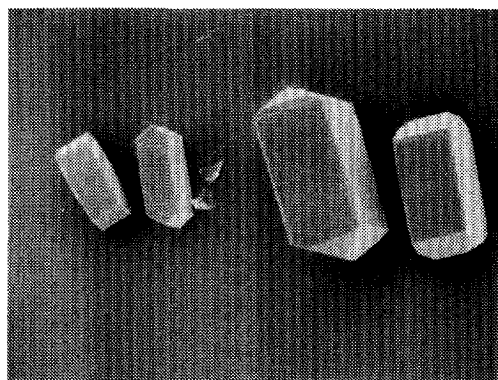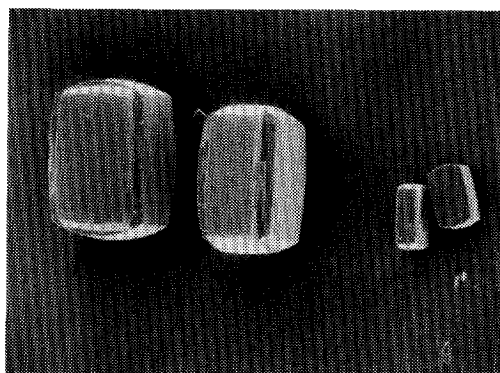
Figure 4   SEM-pictures of the synthesized silicalite crystals
            (a) cube/tile silicalite, (b) fluoride-synthesized, (c) VS-1 (cf. Table 3)

All silicalite samples can be fully activated (removal of TPA) by calcining at 550°C, but for large crystals cracking is observed (cf. Chapter 4). In fact, only the small VS-1 cubes, small silicalite single crystals (< 100 μm), and small hydroxide-synthesized prisms (< 150 μm) have been found to remain crack-free consistently. Large, cube shaped crystals (> 100 μm) have been found to be very liable to crack. If, however, TPABr and NaOH in the

original synthesis mixture are replaced by TPAOH (40% hydrous solution; CFZ, Zaltbommel, The Netherlands), the cube shaped crystals are transformed to rather flat (tile shaped) prisms (100x25x230 μm). These prisms remain generally uncracked upon calcination, even up to 900°C (cf. Chapter 4, section 4.5).

2.3 Orientation and Fixation

The orientation of the MFI crystals in a membrane configuration is important with respect to the two dimensional pore structure. It has been shown that at moderate temperatures (< 60°C) the migration of several molecules (e.g. aromatics) can be restricted to the b-direction.[9,25,26] In addition, the diffusivity of small molecules varies with the different crystallographic directions as a result of the deviating diffusional pathways.[27,28] Silicalite prisms are generally oriented in the a- or b-direction, hence both the straight and the sinusoidal channels will serve as the membrane pores. The cube shaped silicalite single crystals, due to their relatively small [010] length, are normally oriented in such a way that only the straight channels serve as the membrane pores. For 90° intergrown vanadium silicalite cubes, the sinusoidal channels might serve mainly as the membrane pores, because of the additional (100) crystal faces on the (010) external surface of the crystals.

Monolayers of as-synthesized or calcined silicalite crystals (prisms and 90° intergrown VS-1 crystals) can be established on any flat surface, either porous or non-porous. The crystals can be simply spread over the surface, and further orientation is achieved by low frequency-vibrations. Larger silicalite single crystals are positioned manually in the [010] direction. Upon drying, the small VS-1 cubes tend to adhere to each other with the (010) faces, and need to be oriented from suspension. An interesting alternative way of orienting crystals is related to the observed phenomenon that even large crystals remain floating on the water surface. Based on this principle, large surface areas of closely packed MFI crystals can first be oriented, and successively be deposited upon a support by lowering the water level below the surface of the macroporous support.

Orientation is favourably accompanied by bonding (fixation) of the crystals to the support, because fixation reduces the constraints on the final preparative step (formation of a gas-tight matrix in between the zeolite crystals) in two ways: (i) deposition underneath the crystals cannot occur or is strongly reduced, and (ii) strong adherence of the crystals to the support is required for several deposition techniques.

Commercially available two layer α-alumina supports (National Ceramics Centre, NKA, Petten, The Netherlands) with a thin (20 μm) mesoporous top layer (average pore size 0.15 μm) are sufficiently smooth to establish a monolayer of silicalite crystals. After covering the support with oriented zeolite crystals, the pores of the substrate are completely filled with water. Subsequently the support is dried at 50°C in air. The crystals are slightly adhering to the support, which is attributed to condensation reactions between the SiOH groups present at the external surface of the zeolite crystals and the hydroxyl groups on the oxidic (alumina) support, proceeding under these mild conditions.

When stronger adherence between the zeolite crystals and the support is required, a mesoporous interlayer (or precursor material) is first deposited. A separately prepared monolayer of zeolite crystals on a smooth (non-porous) surface is impressed into the deposited and adhering film. After calcination a porous top layer results, partially incorporating the MFI crystal monolayer (Figure 5).

The adhering film can be deposited by a slip casting procedure of a suspension of a ceramic powder (zirconia wash coat, Zyp coatings; clay suspension, Royal Delft Ware, Delft, The Netherlands), or by doctor blading of a solution of a precursor of ceramics (silicone solution; section 2.4.1). Figure 6 shows the monolayer of silicalite prisms on top of a macroporous α-alumina support in a thin clay film after calcination at 900°C. Zeolite surface coverages of approximately 75% have been achieved. In most cases the orientation/fixation process of the zeolite crystals is related to the matrix deposition procedure. Therefore, the former is described in more detail in view of the various deposition techniques as discussed in the next section.
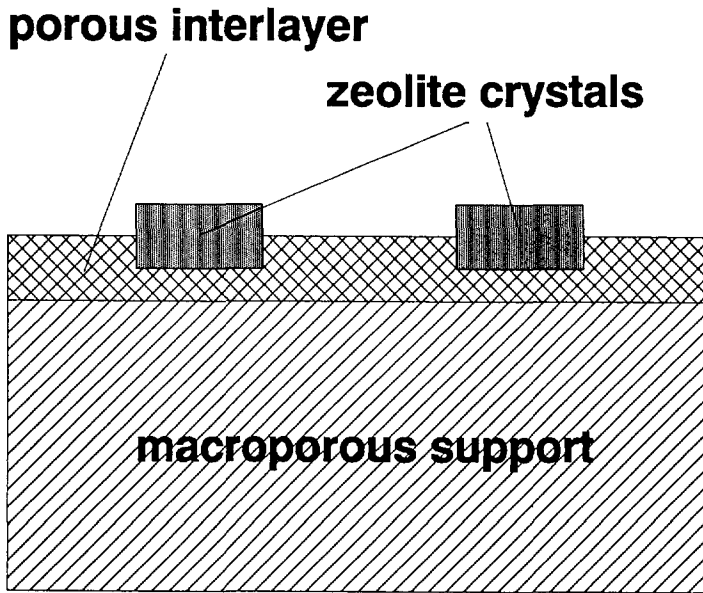
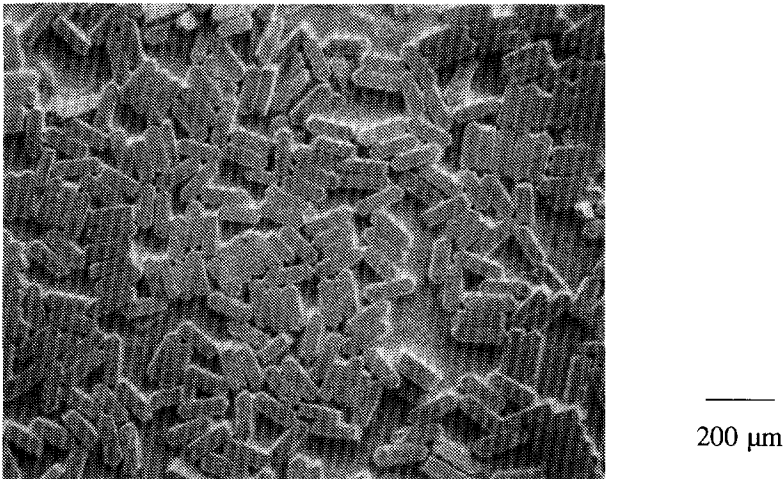Figure 5   Schematic view of zeolite crystals, embedded within a mesoporous interlayer

200 μm

Figure 6   SEM-picture of fluoride-synthesized silicalite prisms, embedded as a monolayer
in a thin clay film on a one layer α-alumina support

2.4 Gas-Tight Matrix Deposition

Two well known deposition techniques have been investigated to effect selective deposition of matrix material in between the zeolite crystals, viz. sol-gel and CVD procedures. Furthermore, as an alternative, the utilization of low-melting glazes has been explored. The first objective for each technique involved the formulation of a compatible matrix/support system as the starting point for the incorporation of the silicalite crystals within the membrane system.

For the sol-gel technique two composite systems have been studied: γ-alumina on α-alumina,[29] and silica on porous, sintered stainless steel supports.[30] As to investigate the use of CVD techniques, the deposition of yttria-stabilized zirconia (YSZ) on porous calcia-stabilized zirconia (CSZ) supports has been performed, generally referred to as Electrochemical Vapour Deposition (EVD).[31,32] The application of low-melting glazes has been studied, because of the simple fine-tuning of the thermomechanical properties of the composite system. For the glazing technique, a compatible matrix/support system has been formulated by optimization of available materials (cf. section 5.4.1).

2.4.1 Sol-Gel Technique

For sol-gel techniques good adhesion of the sol to the external zeolite surface is required, because the gas-tight matrix should be strongly bound to the zeolite phase. On the other hand, the adhesion should not be too strong in order to avoid deposition on top of the zeolite crystals or in between the zeolite crystals and the porous support. The actual deposition of the matrix material depends, however, upon gelation, as a result of the removal of the solvent from the sol phase. Therefore, selective deposition can be achieved when the gelation proceeds exclusively in between the zeolite crystals. Local gelation in between the zeolite crystals has been tried by dip-coating of boehmite sol,[33] and by solvent (ethanol) extraction from a tetraethyl orthosilicate (TEOS) sol by a second liquid phase.[34] Both approaches will be discussed in more detail.

Dip-coating of a γ-alumina film on α-alumina supports

The dip-coating technique, formerly used to prepare high-temperature gas separation membranes exhibiting Knudsen selectivity,[29,35] leads to selective deposition in between the zeolite crystals. The selective deposition is due to the filtering process of sol particles from the suspension, as the suspending liquid is absorbed by the initially dry support. A mesoporous top layer (α-alumina; pore diameter 0.15 μm) is required to smoothen the rough macroporous α-alumina support, and to improve the wetting of the boehmite sol to the support.

Silicalite prisms are oriented on two-layer α-alumina supports by low-frequency vibrations. A slight adherence is achieved by successive absorption of water and drying at 50°C (section 2.3). Large silicalite cubes are positioned with the (010) parallel to the support surface. Dip-coating experiments are performed with a boehmite (γ-AlOOH) sol,[35] and a similar sol to which glycerol (1% by volume) has been added. The optimal dipping time in the sol of 6 seconds (established on reference supports) has been applied in all cases. A careful calcination procedure is required (drying at 35°C for at least 24 hours, subsequently heating at 25°C/h to 100°C, and finally heating at 100°C/h to 500°C). During this calcination procedure the boehmite is transformed into γ-alumina.

The presence of the zeolite crystals results in severely cracked films with the original boehmite sol, whereas only limited cracking occurs in the presence of glycerol (Figure 7a). The reference supports (without crystals) remain uncracked, irrespective of the applied sol. The occurrence of cracks upon drying is attributed to the inhomogeneous shrinkage of the boehmite film near the large silicalite crystals. Moreover, the sharp corners of the silicalite prisms are liable to initiate the cracks.

In Figure 7b it is shown that due to the slight adherence of the silicalite crystals to the mesoporous top layer, no deposition has occurred underneath the zeolite crystals. According to EDAX chemical analysis, no deposition of alumina has proceeded on top of the silicalite prisms. Some alumina is observed by EDAX on the much larger cubes, which is attributed to the larger hold-up of sol on top of the crystals. Apparently, the hold-up of sol depends on the surface area and the shape of the virtually non-absorbing silicalite crystals.
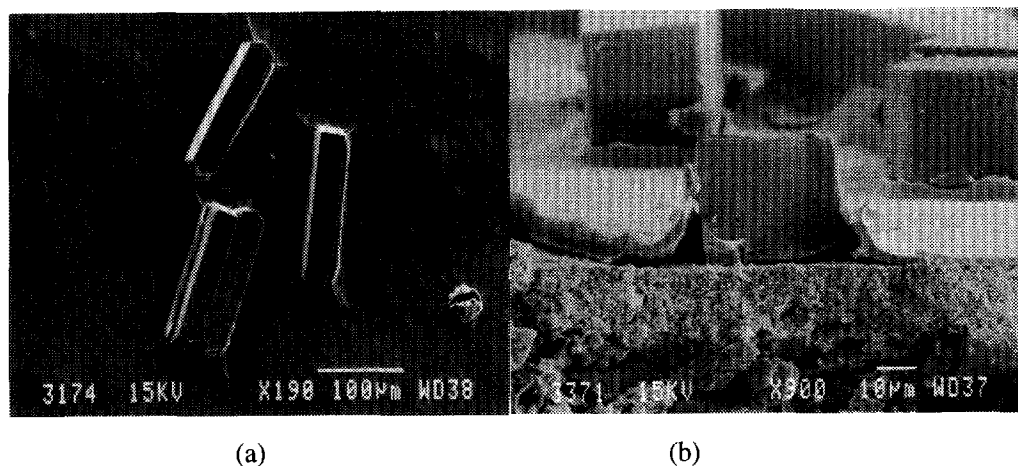
(a)   (b)

Figure 7   SEM-pictures of silicalite prisms on top of a two layer α-alumina support,
            embedded in a cracked γ-alumina matrix (a) top view, (b) cross section,
            revealing the selective deposition in between the zeolite crystals

The initially formed cracks cannot be repaired by a second and similar treatment. After the
second treatment, some alumina is deposited on top of the silicalite prisms as well.
Absorption proceeds much slower into the narrow pores of the γ-alumina top layer after
the first treatment, hence a larger hold-up of sol remains after the second dipping. Although
the porous γ-alumina film is not gas-tight, it demonstrates the applicability of dip-coating
for selective deposition in between the zeolite crystals.

Sol-gel deposition of silica on silica-modified stainless steel supports
An alternative route to direct the gelation between the zeolite crystals makes use of the
immiscibility of a hydrous silica sol with a second liquid that is present within the
macroporous support. The procedure has been developed for the preparation of high-
temperature gas separation silica membranes on porous sintered metal supports.[30,36] The
crystals are fixed to the metal support by means of an adhering silicone (main constituent
polydimethyl siloxane; PDMS, Bison, The Netherlands) phase, which is afterwards calcined
in air to render a mesoporous silica layer.
The silicone layer is applied on top of the porous stainless steel support (AISI 316,

Krebsöge, Germany) by doctor blading, in which a monolayer of silicalite prisms is impressed. Upon calcination at 450°C (heating rate 100°C/h) the zeolite crystals protrude from a thin mesoporous silica film with a narrow pore size distribution (4 nm diameter). The silica interlayer has near to Knudsen type selectivity.[36]

The metal support is temporarily filled with 1,1,1-trichloroethane (TCE), that is immiscible with water, and a TEOS sol (TEOS:H$_2$O:EtOH:HCl = 1:2:8:0.03) is subsequently spread over the support. The solvent (ethanol) dissolves rapidly in TCE, resulting in gelation on top of the support besides the zeolite crystals (Figure 8). However, the resulting silica films turned out to be very sensitive towards cracking upon drying. Even for the above mentioned (optimized) sol composition some cracking occurs, especially when crystals are close to each other.
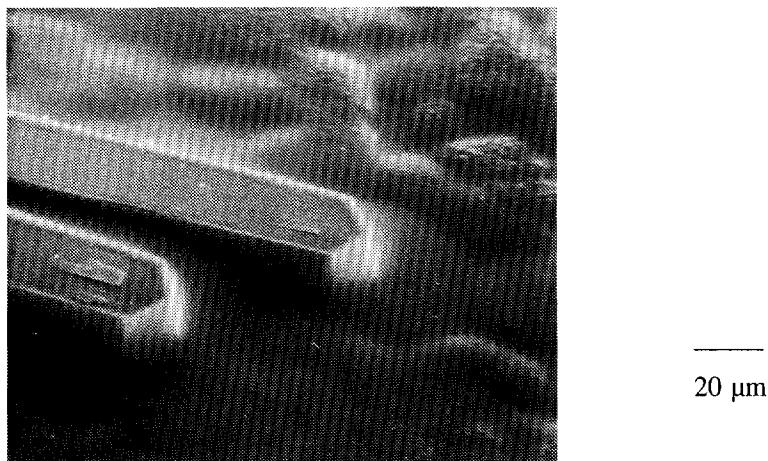

20 µm

Figure 8   SEM-picture (top view) of two silicalite prisms in a silica (sol-gel) matrix on top of a silica-coated stainless steel support

2.4.2 CVD Technique

As deposition by CVD techniques proceeds via the gas phase, even very narrow interstices between zeolite crystals can in principle be closed. A disadvantage is that in general a homogeneous film is deposited, covering both the zeolite crystals and the macroporous support. Moreover, deposition within the MFI micropores might occur as well, although the accessibility of the reactant molecules (metal halides, metal alkyls, or metal alkoxides)
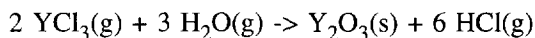
depends strongly on the temperature, and the size and shape of the reacting species.[37] However, the usual CVD process can be modified in such a way that the reactants are introduced on different sides of a porous support. The location of the reaction front can then be controlled to be present on one side of the membrane by differences in diffusivity of the reactants, or by a small pressure difference over the porous support. Formation of the gas-tight matrix between the zeolite crystals should proceed fast if the reactants can diffuse through the zeolite micropores as well, which would result in the deposition of a similar non-porous layer on top of the zeolite crystals. Moreover, neither reactant may give rise to the formation of a gas-tight film via decomposition reactions.
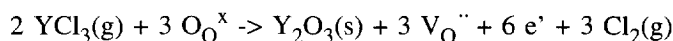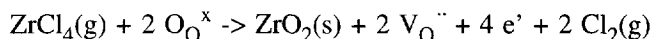
To explore the feasibility of CVD by means of separate introduction of reactants, the deposition of yttria-stabilized zirconia (YSZ) has been investigated. The growth of YSZ has been studied in detail, because YSZ-films are employed in Solid Oxide Fuel Cells (SOFC) as an oxygen ion conducting solid electrolyte[31,32] The chlorides of zirconium and yttrium, and a mixture of steam and oxygen are introduced separately on either side of a macroporous support. The CVD-reaction of YSZ proceeds according to:
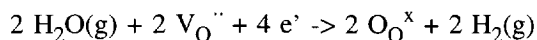
$$ZrCl_4(g) + 2\ H_2O(g) \rightarrow ZrO_2(s) + 4\ HCl(g)$$
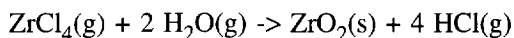
while the dopant (yttrium) is formed via the reaction:

$$2\ YCl_3(g) + 3\ H_2O(g) \rightarrow Y_2O_3(s) + 6\ HCl(g)$$

Initially, the deposition proceeds via the usual CVD process. After the pores are closed, the chemical potential gradient remains over the YSZ layer. Via gas-solid interactions at either side of the layer a gradient in defects arises, which provides the driving force for further growth of a gas-tight matrix between the zeolite crystals (EVD-stage). This stage is represented by the reactions (according to the Kröger-Vink notation):

$$ZrCl_4(g) + 2\ O_O{}^X \rightarrow ZrO_2(s) + 2\ V_O{}^{\cdot\cdot} + 4\ e' + 2\ Cl_2(g)$$

$$2\ YCl_3(g) + 3\ O_O{}^X \rightarrow Y_2O_3(s) + 3\ V_O{}^{\cdot\cdot} + 6\ e' + 3\ Cl_2(g)$$

and

$$2\ H_2O(g) + 2\ V_O{}^{\cdot\cdot} + 4\ e' \rightarrow 2\ O_O{}^X + 2\ H_2(g)$$

Growth proceeds through diffusion of oxygen ion vacancies ($V_O^{\cdot\cdot}$) and electrons (e') from the metal halide side to the steam side. Therefore, this process is referred to as Electrochemical Vapour Deposition (EVD).

Silicalite crystals (both prisms and large single crystal cubes) are oriented on a macroporous calcia-stabilized zirconia (CSZ; Groneman, The Netherlands) support, and are fixed by means of a thin clay film. The zeolite crystals are bound to the support during a calcination step at 900°C (heating rate 1°C/min), since the deposition is carried out at this temperature. The substrate is installed on top of a non-porous α-alumina tube with a gas-tight kit (Aremco 569), with the zeolite crystals facing the metal chloride side and heated to 900°C (heating rate appr. 5°C/min). The EVD process is performed for 1.5 hours. Afterwards, the system is cooled down at the same rate.

A YSZ film has been deposited on top of the macroporous support. Also, some deposition with a different morphology is observed on the zeolite crystals. The YSZ composition has been determined by X-ray diffraction to contain 21 mol% yttrium. This is in agreement with the chemical analysis by Electron Probe Micro Analysis (EPMA) yielding 22 mol% yttrium. Figure 9 shows a cross-sectional view of the composite system.
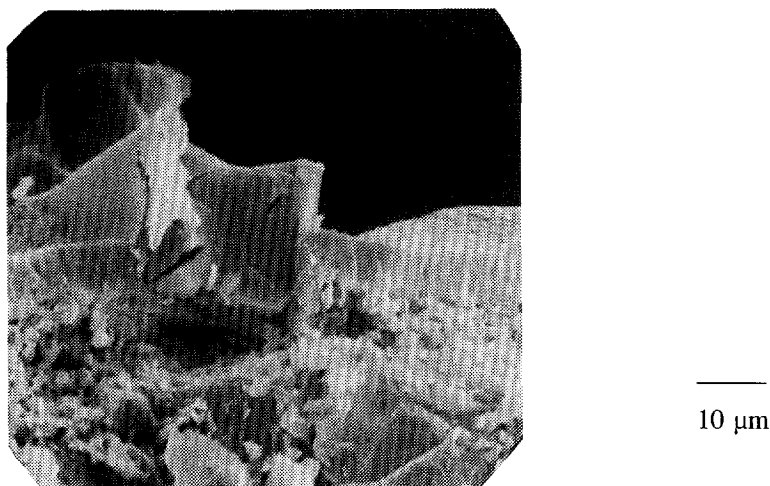

10 μm

Figure 9   SEM-picture (cross section) of a cracked silicalite prism, embedded within a
YSZ matrix on top of a clay-coated CSZ support

The inner section of the silicalite crystal is cracked, whereas the outer part is transformed into an amorphous phase. From EDAX analysis it is concluded that the latter phase consists of silicon, yttrium, and zirconium oxides. In a separate experiment it has been established that the silicalite crystals remain stable at high temperatures when exclusively metal chlorides are present.

In Figure 10 a large cube shaped silicalite crystal is shown on which YSZ material of a similar morphology as on the macroporous support is present. Apparently, the previously mentioned cracks in large silicalite crystals allow for equally fast transport of oxygen to the metal chloride side as through the macroporous support itself. It is concluded that the YSZ deposition on meso- and macropores proceeds in a different way than on micropores, probably as a result of the slower transport rate of oxygen through the zeolite micropores.
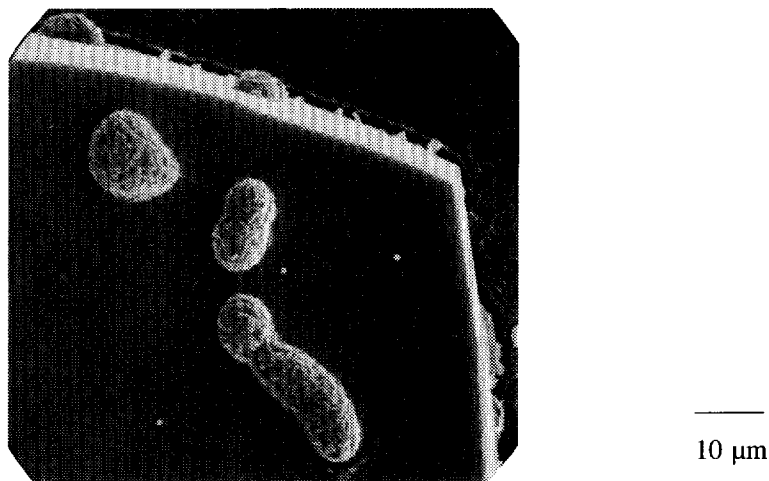

10 μm

Figure 10   SEM-picture (top view) of a silicalite cube within a YSZ matrix; on top of the cube the same YSZ phase is present

2.4.3 Deposition of Glazes

Glazes are commonly used for the production of china (pottery), in which a porous substrate is immersed in a glaze suspension, resulting in a homogeneous layer covering the substrate completely. Upon calcination a continuous glaze layer is formed, both from a melting process and by chemical reactions. Generally, thick glaze layers are applied (well over 100 µm) to ensure total coverage of the substrate. A great advantage of glazes is found in the easy adaptation of the chemical composition for specified properties such as the impermeability for gases[38] or the thermomechanical compatibility.

An often encountered problem in the application of glazes is the occurrence of cracks in the glaze phase as a result of the tensile stresses imposed by the support material. Glazes are in principle more stable upon compressive stresses (cf. Chapter 5), for which reason the thermal expansion of the glaze material is generally substantially lower than that of the substrate. Some selected properties of three in this work applied glazes (provided by Ferro B.V., Rotterdam, The Netherlands) are listed in Table 4. In view of its low melting (application) temperature and low thermal expansion, the lead-boron silicate glaze has been used in particular, although this choice is in part arbitrary.

Two materials have been applied as the basic porous support material: α-alumina (both one and two layer supports) and home-made clay (pottery) disks (original clay suspension provided by Royal Delft Ware). The composition of the clay supports can be varied to optimize the thermomechanical properties (cf. section 5.4.1). In this case the optimization is focused on the formation of thick (> 150 µm), crack-free layers of the above lead-boron silicate glaze. The overall composition of the optimized clay composition amounts to 10.8% kaolin clays, 13.3% ball clays, 4.3% feldspars, 26.1% calcium oxide, 21.1% quartz, and 22.9% cristobalite (weight percentages).

Deposition is generally achieved by spraying a hydrous glaze suspension on a substrate or by immersion. Here, some different ways of deposition have been tried, like applying dry glaze powder onto a surface and pouring a glaze suspension over an initially dry, macroporous support. The latter procedure leads to a reasonably selective deposition. Dip-coating of a dilute glaze suspension, similar to dip-coating of a boehmite sol, however,

proved to result in a highly controlled deposition of thin homogeneous glaze films (< 5 μm). The optimal procedure makes use of a vacuum on one side of the support, while the other side is dipped into a glaze suspension. In this way much longer dipping times, and very dilute suspensions (< 5 m%) can be applied, which is an advantage over the original dip-coating technique (which is limited by the absorption capacity of the support).

Table 4   Properties of different glazes

Glaze	$NaBSiO_4$ 11.37025.09	$PbBSiO_4$[@] 11.35300.09	PbBO-flux V151
Chemical composition (molar ratios)			
Si	100	100	100
Al	0.4	4	2
Na	60	4	8
Pb	1	6	15
B	115	166	223
Glass temperature (°C)[#]	520	425	425
Minimum application temperature (°C)	800	550	500
Thermal Expansion Coefficient[#] $(10^{-7}°C^{-1})$	77	75	85
Permeability at 22°C (mol.m/m^2.s.Pa)			
H_2	$9.5*10^{-16}$	$12.2*10^{-14}$	
N_2	$<2.5*10^{-15}$	$3.4*10^{-14}$	
CH_4[&]		$4.5*10^{-14}$	$<10^{-14}$
CF_2Cl_2		$2.0*10^{-14}$	

[@]   lead-boron silicate glaze
[#]   data from Ferro B.V., Rotterdam, The Netherlands
[&]   value for PbBO-flux measured in a Wicke-Kallenbach configuration (no pressure difference)

The thermal treatment of the glaze powder after deposition to produce a continuous glaze layer can be controlled by three parameters, viz. the heating rate, the maximum calcination temperature, and the dwell period at the maximum (burning) temperature. Figures 11a-d show the results of some different thermal treatments for the lead-boron flux (M-151), in which the heating and cooling rates are equal.
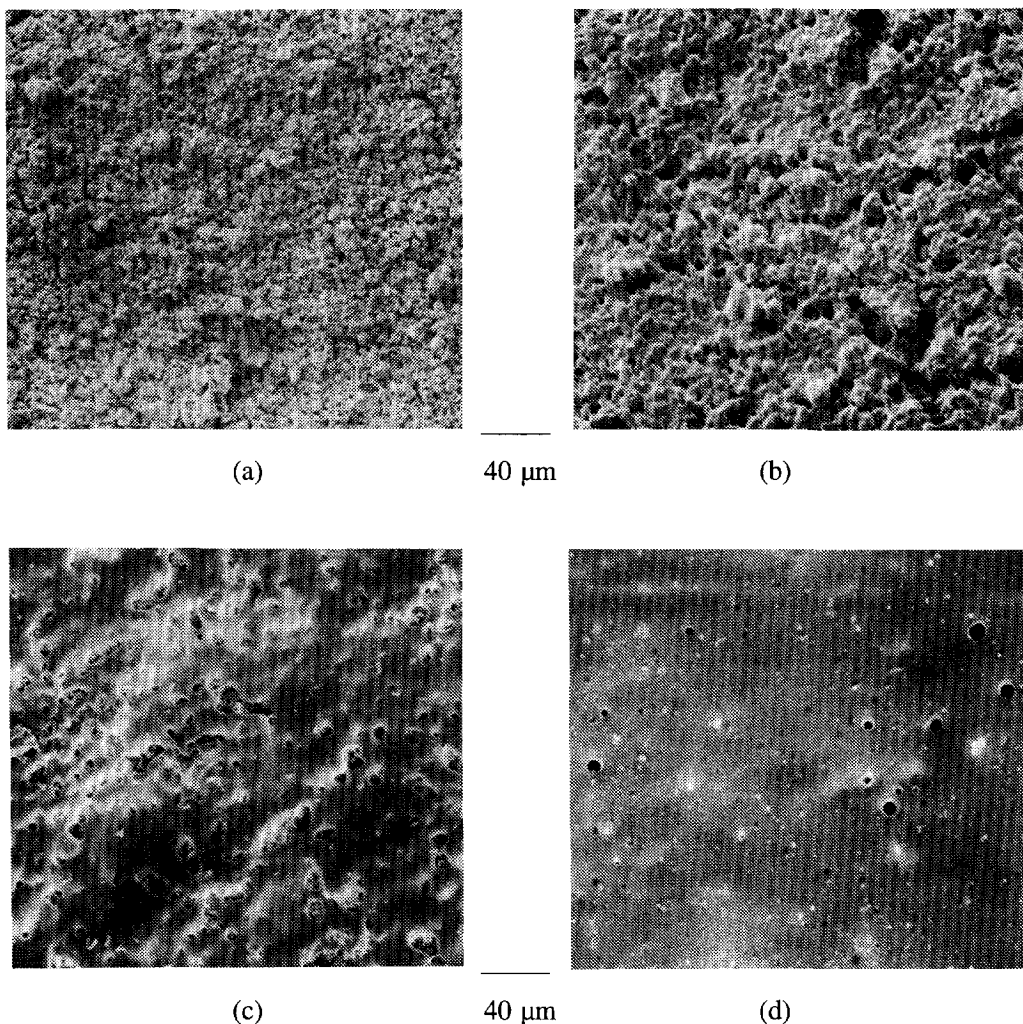

(a)   40 μm   (b)

(c)   40 μm   (d)

Figure 11   SEM-pictures of lead-boron flux (M-151) layers after different heat treatments: (a) 4°C/min to 525°C, no dwell; (b) 6°C/min to 550°C, no dwell; (c) 4°C/min to 550°C, no dwell; (d) 4°C/min to 525°C, dwell 30 min

35

At a relatively fast heating rate up to the minimal burning temperature (4°C/min, 525°C, no dwell; Figure 11a) a slight sintering of the glaze material does occur. At a somewhat higher heating rate and burning temperature (6°C/min, 550°C, no dwell; Figure 11b), the glaze particles are partly aggregated to a layer of a high porosity. When the melting process starts before the maximum temperature is reached, the total time at and above the application temperature should be considered as part of the dwell time (4°C/min, 550°C, no dwell; Figure 11c). In fact, only short dwell times are needed to form a near to completely smooth glaze layer (4°C/min, 525°C, 30 minutes; Figure 11d). Besides melting of the glaze particles, chemical reactions may occur as well, from which gases are produced.[39] These gases, and volatiles released by the support material, may be trapped within the highly viscous glaze melt, leading to bubbles or even a glaze foam. For this reason the clay material (both as a support and as a thin interlayer) has to be calcined up to at least 900°C to avoid the production of volatiles such as CO_2 and H_2O. The optimal heat treatment as determined for the lead-boron silicate glaze has been applied in all experiments in the following section, and involves heating at 1°C/min up to 550°C with a dwell time of 60-180 minutes.

Figures 11a-d also demonstrate the glazing behaviour upon the thermal treatment. The glaze particles tending to form aggregates upon thermal treatment suggest that the cohesion forces between the melting particles are strong. Thin glaze layers, therefore, inevitably will contain pinholes, although such leaks can be closed by a second glazing procedure. The wetting behaviour of the glaze melt is in fact quite complex, and introduces several limitations to the application of glazes. In the first place, the silicalite crystals have to be fixed to the support as it has been frequently observed that they (both small prisms and large cubes) are drawn into the glaze melt at one edge, leaving an open space on the macroporous support (Figure 12a). The slight adherence to the α-alumina mesoporous top layer is not sufficient for the crystals to remain in the required position. In some cases the crystals are lifted from the support by the strong adhesion forces of the glaze melt (Figure 12b).

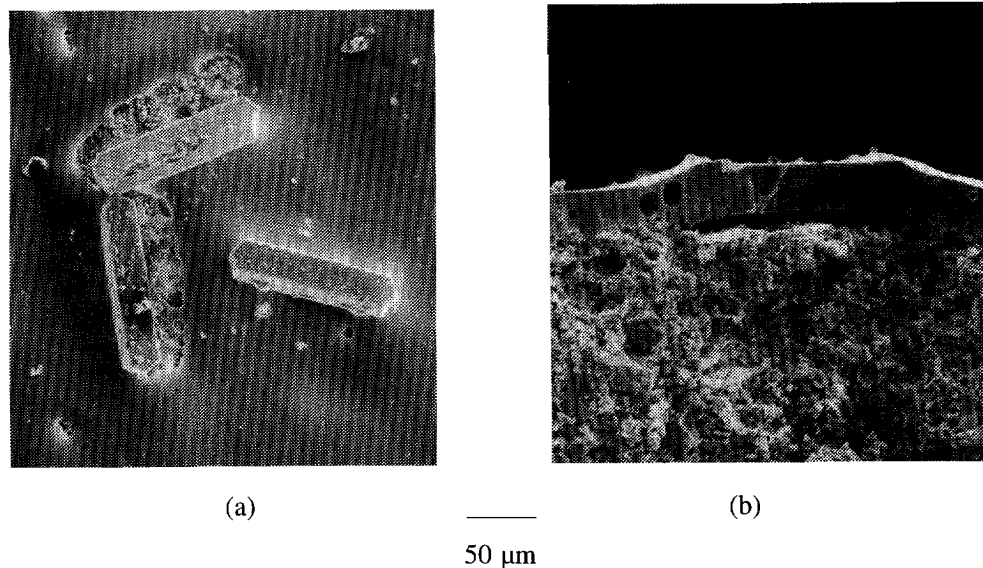(a)   _____   (b)

50 µm

Figure 12   SEM-pictures of silicalite/glaze/clay composites, demonstrating the adherence
behaviour during thermal treatment: (a) silicalite prisms, rotated by the glaze
melt (top view); (b) silicalite tile, lifted by the glaze melt (cross section)

Therefore, strong fixation of the crystals within a porous interlayer is essential to apply

glazes successfully. The zirconia and clay suspensions as mentioned in section 2.3 have

been used as a porous interlayer. However, the presence of a zirconia interlayer on either

α-alumina or clay resulted in cracked glaze layers. Apparently, zirconia, applied as a

mesoporous interlayer, gives rise to a reduced thermomechanical compatibility between the

glaze and the macroporous support. In addition, the wetting of zirconia by the glaze melt

is poor. This may, however, be partly attributed to the fact that the level of the porous

interlayer around the crystals is slightly higher than elsewhere on the support (Figure 13).

As the crystals are pressed into the mesoporous layer, the interlayer material around the

crystals is slightly lifted. Hence, the glaze melt may flow away from the zeolite crystals,

if the wetting of the zeolite surface by the glaze melt is poor. As the adherence between

the glaze and clay material is excellent, the latter material is favourably used as the
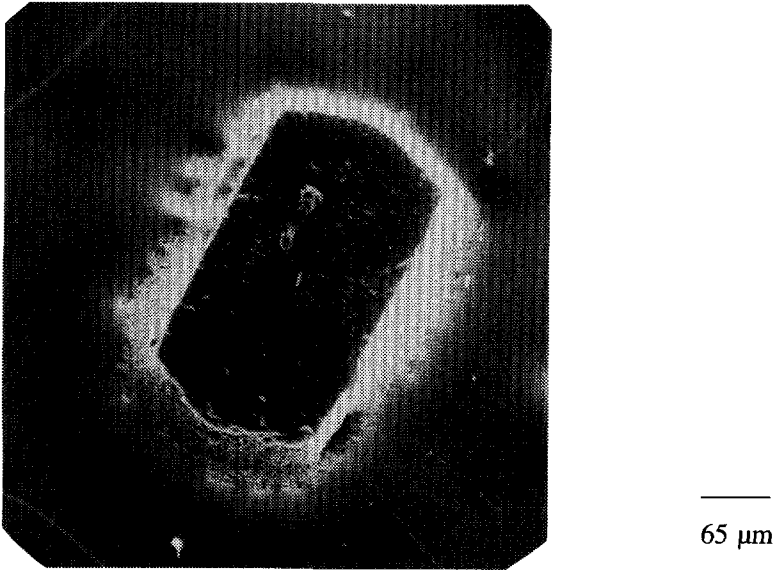
mesoporous interlayer.

65 µm

Figure 13   SEM-picture (top view) of a silicalite tile on a zirconia-coated α-alumina
support

Several experiments have been performed using large tile shaped silicalite crystals to investigate the thermomechanical stability of the zeolite/glaze/support composite system. A number of crystals is manually positioned on a thin and nearly dry clay film, deposited on top of either a clay or an α-alumina support. The crystals can be randomly oriented and are not pressed into the interlayer. Next, the support is repleted with water, and due to the adhesion forces (water and silicalite), the crystals are uniquely oriented with the ac-plane parallel to the surface of the support. Thus, the angle between the zeolite crystal side faces and the porous support is nearly 90°, which prevents the glaze melt from flowing away from the silicalite crystals. After drying and calcining at 900°C a relatively thick lead-boron silicate glaze layer is deposited besides the zeolite crystals as described above. The glazing procedure is once repeated to obtain a fully covered macroporous support.

When α-alumina serves as the macroporous support some cracks are observed in the glaze film besides the zeolite crystals (Figure 14).

65 μm
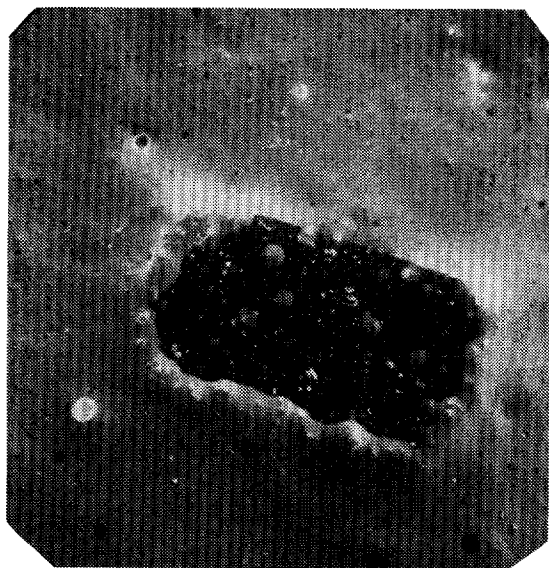
Figure 14   SEM-picture (top view) of a silicalite tile on a clay-coated α-alumina support; within the surrounding lead-boron silicate glaze matrix some cracks are visible

In the case of a clay support, the glaze material that is partly covering the silicalite top face (thick film) reveals some cracks (Figure 15a). Smaller silicalite prisms of some 160 μm length, however, are embedded in a completely crack-free glaze film (Figure 15b). These observations are discussed in view of the thermomechanical theory in Chapter 5 (section 5.4).

For scaling-up of this type of inorganic zeolite membrane the use of the α-alumina support is favoured for its high (open) porosity. The α-alumina support, the clay interlayer, the lead-boron silicate glaze and the silicalite prisms are compatible, provided small crystals and thin glaze layers are applied (< 5-10 μm). In Figure 16 a four layer composite system is shown, that is prepared by (i) orienting a monolayer of silicalite prisms on a two layer α-alumina support, (ii) slightly adhering the crystals to the α-alumina top layer by successive absorption of water and drying, (iii) dipping in a dilute clay suspension and calcining at 900°C for strong fixation to the support, and (iv) dipping in a lead-boron silicate glaze suspension and calcining at 550°C. The final preparation step is repeated to obtain a fully closed top layer.
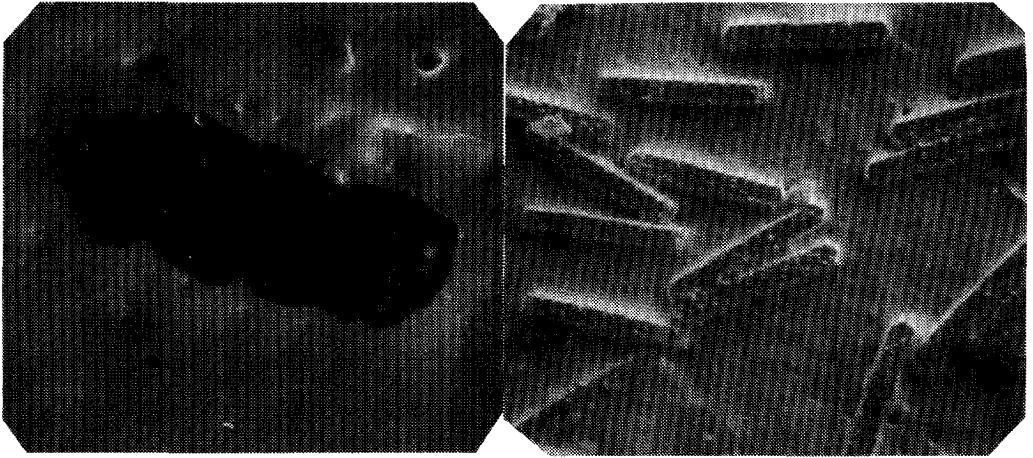
(a) _____ = 40 µm   (b) _____ = 65 µm

Figure 15   (a) SEM-picture of a silicalite tile on top of a clay support (top view): the glaze on top of the crystal is cracked in the c-direction; (b) SEM-picture of silicalite prisms on top of a clay-coated α-alumina support (top view), embedded within a lead-boron silicate glaze matrix (no cracks)
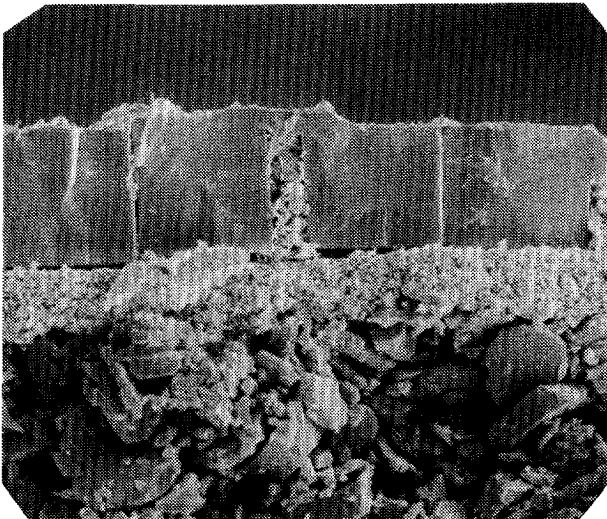
_____
15 µm

Figure 16   SEM-picture (side view) of four silicalite prisms on a clay-coated, two layer α-alumina support; the lead-boron silicate glaze is present on top of the clay phase

Either silicalite prisms (< 150 µm) or the small VS-1 cubes may be applied. The latter are favoured for both the typical crystal dimensions and the narrow particle size distribution of the resulting crystals, which does not require further processing.

The stability of silicalite is essential, as the microporous nature has to be preserved after all preparative steps. Powder X-ray diffraction on different silicalite samples after calcination at 900°C does not suggest any degeneration, in accordance with the literature.[14] The adsorption behaviour of a silicalite single crystal membrane model has been studied by FTIR-spectroscopy for n-butane adsorption after each preparative step. Unsupported silicalite/clay layers are prepared by applying a clay suspension over large, silicalite cubes on a gypsum support.[40] The composite layer is left to dry, removed from the gypsum support and calcined at 900°C (1°C/min, 1 hour). Next, lead-boron silicate glaze powder is applied on the clay material next to and partly on top of the silicalite crystals, and calcined at 550°C (1°C/min, 1 hour). The crystal is studied by means of microscope FTIR-spectroscopy in the transmission mode (Bruker, IFS 66) in a flow-cell with a conditioned atmosphere (cf. Chapter 6). The adsorption of n-butane remains constant and equal to that of a reference crystal that is calcined at 550°C (comparison of the ratio of absorption bands of C-H around 2900 cm^{-1} and Si-O at 2000-1800 cm^{-1}). The IR-absorbance of hydroxyl groups (3500-3000 cm^{-1}) under ambient conditions is, however, negligible after calcination at 900°C. It seems that the Si-OH groups present within the silicalite framework disappear during the severe thermal treatment.

2.5 Concluding Remarks

All three deposition techniques (sol-gel, CVD/EVD, and glazing) can in principle be applied to achieve selective deposition in between zeolite crystals on top of a porous substrate. Sol-gel films are, however, liable to crack upon drying and calcination,[41,42] which is aggravated by the presence of relatively large zeolite crystals on the support. A non-continuous gel film has to be deposited, and the sharp corners of the zeolite crystals introduce points where

cracks can initiate. The mechanical stability is expected to improve when smaller crystals and thin films (< 5 μm; cf. Chapter 5) are applied, while the addition of binders (glycerol) or drying control chemical agents (DCCA's) may further reduce the occurrence of cracks.[43] In view of the presence of steam and metal chlorides at very high temperatures, the EVD process is not expected to be the optimal procedure, but the possibility to control the film growth to a selected area is demonstrated. The applied reactants do not lead to a gas-tight deposit upon decomposition. The slow diffusion through the zeolite micropores might be advantageous, when large reactant molecules are applied (hindered diffusion).

The application of glazes will be restricted to relatively large zeolite crystals due to the particle size of the glaze material. If a sol of a composition similar to the glazes investigated in this work can be prepared, selective deposition will be viable as has been demonstrated for the boehmite dip-coating procedure. Thin (1-5 μm) films can be deposited, and upon thermal treatment the melting process leads to the formation of a gas-tight film. The minimal thickness of the zeolite composite film is then limited by the size of the zeolite crystals, and perhaps even more so by the smoothness of the support top layer. The vanadium containing silicalite cubes are expected to be optimal for the present zeolite composite membrane. Apart from the optimal shape and size, the crystallization can be easily manipulated to obtain crystals with a very narrow size distribution.

2.6 Literature

1. D.W. Breck, *Zeolite Molecular Sieves, Structure, Chemistry, and Use*, John Wiley-Interscience, New York, 1974.
2. R.M. Barrer, *Hydrothermal Chemistry of Zeolites*, Academic Press, London, 1982.
3. J.C. Jansen, in: *Introduction to Zeolite Science and Practice*, H. van Bekkum, E.M. Flanigen, and J.C. Jansen (Eds), Stud.Surf.Sci.Catal. Vol. 58, Elsevier, Amsterdam, 1991, 77.
4. S.T. Wilson, B.M. Lok, C.A. Messina, T.R. Cannan, and E.M. Flanigen, *J.Am.Chem.Soc.*, 104 (1982) 1146.
5. H. Kessler, in: *Synthesis/Characterization and Novel Applications of Molecular Sieve Materials*, R.L. Bedard, T. Bein, M.E. Davis, J. Garces, V.A. Maroni, and G.D. Stucky

(Eds), MRS Symp.Ser. Vol. 233, Materials Research Society, Pittsburgh, 1991, 47.

6. R.L. Bedard, S.T. Wilson, L.D. Vail, J.M. Bennett, and E.M. Flanigen, in: *Zeolites: Facts, Figures, Future*, P.A. Jacobs, and R.A. van Santen (Eds), Stud.Surf.Sci.Catal. Vol. 49, Elsevier, Amsterdam, 1989, 375.

7. H. van Koningsveld, H. van Bekkum, and J.C. Jansen, *Acta Cryst.*, B43 (1987) 127.

8. H. van Koningsveld, J.C. Jansen, and H. van Bekkum, *Zeolites*, 10 (1990) 235.

9. H. van Koningsveld, F. Tuinstra, H. van Bekkum, and J.C. Jansen, *Acta Cryst.*, B45 (1989) 423.

10. P. Voogd, PhD Thesis, Delft University, The Netherlands, 1991.

11. D.L. Wernick, E.J. Osterhuber, in: *Proc. 6th Int.Zeol.Conf.*, D. Olson, and A. Bisio (Eds), Butterworths, London, 1984, 122.

12. A.R. Paravar, and D.T. Hayhurst, in: *Proc. 6th Int.Zeol.Conf.*, D. Olson, and A. Bisio (Eds), Butterworths, London, 1984, 217.

13. E.R. Geus, A.E. Jansen, J.C. Jansen, J. Schoonman, and H. van Bekkum, in: *Catalysis and Adsorption by Zeolites*, G. Öhlmann, H. Pfeifer, and R. Fricke (Eds), Stud.Surf.Sci.Catal. Vol. 65, Elsevier, Amsterdam, 1991, 457.

14. E.M. Flanigen, J.M Bennett, R.W. Grose, J.P. Cohen, R.L. Patton, R.M. Kirchner, and J.V. Smith, *Nature*, 271 (1978) 512.

15. US Patent 3.702,886 (1972) to Mobil Corp.

16. M. Ghamami, and L.B. Sand, *Zeolites*, 3 (1983) 155.

17. G.H. Kuehl, European Patent 0,093,519 (1983) to Mobil Corp.

18. H. Lermer, M. Draeger, J. Steffen, and K.K. Unger, *Zeolites* 5 (1985) 131.

19. D.T. Hayhurst, and J.C. Lee, in: *Proc. 7 IZC Tokyo*, Y. Murakami, A. Iijima, J.W. Ward (Eds), Elsevier, Amsterdam, 1987, 113.

20. U. Mueller, A. Brenner, A. Reich, and K.K. Unger, in: *Zeolite Synthesis*, M.L. Occelli, and H.E. Robson (Eds), ACS Symp.Ser. Vol. 398, 1988, 346.

21. J.L. Guth, H. Kessler, and R. Wey, in: *Proc. 7 IZC Tokyo*, Y. Murakami, A. Iijima, J.W. Ward (Eds), Elsevier, Amsterdam, 1987, 121.

22. M.S. Rigutto, and H. van Bekkum, *Appl.Catal.*, 68 (1991) L1.

23. J.C. Jansen, C.W.R. Engelen, and H. van Bekkum, in: *Zeolite Synthesis*, M.L. Occelli, and H.E. Robson (Eds), ACS Symp.Ser. Vol. 398, 1988, 257.

24. D.G. Hay, H. Jaeger, and K.G. Wilshier, *Zeolites*, 10 (1990) 571.

25. K. Beschmann, G.T. Kokotailo, and L. Riekert, *Chem.Eng.Proc.* 22 (1987) 223.

26. E.R. Geus, J.C. Jansen, and H. van Bekkum, in: *Zeolites for the Nineties*, J.C. Jansen, L. Moscou, and M.F.M. Post (Eds.), Recent Research Reports 8th Int.Zeol.Conf., 1989, 293.

27. U. Hong, J. Kärger, R. Kramer, H. Pfeifer, G. Seiffert, U. Müller, K.K. Unger, H.B. Lück, and T. Ito, *Zeolites*, 11 (1991) 816.

28. D. Shen, L.V.C. Rees, J. Caro, M. Bülow, B. Zibrowius, H. Jobic, *J.Chem.Soc.Faraday*

Trans., 86 (1990) 3943.

29. A. Leenaars, PhD Thesis, Twente University, The Netherlands, 1984.

30. A. Mulder, E.R. Geus, J.H. Hanemaaijer, J.W. Geus, Dutch Patent Application 90.00417, (1990).

31. U.B. Pal, and S.C. Singhal, *Proc. 1st Int.Symp. on Solid Oxide Fuel Cells*, Volume 89-11, The Electrochemical Society, 1989, 41.

32. J. Schoonman, J.P. Dekker, J.W. Broers, and N.J. Kiwiet, MRS Symp.Proc. Vol. 210, Materials Research Society, Pittsburgh, 1991, 13.

33. E.R. Geus, H.M. van Veen, H.J. Veringa, J. Schoonman, and H. van Bekkum, in: *Inorganic Membranes*, A.J. Burggraaf, J. Charpin, and L. Cot (Eds), Proc. 2nd Int.Conf. on Inorg.Membr., Key Eng.Mat. Vol. 61&62, Trans Tech Publ., 1991, 461.

34. E.R. Geus, A. Mulder, D.J. Vischjager, J. Schoonman, and H. van Bekkum, in: *Inorganic Membranes*, A.J. Burggraaf, J. Charpin, and L. Cot (Eds), Proc. 2nd Int.Conf. on Inorg.Membr., Key Eng.Mat. Vol. 61&62, Trans Tech Publ., 1991, 57.

35. H.M. van Veen, R.A. Terpstra, J.P.B.M. Tol, H.J. Veringa, in: *Proc. 1st Conf. on Inorg.Membr.*, L. Cot, and J. Charpin (Eds), 1989, 329.

36. A. Mulder, F. van Looij, P.A. Dekker, E.R. Geus, and J.W. Geus, in: *Inorganic Membranes*, A.J. Burggraaf, J. Charpin, and L. Cot (Eds), Proc. 2nd Int.Conf. on Inorg.Membr., Key Eng.Mat. Vol. 61&62, Trans Tech Publ., 1991, 411.

37. R. de Ruiter, J.C. Jansen, and H. van Bekkum, in: *Molecular Sieves*, M.L. Occelli, and H.E. Robson (Eds), Synthesis of Microporous Materials, Vol. 1, Van Nostrand Reinhold, New York, 1992, 167.

38. O.V. Mazurin, M.V. Streltsina, T.P. Shvaiko-Shvaikovskaya, *Handbook of Glass Data, Part C, Ternary Silicate Glasses*, Elsevier, Amsterdam, 1987.

39. H. Scholze, *Die physikalischen und chemischen Grundlagen der Keramik*, Springer-Verlag, Berlin-Heidelberg, 1968.

40. E.R. Geus, J. Schoonman, and H. van Bekkum, in: *Synthesis/Characterization and Novel Applications of Molecular Sieve Materials*, R.L. Bedard, T. Bein, M.E. Davis, J. Garces, V.A. Maroni, and G.D. Stucky (Eds), MRS Symp.Ser. Vol. 233, Materials Research Society, Pittsburgh, 1991, 231.

41. M.A. Anderson, F. Tiscareno-Lechuga, Q. Xu, and C.G. Hill, in: *Novel Materials in Heterogeneous Catalysis*, R.T.K. Baker, L.L. Murrell (Eds), ACS Symp.Ser. Vol. 437, 1990, 198.

42. C.J. Brinker, and G.W. Scherer, *Sol-Gel Science, The Physics and Chemistry of Sol-Gel Processing*, Academic Press, London, 1990, 453.

43. L.L. Hench, in: *Science of Ceramic Chemical Processing*, L.L. Hench, and D.R. Ulrich (Eds), John Wiley & Sons, New York, 1986, 52.

3. Preparation of Supported Zeolite Layers by In Situ Growth

The direct crystallization of MFI layers on both ceramic and stainless steel porous supports for the preparation of zeolite membranes is discussed. For reactive support materials, such as α-alumina and clay materials, other solid phases can be formed as a result of the leaching of mainly aluminium ions. The use of inert support materials which properties are not affected by the hydrothermal treatment is therefore attractive. For reactive materials the extreme hydrothermal conditions (180°C, pH > 13) give rise to a reduction of the mechanical strength (α-alumina) and/or to a lower porosity (clay) of the support. The porous, sintered stainless steel support allows for a relatively straightforward membrane module construction, as assemblage of porous and non-porous parts (module housing) does not introduce compatibility problems. It is shown that in principle only two materials (stainless steel and zeolite) are required to realize a high-temperature membrane with molecular sieve properties.

3.1 Introduction

In this chapter the direct crystallization, or in situ growth, of zeolites on inorganic supports for the preparation of zeolite membranes is dealt with. The in situ growth concept has been suggested for several applications, such as sensors,[1] catalysts,[2] and membranes.[3-5] The formation of continuous zeolite layers or films, however, has proved to be difficult to achieve, especially on macroporous substrates.

Zeolite crystallization is still not fully understood, and the direct crystallization of zeolites on a substrate may be further complicated by possible chemical and/or physical effects. Recently, controlled growth of small MFI crystals on silicon [100] wafers has been reported.[6] The crystals have either laterally (ac-plane parallel to the silicon wafer), or axially (more or less random with the c-direction perpendicular to the silicon wafer) grown, but even on the well-defined, smooth silicon surface no full coverage has been achieved. In most cases, however, the in situ growth of zeolite coatings leads to randomly oriented crystals. As was already discussed in Chapter 2, the orientation of the zeolite crystals may give rise to different properties of the zeolite-based composite system.

The direct growth process of zeolite layers is expected to allow the preparation of large membrane surface areas. Moreover, rather complex membrane modules with high specific surface areas may be developed. Only two materials are involved in the design for inorganic zeolite membranes presented in this chapter, i.e. the support (containing both porous and non-porous parts) and the zeolite layer (Figure 1). Thus far, the industrial application of inorganic membranes has been limited to 150°C, because of the lack of compatible high-temperature sealing techniques.[7] In the proposed configuration, the use of gas-tight, high-temperature resistant sealants can be avoided.

This chapter is divided into three sections. First, the reason for choosing MFI as the membrane separating phase will be discussed. The effect of inert and reactive ceramic substrates on the zeolite crystallization is dealt with in section 3.3. Finally, the preparation of zeolite membranes of the MFI-type on porous, sintered stainless steel supports will be presented. The construction of high-temperature membrane modules is also addressed.
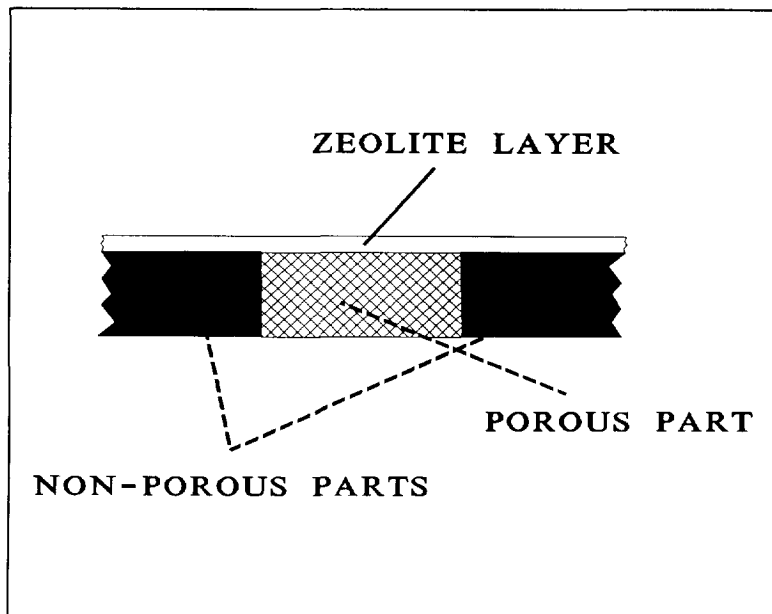
ZEOLITE LAYER

POROUS PART

NON-POROUS PARTS

Figure 1   Schematic view of a zeolite layer on top of a support, built up by connecting porous and non-porous parts

3.2 MFI-Type Zeolite as the Membrane Material

Synthetic zeolite crystals seldomly grow as large single crystals with dimensions above some 500 μm. It is therefore unlikely that large surface areas may be covered by a monocrystalline zeolite layer. As a result of the high supersaturation of the zeolite synthesis mixture, many nuclei are formed on the substrate. The zeolite nuclei grow separately, and meet after some time to form a continuous layer of intergrown and randomly oriented crystals. Therefore, one of the main constraints on the zeolite type is related to the possible interconnection of the micropores of separately growing crystals. Otherwise, the interfaces developing during growth of the layer may be either non-porous, or may give rise to larger pores thus leading to by-passing.

A number of publications deals with the preparation of zeolite composite systems by in situ growth. The results reported thus far involve the crystallization of primarily zeolite A (LTA) and MFI (cf. Table 1).

Table 1   In situ growth synthesis procedures for zeolite layers and films

Composite	Reactants	Gel composition (molar ratio)	Conditions	Ref.
MFI, FAU, and MOR crystals on monoliths (discontinuous)	Ludox HS-40, alumina, NaOH, TPABr	$100 \ SiO_2 : 0.6 \ Al_2O_3 : 6.3 \ Na_2O : 6.7 \ (TPA)_2O : 1736 \ H_2O$	170°C 70 hours	2
zeolite (MFI?) layer on porous glass	Borosilicate glass, NaOH, TPABr, NaCl	$100 \ SiO_2 : 0.16 \ Al_2O_3 : 2.6 \ B_2O_3 : 3 \ Na_2O : 5.2 \ (TPA)_2O : 10940 \ H_2O$	193°C 44 hours	4
LTA on porous alumina and metal; several consecutive dippings	not specified	$100 \ SiO_2 : 55 \ Al_2O_3 : 140 \ Na_2O : 4900 \ H_2O$	80°C 4 hours	8
	$NaAlO_4$, sodium silicate	$100 \ SiO_2 : 56 \ Al_2O_3 : 103 \ Na_2O : 7466 \ H_2O$	90°C 24 hours	5
MFI (orientation [010]) on silicon [100] wafer	TEOS, TPAOH	$100 \ SiO_2 : 14.7 \ (TPA)_2O : 42640 \ H_2O$	163°C 12 hours	6
unsupported MFI layers (grown teflon and/or silver)	Ludox AS-40, NaOH, TPABr	$100 \ SiO_2 : 2.2 \ Na_2O : 2.61 \ (TPA)_2O : 2832 \ H_2O$	180°C 0.3-9 days	9,10
	Cataloid SI-30 and AlNO$_3$, NaOH, TPABr	$100 \ SiO_2 : 1 \ Al_2O_3 : 5 \ Na_2O : 5 \ (TPA)_2O : 8000 \ H_2O$	170°C 48 hours	11
MFI and/or FER layer; preformed gel treated with template and/or water vapour	sodium silicate, $Al_2(SO_4)_3$, NaOH, EDA, Et$_3$N	$100 \ SiO_2 : 1.16 \ Al_2O_3 : 1.97 \ Na_2O : 475 \ H_2O$ (gel) 1 EDA : 3.8 Et$_3$N : 7.5 H_2O (liquid)	200°C 5 days	12, 13
	$NaAlO_4$, LiOH, precipitated silica, TPABr	$100 \ SiO_2 : 10 \ Al_2O_3 : 5.87 \ Li_2O : 10 \ Na_2O : 10 \ (TPA)_2O : 327 \ H_2O$ (gel)	170°C 10 hours	14

In Chapter 2 the templating function of the tetrapropyl ammonium (TPA) ions in the MFI crystallization has already been mentioned. MFI is one of the most studied and applied zeolites, and the crystallization under various synthesis conditions is well-documented.[15-18] Moreover, relatively large crystals can be synthesized (cf. Chapter 2). Control of the crystal morphology has been demonstrated by the incorporation of other T-atoms, such as boron.[19] Instead of regular crystals, such as cubes and prisms, or 90° intergrown crystals, MFI may also crystallize as more irregularly shaped bodies. Large aggregates (over several millimeters in length) of secondary nucleated and intergrown MFI crystals are sometimes obtained. Obvious examples of strongly intergrown MFI aggregates are unsupported layers or films, as reported by several workers.[9-13] The tendency to form crystal aggregates might be related to the pentasil layers from which the MFI lattice is built up, together with the presence of TPA as an excellent nucleation and structure directing agent. By means of high resolution electron microscopy (HREM) it was concluded that the lattice pattern can continue over two intergrown MFI crystallites.[20]

Zeolite single crystals, on the other hand, should guarantee the interconnection of the micropores throughout the crystal. For the earlier mentioned single crystal MFI cubes, of which the single crystal nature has been established by X-ray single crystal structure analysis,[21], a step-wise crystal growth process has been reported.[18] The apparently existing interfaces between the subsequently grown crystal parts may, however, give rise to hampered diffusion (cf. Chapter 4, section 4.5).

The above discussion does not prove that interconnection of micropores within MFI-type aggregates occurs consistently, but the preparation of microporous membranes by in situ growth of continuous polycrystalline MFI layers is plausible. Figure 2a presents a SEM image of an aggregate of some large MFI crystals from a mixture aiming at the synthesis of cube shaped single crystals, first reported by Lermer et al.[17] In this particular case the sodium ions are deliberately omitted by the use of TPAOH (section 4.5). The crystals are strongly connected, and can only be separated by crushing. In Figure 2b a visible light micrograph of the same aggregate is shown obtained with polarized light and a gypsum compensator (Olympus BH-2 light microscope). The different colours of the various crystal sections reveal that different orientations are present within the aggregate, in agreement with

the crystal morphology as shown in Figure 2a. Apparently, the aggregate is formed from several growing nuclei, that are interconnected in some later stage. The occurrence of these MFI aggregates is in favour of the supposition that separately growing crystals may be interconnected to form a continuous layer.
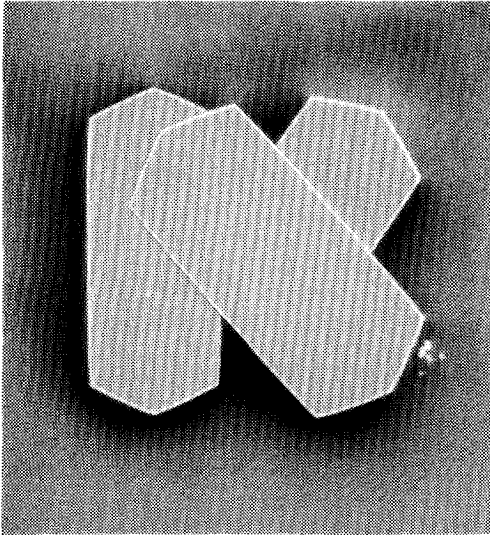
40 µm

Figure 2a   SEM-picture of a small MFI aggregate
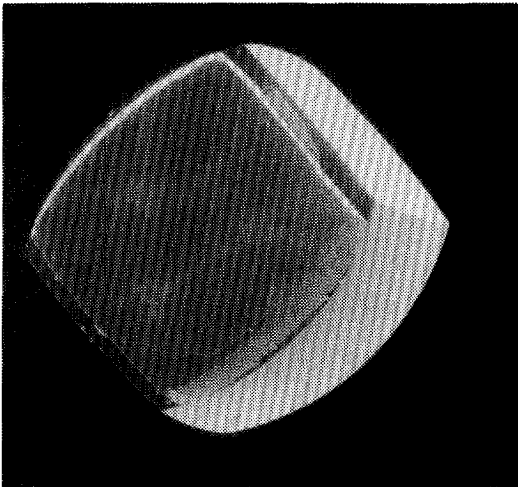
100 µm

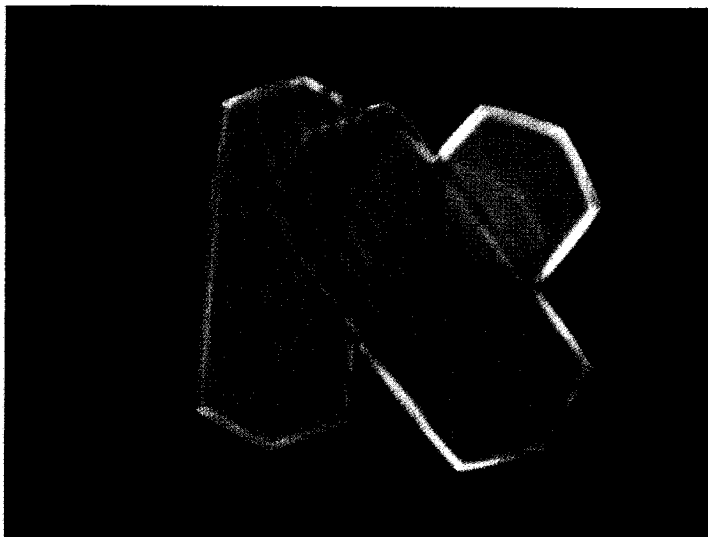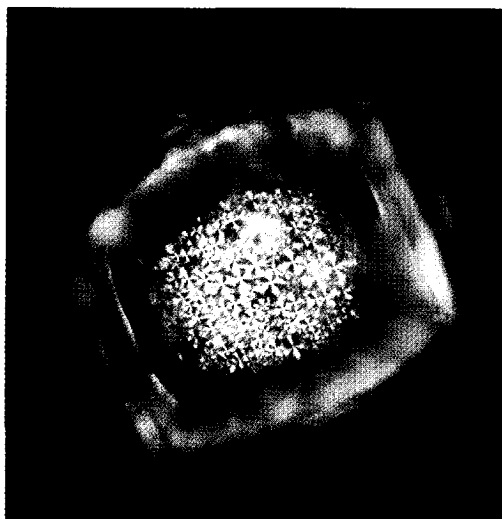Figure 3a   SEM-picture of an 90° intergrown silicalite cube

Figure 2b   Visible light micrograph of a small MFI aggregate

| (b) | (c) |

Figure 3   Visible light micrograph of the large silicalite cube: (b) view through the b-direction; (c) view through the a-direction

Other peculiarities of the MFI crystallization of cube shaped single crystals are shown in Figure 3. A 90° intergrown cube is shown in Figure 3a. The visual light micrograph of Figure 3b shows the crystal again in the 90° intergrown face, similarly to Figure 3a, exhibiting an internally present mosaic structure. A view of this mosaic structure in the a-direction (Figure 3c) reveals that different parts can be distinguished within the crystal.

In some cases these parts can be separated (Figure 4a). Previously, this has been reported for 90° intergrown sections of MFI prisms after ultrasonic treatment.[22]

In Figure 4b the largest part of the silicalite cube is shown in more detail, which shows that both parts are only connected in some areas at the outer rim of the crystal. In all other areas some interface may be present between both crystal parts, possibly giving rise to larger pores. This may be generally the case for 90° intergrown crystals, so this type of intergrowth may be unfavourable for the molecular sieving properties in the preparation of continuous MFI layers as membranes.
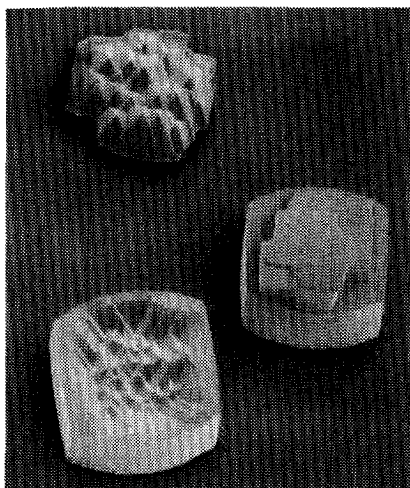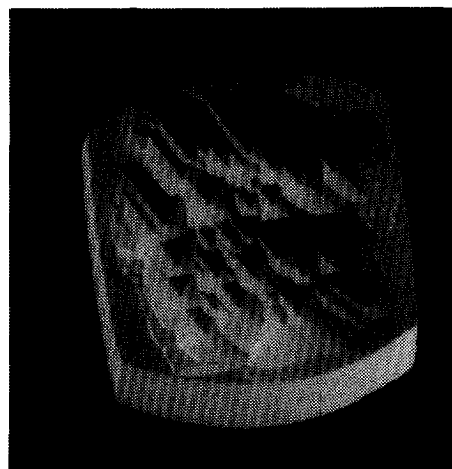
(a) _____ = 80 µm   (b) _____ = 40 µm

Figure 4   SEM-picture of an MFI intergrown cube: (a) cube and the two crystal parts that can be separated; (b) the main crystal part; the attachment to the other crystal part is visible at the outer rim

3.3 Zeolite Growth on Ceramic Porous Supports[23]

3.3.1 Experimental Aspects; Different Ceramic Support Materials

Three different types of ceramic macroporous supports are investigated, which have been described earlier in Chapter 2, viz. α-alumina, clay (pottery), and calcia-stabilized zirconia. Thin mesoporous top layers have been deposited on the above macroporous supports via slip casting. Metakaolin layers are prepared on clay and zirconia by deposition of kaolin, provided by Ferro B.V., Rotterdam, The Netherlands, from suspension. The kaoline is transformed into metakaolin by calcination at 900°C. An α-alumina support is fully covered by a mesoporous zirconia layer (ca. 20 μm) by deposition from a zirconia wash-coat (ZYP coatings) and calcination at 900°C.

Zeolite layers are grown hydrothermally on disks of the above ceramic porous supports with a standard synthesis mixture. The chemical composition resembles the previously mentioned synthesis mixture for the preparation of large cube shaped single crystals,[17] and consists of silica (Aerosil 200), NaOH (Baker), and TPABr (CFZ, Zaltbommel, The Netherlands) in water. The molar ratio amounts to 100 SiO_2 : 160 Na_2O : 150 TPA_2O : 16666 H_2O. All reactants are mixed and aged under ambient conditions for 1-6 hours while stirring. The experiments are performed in Teflon-lined stainless-steel autoclaves (30 cm^3) at 180°C for 1-5 days. The substrates are positioned on the bottom of the autoclave, and the synthesis mixture is added. Modified supports are always positioned with the mesoporous layer on top. In some experiments the TPA source is left out.

After hydrothermal treatment the disks are washed with water and then ethanol, and dried in ambient. First inspection of the deposited layers is always carried out by visible light microscopy. The layers are studied in more detail by SEM. The crystallographic nature of the layers is confirmed by powder X-ray diffraction (XRD). To avoid shadow effects in the XRD experiment, the MFI layers are polished. Qualitative chemical analysis of the supports is obtained by EDAX elemental analysis. The chemical composition of the clay material, of separately formed MFI material, and of supernatants of various reaction mixtures has been analyzed quantitatively by ICP and AAS.

3.3.2 Support-Dependent Zeolite Crystallization

In Table 2 an overview of the preparative results is given. The resulting zeolite phases and the required crystallization times strongly depend on the support material. Analcime (ANA) crystals are grown on α-alumina within 48 hours, in contrast to zirconia, on which some MFI crystals are observed only after 120 hours. Crystallization on the clay substrate, on the other hand, proceeds rapidly (within 48 hours), but the product varies over the support. A continuous layer of large MFI crystals is formed on the top side (Figure 5), whereas the bottom side of the disk, facing the Teflon-lining during crystallization, is covered with ANA and needle shaped crystals (Figure 6). The XRD patterns confirm both the MFI and ANA phase, although the low-angle peaks for MFI are only observed when the top layer is smoothed by polishing (Figure 7).

Table 2   Zeolite crystallization onto various ceramic supports

Support	Product	Remarks
clay	MFI	continuous layer
α-alumina	ANA	non-continuous layer, independent of presence of TPA
zirconia	MFI	few crystals, strongly intergrown
metakaolin	ANA	transformation of support, TPA-free
metakaolin on zirconia	MFI	non-continuous layer; large irregular crystals
metakaolin on clay	ANA	near to continuous layer; TPA-free
zirconia on α-alumina	ANA/MFI	non-continuous layer

The top layer of the MFI/clay composite consists of an array of randomly oriented, intergrown MFI crystals *next to*, and not *on top* of each other with a 50-80 μm layer thickness (Figure 8). The film seems strongly bound to the clay phase, which is denser than a non-treated clay

support. Qualitative elemental analysis by means of EDAX (cf. Figure 9a and b) reveals a layer with high silica content on top of a non-homogeneous support, consisting of mainly silicon, aluminium, and calcium oxides.
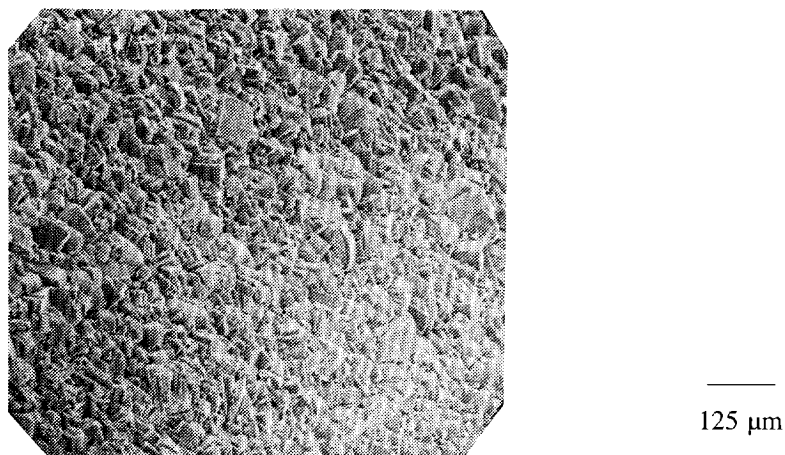

125 μm

Figure 5   SEM-picture of the top side of the clay substrate, fully covered by a continuous polycrystalline MFI layer
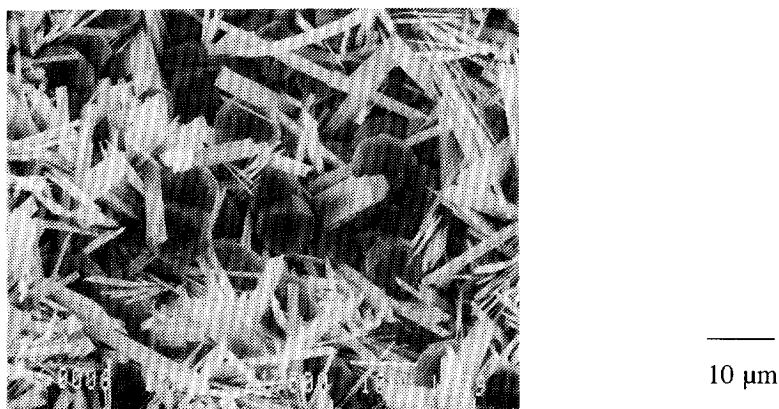

10 μm

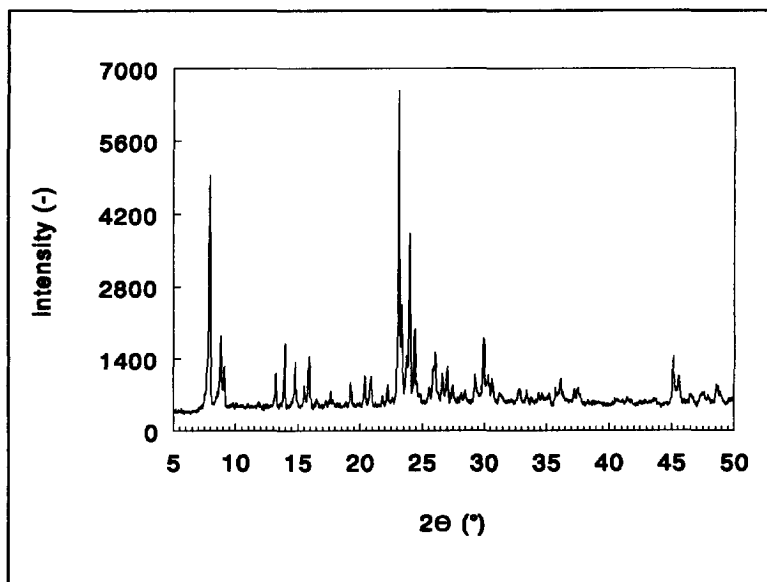Figure 6   SEM-picture of the bottom side of the clay substrate, partly covered by ANA and presumably ferrierite (FER) crystals

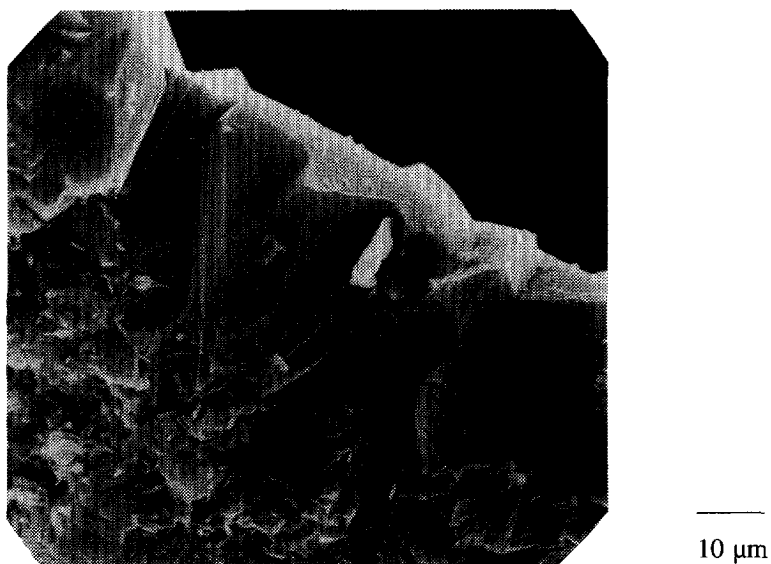Figure 7   XRD-pattern of a polished, as-synthesized MFI layer on top of a clay support

10 μm

Figure 8   SEM-picture (cross-section) of the MFI top layer on a clay substrate

The chemical composition of the synthesis mixture after hydrothermal treatment depends on the support material (Table 3). Owing to the alkaline leaching of the α-alumina phase, the Si/Al ratio of the synthesis mixture decreases from over 100,000 to 5. Thus, the composition of the synthesis mixture shifts from the range for MFI crystallization, and phases with higher aluminium content, such as ANA (natural Si/Al ratio 1.8-2.8) are formed, regardless of the presence of TPA. The zirconia support remains inert under the applied conditions, and the crystallization of MFI is not affected. The clay support is less liable to alkaline leaching (Si/Al = 2500 after hydrothermal treatment) than α-alumina. As shown in Table 3, other cations (Ca, K) are, however, also leached from the clay phase.

Table 3   Molar chemical composition ratios (ICP and AAS analysis) of the standard synthesis mixture (Gel), the clay support (Clay), and supernatants after zeolite crystallization on different supports

Element	Gel	Clay	Supernatants after zeolite growth		
			Clay	Alumina	Zr-Alumina[&]
Si	100	100	100	100	100
Al	<0.001	42.7	0.04	19.4	0.11
Na	320	4.52	305	1942	363
K	<0.001	3.82	1.23	1.61	0.23
Ca	<0.001	19.6	0.06	<0.17	<0.01
Zr	<0.001	<0.001	<0.001	<0.001	<0.001
Fe	<0.001	0.66	<0.01	<0.001	<0.001
Mn	<0.001	0.03	0.01	<0.001	<0.001

[&] α-alumina support, coated with a thin, mesoporous zirconia film

80 µm   (a)

■ SI
■ AL
□ SI+AL
■ CA
■ SI+CA
■ AL+CA
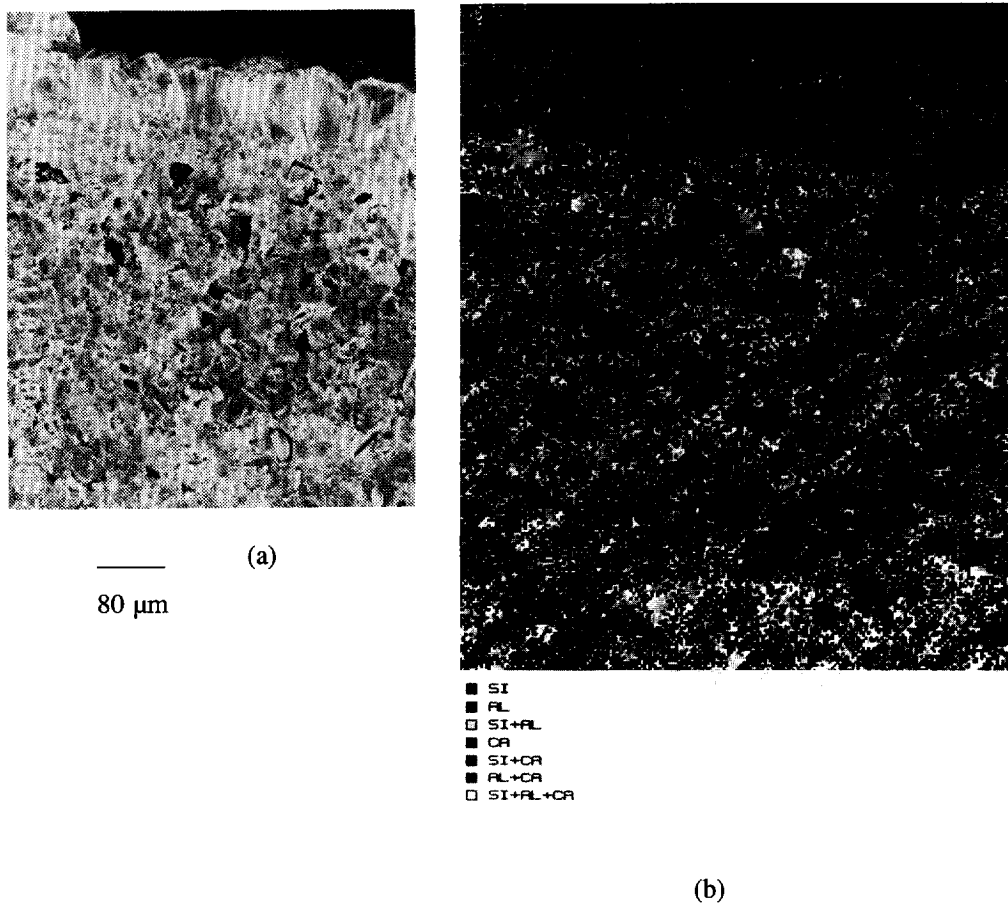□ SI+AL+CA

(b)

Figure 9   SEM-picture (cross section) of the MFI/clay composite system, and (b) EDAX
            element mapping of the same area

The presence of ANA on the bottom face of the clay support is attributed to a thin, stagnant
liquid film located in between the clay disk and the Teflon-lining. As leaching proceeds
homogeneously throughout the clay support due to the high pH, the local Si/Al ratio of the
crystallization liquid may be lower than that of the bulk synthesis mixture. The accompanying
needle-shaped phase may be ferrierite,[24] another zeolite which is formed at lower Si/Al ratios.

In contrast to the MFI/clay composite the ANA crystals do not cover the α-alumina support completely. For long crystallization times (over 168 hours), a near to continuous layer is obtained, although other (crystalline) phases may have formed as well. According to the chemical analysis in Table 3, nearly 85% of the silicon within the synthesis mixture is consumed, indicating that the available nutrients are not efficiently used. In order to favour nucleation over crystal growth two layer instead of one layer α-alumina supports have been used, but similar large ANA crystals result (Figure 10). For both α-alumina supports, the crystallization is limited to the outer surface of the support, and the crystals are hemispheres. The mechanical strength of the α-alumina supports is substantially lower, which is attributed to the alkaline leaching.

100 μm
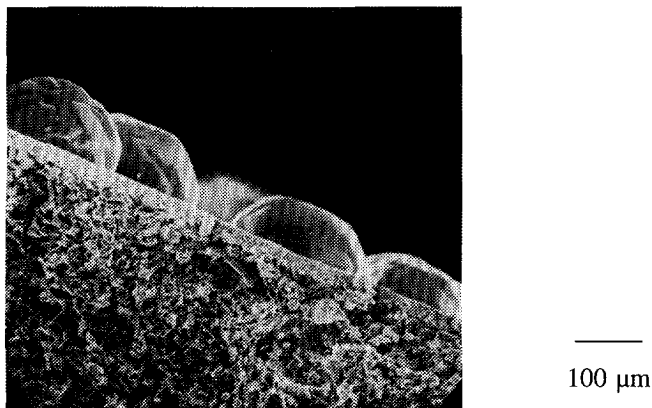
Figure 10   SEM-picture (cross-section) of large ANA crystals on a two layer α-alumina support

An alternative route to prepare continuous ANA layers has been tried, using metakaolin as a precursor mineral.[25,26] According to XRD analysis, a thin metakaolin layer (thickness 50 μm) on a clay support is fully transformed into ANA, but larger pores remain present. Thick, self-supporting metakaolin layers of a thickness of some 3 mm thickness are almost completely transformed into ANA after 120 hours at 180°C, but still larger pores remain present.

Enhanced MFI Crystallization on Reactive Clay Supports

The crystallization of MFI on clay substrates proceeds relatively rapidly (within 48 hours), as opposed to the original synthesis of cube shaped single crystals (at least 5 days). On zirconia substrates, MFI is again observed after only 5 days, in accordance with the inertness of the support. In the absence of a clay substrate crystallization from the synthesis mixture investigated has been reported to proceed via the formation of a dense silica gel phase as a result of the presence of trivalent cations, such as aluminium or iron.[18] In one of the experiments, such a gel was formed after 30 hours on top of a clay support (Figure 11), which has partly crystallized into MFI.
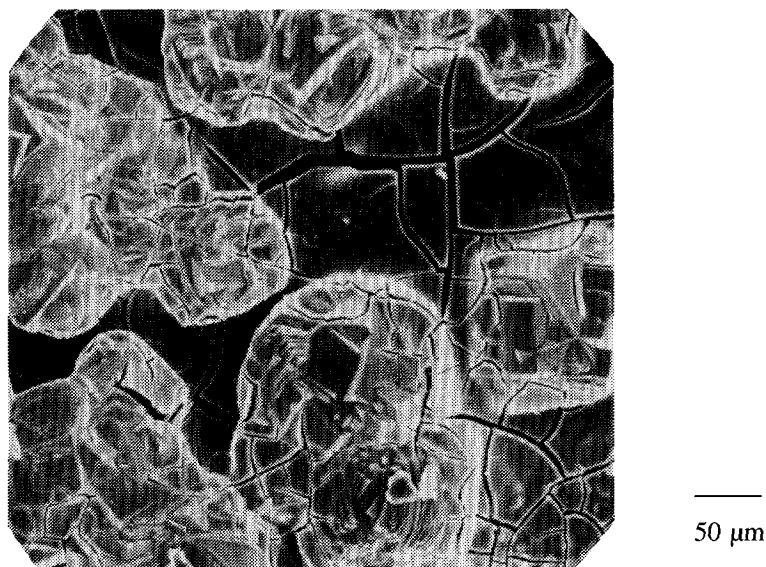

50 µm

Figure 11   SEM-picture of a partly crystallized dense silica gel phase fully covering a clay support

The gel phase virtually isolates the clay substrate from the synthesis mixture, but the case represented in Figure 11 is considered to be exceptional. In this particular experiment a rather narrow autoclave was used, in which the clay substrate could just fit. The growth of the continuous MFI layer may, however, proceed via the formation of a much thinner and perhaps

60

even non-continuous dense gel phase on the clay support. The expected growth from a dense gel is supported by the morphology of the MFI crystals, resembling that of separately grown MFI cubes.[18]

The rapid crystallization of MFI on the clay substrate is thought to be the result of the presence of a heterogeneous (alumino)silicate surface, from which additional nutrients and trivalent cations are leached. The chemical composition of the synthesis mixture changes *in situ* by the leaching process, and the required supersaturation for nucleation is reached in shorter times as compared to the crystallization of silicalite single crystals. Nucleation and growth proceed exclusively on the outer surface of the clay support, where the nutrients are abundant. The leaching process apparently leads to the growth of an array of randomly oriented MFI crystals exclusively next to each other.

Additional evidence of the accelerated nucleation and growth of MFI crystals in the presence of aluminium ions is provided by the hydrothermal treatment of an α-alumina support that is completely covered by a thin (20 μm) mesoporous zirconia coating. Both ANA and MFI crystals are formed after 66 hours (Figure 12).
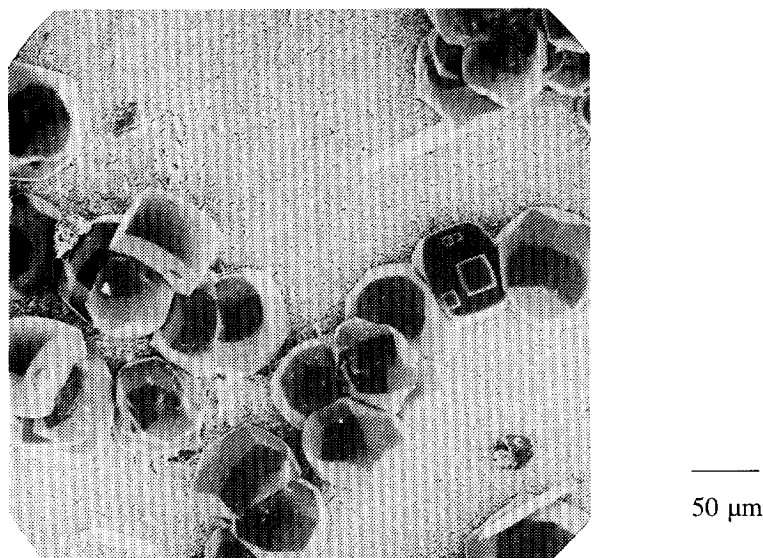

50 μm

Figure 12   SEM-picture of MFI and ANA crystals on top of a zirconia-coated α-alumina support

The aluminium concentration in the supernatant after synthesis is over two orders of magnitude lower than that with the uncoated α-alumina support (Table 3). The presence of an inert, mesoporous layer obviously reduces alkaline leaching of α-alumina. Nevertheless, ANA is formed as well. It is therefore concluded that the aluminium concentration near the support varies to such an extent that, as discussed previously, phases with a low Si/Al ratio are formed as well. The experimental results for zirconia, either as a support or as a thin top layer, indicate that the induction and acceleration of nucleation and growth are strongly dependent on the nature of the heterogeneous (oxidic) surfaces. As the chemical composition of the synthesis mixture applied here has not been varied, this may not be generally true.

3.4 MFI Layers on Porous Sintered Stainless Steel Supports[27]

3.4.1 Experimental Aspects: Variable Gel Compositions

Porous, sintered stainless (AISI 316) steel supports (diameter 25 mm; thickness 3 mm) were provided by Krebsöge (Radevormwald, Germany). The high porosity disks are provided with a 50-150 μm thick top layer of metal wool (R/F 1). For the construction of two high-temperature membrane modules similar substrates (diameter 20 mm) have been incorporated in larger non-porous stainless steel (AISI 316) disks as shown in Figure 1. Intimate contact between both parts is achieved by non-isothermic assemblage, viz. the porous support cooled at liquid nitrogen temperature (77 K) is inserted into the circular gap in the non-porous disk heated at 400°C. Two stainless steel cylinders, provided with commercial flange connections (Leybold-Heraeus), are subsequently connected to the non-porous part of the disks with a gold alloy. In Figure 13 a photograph of the high-temperature module is shown. During hydrothermal treatment the top section of the module (with the smooth top layer) is filled with the synthesis mixture, and the lower section is effectively closed by a Teflon cylinder (also shown in Figure 13). Both sides of the module are closed with flange connections and Teflon sealing rings.
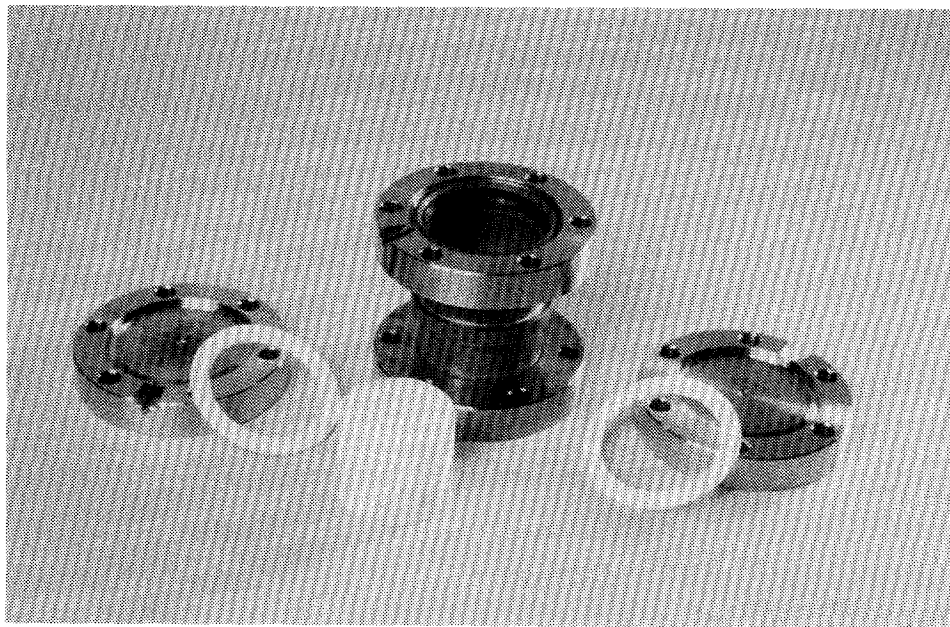
Figure 13   Picture of the high-temperature stainless steel membrane module and Teflon sealing rings and cylinder

Prior to the formation of MFI layers within the above-described high-temperature modules, several hydrothermal syntheses are performed on separate porous supports within Teflon lined (30 cm³) autoclaves. In these experiments the chemical composition of the synthesis mixture is optimized for the preparation of a continuous polycrystalline layer, fully covering the porous metal substrate. The metal disks are installed into tight-fitting Teflon holders, thus exposing only the top face of the disks to the synthesis mixture.

All synthesis mixtures contain in principle only silica, TPA, and water. In the first experiments, gel compositions have been based on the procedure according to Ghamami and Sand,[16] using Ludox AS-40 (Dupont), NH_4OH (Baker), and TPAOH (CFZ, Zaltbommel, The Netherlands). Later on, more diluted synthesis mixtures have been applied at high pH (13.5-14) in the presence of much higher template (TPA) concentrations. In these experiments Aerosil 200 (Degussa) is the silicon source, and TPA is added from two sources: TPABr (CFZ) and TPAOH. The introduction of alkali atoms (Na, K) has been avoided to ensure a

maximal incorporation of TPA (four per unit cell) in the framework. Nevertheless, low concentrations of potassium and sodium are present in the synthesis mixture from the TPAOH source (1.2 wt% K; 0.04 wt% Na). The synthesis mixture, as used in the previous section for MFI crystallization on ceramic supports (in the presence of sodium ions), is included for comparison.

All synthesis mixtures are aged while stirring for 5 hours at room temperature. The hydrothermal synthesis is always performed at 180°C. After reaction, the disks are washed with water and then ethanol, and dried under ambient conditions. Characterization of the produced layers is performed by light and electron microscopy (SEM), and by powder X-ray diffraction. Both the initial synthesis mixtures and the supernatants after the hydrothermal treatment are chemically analyzed by ICP and AAS. On one MFI/stainless steel composite membrane, as prepared by the optimized synthesis procedure, qualitative elemental analysis is performed by EDAX.

The optimized synthesis gel composition is applied to prepare continuous MFI layers within the high-temperature membrane modules. In addition, some blanc experiments are performed within the Teflon lined autoclaves in the absence of stainless steel to study the effect of the metal substrate on the crystallization.

It is found that a calcined MFI layer can be completely removed from the membrane module by treatment with a 4 M KOH solution at 180°C for 12 hours. Afterwards, the module is thoroughly washed with water, and a new MFI layer is grown within the module. Therefore, zeolite membranes prepared according to the present design can readily be rejuvenated by removing the old membrane layer and applying a fresh layer.

3.4.2 Composition-Dependent Nature of the MFI Coating

An overview of the resulting MFI products for different gel compositions (M and SS series) is presented in Table 4, also including the experiments within the membrane modules (HTSS series). Exclusively MFI material is formed, which is confirmed by XRD and visible light/electron microscopy. However, the nature of the MFI phase on top of the stainless steel disks depends strongly on the gel composition.

Table 4   Preparation results of the in situ growth crystallization of MFI material on porous, stainless steel supports (temperature 180°C)

Exp.[$]	Gel composition (molar ratio)	Time (h)	Product
M-1[&]	100 SiO_2 : 54 NH_3 : 3 $(TPA)_2O$: 6330 H_2O	58	Thick layer (100 µm), containing mesopores (Figure 14)
SS-1	100 SiO_2 : 50 $(TPA)_2O$: 50 OH : 10000 H_2O	48	Continuous, polycrystalline layer (75 µm) (Figure 15)
SS-2[%]	100 SiO_2 : 75 $(TPA)_2O$: 50 OH : 100,000 H_2O	26	Many, small (60 µm length) crystals (Figure 17)
SS-3	100 SiO_2 : 200 $(TPA)_2O$: 150 OH : 26000 H_2O	45	Near to continuous layer of intergrown crystals (Figure 18a)
SS-4	100 SiO_2 : 115 $(TPA)_2O$: 230 OH : 25000 H_2O	102	Some crystals, partly covering the support (Figure 18b)
SS-5[%]	100 SiO_2 : 150 $(TPA)_2O$: 300 OH : 16667 H_2O	174	Separate large crystals (up to 400 µm length)
HTSS-1	100 SiO_2 : 50 $(TPA)_2O$: 50 OH : 11000 H_2O	49	Continuous, polycrystalline layer
HTSS-1a	100 SiO_2 : 50 $(TPA)_2O$: 50 OH : 9000 H_2O	36	Continuous, polycrystalline layer
HTSS-2	100 SiO_2 : 115 $(TPA)_2O$: 75 OH : 14000 H_2O	45	Continuous, polycrystalline layer
B-2[#]	100 SiO_2 : 115 $(TPA)_2O$: 75 OH : 15000 H_2O	45	Inhomogeneous, polycrystalline layer (Figure 19)

[$]   M and SS denote metal support in teflon holder; HTSS denotes high temperature membrane modules (No. 1 & 2)

[&]   with Ludox AS-40 and ammonia

[%]   TPABr and NaOH (no TPAOH)

[#]   Blanc experiment of HTSS-2 (no metal present)

A seemingly continuous MFI layer is obtained from the synthesis mixture indicated by M-1 in Table 4. The layer contains, however, mesopores. The presence of mesopores has been established by applying some water on top of the dried, as-synthesized layer. In all cases, the water is readily absorbed through the deposited MFI layer into the porous support, which should be - in view of the template molecules present - non-permeable. In Figure 14 a cross-sectional view of the MFI layer is shown. The layer consists of small aggregated crystals, in which some mesopores are visible. Therefore, this synthesis approach has been abandoned in an early stage of the research. It is, however, noteworthy that unsupported MFI membranes have been grown on Teflon slabs by Haag and Tsikoyiannis[9,10] from a synthesis mixture of a comparable composition (100 SiO_2 : 5.2 TPABr : 4.4 NaOH : 2832 H_2O).
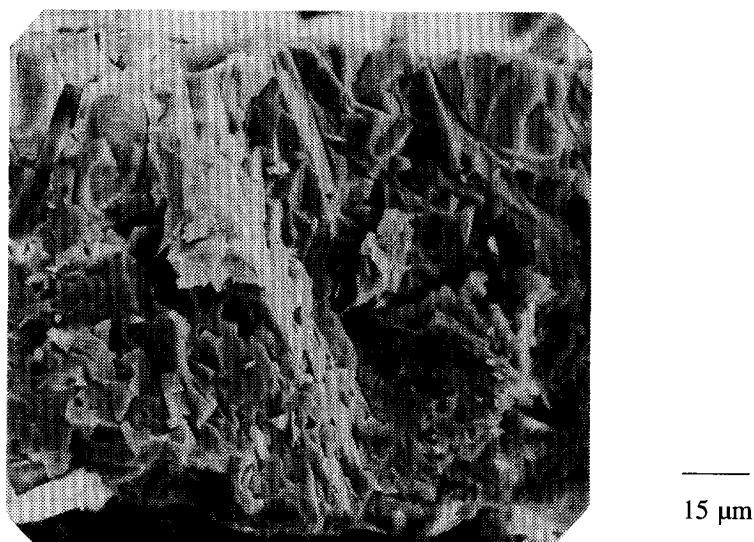

15 μm

Figure 14   SEM-picture (cross-section) of the MFI layer on stainless steel, prepared according to M-1, some larger pores are visible

In contrast to the above mesoporous layers, the synthesis mixture according to SS-1 (cf. Table 4) yields continuous MFI layers (Figure 15a). No water absorption is observed for the as-synthesized material. The cross-section of this layer (approximately 75 μm thickness) is shown in Figure 15b.

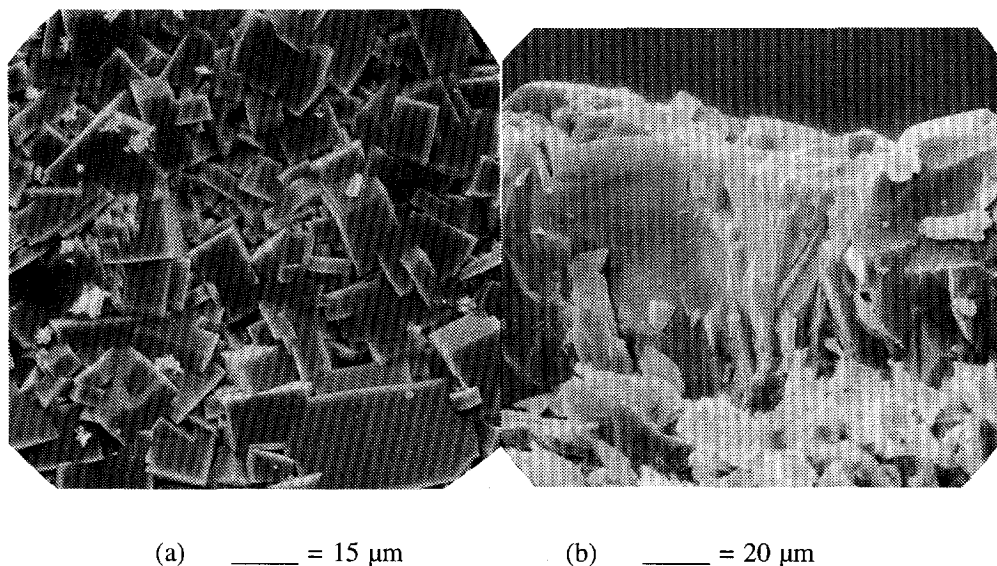(a) _____ = 15 μm   (b) _____ = 20 μm

Figure 15   SEM-picture of a two-layer stainless steel supported MFI layer, prepared according to SS-1: (a) top view; (b) cross-section

In Figure 16 the EDAX element mapping of the cross-section of the composite membrane is shown. A pure silica MFI layer (red) is supported by the (blue) stainless steel substrate, consisting of mainly iron, chromium, and nickel. Some small MFI crystals can be observed on the stainless steel within the wide pore section (the small red dots within the blue support). Even the thin (metal wool) top layer with substantially smaller pores has retained the greater part of its porosity. This is rationalized by the applied low silica concentration in connection with the limited hold-up of the synthesis mixture within the macropores of the support. During the crystallization process, the pores within the support become isolated from the bulk solution by the developing MFI layer. On the outer surface, on the other hand, the crystal growth continues by the supply of nutrients from the bulk solution.
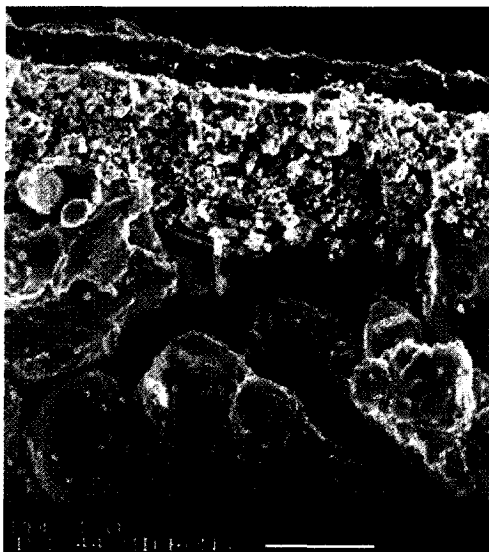
(a)
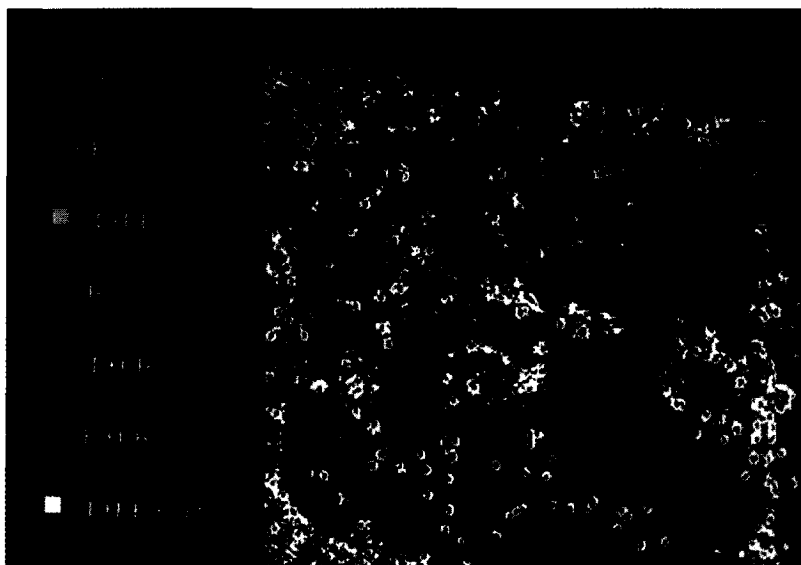
(b)

Figure 16   Cross sectional overview of the two layer stainless steel supported MFI membrane, prepared according to SS-1: (a) SEM-picture; (b) EDAX element mapping

Unless the crystallization is favoured in a specific direction as on extremely smooth and non-porous Si-wafers,[6] it is expected that the complete coverage of the porous support requires a minimal layer thickness. Inevitably, the growth on a macroporous support will lead to a randomly grown zeolite layer, because the crystal growth proceeds from differently oriented nuclei. Hence, the minimal layer thickness is expected to be correlated to the maximal pore size of the porous support, and also to depend on the smoothness of the surface of the support. For this reason two layer stainless steel supports have been used, thus combining a support with a high porosity and a smooth top layer with a small pore size (ca. 10 µm). On one layer stainless steel supports with a comparable pore diameter, but less smooth, however, the nucleation proceeds on each metal particle separately and no continuous layers have been obtained.

The crystallization process is not limited to the stainless steel support, but also proceeds on the exposed Teflon parts within the autoclave. In Figure 17 the resulting MFI phase is shown (SS-2), prepared from a tenfold diluted mixture as compared to SS-1. The available silica is sufficient to yield a 100 µm thick MFI layer on top of the stainless steel disk, provided that the crystallization only proceeds on the support (surface area 5 cm^2). Instead, the support is only partly covered by thin crystals of a length of approximately 60 µm.

40 µm

Figure 17   SEM-picture of small MFI crystals on top of a two-layer stainless steel support, prepared according to SS-2

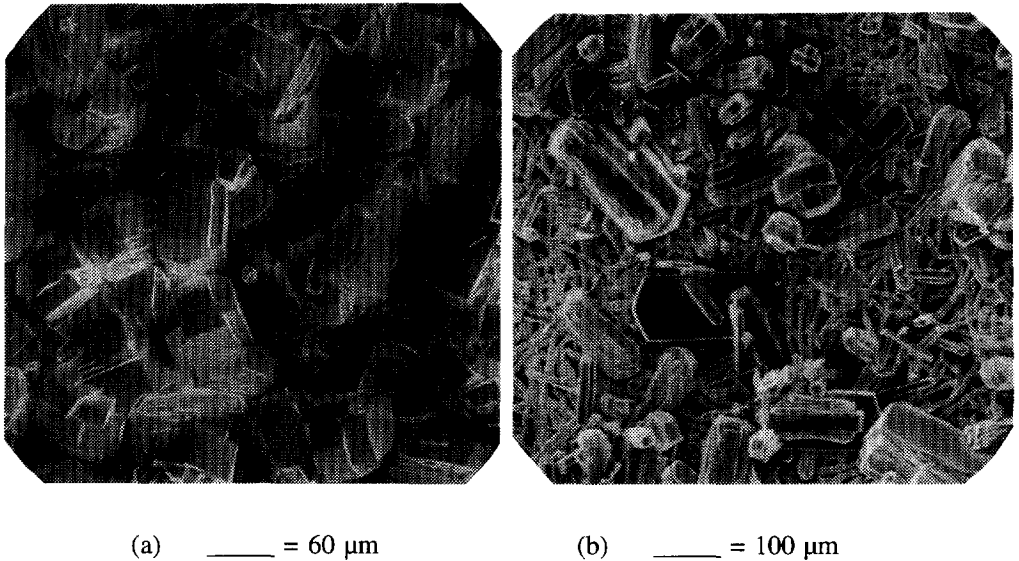(a) _____ = 60 μm   (b) _____ = 100 μm

Figure 18   (a) SEM-picture of a near to continuous layer of intergrown MFI crystals on a
two layer stainless steel support, prepared according to SS-3; (b) SEM-picture of
a partly covered two layer stainless steel support, prepared according to SS-4

The availability of nutrients for crystallization is further limited by the silica-to-hydroxide
(SiO_2/OH^-) ratio (cf. Table 4: SS-3,4,5). For decreasing SiO_2/OH^- ratios the solubility of silica
is enhanced, and a substantial amount of the nutrients for crystallization remains in solution.
In Table 5 the chemical analyses of the supernatants before and after hydrothermal synthesis
are presented for some experiments. After long synthesis times (174 hours), the consumed
silica (yield) for SS-5 ($SiO_2/OH^- = 0.3$) is approximately 57%. For higher SiO_2/OH^- ratios
(0.7-2.0) the yield is at least 80%, even after only 36 hours. The layer thickness within the
high-temperature modules can be estimated from the amount of silica deposited according to
Table 5, assuming homogeneous deposition on all exposed surfaces (surface area
approximately 37 cm^2 for both modules). Accordingly, layer thicknesses amount to 42 μm
(HTSS-2) and 56 μm (HTSS-1a).

Table 5   ICP and AAS analysis data on synthesis gels (in) and supernatants after crystallization (out) for the in situ growth of MFI layers

Experiment$		SS-3	SS-4	SS-5	HTSS-1a	HTSS-2	B-2
Si (g/kg)	in	4.8	5.5	7.0	14.4	9.1	8.4
	out	1.0	3.5	3.0	2.7	0.6	0.8
SiO_2 deposited (g)		0.29	0.14	0.33	0.40	0.31	0.46
Yield (%)		79	36	57	81	93	90
Na (mg/kg)	in	50	90	1700	53	50	47
	out	60	110	1900	54	53	52
K (g/kg)	in	1.6	2.8	0.0005	1.8	1.5	1.5
	out	1.8	3.2	0.00013	1.6	1.5	1.6
pH (formal)		13.5	13.7	14.0	13.5	13.5	13.5
Leached materials (mg)		0.03 (Mo)	0.21 (Mo)	0.34 (Mo)	0.001 (Cr)	0.03 (Mo)	-

$ gel compositions according to Table 4

From the data in Table 5 it can be concluded that high silica MFI (silicalite) is formed. Generally, no other T-atoms (Al, Fe, Cr), originating from the metal support and/or the silica source, are detected in either the synthesis gels or the supernatants (< 0.2 ppm). Only some molybdenum (maximal concentration of 10 ppm) is detected in all analyzed supernatants, especially under more severe conditions (SS-5; pH=14, 174 hours). Under the assumption that the chemical compositions of the synthesis mixture and the MFI phase are equal, all Si/T ratios are higher than 5000. The concentration of alkali (Na, K) ions within the framework is also low. The generally slightly higher alkali concentrations in the supernatants (after synthesis) are attributed to the reduced liquid density, because substantial amounts of silica and TPA have been consumed in the crystallization. Due to the relatively low accuracy of the data presented in Table 5, only a minimal Si/Na ratio of 3000 can be given (assuming 10% error). The same holds for potassium, but as a result of the tenfold higher potassium

concentration, the minimal Si/K ratio amounts to 300. It is, however, expected that hardly any potassium is present within the layer, because the incorporation of TPA in the MFI framework is strongly favoured.

Homogeneous MFI Layers on Stainless Steel Supports

Considering the low iron, nickel, and chromium concentrations in the supernatants, even with the high-temperature modules, the stainless steel used appears to be inert under the applied hydrothermal synthesis conditions. The inertness of the stainless steel is confirmed by experiment SS-5, which synthesis mixture has been applied in section 3.3 on various ceramic (oxidic) supports. On inert zirconia substrates, large, separately grown crystals are formed only after five days, as is the case in experiment SS-5. The chemical composition of the synthesis mixture is not affected by the presence of the inert support, and the crystallization proceeds in a similar way as for large, single crystals of MFI, previously described by Jansen et al.[18] From the blanc experiments (MFI crystallization in the absence of stainless steel), however, it seems that the stainless steel does affect the crystallization process, both in a chemical and a physical sense. Similar to the high-temperature modules, the Teflon lining in contact with the crystallization liquid is covered by MFI material. Several open spaces, on the other hand, remain present (Figure 19a). From the inhomogeneous nature of the MFI-layer the crystallization is expected to proceed in subsequently occurring stages (Figure 19b). Initially, small and slightly aggregated crystals are formed, which is attributed to the high supersaturation of the synthesis mixture, followed by the growth of a more continuous layer on top of these aggregated crystals. Figure 19c represents the bottom side of the layer (facing the Teflon lining during hydrothermal synthesis) near one of the open spaces in the layer. Next to the open space, a rather dense MFI phase is formed, probably as a result of the second crystallization stage. In the final stage, a top layer, similar to the one on the stainless steel support, is formed.
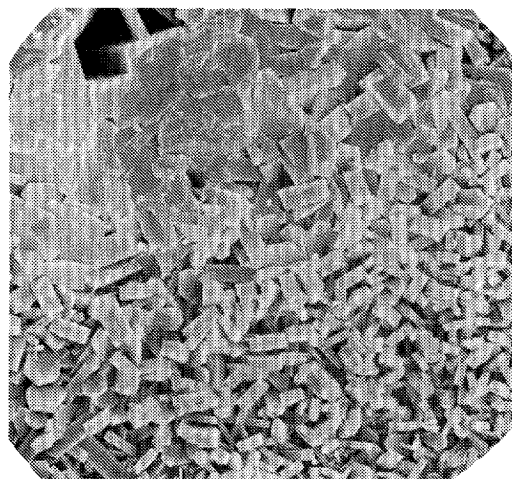
The occurrence of large open spaces within the layer is attributed to the relatively poor adhesion between the synthesis mixture and the hydrophobic Teflon surface (physical effect). In all experiments large amounts of TPA are introduced, and a high propene production due to the Hofmann degradation reaction of TPA is expected.[18]

(a) _____ = 240 μm   (b) _____ = 50 μm
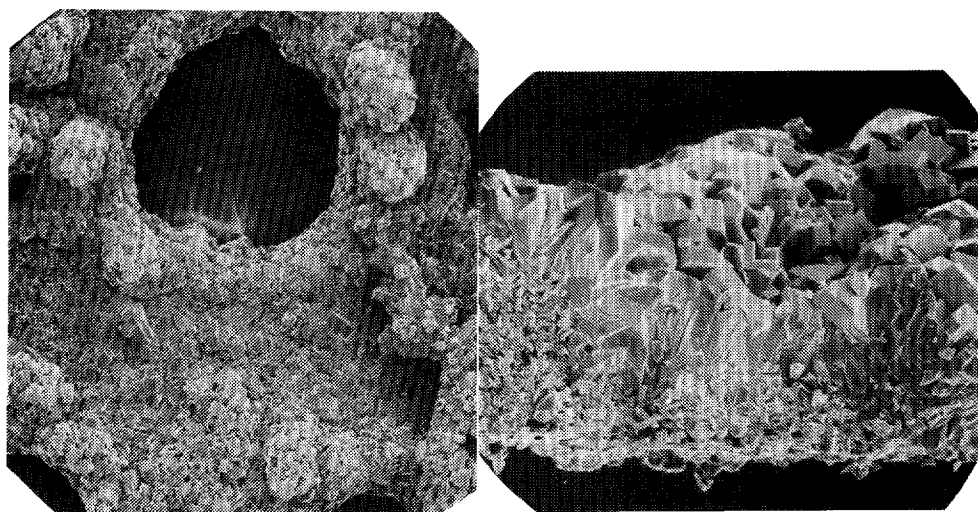
(c) _____ = 20 μm

Figure 19   SEM-pictures of an inhomogeneous, unsupported MFI layer, grown on a Teflon
surface according to B-2: (a) top view; (b) cross section; (c) bottom side, facing
the Teflon lining during hydrothermal synthesis, near an open space in the layer
(upper left corner)

The resulting volatiles (mainly propene and water) are concentrated in gas bubbles that may adhere to the Teflon surface. Obviously, these gas bubbles impede the formation of a layer completely covering the Teflon lining. The wetting of the hydrous solution to the more hydrophilic stainless steel, on the other hand, is excellent. Therefore, the produced gas bubbles are forced from the stainless steel support by the hydrous solution.

The presumed chemical effect is based on the fact that no small aggregated crystals are observed in the case of the stainless steel supported MFI layers. The layer consists of large MFI crystals *next to* each other, similar to the above clay supported MFI layers. Apparently, the nucleation proceeds in an essentially different way on the stainless steel surface as compared to the inert Teflon lining, leading to a continuous and homogenous zeolite layer. This may be caused by a local higher concentration of T-atoms, such as Fe^{3+} and Cr^{3+}, near the metal support. The occurrence of a dense silica gel phase, prior to the crystallization of cube shaped single crystals of MFI, has been attributed to the presence of low concentrations of trivalent cations.[18] Thus, the stainless steel material is not expected to be fully inert, but the concentration of leached metal ions remains below the detection level of the chemical analysis.

The relative inertness of the stainless steel material under the required hydrothermal conditions at high pH allows for recycling of the module. This compensates for the fact that in order to achieve a high specific membrane surface area, rather complex modules have to be constructed for inorganic membranes. Upon removal of the calcined MFI layer from the membrane module (HTSS-1) by alkaline treatment, some leaching of iron, chromium, and molybdenum (<0.5 mg) has been observed. Less extreme conditions (0.5 M KOH; 180°C; 2 hours) are, however, expected to suffice to dissolve all silica within the module.

3.5 Concluding Remarks

MFI layers as membranes can be prepared on ceramic substrates, but the preparation is strongly dependent on the reactivity of the substrate in relation to the composition of the synthesis mixture. With α-alumina, for instance, it is expected that a continuous MFI layer may be formed, provided the pH of the synthesis mixture is sufficiently low to avoid excessive leaching.

The results of section 3.4, however, demonstrate that continuous, polycrystalline MFI layers can be prepared on rather inert stainless steel substrates, but only within a restricted chemical composition of the synthesis mixture. First of all, relatively thick (> 10 µm) layers are required to achieve a complete coverage of the porous parts within the membrane module. Secondly, a rapid but homogeneous nucleation and crystal growth should proceed on all (externally) exposed surfaces. A relatively high SiO_2/OH^- ratio gives rise to a high nucleation rate (high supersaturation), and, moreover, leads to high silica yields. In addition, a high TPA concentration within the synthesis gel is expected to enhance nucleation, and favours the growth of large MFI crystals. Therefore, the MFI membrane preparation according to HTSS-2 (very high TPA concentration, cf. Table 4), is considered to be optimal.

From this perspective, the supported MFI layers (both on clay and on stainless steel) are essentially different from the unsupported MFI layers as prepared by Tsikoyiannis and Haag.[9,10] These layers have been prepared in the presence of substantially lower TPA concentrations and may consist of aggregates of crystals, both next to and on top of each other. With the MFI crystallization for the preparation of catalysts, the TPA concentration within the synthesis mixture is minimized to reduce the production costs. For membranes, on the other hand, relatively small amounts of active material are needed. The required high quality of the membrane layer justifies the use of expensive reactants.

3.6 Literature

1. K.E. Creasy, Y.P. Deng, J. Park, E.V.R. Borgstedt, S.P. Davis, S.L. Suib, and B.R. Shaw, in: *Synthesis/Characterization and Novel Applications of Molecular Sieve Materials*, R.L. Bedard, T. Bein, M.E. Davis, J. Garces, V.A. Maroni, and G.D. Stucky (Eds), MRS Symp.Ser. Vol. 233, Materials Research Society, Pittsburgh, 1991, 157.
2. I.M. Lachman, and M.D. Patil, US Patent 4,800,187, (1989) to Corning Glass Works.
3. H. Suzuki, US Patent 4,699,892, (1987)
4. S. Sakurada, N. Tagaya, T. Maeshima, and T. Isoda, Canadian Patent 1235684, April 26 (1988), to Toa Nenryo Kogyo Kabushiki Kaisha
5. S.A.I. Barri, G.J. Bratton, and T. de V. Naylor, European Patent Application 0 481 660 A1, (1991) to British Petroleum Company.
6. J.C. Jansen, W. Nugroho, and H. van Bekkum, in J.B. Higgins, R. von Ballmoos, and

M.M.J. Treacy (Eds.), Proc.9th Int.Zeol.Conf., Butterworth-Heinemann, Stoneham, Massachusetts, 1992, in press.

7.   H.P. Hsieh, *Catal.Rev.-Sci.Eng.*, 33 (1991) 1.

8.   R. Schulten, and L. Lücke, German Patent Application 38 27 049 A1, (1988).

9.   J.G. Tsikoyiannis, and W.O. Haag, *Zeolites*, 12 (1992) 126.

10.   J.G. Tsikoyiannis, and W.O. Haag, US Patent 5,019,263 (1991) to Mobil Oil Corp.

11.   T. Sano, Y. Kiyozumi, M. Kawamura, F. Mizukami, H. Takaya, T. Mouri, W. Inaoka, Y. Toida, M. Watanabe, and K. Toyoda, *Zeolites*, 11 (1991) 842.

12.   W. Xu, J. Dong, J. Li, J. Li, and F. Wu, *J.Chem.Soc. Chem.Comm.*, (1990) 755.

13.   J. Dong, T. Dou, X. Zhao, and L. Gao, *J.Chem.Soc. Chem.Comm*, (1992) 1056.

14.   F. Crea, R. Aiello, A. Nastro, and J.B. Nagy, *Zeolites*, 11 (1991) 521.

15.   J.L. Guth, H. Kessler, and R. Wey, in: *Proc. 7 IZC Tokyo*, Y. Murakami, A. Iijima, and J.W. Ward (Eds), Elsevier, Amsterdam, 1987, 121.

16.   M. Ghamami, and L.B. Sand, *Zeolites*, 3 (1983) 155.

17.   H. Lermer, M. Draeger, J. Steffen, and K.K. Unger, *Zeolites* 5 (1985) 131.

18.   J.C. Jansen, C.W.R. Engelen, and H. van Bekkum, in M.L. Occelli, and H.E. Robson (Eds.), *Zeolite Synthesis*, ACS Symp.Ser. Vol. 398, ACS, Washington DC, 1989, p. 257.

19.   J.C. Jansen, R. de Ruiter, E. Biron, and H. van Bekkum, in: *Zeolite: Facts, Figures, Future*, P.A. Jacobs, and R.A. van Santen (Eds), Stud.Surf.Sci.Catal. Vol. 49, Elsevier, Amsterdam, 1989, 679.

20.   Private communication with R. Szostak.

21.   H. van Koningsveld, H. van Bekkum, and J.C. Jansen, *Acta Cryst.*, B43 (1987) 127.

22.   D.G. Hay, H. Jaeger, and K.G. Wilshier, *Zeolites*, 10 (1990) 571.

23.   E.R. Geus, M.J. den Exter, and H. van Bekkum, *J.Chem.Soc. Faraday Trans.*, 88 (1992) 3101.

24.   G. Gottardi, and E. Galli, *Minerals and Rocks, Natural Zeolites*, Springer-Verlag, Berlin, (1985), 246.

25.   D.W. Breck, *Zeolite Molecular Sieves, Structure, Chemistry, and Use*, John Wiley-Interscience, New York, 1974, 313.

26.   J. Rocha, J. Klinowski, and J.M. Adams, *J.Chem.Soc. Faraday Trans.*, 87 (1991) 3091.

27.   E.R. Geus, H. van Bekkum, W.J.W. Bakker, and J.A. Moulijn, *Microporous Materials*, in press.

4. The Calcination of As-Synthesized, TPA-Containing MFI-Type Crystals

The development of cracks within large, TPA-templated MFI crystals upon calcination has been studied by visible light microscopy and microscope FTIR-spectroscopy. Upon calcination in air differently prepared silicalite crystals appeared to exhibit deviating TPA-stability and crystal cracking. Temperature-programmed X-ray powder diffraction has been performed to assess the thermal expansion/contraction behaviour of both as-synthesized (TPA-containing) MFI upon calcination and activated MFI material when subjected to thermal cycling.

4.1 Introduction

Separation on a molecular level by means of inorganic membranes requires microporous layers, in which no meso- or macropores are present. Application of crystalline molecular sieves as the membrane material offers in principle the possibility to prepare microporous membranes with a narrow pore size distribution. However, the relatively large MFI crystals, which have been used in this study, tend to crack upon removal of the template molecules (TPA) by calcination. These cracks impose strong limitations on the size of the MFI crystals to be incorporated into the monolayer concept dealt with in Chapter 2. The in situ grown MFI layers (Chapter 3) are also subjected to calcination to provide a permeable membrane. With the in situ grown layers the removal of TPA may also lead to undesired cracking and consequently to the introduction of larger pores within the membrane layer. If permeation experiments are performed on zeolite-based membranes containing cracks and, hence, larger pores, the cracks will give rise to inaccurate or erroneous data on the separation potential. Therefore, the decomposition of TPA has been studied in detail by several techniques to assess the formation of cracks and to establish a 'safe' calcination procedure. The emphasis is on large, cube shaped silicalite crystals, studied by visible light microscopy and microscope FTIR-spectroscopy to establish the stage in which cracking occurs. For comparison some other TPA-containing silicalite materials have been studied, together with tripropylamine-templated AFI. In addition, temperature-programmed powder X-ray diffraction has been performed to study the thermal expansion behaviour of MFI materials upon calcination and thermal cycling. In Chapter 7 the development upon calcination of the permeation through a membrane layer of MFI is described.

4.2 Degradation Mechanism

The activation of molecular sieves containing tetra-alkyl ammonium ions has been studied extensively. Commonly used techniques are thermogravimetry (t.g.), differential thermal analysis (d.t.a.), and differential scanning calorimetry (d.s.c.), techniques which may be coupled to mass spectrometry.[1-5] In some cases the thermal decomposition has been

interrupted to study the partly calcined material.[6] Thus far FTIR-spectroscopy has been applied only once during the TPA decomposition in fluoride-synthesized MFI.[7]

There is a reasonably good agreement about the mechanism of the TPA decomposition. The first reaction involves the Hofmann elimination reaction of TPA to tripropylamine (Pr_3N) and propene, and the major resulting species (tripropylamine or ammonium) depend on the framework composition.[3] Associated with negatively charged lattice sites (in the presence of trivalent T-atoms), TPA is more stable than the ionic pairs, such as TPAOH or TPAF, which are present in silicalite. In the latter case, the degradation is supposed to be induced by a nucleophilic species (OH^-, SiO^-, and F^- for fluoride-synthesized MFI) compensating the charge of TPA, and attacking a ß-C-H proton according to:

$$Pr_4N^+ \; X^- \; \longrightarrow \; CH_2=CH-CH_3 + Pr_3N + HX \qquad (1)$$
with X being OH^- or SiO^-
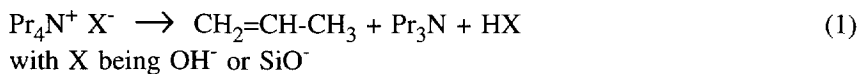
Generally, a concerted bond breaking mechanism (E_2) is assumed for the ß-elimination leading to propene and tripropylamine. According to mass spectrometry, a significant amount of secondary amines (e.g. di-n-propylamine, and n-propylhexylamine) also evolves from Si-rich MFI,[2] showing consecutive fragmentation of tripropylamine and propene dimerization, followed by alkylamination of alkenes.

The presence of SiO^- groups, in fact, is due to broken Si-O-Si bonds or crystal defects.[8] The SiO^- groups may be considered to be in equilibrium with the TPAOH ion pair according to:

$$Si-O-Si + Pr_4N^+ \; OH^- \; \rightleftarrows \; Si-O^- \; Pr_4N^+ + Si-OH \qquad (2)$$
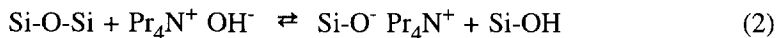
Alkali ions, such as Na^+, may be incorporated within the zeolite framework instead of a silanol group as $Si-O^- \; Na^+$. The occurrence of $SiO^- \; TPA^+$ groups within the as-synthesized and effectively neutral silicalite framework may be established from the concentration of silanol groups. ^{13}C n.m.r. provides an estimate of the number of Si-OH (and SiO^-) groups per unit cell, which is correlated to the number of broken Si-O-Si bonds. For intergrown MFI material, prepared as relatively thick membrane layers, a concentration of some 1.5 silanol groups per unit cell has been reported, which indicates a high extent of crystallinity.[9]

Both OH⁻- and SiO⁻-induced TPA degradation leads to the formation of water according to reaction (1). With SiO⁻, the initially formed silanol group may lead to an Si-O-Si bond by the condensation reaction producing water:

$$\equiv\text{Si-OH} + \text{HO-Si}\equiv \; \rightleftarrows \; \equiv\text{Si-O-Si}\equiv + H_2O \qquad\qquad (3)$$
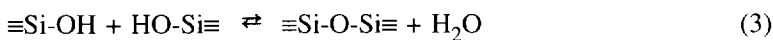
The presence of either OH⁻ or SiO⁻ groups in hydroxide-synthesized Si-rich MFI seems to initiate the TPA-degradation at relatively low temperatures as compared to the TPAF ionic pair. In fluoride-synthesized silicalite, no hydroxyl absorption bands are observed, and TPA remains stable up to at least 350°C.[7]

4.3 Crack-Development upon Calcination: A Microscope FTIR-Spectroscopy Study

The physical and chemical processes within large molecular sieve crystals can be excellently monitored by means of FTIR-spectroscopy.[7,10] In addition, large crystals allow observation by means of visible light microscopy. Microscope FTIR-spectroscopy combines both techniques, and is able to provide complementary data as compared to the previously mentioned thermo-analytical techniques.

The synthesis of the materials studied (cube shaped silicate crystals of different sizes, VS-1 crystals as small cubes and larger 90° intergrown crystals, and fluoride-synthesized silicalite prisms (Si/F = 1.2)) has been addressed previously (Chapter 2, Table 3). AlPO₄-5 crystals (AFI; templated with tripropylamine) have been included for comparison. The AFI crystals are synthesized from a mixture (aged for 2 hours) of phosphoric acid (Baker), aluminiumisopropoxide (Janssen Chimica), hydrogen fluoride (Merck), and tripropylamine (Janssen Chimica), the molar composition being 1 Al_2O_3 : 1 P_2O_5 : 1 HF : 1 Pr_3N : 300 H_2O.[11] Large, rod shaped AFI crystals are obtained after hydrothermal treatment at 180°C for 15 hours.

All crystals are attached to a silicon wafer by means of a ceramic kit (Royal Delft Ware

Manufactory): the silicalite crystals generally with the ac plane perpendicular to the VIS/IR-beam; the rod shaped AFI crystals in such a way that the beam is transmitted through two crystal faces (cf. Figure 1). The crystals can thus be positioned with the crystal surfaces exposed to the gas phase within a high-temperature cell. IR-spectra can be taken from each crystal separately via a microscope in the transmission mode (total magnification 150x). The experimental set-up is described in more detail in Chapter 6, which is devoted to this newly developed technique to study sorption/diffusion processes within molecular sieve materials.

(a)

_____ = 100 μm

(b)
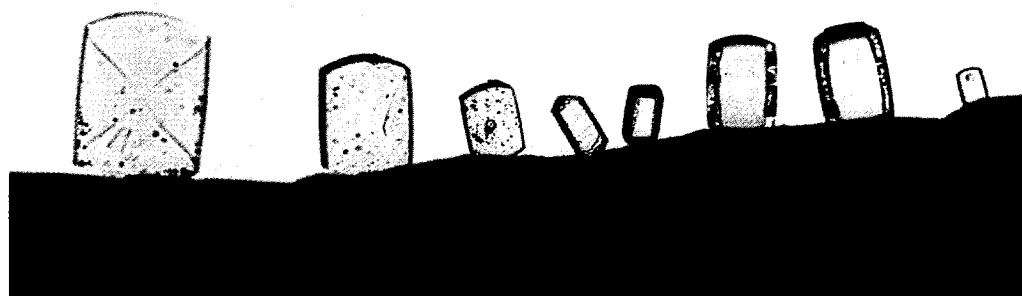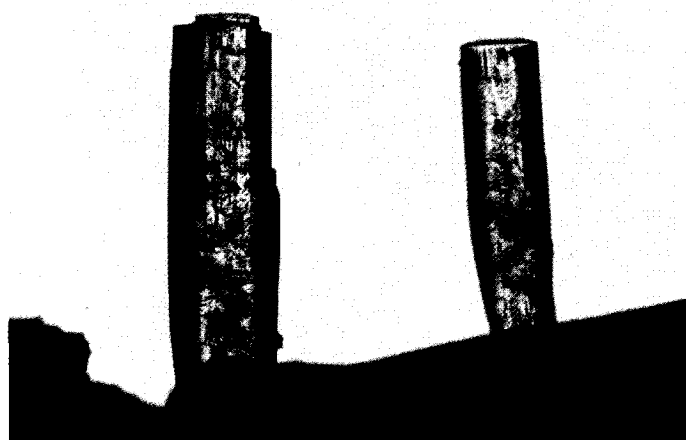
_____ = 200 μm

Figure 1   Visible light micrographs of (a) left to right: three silicalite cubes of varying sizes, two fluoride-synthesized prisms in the a and b-direction, two 90° intergrown VS-1 crystals, and a small VS-1 cube; (b) two AFI crystals

4.3.1 Microscope FTIR-Spectroscopy

The IR-spectra of the as-synthesized crystals are presented in Figure 2. For the MFI-type crystals the IR-vibrations of C-H (2981, 2943, and 2883 cm^{-1} stretching; 1473, 1459, and 1382 cm^{-1} deformation), Si-O (1971, 1861, 1641 cm^{-1}), and the broad hydroxyl signal (on which the C-H stretching vibrations are superimposed) are apparent. In fluoride-synthesized silicalite (Figure 2b), no hydroxyl bands are apparent. In the IR-spectrum of the AFI crystal (Figure 2d), different hydroxyl bands can be observed at 3621, 3540, and 3105 cm^{-1}. The C-H vibrations within the AFI crystal (at 2977, 2950, 2888, and 2805 cm^{-1}) deviate from those of as-synthesized MFI, since tripropylamine serves as the template, which is probably transformed by HF into the ion pair ($Pr_3NH^+ F^-$).

(a)

(b)

(c)

(d)
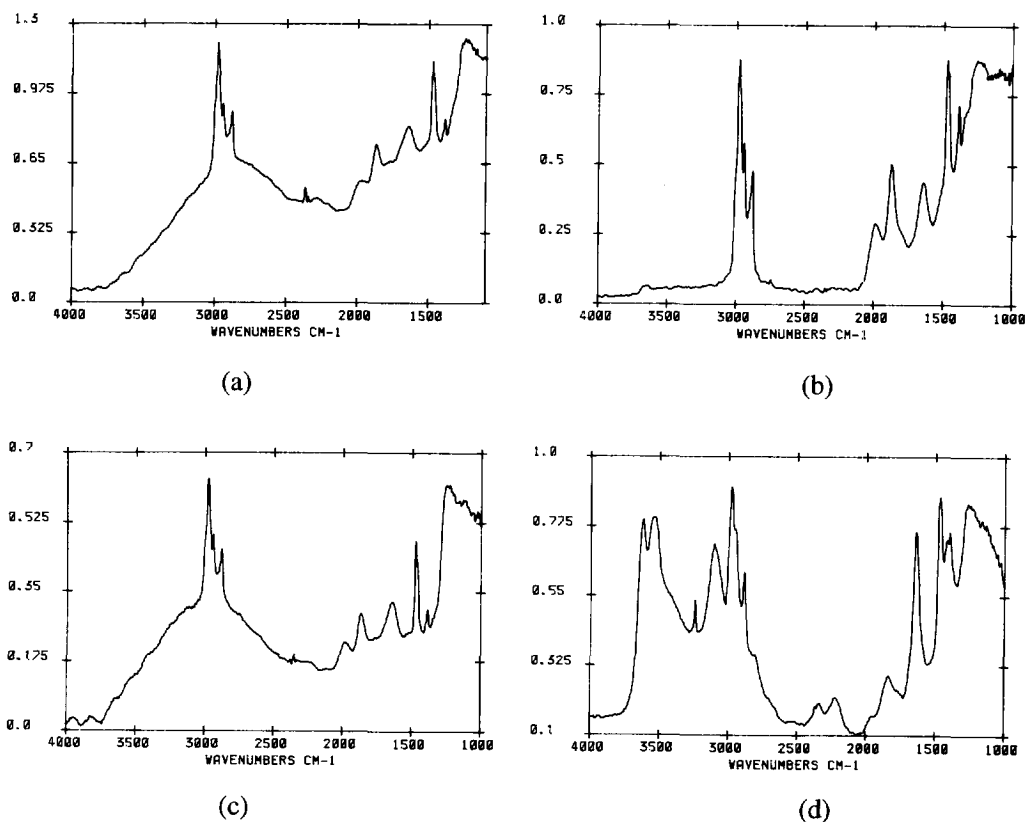
Figure 2   IR-spectra of (a) a silicalite cube, (b) a fluoride-synthesized prism, (c) a small VS-1 cube, and (d) an AFI rod shaped crystal

In Figure 3 some IR-spectra are shown of the silicalite cube at rising temperatures (1°C/min). Up to ca. 260°C, some dehydration proceeds, and the C-H deformation band at 1459 cm^{-1} merges into the 1473 cm^{-1} band. Within the temperature interval of 270-280°C, the C-H vibration bands shift to lower frequencies (2966, 2939, and 2877 cm^{-1}), and the hydroxyl absorption bands disappear within the same temperature interval. The C-H deformation bands, however, remain unchanged. From 330 to 350°C the C-H absorption bands diminish rapidly, which process is slightly more rapid within small cubes (100 μm length) as compared to larger crystals (up to 300 μm length). At ca. 380°C a weak hydroxyl band arises at 3726 cm^{-1}.
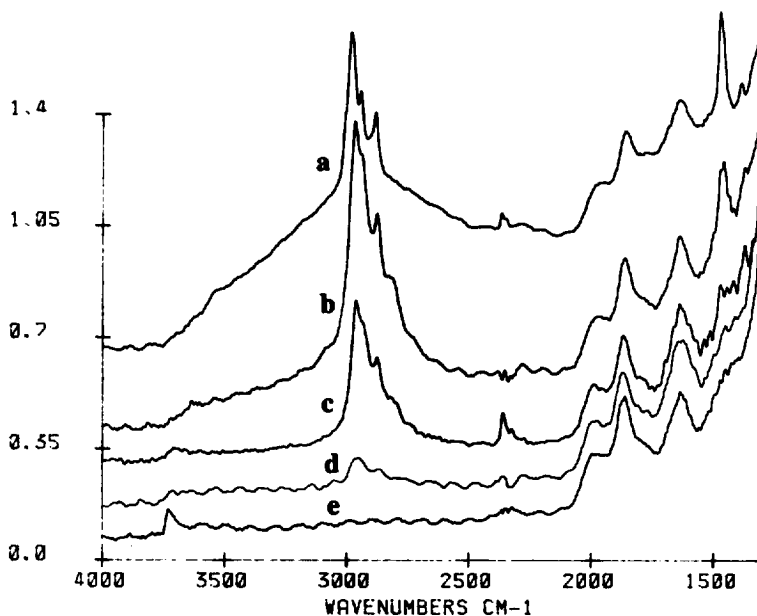

Figure 3   IR-spectra of the silicalite cube (Figure 2a) during calcination at (a) 200°C, (b) 300°C, (c) 330°C, (d) 340°C, and (e) 400°C

According to the decomposition mechanism as described in section 4.2, the first step in the activation of as-synthesized (TPA-containing) MFI material involves the Hofmann elimination of TPA. The successive ß-elimination steps, however, do not take place at temperatures below 300°C, and the produced tripropylamine seems to remain stable up to at least 330°C. This has been verified by IR-spectroscopy on a partly calcined silicalite cube by rapid cooling from ca. 320°C to room temperature. The IR-spectrum under ambient conditions is shown in Figure 4, revealing an almost completely dehydrated crystal, and C-H absorption bands at 2964, 2939, 2877, and 2805 cm^{-1}. A weak absorption band at approximately 3078 cm^{-1} is attributed to the weakly absorbing alkene C-H vibration band of propene.
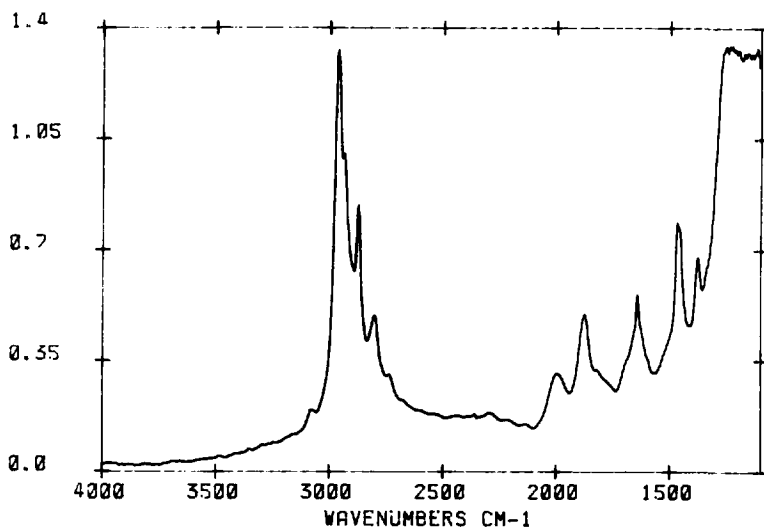

Figure 4   IR-spectrum of a partly calcined cube shaped silicalite crystal at 320°C

The C-H vibrational bands of the tripropylamine assumed to be present within the partly calcined silicalite crystal are slightly shifted to lower frequencies as compared to the as-synthesized tripropyl ammonium-containing AFI crystal represented in Figure 2d. According to X-ray diffractometry (Diffractis 601, Enraf-Nonius), the crystal is still orthorhombic, presumably since the tripropylamine molecules are accommodated within the framework

in the same way as TPA. The assumption that tripropylamine remains within the zeolite is supported by the fact that tripropylamine is not observed by mass spectrometry.[2] As a substantial amount of propene is present within the partly calcined crystal, according to the weak absorption band above 3000 cm^{-1} (cf. Chapter 6, Table 1), it is concluded that after the initial TPA degradation neither tripropylamine, nor propene is desorbed from the MFI framework. Apparently only water is sufficiently mobile and able to desorb from the zeolite micropores. In view of the breakage and formation of Si-O-Si bonds according to equation (3) the desorption of water may be related to the initial cracking of large silicalite cubes (*vide infra*).

For the small VS-1 cube (Figure 5) the same sequence of events is observed at slightly higher temperatures (for instance, the Hofmann elimination proceeds at ca. 290-300°C). According to Figure 5 somewhat different species appear to be produced, that remain present up to ca. 370°C (Figure 5c).
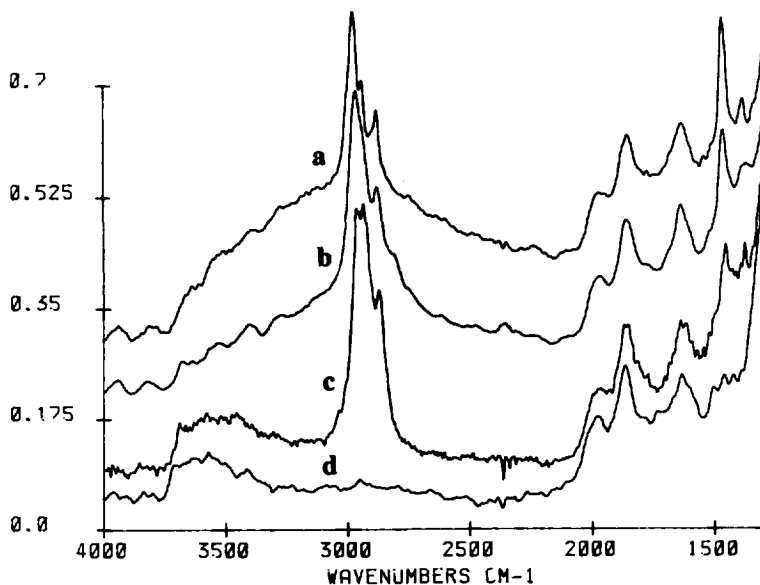

Figure 5   IR-spectra of the small VS-1 cube (Figure 2c) during calcination at (a) 200°C, (b) 300°C, (c) 370°C, and (d) 400°C

The TPA degradation is more different with fluoride-synthesized silicalite, which is attributed to the absence of hydroxyl groups. Up to 360°C, the IR-spectrum remains very similar to that of Figure 2b. Subsequently, the Hofmann elimination and further degradation proceed rapidly (380-400°C). The fluoride-synthesized silicalite framework is more hydrophobic as compared to the hydroxide-synthesized silicalite and the VS-1 framework: no hydroxyl absorption bands are observed after calcination.

For AFI the dehydration proceeds well below 100°C (Figure 6a). The sharp band at 3243 cm^{-1} remains present up to ca. 300°C (Figure 6b), and may be related to ammonium ions. The C-H absorption bands only diminish above 300°C, but at 425°C, some hydrocarbon species are still apparent. The AFI crystals become segmented upon calcination at ca. 275°C. It is tempting to attribute the development of segments to the one dimensional pore system. As axial transport through the channels (12 membered rings) might be hampered by rather immobile oligomeric amines and hydrocarbons, the volatile degradation products force their way out in the radial direction. The crystal length parallel to the long axis is thus reduced by the segments. No significant differences are observed between IR-spectra of different parts of the AFI crystal.
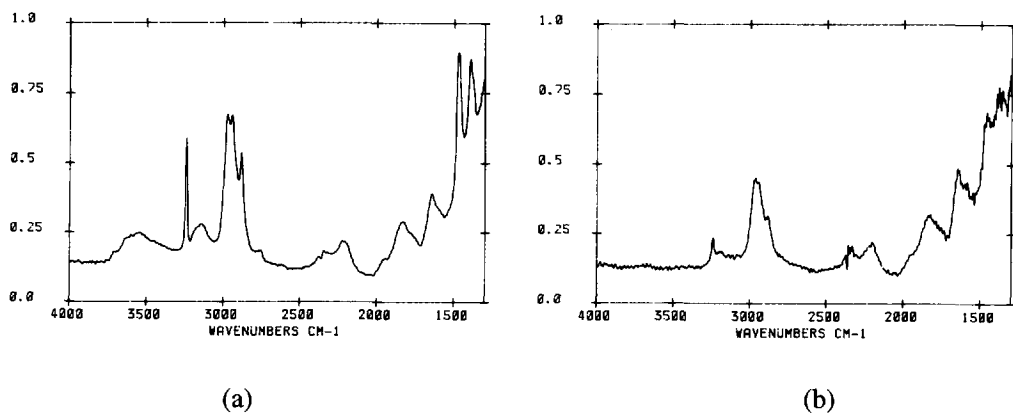

(a)   (b)

Figure 6   IR-spectrum of the AFI crystal during the calcination process at (a) 100°C, and (b) 300°C

For comparison, some calcination experiments have been carried out for cube shaped hydroxide-synthesized and prismatic shaped fluoride silicalite crystals in a pure nitrogen atmosphere (heating rate 1°C/min). From these experiments it is concluded that within the silicalite cubes the Hofmann elimination reaction of TPA takes place at the same temperature (i.e. 260-310°C) as in air. For both silicalites, the void spaces are, however, emptied at a slightly higher calcination temperature (390°C for the cubes) or by prolonged calcination at 400°C (> 3 hours for the fluoride prisms). Nevertheless, it seems possible to render fully activated MFI crystals at approximately 400°C, even while oxygen is not present.
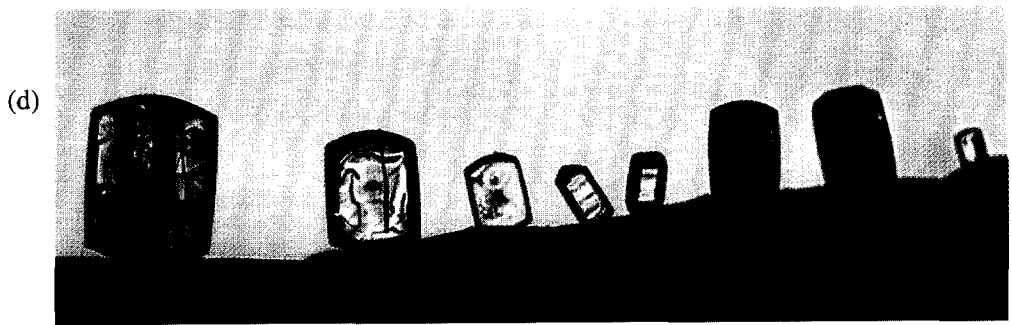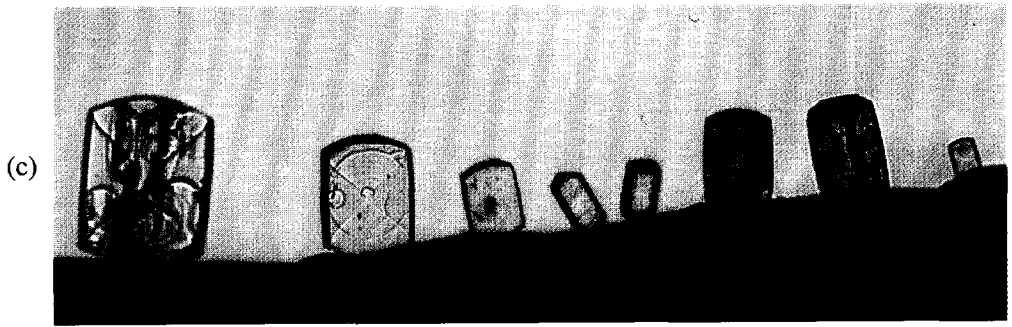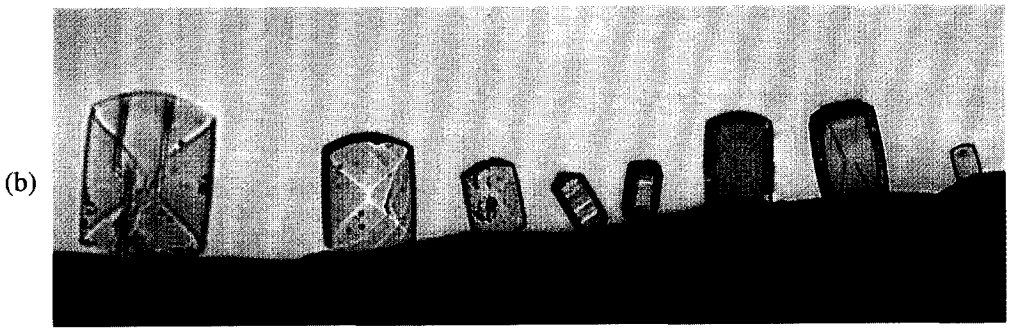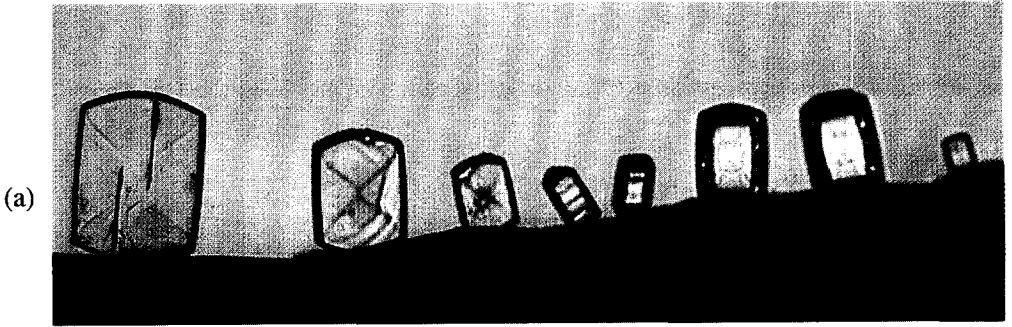
4.3.2 Visible Light Microscopy

The calcination experiments have also been performed in a different set-up, only using visible light microscopy (magnification 50x; Olympus BH-2 with camera) to study the crack-formation and colour changes within the crystals in more detail. In Figure 7 visible light microscopy pictures of the MFI crystals of Figure 1a are shown at different calcination stages. From light microscopy only it may be concluded that the synthesis procedure of the silicalite crystals significantly affects the behaviour during calcination.

The effect of the crystal size of the cube shaped silicalite crystals on the behaviour during calcination is thus revealed. In large crystals (> 300 µm length) some straight cracks along the c-axis develop at 260°C. For all cubes cracking proceeds at random within the temperature interval of 340-350°C. Only small cube shaped crystals (length < 150 µm) remain crack-free.

The behaviour during calcination of the two VS-1 type crystals is very different. Already at low temperatures, the much larger 90° intergrown crystals are turning brown, whereas the smaller cubes are still completely colourless. The brown colour suggests that within the larger 90° intergrown VS-1 crystals the degradation reactions proceed at substantially lower temperatures than within the smaller VS-1 cubes. It is interesting that in the intergrown VS-1 crystals, the growth lines of a small cube shaped crystal are visible. During the calcination of the large 90° intergrown VS-1 cubes, some lines (presumably growth lines) become more pronouncedly visible in the intergrown crystals. Both VS-1 types reveal an hour-glass pattern at high temperatures while the brown crystals turn transparent.
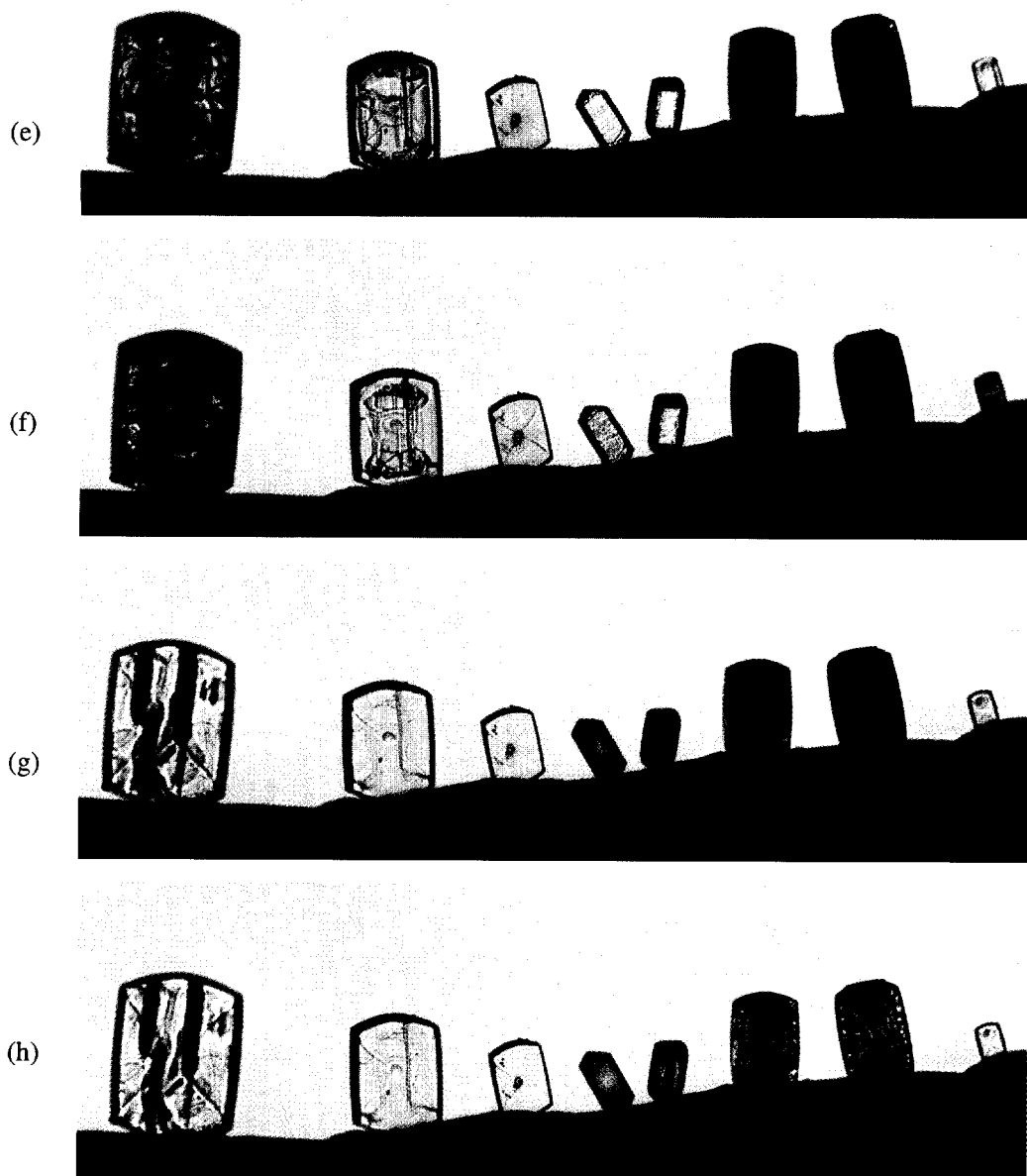
(a)

(b)

(c)

(d)

Figure 7   Visible light micrographs of the MFI-type crystals (Figure 1a) during calcination at (a) 260°C, (b) 324°C, (c) 342°C, (d) 352°C, (e) 359°C, (f) 367°C, (g) 387°C, and (h) 400°C

Table 1   Main events in the calcination of TPA-templated MFI-type crystals

T (°C)	Event
Cube shaped silicalite	
<260°C	some dehydration
260-310°C	dehydration and Hofmann elimination of TPA to tripropylamine and propene large crystals (> 300 μm): straight cracks in c-direction
>320°C	brown colouring of cracked area (large crystals)
330-360°C	at random cracking in crystals >150 μm disappearance of C-H absorption bands (most rapid within small crystals
>350°	brown colouring (strongest for large crystals)
VS-1: small (60 μm length) cubes and 90° intergrown crystals	
<260°C	significant dehydration
280-320°C	dehydration and Hofmann elimination of TPA (small cubes)
320-360°C	crack-formation within 90° intergrown crystals turning brown (first) and black (eventually)
340-350°C	tripropylamine species transforms at least partly into some other species (small cubes)
360-380°C	small cubes turn brown; C-H absorption bands disappear
Fluoride-synthesized silicalite	
20°C	fully dehydrated
ca. 360°C	Hofmann elimination of TPA
375-390°C	disappearance of C-H absorption bands; at random cracking and brown/black colouring

The fluoride-synthesized crystals are also heavily cracked during the calcination. The cracks develop within the same temperature interval in which the fluoride-synthesized crystals turn dark brown.

For all types of silicalite, the brown colouring of the crystals takes place within the temperature interval in which the further degradation of tripropylamine proceeds, according to FTIR-spectroscopy. An overview of the main events during calcination is presented in Table 1 for all MFI-type crystals, including the observations by FTIR-spectroscopy. The straight cracks within the large silicalite cubes, on the other hand, seem to be related to the dehydration of the framework during the initial Hofmann elimination reaction of TPA. Cracking may be initiated by the condensation reaction of two silanol groups, as internal stress is developed within the silicalite cube. Apparently, only very large crystals are liable to crack-propagation, which process has been observed by visible light microscopy.

4.3.3 Comparison of FTIR-Spectroscopy with Thermoanalytical Techniques

To verify the temperatures at which the TPA-degradation occurs according to FTIR-spectroscopy, the calcination in air of silicalite cubes (initial weight 48.8 mg) is also studied by thermogravimetry (heating rates 1 and 10°C/min). In Figure 8 the weight loss upon calcination at 1°C/min is shown. The first significant change in weight is observed below 300°C, which is also the case at a heating rate of 10°C/min. Above 390°C no further weight loss takes place.

Based on four TPA per unit cell, the total removal of TPA from the MFI framework amounts to 11.4 wt% loss. Since a total weight loss of 13.2 wt% has been observed, the remaining 1.8 wt% may be attributed to incorporated water. From the size of the crystals (and the assumed smoothness of the external surface), it is unlikely that a significant weight loss will arise from dehydration of the external surface. Up to 310°C, hence below the temperature at which the further degradation of tripropylamine takes place, the weight loss amounts to ca. 2 wt%. The weight loss below 310°C thus seems to be mainly due to water desorption, in accordance with the FTIR-spectroscopy results. The total water content thus corresponds to 6.6 water molecules per unit cell.
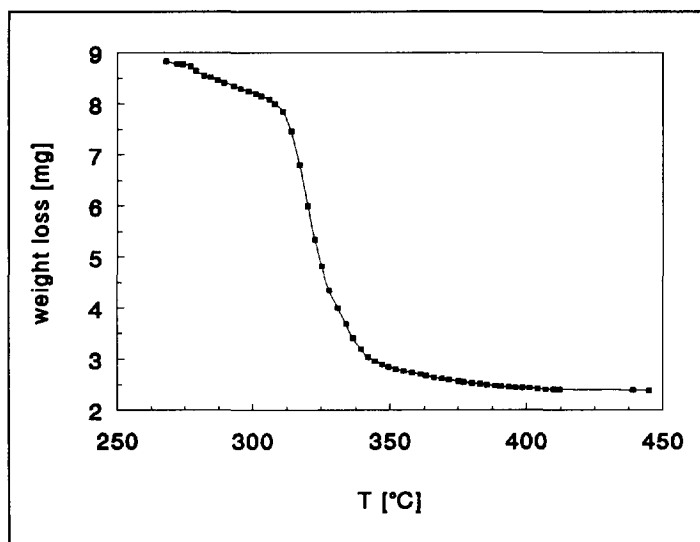
Figure 8   Weight loss (initial weight 48.8 mg) upon calcination of hydroxide-synthesized silicalite cubes (heating rate 1°C/min)

In contrast with the good agreement between the data presented here on the calcination of cube shaped silicalite crystals by FTIR-spectroscopy and t.g., the TPA decomposition is observed to proceed at much lower temperatures than mentioned in the literature, viz. at approximately 400°C.[2,3] Only the FTIR-spectroscopic study on fluoride-synthesized MFI by Nowotny,[7] and the t.g. data on hydroxide-synthesized MFI published by Engelen[12] are in agreement with the low temperatures observed in this work. Qualitative agreement exists, however, on the difference in calcination behaviour between fluoride- and hydroxide-synthesized silicalite.[2,6] It should be noted that the FTIR-spectroscopic results are based directly on the chemical and physical processes within the zeolite framework.[10] The thermoanalytical techniques refer to changes in the surrounding gas phase, rather than monitoring directly the decomposition processes taking place within the zeolite micropores. Still, the origin of the sample may be more decisively affecting the TPA stability, and, hence, the calcination process. Silicalite prisms, prepared from a dispersed silica gel[13] (as opposed to the dense gel phase for silicalite cubes[14]), are calcined at 500°C in order to remove all organics.

For a proper comparison, the heating rate has to be taken into account. The generally applied heating rate of 10°C/min (minimal 6°C/min)[6] gives rise to much shorter contact times for species, such as propene, to react. The same difference in contact time holds for large crystals as compared to small ones. As mentioned earlier for the silicalite cubes of different sizes, the temperature at which all hydrocarbons are removed from the framework depends on the crystal size. Thus, for low heating rates and/or large crystals other degradation products may be formed, that may be more persistent upon calcination.

The presence of for instance oxygen may affect the nature of the degradation products for the same reason. From the thermogravimetric results, Engelen concludes that the calcination of MFI material does not depend on the presence of oxygen in the surrounding atmosphere (heating rate 10°C/min).[12] The above results obtained with FTIR-spectroscopy (heating rate 1°C/min) point out, however, that in a nitrogen atmosphere the further degradation of tripropylamine differs significantly from that during calcination in air. The effect of the gas phase seems to be at least partly due to the low heating rate. The calcination of TPA-templated MFI crystals thus depends mainly on the synthesis procedure (fluoride or hydroxide; dispersed or dense silica gel). Secondary effects involve the heating rate, crystal size, and calcination atmosphere.

4.4 Temperature-programmed Powder XRD

The thermal expansion behaviour of TPA-templated cube shaped (hydroxide) and prismatic shaped (fluoride) silicalite upon calcination has been studied by temperature-programmed X-ray powder diffraction. Finely ground samples are applied on a platinum wire gauze, which serves as an internal standard. The X-ray diffraction patterns are obtained with a high-temperature Guinier camera, using CuK_α radiation. The calcination experiment is carried out in a nitrogen/oxygen mixture (80/20) at a heating rate of 1°C/min up to 600°C, and immediately cooling down at the same rate.

The films are read with a densitometer (50°C increments), and the difference in Bragg's

angle (Θ) of the (432), (352), (153), (632), (552), (1000), and (0100) MFI diffraction maxima with the Pt (111) diffraction maximum are determined. The position of Pt (111) is calculated from the thermal expansion of the cubic platinum lattice ($\alpha_{Pt}=90*10^{-7}$ °C^{-1}), using Bragg's law, differentiated to Θ:[15]

$$\alpha_{Pt} = \frac{\Delta a}{a} = \frac{\Delta d}{d} = -\frac{\Delta\theta}{\tan\theta} \tag{4}$$

with a the unit cell parameter of platinum (cubic), and d the d spacing of the lattice. The d spacings of the MFI diffraction maxima are then calculated from Bragg's law.

In Figure 9 the variation of the (352), (153), (632), and (552) d spacings with temperature is presented; the (432), (1000), and (0100) d spacings show similar behaviour. The thermal expansion/contraction for both samples is listed for three temperature regions (cf. Table 2a and b): (i) heating of TPA-MFI, (ii) degradation of TPA, and (iii) cooling of calcined MFI. For the a- (1000) and b-direction (0100), the results may be less reliable, because other diffraction maxima are superimposed.

Both silicalite types reveal similar behaviour, but the phenomena are more pronounced for the (hydroxide-synthesized) silicalite cubes. The strong contraction within the temperature interval of 300-400°C (while heating) coincides with the removal of the TPA-degradation products, in accordance with FTIR-spectroscopy. The shrinkage process continues to 500-550°C, and seems to continue to slightly higher temperatures with the fluoride-synthesized prisms. Upon cooling to 100-200°C (fully activated material), only a slight change in the d spacings is observed, leading to an overall contraction of the orthorhombic lattice, comparing the dimensions of the as-synthesized TPA-containing framework and the calcined, still orthorhombic framework at 100°C (0.5-0.9% for OH$^-$; 0-0.3% for F$^-$). Only for the fluoride-synthesized prisms, an eventual expansion in the a-direction (0.1% for the (1000) d spacing) due to the calcination is observed.
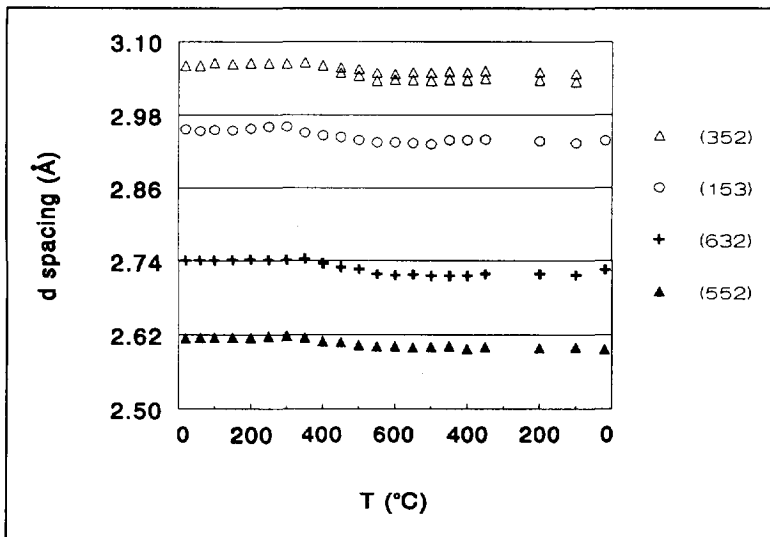
(a)
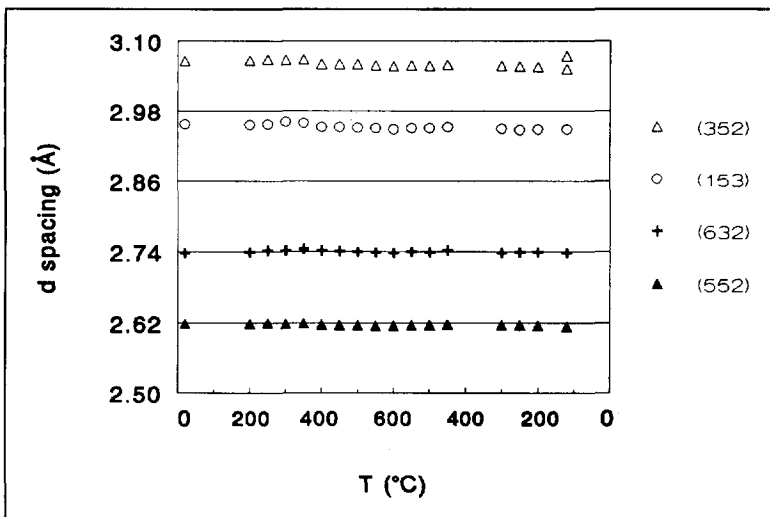
(b)

Figure 9   Relative position of (352), (153), (632), and (552) MFI d spacings during calcination in a 80/20 nitrogen/oxygen mixture for (a) silicalite cubes, and (b) fluoride-synthesized silicalite prisms

95

Table 2a   Thermal expansion/contraction of hydroxide-synthesized silicalite upon calcination and cooling to ambient conditions

d spacing	thermal expansion/contraction $(°C^{-1})/10^{-7}$		
	20-300°C	350-500°C	600-100°C
(432)	57	-408	-5
(352)	41	-	-
(153)	10	-327	-
(632)	27	-430	-9
(552)	26	-267	9
(10̲00)	83	-357	-20
(01̲00)	-16	-320	19

Table 2b   Thermal expansion/contraction of fluoride-synthesized silicalite upon calcination and cooling to ambient conditions

d spacing	thermal expansion/contraction $(°C^{-1})/10^{-7}$		
	20-350°C	350-600°C	600-200°C
(432)	66	-179	4
(352)	30	-124	13
(153)	30	-120	16
(632)	72	-94	5
(552)	9	-57	2
(10̲00)	32	-48	-32
(01̲00)	3	-54	-3

The X-ray powder diffraction results on the hydroxide-synthesized silicalite cubes may be compared with the lattice parameters according to X-ray single crystal structure analysis (crystal structure elucidation), in which similarly prepared silicalite cubes have been used.[16] The lattice parameters of the as-synthesized[17] and the calcined (either orthorhombic[18] at 80° or monoclinic[19] at 20°C) from the literature are shown in Table 3. The lattice parameters of the MFI framework, completely filled with 8 molecules of adsorbed p-xylene per unit cell[20] are included as well to demonstrate the difference in unit cell sizes. Table 3 indicates a rather anisotropic contraction/expansion behaviour of the MFI framework, in contrast to the isotropic and overall shrinkage according to the powder diffraction data for hydroxide-synthesized silicalite.

Table 3   MFI lattice parameters and unit cell volumes of the as-synthesized, calcined (monoclinic and high-temperature orthorhombic), and p-xylene filled MFI framework

Structure	a (Å)	b (Å)	c (Å)	ß (°)	Volume (Å^3)	Ref.
TPA-MFI (Orthorhombic; Pnma) 20°C, as-synthesized	20.022	19.899	13.383	-	5332	17
MFI (Orthorhombic; Pnma) 77°C, calcined	20.078	19.894	13.372	-	5341	18
MFI (Monoclinic; P2$_1$/n.1.1) 20°C, calcined	19.879	20.107	13.369	90.67	5343	19
p-xylene-MFI (Orthorhombic; P2$_1$2$_1$2$_1$) 20°C, 8 molec./u.c.	20.121	19.820	13.438	-	5359	20

Another difference with X-ray single crystal structure analysis is the splitting of the (352) d spacing in Figure 9a. For fluoride-synthesized silicalite (Figure 9b) a doublet (with larger difference in d spacing) is observed at room temperature after calcination. The occurrence

of the doublet (d ≈ 3.04 Å) is in principle connected to the monoclinic structure of MFI (cf. simulated powder diffraction patterns of the orthorhombic and monoclinic structure).[21] There is, indeed, general agreement that for high-silica MFI (Si/Al>8000) the orthorhombic-to-monoclinic phase transition is situated around 70°C.[22,23] For similar powder X-ray diffraction measurements on calcined MFI (hydroxide-synthesized) material by Kokotailo et al., however, the occurrence of doublets has also been observed at temperatures in excess of 70°C.[24] In their study they conclude that the calcined MFI framework remains monoclinic at all temperatures, irrespective of the Si/Al ratio.

Thus, the X-ray powder diffraction data on the calcination of TPA-templated silicalite (hydroxide-synthesized) are not consistent with results on X-ray single crystal structure analysis. Nevertheless, both techniques are based on the same principle and theory. Jansen et al. have demonstrated the applicability (and the consistency) of each technique for the cell contraction by isomorphous substitution of boron in the MFI framework.[25]

Results obtained with powder X-ray diffractometry being different from that from X-ray single crystal structure analysis may, however, arise from the differences within one sample. Many crystals (usually from one batch) are used with X-ray powder diffraction, and thus refer to the average of the sample. The results therefore strongly depend on the homogeneity of the sample. For single crystal structure analysis a carefully selected crystal is used, intrinsically containing only a small number of defects. The selected single crystal may not necessarily be representative for the whole sample. In section 2.2 it has been mentioned that apart from cube shaped single crystals also more intergrown crystal aggregates are formed. The inconsistent results of X-ray powder diffraction and single crystal structure analysis for, in principle, the same hydroxide-synthesized silicalite crystals may therefore be related to the inhomogeneous nature of the sample.

In view of the thermal expansion/contraction behaviour of zeolites the influence of water cannot be neglected. During dehydration by thermally treating hydrophilic zeolites such as (Na, Ca, Mg)-A zeolites, a steady contraction of the unit cell has been reported, upon which an abrupt and strong expansion, attributed to the repositioning of cations, is superimposed.[26] These effects are not likely to occur with hydrophobic zeolites such as silicalite, but

breaking of Si-O-Si bonds by the reaction with water, especially after long exposure to humid air, may take place. Broken Si-O-Si bonds are expected to give rise to an expansion of the unit cell. It is therefore noteworthy that the X-ray single crystal structure analyses have been performed under ambient conditions,[27] whereas the here described powder X-ray diffraction measurements are carried out in a nitrogen/oxygen mixture in the absence of water. For fluoride-synthesized silicalite the absence of water is not expected to give rise to a significantly different expansion behaviour, because this material is very hydrophobic (according to FTIR-spectroscopy).

It is obvious that the thermal expansion behaviour of TPA-templated MFI materials upon calcination is not yet fully understood. This X-ray powder diffraction study has nevertheless demonstrated that substantial changes in the unit cell dimension may take place, in particular during the removal of TPA-degradation products. Due to the transient character of these phenomena, it is rather difficult to perform the same measurements by X-ray single crystal structure analysis. This technique requires relatively long exposure times to collect sufficient data, which makes it worthwhile to reconcile the results by X-ray powder diffractometry with crystal structure elucidations of zeolite single crystals.

4.5 Non-Uniform Calcination of Prismatic Overgrown MFI Crystals[28]

It this section attention is drawn to the possibility of inhomogeneities within MFI single crystals. In a separate study, the calcination of a silicalite prism, prepared from a similar synthesis mixture as the silicalite single crystal cubes, has been found to proceed inhomogeneously. These crystals have been previously mentioned in Chapter 2 as very flat (short b-axis) silicalite crystals. Even relatively large crystals (>200 μm length) remain crack-free upon calcination up to 900°C, which is of utmost importance with a view on zeolite-based membranes.

4.5.1 Silicalite Cubes with a Prismatic Overgrowth

The prismatic shaped silicalite single crystals are prepared from a synthesis mixture similar to that recommended by Lermer et al.[16] To avoid the introduction of alkali ions, TPAOH (CFZ, Zaltbommel, the Netherlands) is used as the TPA source. The molar composition of the synthesis gel amounts to 100 SiO_2 : 119 TPA_2O : 27740 H_2O. The hydrothermal treatment comprises heating for ca. 110 hours at 180°C.
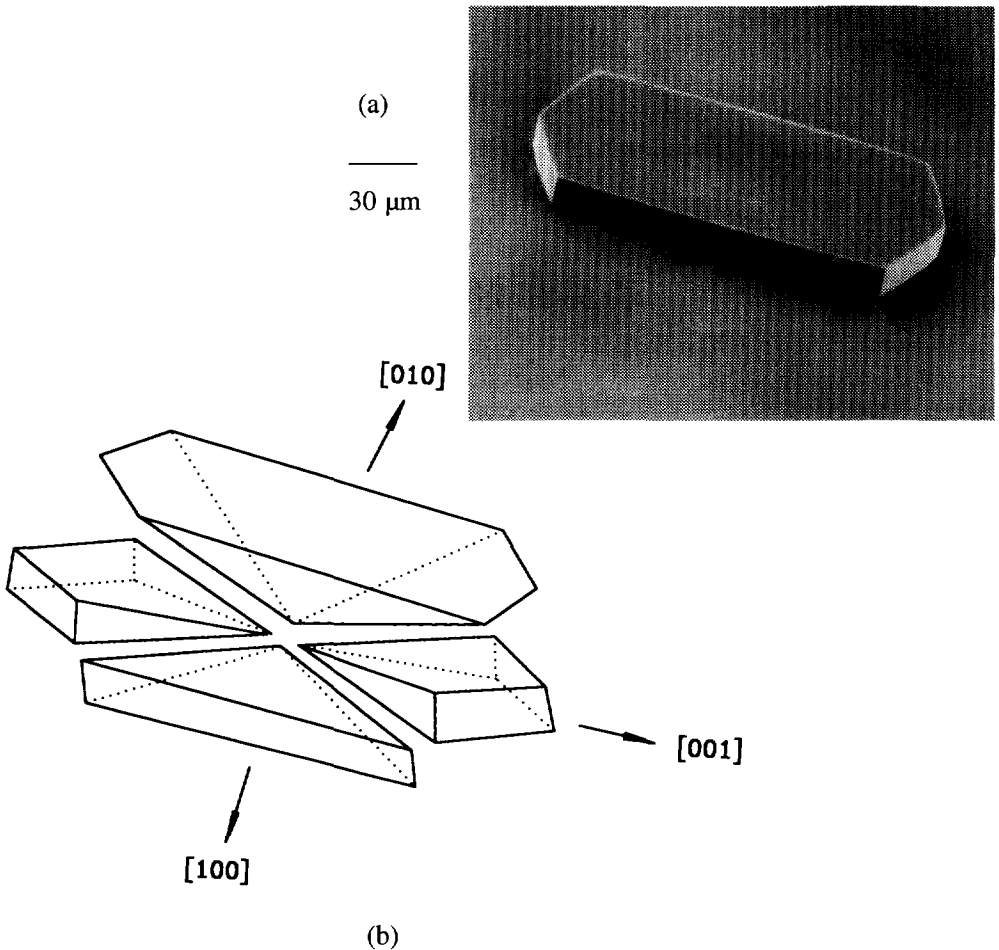
(a)

─────

30 µm

[010]

[001]

[100]

(b)

Figure 10 (a) SEM picture of a prismatic overgrown silicalite crystal, and (b) MFI crystal sections (for clarity, of both the [100] and [010] section only one is shown)

A SEM-picture of a synthesized prism is shown in Figure 10a. The sector lines become apparent by (transmission) light microscopy, and divide the crystal into six, pair-wise related sections as shown in Figure 10b. Moreover, the growth lines of a cube are slightly visible by transmission light microscopy within the prism, similar to the 90° intergrown VS-1 crystals. Still, according to X-ray diffractometry (Diffractis 601, Enraf-Nonius), the as-synthesized (TPA-containing) silicalite prism can be considered a single crystal.

The typical crystallization process of cube shaped single crystals of the MFI type is based on the observation that the initial growth proceeds within a high density silica gel phase, resulting in pyramid shaped MFI crystals.[14] Next, the pyramid shaped crystal transforms into a cube under still high supersaturation conditions. The crystal thickness (b-direction) is determined by the height of the initially formed MFI pyramid, related to the asymmetric crystal growth under heterogeneous nucleation conditions (wall-effect). Prolonged crystallization changes the cube into a prism as the supersaturation has decreased significantly.[29] The fact that for this particular gel the cube to prism transformation takes place in less than 5 days (the normal crystallization time to form cubes) may be related to the absence of other dissolved ions (Na^+ and Br^-).

4.5.2 Inhomogeneous Calcination Process

Upon calcination in air (heating rate 1°C/min), the sector lines and the growth lines of the cube become more pronouncedly visible, which suggests the development of cracks within the crystal. In addition, an 'interface', initially coinciding with the growth lines of the cube, moves along the ac-plane into the prismatic overgrowth. At 320°C, *in situ* IR-spectra taken (with a small spot) reveal that the intensity of the C-H absorption bands decreases more rapidly within the area defined by the moving interface, than outside of that area. A brownish coloured body having the shape of an hour-glass develops within the cube shaped part of the crystal at approximately 330°C (Figure 11). The location of this area within the crystal coincides with the two [001] crystal sections as defined according to Figure 10b. At slightly higher temperatures (340-350°C) the crystal turns completely brownish.
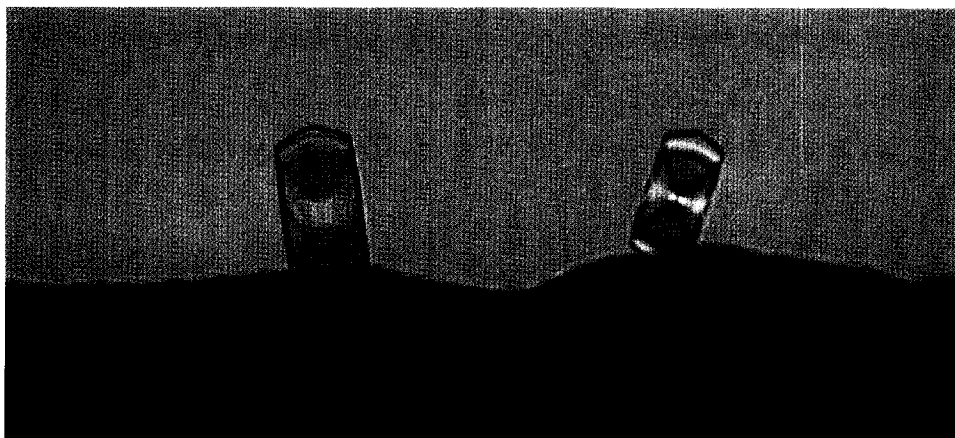
Figure 11   Visible light micrograph of two prismatic overgrown silicalite crystals during calcination at 335°C, revealing the development of the hour glass
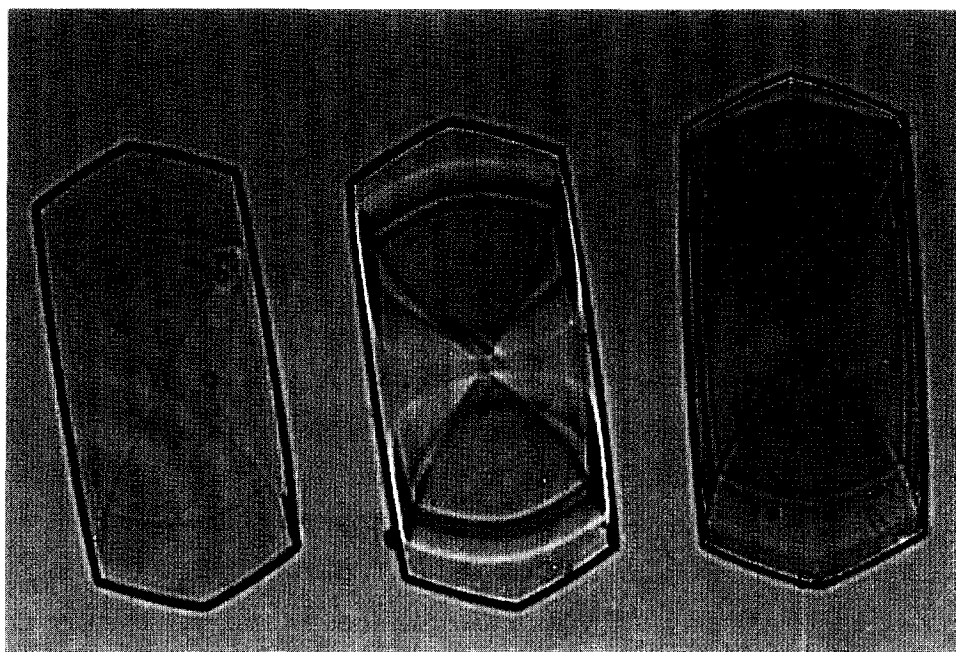

Figure 12   Visible light micrograph of an as-synthesized TPA-containing prismatic overgrown crystal, and of two crystals calcined at 320°C and 330°C

An as-synthesized crystal, together with two partly calcined crystals (cooled from 320 and 330°C) is shown in Figure 12 (observed through the ac-plane). In the crystal calcined at 320°C several 'interface' lines are apparent, partly obscuring the earlier mentioned sector lines and growth lines of the cube. The well-defined sector and growth lines are clear in the crystal calcined at 330°C. A micrograph of the latter crystal through the a-direction is presented in Figure 13. One [010] crystal section extends over nearly the entire crystal thickness, and is still hardly coloured. Thus, the colouring of the crystal according to the hour-glass shape arises exclusively from the [001] crystal sections within the cube shaped part of the crystal.
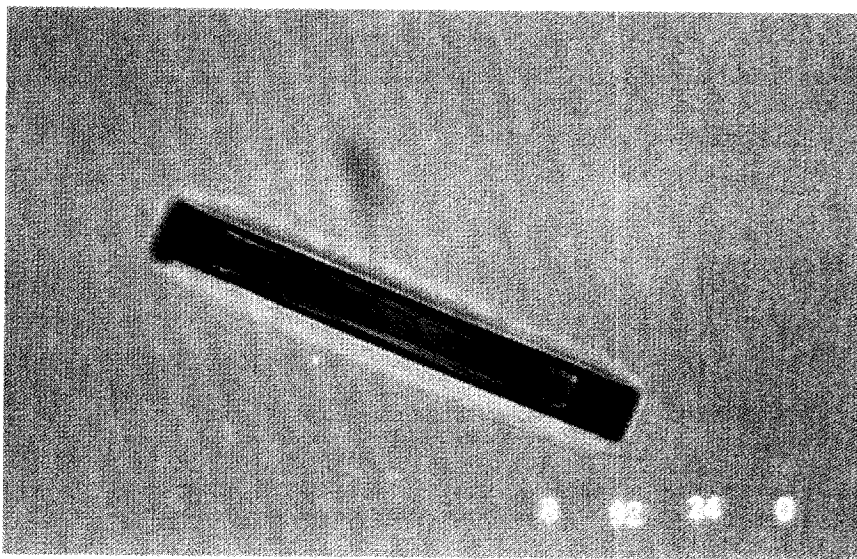

Figure 13   Visible light micrograph of the MFI crystal calcined at 330°C, observed through the (100) plane

IR-spectroscopy on the partly calcined crystal at 320°C reveals that the intensity of the C-H vibrations in the two [001] crystal sections within the cube shaped part are substantially weaker than in the exact centre of the crystal (Figure 14). The spectrum in Figure 14a is also representative for the [100] crystal sections (slightly lower absorbance), and the area outside of the cube shaped part of the [001] sections (all spectra taken through the ac-

plane). The hydroxyl bands in the IR-spectrum in Figure 14b are attributed to the prolonged exposure to ambient conditions. With *in situ* measured spectra, these hydroxyl bands have not been observed (*vide supra*).
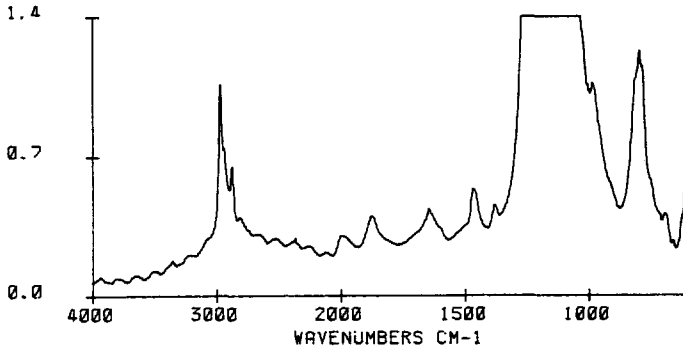
(a)
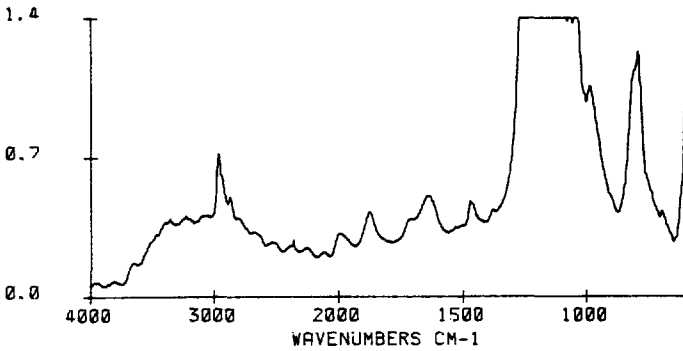
(b)

Figure 14   IR-spectrum of the crystal partly calcined at 320°C, (a) focused on the centre, and (b) focused on the [001] section within the cube shaped part of the crystal

These observations suggest that in comparison with the other parts of the silicalite prism, the two [001] crystal sections within the cube shaped part are ahead in the degradation process. The inhomogeneous calcination behaviour has, however, not been observed with

cube shaped crystals. Hence, the development of the hour glass pattern is not related to a possibly deviating chemical composition of the MFI material grown during the second crystallization stage as compared to the pyramid (first stage). Instead, the inhomogeneous calcination behaviour seems to be due to the presence of additional MFI material, transforming the cube into a prismatic shaped crystal during the final crystallization stage. The above observations suggest that the hour glass pattern is not related to the initial Hofmann elimination reaction of TPA, but rather to the further degradation of tripropylamine to lower amines. The transport of TPA degradation products (initially mainly propene and water) favourably proceeds through the b-direction (straight channels), which is the shortest crystal length of the silicalite prism. For the species under consideration, however, the diffusivities through the straight and the sinusoidal channels are hardly different. Transport in the [001] direction is more hindered, and proceeds via alternating movements through the straight and the sinusoidal channels. Both tripropylamine and propene, arising from the initial Hofmann elimination reaction of TPA, are expected to remain immobile, and water is the only mobile species within the framework below 320°C (cf. section 4.3.1).

The stability of TPA within the silicalite framework is strongly affected by the presence of water and/or hydroxyl groups. The consecutive degradation reactions (ß-eliminations) may be enhanced by water as well. Two silanol groups are again produced according to reaction (3), leading to the formation of a tripropyl ammonium ion:

$$\equiv Si\text{-}OH + Pr_3N \ \rightleftarrows \ \equiv SiO^- \ Pr_3NH^+ \qquad\qquad (5)$$

The degradation reaction of the $Si\text{-}O^- \ Pr_3NH^+$ group may then proceed similarly to reaction (1) to form dipropylamine and again propene.

Hardly any water and/or hydroxyl groups are, however, observed within the silicalite cubes after the Hofmann elimination reaction (cf. Figure 4). The fact that the further degradation process proceeds first in the two [001] crystal sections may therefore be related to the slower dehydration process in these parts of the crystal, due to the lower diffusivity of

water in the c-direction. Under these conditions, however, the molecular transport from one crystal section to another must be hindered as well. The diffusional distance from within the [001] crystal section to the external surface is minimal in the b-direction, but involves the crossing of an interface, separating the [001] from the [010] crystal section.

The lower absorbance of the C-H vibrational bands in Figure 14b is not attributed to the desorption of degradation products, but rather to the formation of alkene bands of a lower IR-absorbance at the expense of the alkyl (CH_2) groups (cf. Table 1 in Chapter 6). The reaction to alkenes also accounts for the brownish colouring of the crystal with the shape of an hour glass at relatively low temperatures. The degradation products (mainly propene) are trapped, which, together with the slow heating rate of 1°C/min, gives rise to long contact times enabling oligomerization reactions to take place.

The apparent development of cracks is also related to the fact that the two [001] sections within the cube shaped part of the crystal are ahead in the calcination process. As has been shown by temperature-programmed X-ray powder diffractometry (section 4.4), a strong contraction of the framework proceeds after the initial Hofmann elimination reaction. Thus, tensile stresses develop at the interface of the two [001] sections.

In spite of the single crystal nature of the silicalite cubes, confirmed by X-ray single crystal structure analysis,[17] it may be questioned whether the micropores extend over the entire crystal lattice. The different crystal sections may be separated by interfaces, that can be observed by visible light microscopy (sector lines). In this respect the 90° intergrowth components of MFI prisms, that can be separated by ultrasonic treatment,[30] can again be mentioned (cf. section 3.2). The suggested weak bonding of different crystal sections may only be true for 90° intergrown crystals, and it seems worthwhile to study the crystal interfaces within single crystals.

4.6 Concluding Remarks; 'Safe' Calcination Procedure

The liability of large, TPA-templated MFI crystals towards cracking seems to be dependent on the crystal thickness (b-direction), rather than the crystal length (c-direction). The calcination is favourably performed in the presence of oxygen, in which case the temperature may remain below 400°C (heating rate 1°C/min). Especially for supported MFI layers as membranes the relatively low calcination temperature may be favourable (cf. Chapter 5). The introduction of vanadium within the framework as an intrinsic oxidation catalyst seems to give rise to a somewhat different degradation mechanism. Somewhat higher temperatures are required to achieve complete calcination.

Even small fluoride-synthesized silicalite crystals crack consistently. This may be related to the higher temperature at which the TPA-degradation is initiated. It has also been suggested that the lattice of fluoride-synthesized silicalite contains fewer crystal defects, and is therefore more liable to crack. This is, however, still a matter of debate. Due to the crack-formation, fluoride-synthesized silicalite is considered unsuitable for the preparation of zeolite membranes.

4.7 Literature

1. M. Soulard, S. Bilger, H. Kessler, and J.L. Guth, *Zeolites*, 7 (1987), 463.
2. S. Bilger, M. Soulard, H. Kessler, and J.L. Guth, *Zeolites*, 11 (1991) 784.
3. L.M. Parker, D.M. Bibby, and J.E. Patterson, *Zeolites*, 4 (1984) 168.
4. V.N. Romannikov, V.M. Mastikhin, S. Hocevar, and B. Drzaj, *Zeolites*, 3 (1983) 311.
5. E. Bourgeat-Lami, F. Di Renzo, F. Fajula, P.H. Mutin, and T. Des Courieres, *J.Phys.Chem.*, 96 (1992) 3807.
6. M. Soulard, S. Bilger, H. Kessler, and J.L. Guth, *Zeolites*, 11 (1991) 107.
7. M. Nowotny, J.A. Lercher, and H. Kessler, *Zeolites*, 11 (1991) 454.
8. S.A. Axon, and J. Klinowski, *J.Appl.Catal.A: General*, 81 (1992) 27.
9. J.G. Tsikoyiannis, and W.O. Haag, *Zeolites*, 12 (1992) 126.
10. E.R. Geus, J.C. Jansen, and H. van Bekkum, in J.C. Jansen, L. Moscou, and M.F.M. Post (Eds.) *Zeolites for the Nineties*, Recent Research Reports of 8th Int.Zeol.Conf., 1989, 293.

11. S. Qiu, W. Pang, H. Kessler, and J.L. Guth, *Zeolites*, 9 (1989) 440.
12. C.W.R. Engelen, PhD Thesis, Eindhoven, (1986).
13. M. Ghamami, and L.B. Sand, *Zeolites*, 3 (1983) 155.
14. J.C. Jansen, C.W.R. Engelen, and H. van Bekkum, in M.L. Occelli, and H.E. Robson (Eds), *Zeolite Synthesis*, ACS Symp.Ser. Vol. 398, ACS, Washington, D.C., 1989, 257.
15. B.D. Cullity, *Elements of X-Ray Diffraction*, 2nd Ed., Addison-Wesley Publ.Comp., Reading Massachusetts, (1978), 350.
16. H. Lermer, M. Draeger, J. Steffen, and K.K. Unger, *Zeolites*, 5 (1985) 131.
17. H. van Koningsveld, H. van Bekkum, and J.C. Jansen, *Acta Cryst.*, B43 (1987) 127.
18. H. van Koningsveld, *Acta Cryst.*, B46 (1990) 731.
19. H. van Koningsveld, J.C. Jansen, and H. van Bekkum, *Zeolites*, 10 (1990) 235.
20. H. van Koningsveld, F. Tuinstra, H. van Bekkum, and J.C. Jansen, *Acta Cryst.*, B45 (1989) 423.
21. H. van Koningsveld, J.C. Jansen, and H. van Bekkum, in: R. von Ballmoos, and J.B. Higgins (Eds), *Zeolites*, 10 (1990) 442s.
22. D.G. Hay, H. Jäger, and G.W. West, *J.Phys.Chem.*, 89, (1985) 1070.
23. H. van Koningsveld, J.C. Jansen, and H. van Bekkum, *Zeolites*, 7 (1987) 564.
24. G.T. Kokotailo, L. Riekert, and A. Tissler, in H.G. Karge, J. Weitkamp (Eds), *Zeolites as Catalysts, Sorbents, and Detergent Builders*, Stud.Surf.Sci.Catal. 46, Elsevier, Amsterdam, 1988, 821.
25. J.C. Jansen, E. Biron, and H. van Bekkum, in P.J. Grobet, W.J. Mortier, E.F. Vansant, and G. Schulz-Ekloff (Eds), *Innovation in Zeolite Materials Science*, Stud.Surf.Sci.Catal. 37, Elsevier, Amsterdam, 1988, 133.
26. H. Siegel, W. Schmitz, R. Schöllner, and A. Dyer, *Thermochim.Acta*, 93 (1985) 561.
27. J.C. Jansen, private communication, November 1992.
28. E.R. Geus, J.C. Jansen, and H. van Bekkum, *Zeolites*, submitted.
29. Jansen, J.C., in H. van Bekkum, E.M. Flanigen, and J.C. Jansen (Eds.) *Introduction to Zeolite Science and Practice*, Stud.Surf.Sci.Catal. 58, Elseviers, Amsterdam, 1991, 77.
30. D.G. Hay, H. Jäger, and K.G. Wilshier, *Zeolites*, 10 (1990) 571.

5. Thermal Stability of Inorganic Membranes of the MFI-Type

The stability of inorganic membranes based on MFI-type crystals during both preparation and use is addressed. Thermomechanical compatibility is essential for both the composite membranes consisting of monolayers of oriented zeolite crystals within a gas-tight matrix, and the supported, in situ grown zeolite layers. The former involve the matching of the thermomechanical properties of at least three different materials (support, zeolite crystals, and gas-tight matrix). The latter, if arranged in the optimal configuration, require compatibility between the support and the zeolite material only. Three systems are subsequently discussed in more detail, viz. (i) glaze layer on a clay support, (ii) large crystals, embedded in the glaze layer system, and (iii) supported polycrystalline MFI layers, in which emphasis is on the template (TPA) removal is considered as well. The relation between the thermomechanical stability and the preparation procedure of multilayer systems is demonstrated.

5.1 Introduction

Inorganic, and in particular ceramic, membranes are sensitive towards cracking, during both preparation and use. In practice, the preparation procedure always involves one or more thermal treatments. With an increase or decrease in temperature the difference in thermal expansion of the joined materials inevitably leads to mechanical stress in the composite system. With respect to (organic) polymer membranes, moreover, the main interest in inorganic membranes is based on long life-time under extreme conditions, in particular for high-temperature applications and recycling/reactivation of fouled membranes. Hence, the compatibility problem is very relevant.

Composite zeolite membranes, based on a monolayer of oriented MFI crystals in a gas-tight matrix as described in Chapter 2, are rather complex systems as to the material compatibility. A discontinuous layer of zeolite crystals in a ceramic, gas-tight matrix is bound to a porous support phase. At least three different materials are therefore involved. The thermomechanical stability of the supported, polycrystalline MFI layers of Chapter 3 depends on the calcination procedure of the as-synthesized (TPA-containing) material (Chapter 4; 'safe' calcination procedure), and on the thermal expansion/contraction of the emptied zeolite phase and of the support.

First, the material compatibility for multilayer systems is treated in general. The nature of mechanical stresses, particularly for the supported monolayers of oriented MFI crystals, is discussed. It is further demonstrated (section 5.3) that the deposition technique and the bonding process, on the one, and the development of cracks within the coating, on the other hand, are interrelated. Emphasis is on glassy (oxidic) coatings, which can be prepared by several deposition procedures with different bonding characteristics. In section 5.4 three cases are addressed in connection with either the composite zeolite membrane configuration, or the in situ grown zeolite layers on a macroporous support.

5.2 Thermomechanical Stability of Multilayer Systems

The thermal expansion and the subsequently occurring stresses within multilayer systems may be addressed in view of the thermomechanical stability of glazes and enamels as coatings on ceramic and metal substrates.[1-4] Thermal expansion of a single material layer is generally described by the linear (α) or cubic (ß) expansion coefficient, according to:

$$\alpha = \frac{1}{l_0} \frac{1 - l_0}{\Delta T} \quad , \text{ respectively } \quad \beta = \frac{1}{V_0} \frac{V - V_0}{\Delta T} \tag{1}$$

with l_0 and V_0 the initial length (m) or volume (m^3) of a layer at the reference temperature, and 1 and V the length or volume after the temperature change (ΔT). The contraction/expansion of a single material layer is defined by the relative expansion (ε):

$$\varepsilon = \frac{1 - l_0}{l_0} = \alpha \cdot \Delta T \tag{2}$$

similar to equation (1). For a two-layer system an analogous, but basically different relative expansion has been formulated:

$$\varepsilon^* = \frac{1^* - 1}{1} \tag{3}$$

which is the relative deformation of a layer as a result of a difference in thermal expansion between the two joined materials. Crack formation will take place when the stresses developing exceed the critical stress of one or more of the materials involved. The developing stress may be quantified by Hooke's law, corrected for the Poisson contraction:

$$\sigma = \varepsilon^* \cdot \frac{E}{1 - \mu} = \varepsilon^* \cdot E^{\neq} \tag{4}$$

with σ the stress (N/m^2), E the Young's modulus (N/m^2), and μ the Poisson contraction factor (-). The latter accounts for the non-elastic deformation of the layer, as the material preserves its volume partly. Young's modulus is often denoted as $E^{\neq}$, taking the Poisson contraction factor into account.

The practical use of stress calculations is limited by several assumptions,[3] viz. (i)

homogeneous development of stress, (ii) no temperature gradients, and (iii) no change in the properties of the coating due to the bonding process to the substrate or support. In practice, the thermomechanical stability of multilayer systems is therefore tested under prescribed conditions. Nevertheless, estimates of the occurring stresses can be made, which provide a basis for qualitative conclusions.

Considering a two layer planar system of a coating (index c) and a substrate (index s), the length of each layer at the interface can be considered to be equal, provided no cracking does occur. The stresses in either phase at the interface are considered to be equal but opposite (Figure 1).
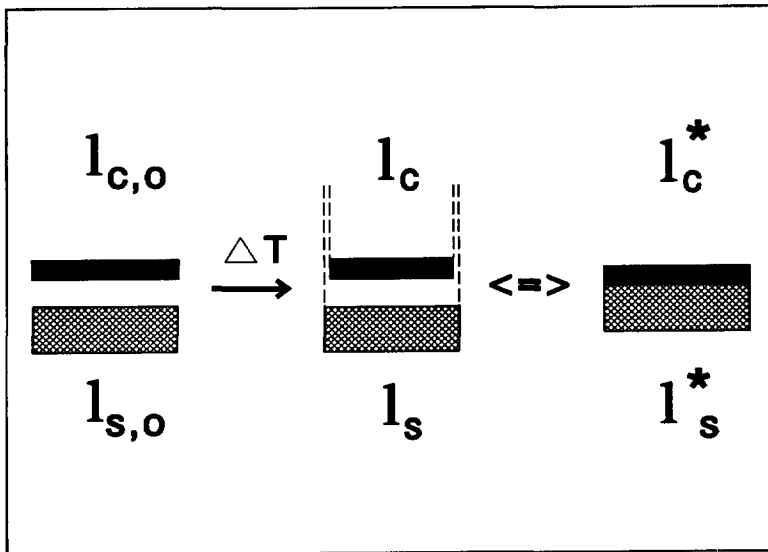
Figure 1   Schematic view of the development of stresses in a two layer system as a result of different thermal expansions (coating (index c) subject to tensile, substrate (index s) to compressive)

For convenience, the occurring stresses are calculated from a zero-stress reference temperature (T_0): $l_{c,0} = l_{s,0}$. The relative expansion of each material is then calculated separately from equation (2). For a crack-free two layer system l_c^* equals l_s^*, and the

resulting stress σ ($= \sigma_c = -\sigma_s$) amounts to:

$$\sigma = \frac{\Delta T \cdot E_C^{\neq} \cdot E_S^{\neq} \cdot (\alpha_S - \alpha_C)}{(E_C^{\neq} + E_S^{\neq}) + \Delta T \cdot E_C^{\neq} \cdot E_S^{\neq} \cdot \left(\dfrac{\alpha_C}{E_C^{\neq}} + \dfrac{\alpha_S}{E_S^{\neq}} \right)} \tag{5}$$

In equation (5) the stress is proportional to ΔT for small temperature differences, whereas the maximal stress (for high values of ΔT) amounts to $(\alpha_S - \alpha_C)/ (\alpha_C/E_C^{\neq} + \alpha_S/E_S^{\neq})$. In the literature the layer thicknesses (d) are included to calculate the average stress:[2,3]

$$\sigma_C = \frac{\Delta T \cdot (\alpha_S - \alpha_C)}{\dfrac{1}{E_C^{\neq}} + \dfrac{1}{E_S^{\neq}} \cdot \dfrac{d_C}{d_S}} \tag{6}$$

for the coating, and correlated to the substrate via $\sigma_s = -\sigma_c \cdot (d_c/d_s)$:

$$\sigma_S = \frac{\Delta T \cdot (\alpha_C - \alpha_S)}{\dfrac{1}{E_S^{\neq}} + \dfrac{1}{E_C^{\neq}} \cdot \dfrac{d_S}{d_C}} \tag{7}$$

where d_c and d_s denote the layer thickness of the coating and the substrate, respectively. Positive values of σ denote compressive stress; negative values refer to tensile stress. Comparison with equation (5) shows that in practice the linear part suffices to describe the stress development. The imposed stresses in each layer near the interface are obtained by substituting $d_s = 0$ or $d_c = 0$ into equation (7) and (6), respectively. For decreasing d_c/d_s ratios, the stress within the coating increases, whereas the stress within the substrate diminishes.[2,5] The occurrence and nature (tensile or compressive) of the stresses developing in a glaze/glass composite system have been studied for glaze layers of varying thickness, in which the glass phase exhibits the higher thermal expansion.[5] The stresses have been determined according to the photo-elastic effect (cf. Figure 2). For thin coatings the stress within the glaze varies only slightly and remains compressive. The stress within the substrate (glass phase) extends over only a minor distance from the interface, and is

altogether low. For higher d_c/d_s ratios, the stress within the glaze layer varies much stronger, and even turns into a tensile stress. The opposite is true for the glass substrate, which, as a result of the larger thermal expansion, experiences an overall tensile stress.
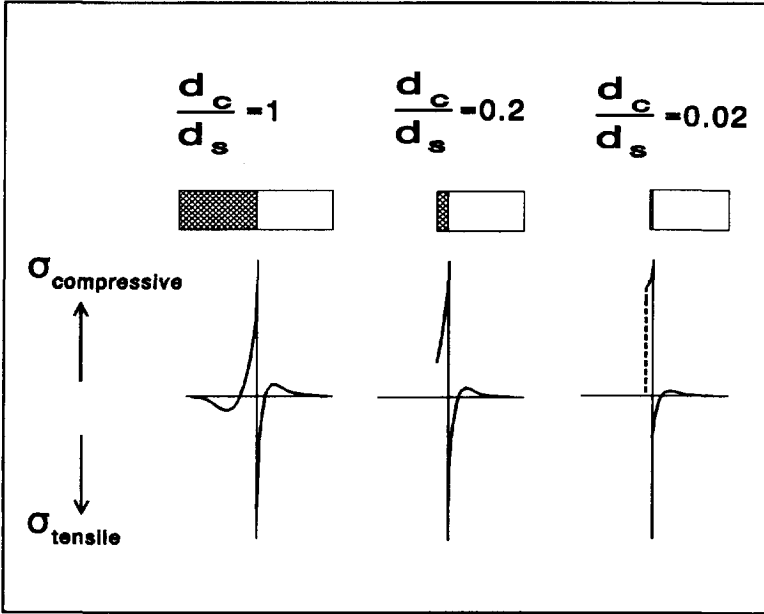

Figure 2   Schematic representation of the nature and magnitude of developing stresses within a glaze/glass composite system as a function of the layer thickness[5]

Thus far only tangentially operating stresses have been considered, based on the planar joining of multilayer systems. For the single crystal-based composite zeolite membranes, on the other hand, the dispersion of zeolite crystals within a continuous ceramic layer (gas-tight matrix) leads to axially imposed stresses (perpendicular to the zeolite/matrix interface; cf. Figure 3).

The axial stresses present are expected to affect the stability of the zeolite/matrix interface, as an overall compressive stress in the coating (matrix) may be changed into a tensile stress in the vicinity of a zeolite crystal. The relative expansion or contraction of the zeolite crystals and the imaginary open space within the gas-tight matrix are again considered

separately (Figure 4). Thus, the anisotropic expansion/contraction of the MFI lattice (Chapter 4, Table 3) can be dealt with.
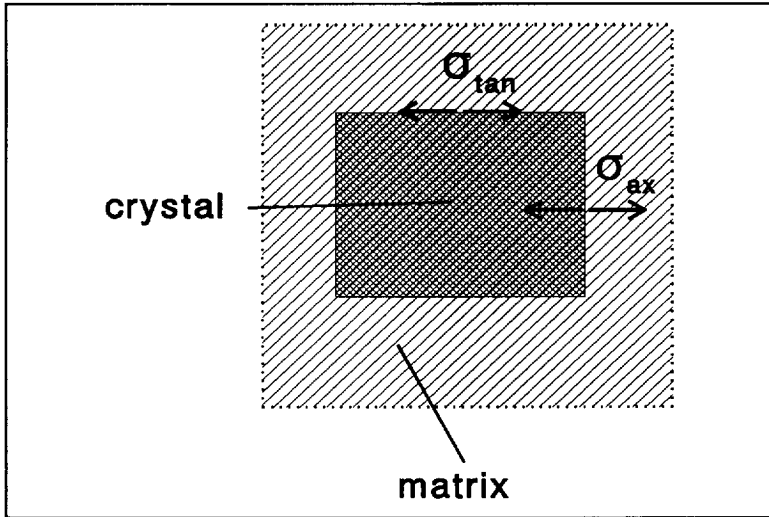

Figure 3   Schematic representation (top view) of the axial (σ_{ax}) and tangential (σ_{tan}) stresses on the zeolite/matrix interface within the composite zeolite membrane
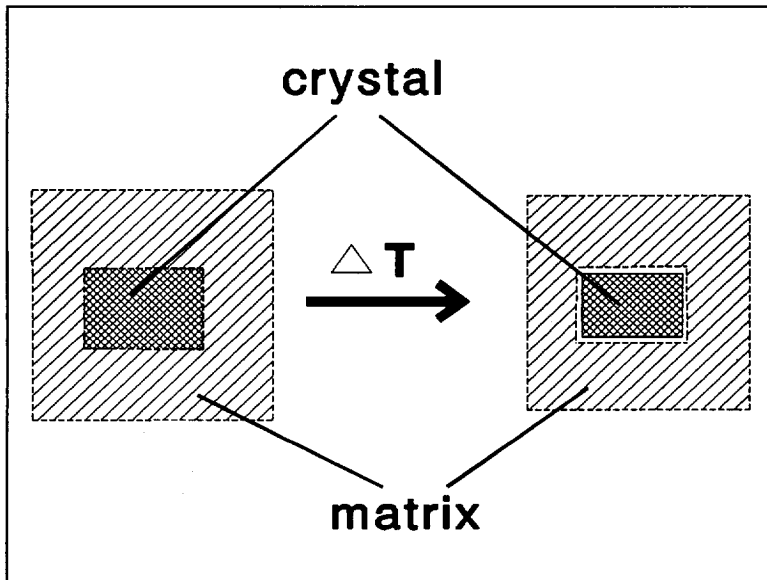

Figure 4   Schematic representation (top view) of the development of axially imposed stresses for a zeolite crystal within a (glaze) matrix

5.3 Thermomechanics and the Bonding Process

In the previous section the mathematics for the thermomechanical stability have been dealt with. Obviously, both the chemical composition of the coating, serving as the matrix material, and the way in which the matrix or precursor matrix material is deposited are essential parameters. The deposition procedure is related to the homogeneity of the coating material and to the earlier mentioned reference or bonding temperature. In Table 1 a summary is given with respect to the deposition and bonding temperature for various coating methods.

Table 1   Characteristic temperatures of various deposition techniques for the formation of metal oxide (glassy) coatings

technique	substrate	deposition	treatment[&]	bonding[@]
sol-gel	metal/ceramic	ambient	> 400°C	> 400°C
CVD	metal/ceramic	400-1200°C	400-1200°C	400-1200°C
glazing	ceramic	ambient	900-1400°C	400-700°C[$]
enamel	metal	ambient	500-1300°C[#]	480-550°C[%]

[&] thermal treatment temperature
[@] temperature at which the bonding between coating and substrate takes place
[$] glass transformation ($T_t$) temperature ($\eta = 10^{13}$); ref. 2
[#] aluminium 520-560°C; iron/steel 710-850°C; titanium/high-temperature enamels 900-1300°C; ref. 3
[%] glass softening (T_s) temperature ($\eta = 10^{10.5}$ Pa·s); ref. 3

The emphasis is on glassy (metal oxide) coatings that can be prepared via the in Chapter 2 mentioned deposition techniques (sol-gel, CVD, and glazing). Especially the difference between glazes (or enamels) and sol-gel glasses is striking (*vide infra*). The polycrystalline layers (γ-alumina and yttria-stabilized zirconia) of Chapter 2 may strongly deviate from the

here described glasses, and for that reason the above layers are not accounted for in this section. The discussion is further limited to multilayer systems in the absence of zeolite crystals, as such a dispersed phase makes the system more complex without adding to the basic understanding of thermomechanics.

Inorganic glasses are generally based on silicates to which different metal oxides may be added to adjust the material properties, such as glass transformation (T_g) and softening temperature (T_s), thermal expansion, elasticity, and surface tension. If a homogeneous glass is assumed, several of these properties can be estimated by the additive equation:

$$F = \Sigma N_i \cdot F_i \qquad (8)$$

in which F_i denotes the property under consideration for each component. For several oxides standard fractional contributions are available,[2,4] although for some elements (Si, B) the contributions are concentration-dependent. In Table 2 an overview of the parameters for some commonly used oxides is presented. It is clear that the parameters for the strength of glasses towards compressive stress is substantially higher than towards tensile stress. A slight compressive stress is therefore commonly applied for glazes on (oxidic) ceramics,[2,4] as well as for enamels on metal substrates.[3] Since the bonding is established at high temperatures, the shrinkage of the substrate upon cooling must be larger than that of the glass material to bring about an effective compressive stress within the coating.

Glasses of a similar chemical composition can be prepared via sol-gel techniques, but the variety is limited by the availability of precursor materials (mainly alkoxides).[6] The liability of sol-gel glasses for crack-formation is related to the drying and calcining (densifying) of the under ambient conditions formed gel phase. Upon drying, the water is removed from the pores within the gel phase by evaporation, first from the large pores, in which the capillary forces due to the water phase are relatively small. Especially when a rather broad pore size distribution is present within the gel, inhomogeneous drying takes place and tensile stresses develop.[7,8] In addition, it seems that drying often proceeds via a process in which the pores of a small volume are abruptly emptied, which further enhances the development of cracks.[9]

Table 2   Partial coefficients for the calculation of thermomechanical properties of glasses[4]

Oxide	$\sigma_{c,t}$ [#]	$\sigma_{c,c}$ [#]	E	α_{20-400}	Application range
	$*10^{-6}$ (N/m^2)			$*10^7$ (°C^{-1})	(mol %)
SiO$_2$	0.90	12.3	650-715	5-38	45-100
Al$_2$O$_3$	0.50	10.0	1140	-30	0-20
CaO	2.00	2.0	1115	130	0-25
MgO	0.10	11.0	920	60	0-25
BaO	1.50	6.0	600	200	0-40
PbO	0.25	4.8	430	130-190	0-50
B$_2$O$_3$	0.65	9.0	100-1800	-50-0	0-30
Na$_2$O	0.20	6.0	595	395	0-25
K$_2$O	0.10	0.5	410	465	0-20

[#]   critical stress (strength)

To solve the crack-formation in sol-gel processes, chemical agents controlling the drying process (DCCA; Drying Control Chemical Agent), such as formamide, have been suggested.[8,10] For the coatings under consideration, however, only the problem of the first stage of the preparation, which involves drying, is solved by the use of DCCA's. Upon calcination the still remaining tensile stresses are aggravated as further shrinkage of the gel takes place, whereas the substrate expands at higher temperatures. To solve the crack-formation upon calcination, organic polymers have been added to the inorganic precursors.[7] Similarly, solutions of inorganic polymers containing organic groups, such as silicones (Chapter 2), may be used as a sol.[11] In both cases the coating formed under ambient conditions is more elastic and possesses an improved strength towards tensile stresses. In fact, the actual bonding process is postponed to the heat treatment, when the organics, cq.

organic fragments, are removed by calcination.

The development of stresses during the preparation of sol-gel glasses and glazes on substrates of a higher thermal expansion is shown in Figure 5. Considering enamels, it can be seen that upon cooling from the treatment temperature the coating first experiences a tensile stress. The tensile stress develops as a result of the strong shrinkage of the enamel within the temperature interval of the glass softening point (T_s) and the glass transformation point (T_t).[3] At still lower temperatures the contraction of the metal substrate is higher than that of the enamel coating.
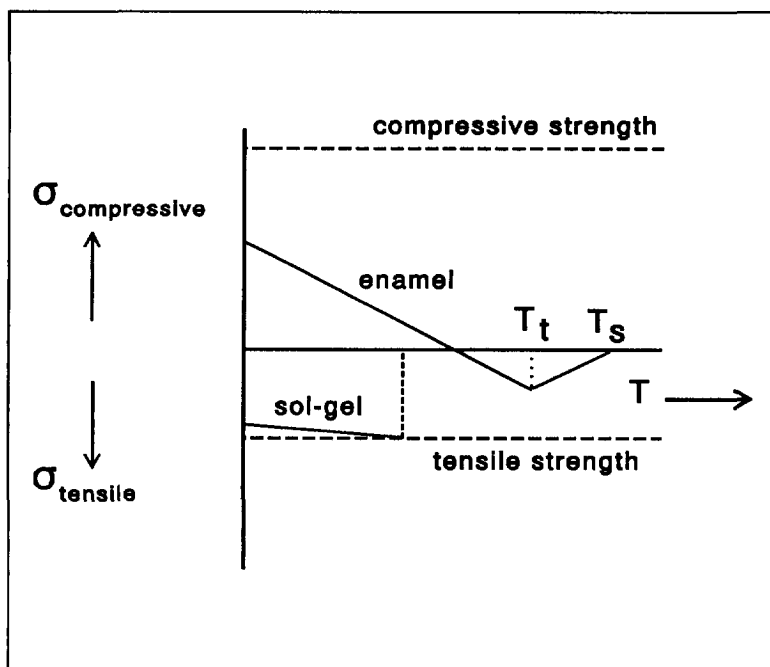
Figure 5   Qualitative evaluation of the developing stresses within supported sol-gel glass and enamel coatings (assuming $\alpha_c < \alpha_s$)

For CVD-prepared (glass) coatings the bonding process takes place at the reaction temperature (cf. Table 1). The reference temperature may be slightly lower as sintering may occur at high temperatures, which allows relaxation within the coating (depending on the cooling rate). The stress development is expected to resemble the glaze/enamel scheme.

5.4 Thermomechanical Stability: Cases

Some theoretical aspects of the thermomechanical stability have been treated in the previous sections. In this section, the material compatibility in practice is demonstrated in three cases. First, the thermomechanical properties within a glaze coating/clay substrate system are adjusted to provide a thermomechanically stable two layer system (*Case 1*). Next, large MFI-type crystals are introduced within the optimized glaze/clay system, in which the material properties of the MFI material are taken into account (*Case 2*). Finally, the thermomechanical behaviour of supported, polycrystalline TPA-containing MFI layers is treated in view of and related to the 'safe' calcination procedure of Chapter 4 (*Case 3*).

5.4.1 Case 1: Lead-Boron Silicate Glaze/Clay Substrate System

Case 1 involves the preparation of crack-free lead-boron silicate glaze/clay substrate composite layers by matching of the thermomechanical properties. The chemical composition of the clay substrate has been varied systematically, whereas the chemical composition of the glaze ($PbBSiO_4$; cf. Table 4, Chapter 2) has not been changed.

The main constituents of clay (pottery) substrates are kaolin clays, feldspars, chalk (calcium carbonate), and crystalline silica (quartz or cristobalite). Upon calcination the kaolin and feldspars are partly or fully transformed into a glass phase and mullite.[2] The thermal expansion of the substrate is mainly determined by the silica content. Chalk reduces the humid expansion of the substrate under ambient conditions, provided that the calcination is carried out in excess of 900°C (transformation into CaO). In practice, the humid expansion should not exceed 0.7%.[12]

Clay substrates of different compositions have been prepared from a commercial clay suspension (Royal Delft Ware Manufactory, Delft, The Netherlands). The overall composition (weight percentages) amounts to 14.7% kaolin clays, 17.9% ball clays, 5.7% feldspars, 27.1% quartz, 4.4% calcium carbonate, and 30.2% water. To this mixture, additional minerals, such as quartz (M 500, Sibelco, Antwerp, Belgium), cristobalite (M 3000, Elvers B.V., Geertruidenberg, The Netherlands), and/or calcium carbonate, have been added for fine tuning of the thermomechanical properties. The thermal expansion of quartz is high ($\alpha_{20\text{-}800} = 190*10^{-7}$ °C^{-1}), as a result of the α/ß-phase transition at 573°C. Cristobalite shows a similar α/ß-phase transition (varies with purity from 200 to 275°C), which leads to a strong expansion at low temperature ($\alpha_{20\text{-}800} = 300*10^{-7}$ °C^{-1}). For smaller temperature intervals (e.g. 20-550°C), the thermal expansion is even higher.

After addition of the extra minerals, the clay mixture is poured into shallow glass rings (diameter 25 mm; height 2-3 mm) on a gypsum support and left to dry. When large amounts of additives are used, some water is added to reduce the viscosity. Next, the supports are calcined at 900°C for 1 hour (heating rate 1°C/min), and polished to smooth disks on larger clay disks to avoid contamination. Thick layers (150-250 µm) of the lead-boron silicate glaze with a molar ratio of Si:Al:Na:Pb:B = 100:4:4:6:166 (cf. Table 4, Chapter 2) are deposited onto the clay substrates from diluted suspensions as described previously. After the heat treatment at 900°C (heating rate 1°C/min), the glaze layers are inspected by visible light and electron microscopy on the occurrence of cracks. The glaze formation and stability of the produced layer has thus been used as the criterion for the optimal clay substrate composition.

Table 3 summarizes the results for the optimization of the clay composition. The crack-formation is clearly reduced by the addition of crystalline silica (either quartz or cristobalite). The optimized clay composition amounts to 100 g of the original clay mixture, 15 g cristobalite, 30 g chalk (calcium carbonate), and 60 g water.

Table 3   Effect of the clay substrate composition on the cracking of thick (150-250 μm) lead-boron silicate glaze layers (11.35300.09; Ferro B.V., Rotterdam, The Netherlands)

clay composition (wt%)				Cracking
clay[#]	quartz	cristobalite	chalk	
100	0	0	0	many cracks
97	3	0	0	many cracks
95	5	0	0	some cracks
95	0	0	5	many cracks
90	5	0	5	some cracks
85	10	0	5	nearly uncracked
80	10	0	10	uncracked
80	20	0	0	uncracked
90	0	5	5	some cracks
70	0	10	20	uncracked

[#] clay mixture, provided by Royal Delft Ware, Delft, The Netherlands, consisting of 32.6% kaoline clays, 5.7% feldspars, 27.1% quartz, 4.4% chalk, and 30.2% water

The humid expansion (measured after 1 hour treatment at 12 bar) is low for both the original (0.2%) and the optimized (0.3%) mixture. In spite of the little effect of the addition of chalk on the material properties, the addition has been maintained. The porosity of both the parent and the modified clay substrates is approximately 20%. The thermal expansion of the original mixture and the optimized suspension (calcined at 900°C) is determined by dilatometry (Netzsch-Dilatometer; courtesy Ferro B.V.).

The thermal expansion coefficients (α) of both clay substrates are presented in Table 4. For comparison the thermal expansions of some other ceramic support materials and stainless steel (AISI-316) are included. Table 4 demonstrates that the addition of cristobalite imparts

a constant and higher thermal expansion as compared with the original substrate. This is in accordance with the fact that the original clay mixture contains exclusively quartz, to which in the modified clay a similar amount of cristobalite has been added.

Table 4   Thermal expansion coefficients of some support materials (crist. is cristobalite)

ΔT (°C)	$\alpha_{\Delta T}$ /(10^{-7} °C^{-1})						
	α-Al$_2$O$_3$	ZrO$_2$[@]	crist.	quartz	Clay1[#]	Clay2[$]	AISI-316[&]
20-320					60	97	
20-550					75	99	
20-650					82	103	
20-871			300	190			193
20-1000	85	110					

[@] Calcia-stabilized zirconia
[#] Earthenware, prepared from a commercial mixture provided by Royal Delft Ware Manufactory, Delft, The Netherlands
[$] earthenware, modified mixture by the addition of 15 g cristobalite and 30 g chalk to Clay1 (cf. text)
[&] stainless steel

For rather thick layers (ca. 100 μm) of the lead-boron silicate glaze (α_{20-800} = 75*10^{-7} °C^{-1}), always some cracks have been observed on α-alumina supports (Chapter 2). This may be attributed to the lower thermal expansion of α-alumina as compared to the optimized clay substrate according to Table 4. Thin glaze layers (< 10 μm), on the other hand, remain crack-free on α-alumina as well as on clay-coated, α-alumina substrates. According to the theory, sufficiently thin glaze coatings remain under a compressive stress, as shown in Figure 2. Moreover, some support material may dissolve into the melt phase during the thermal treatment. Hence, the chemical composition (and properties) of the coating (glaze) towards the support material may shift. Interlayers of a thickness of up to 50 μm may be formed on the glaze/clay interface, which improves the compatibility.[2]

5.4.2 Case 2: MFI Crystals within the Glaze/Support Composite System

For the thermomechanical stability of the zeolite/matrix/support system, silicalite prisms are considered within the lead-boron silicate glaze on top of the optimized clay substrate (cf. section 2.4.3). The orientation of the silicalite prisms within the glaze layer is preferably either with the ac or the bc-plane parallel to the glaze coating. The change in the lattice parameters of the activated (TPA-free) MFI phase is expected to be mainly the result of the orthorhombic-to-monoclinic phase transition, rather than due to thermal expansion of MFI (cf. Chapter 4, Table 2a and 3).

In this case a prismatic shaped silicalite crystal (35x30x180 μm) is considered within a lead-boron silicalite glaze (treatment temperature 550°C), supported by a modified clay substrate. The bonding temperature (T_0) is estimated to be 500°C (zero-stress temperature). The approach shown in Figure 4 is followed to establish the nature of the axially imposed stresses on the zeolite/glaze interfaces, using the following data:

- glaze: $\alpha_{glaze} = 75*10^{-7}\ °C^{-1}$ (20-500°C)
- clay2: $\alpha_{support} = 99*10^{-7}\ °C^{-1}$ (20-550°C)
- zeolite: $\alpha_{a\text{-direction}} = 207*10^{-7}\ °C^{-1}$ (20-500°C)
                   $\alpha_{b\text{-direction}} = -222*10^{-7}\ °C^{-1}$ (20-500°C)
                   $\alpha_{c\text{-direction}} = 5*10^{-7}\ °C$ (20-500°C)

In the calculations it has been assumed that only the orthorhombic-to-monoclinic transformation at about 77°C affects the dimensions of the silicalite prism.

In Table 5 the estimated dimensions of the silicalite prism and of the imaginary void in the glaze coating of the same dimensions as the prism at 500°C are presented before and after cooling from 550°C to 20°C. The contraction of the clay substrate, to which the glaze coating is strongly bound, is even higher than that of the glaze. Hence, the dimensions of the imaginary void upon cooling are expected to be slightly smaller that the values in Table 5. The axially imposed stresses on the silicalite/glaze interface are anisotropic (tensile in the a-direction; compressive in the b and c-direction). The stresses within the glaze coating

in the vicinity of the silicalite prism (oriented in the ac-plane) resulting from the orthorhombic-to-monoclinic phase transition are shown schematically in Figure 6. Cracking may be initiated near the sharp corners of the prism, where the areas of tensile and compressive stress meet.

Table 5   Dimensions (formal) of a silicalite prism, the imaginary void within the glaze coating in which the prism fits at 500°C (T_0), and the resulting length difference (Δl) after cooling from 550°C to 20°C

crystal dimension	crystal/void 500°C	crystal 20°C	void[#] 20°C	Δl[$]
a (µm)	35	34.65	< 34.87	> - 0.22
b (µm)	30	30.32	< 29.89	> 0.43
c (µm)	180	179.96	< 179.35	> 0.61

[#]   maximal value, due to further contraction by the bonding of the glaze to the clay support
[$]   minimal value; negative value relates to a tensile stress, positive values to a compressive stress
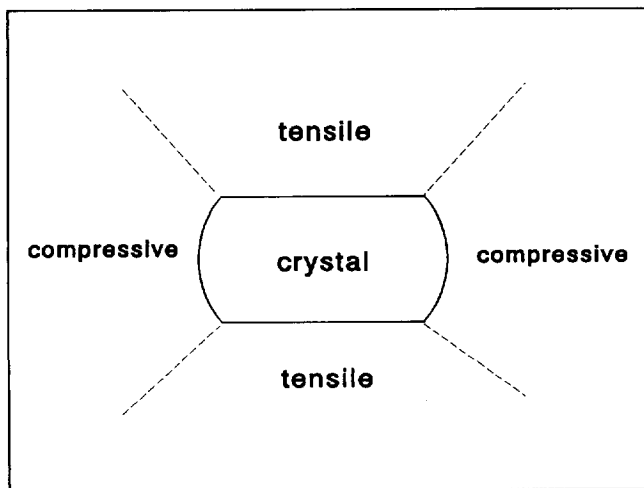
Figure 6   Schematic representation of the occurring stresses in the glaze phase in the vicinity of a silicalite crystal, due to the orthorhombic-to-monoclinic phase transition (horizontally the c-direction of MFI; vertically the a-direction)

It is, however, uncertain whether the orthorhombic-to-monoclinic transition of the activated MFI lattice takes place while present in the composite system. Some experimental results as presented in Chapter 2 may support the above expected development of compressive and tensile stresses. In thin (10-30 µm) lead-boron silicate glaze layers on α-*alumina*, that remain crack-free in the absence of silicalite crystals, cracks develop in the vicinity of large prismatic shaped crystals (TPAOH-synthesized, cf. section 4.5). The cracking starts from the zeolite/matrix interface similarly to Figure 6 (crystals oriented in the b-direction: *Figure 14, Chapter 2*). For the above mentioned smaller silicalite prisms (35x30x180 µm), no cracks are observed (glaze coating of circa 10 µm thickness; *Figure 15b, Chapter 2*).

Large prismatic shaped silicalite crystals oriented in the b-direction on the more strongly expanding clay substrate (optimized composition; α_{20-550} = 99*10^{-7} °C^{-1}; significantly higher than $\alpha_{\alpha\text{-alumina}}$ = 85*10^{-7} °C^{-1}) do not lead to cracks *within* the glaze coating. The additional glaze material that is accidentally deposited on top of the silicalite crystal, however, is cracked along the c-axis of the prism (*Figure 15a, Chapter 2*). Apparently, the resulting stresses do not exceed the tensile strength of the glaze material, as the glaze coating on top of the clay substrate is under a higher compressive stress than on top of α-alumina. The contraction of the silicalite prism in the a-direction is even larger as compared to the shrinkage of the clay substrate. Therefore, the glaze on top of the silicalite crystal experiences a higher tangentially imposed compressive stress than the glaze on top of the clay substrate. The resulting axial stress on the glaze coating leads to surface cracks on top of the silicalite prism.

It should be noted that the bonding of the glaze material to the silicalite crystals is quite strong. As a matter of fact, cracks have never been observed within the silicalite/glaze interface. In the above discussion, all effects have been considered qualitatively, and the elasticity of the different materials has been ignored. In case 3, the elasticity and strength to compressive and tensile stresses of the MFI material are discussed.

5.4.3 Case 3: Supported MFI Layers (Polycrystalline)

The TPA-degradation within the supported, polycrystalline MFI layers of Chapter 3 is addressed with reference to the thermomechanical behaviour of separate MFI-crystals upon calcination (Chapter 4). According to X-ray powder diffractometry, the as-synthesized MFI layer exhibits a significant expansion up to ca. 350°C (α_{20-300} = $50*10^{-7}$ °C^{-1}). Notwithstanding the prolonged hydrothermal treatment at 180°C in alkaline solution, the thermal expansion of the clay substrate is expected to remain unchanged (α_{20-600} = $100*10^{-7}$ °C^{-1}), because the thermal expansion is mainly determined by the relatively inert crystalline silica. During the removal of the TPA-degradation products, a strong contraction occurs ($\alpha_{350-500}$ = $-320*10^{-7}$ °C^{-1}). It is assumed that a number of broken Si-O-Si bonds remains within the lattice, which may be correlated to the shrinkage of the framework. Hence, the shrinkage of the silicalite framework is assumed to depend on the calcination temperature, and is only weakly dependent on the time span of the calcination. The chemical composition (Si/Al ratio) of the zeolite material may also change the thermal expansion (in the present case the zeolite is pure silica).

In Table 6 an overview is presented of the length changes upon calcination to 400°C of an imaginary separated polycrystalline MFI layer and a clay support of optimized composition. In this case, the reference (bonding) temperature is 180°C, at which temperature the MFI layer is formed. At room temperature, the as-synthesized MFI layer is under a compressive stress, similar to the glaze coating. Upon calcination, the zero-stress point is again reached at the bonding temperature (180°C; TPA still present), and at higher temperatures (< 350°C), a weak tensile stress is imposed on the MFI layer. For still higher temperatures, the TPA-degradation products are removed from the framework, which process leads to a steep increase of the tensile stress within the MFI coating (temperature-dependent shrinkage of the lattice upon calcination). Upon cooling, the length of the now calcined MFI layer remains constant ($\alpha \approx 0$ °C^{-1}), whereas the clay substrate shrinks. At 70-80°C the orthorhombic-to-monoclinic phase transition is expected to take place. As polycrystalline MFI layers with a random orientation are considered, the effective (linear) expansion may be calculated from the cube root of the ratio of the unit cell volumes (cf. Chapter 4, Table 3). Hence, under ambient conditions the MFI layer is under a slightly higher compressive stress than before calcination.

Table 6   Absolute (formal) length changes of an as-synthesized, polycrystalline MFI layer (initial length at 180°C: 2.5 cm) upon calcination, imaginary separated from the underlying clay substrate (optimized composition)

Process	Length (formal) (cm)		Variation (cm)		Difference[@] (cm)
	MFI	Clay	MFI	Clay	
Synthesis (180°C)	2.5	2.5	-	-	0.0000
Cooling to 20°C	2.4980	2.4960	-0.0020	-0.0040	0.0020
Heating to 350°C	2.5021	2.5042	0.0041	0.0082	-0.0021
Removal of organics (400°C)[#]	2.4981	2.5055	-0.0040	0.0013	-0.0074
Cooling to 100°C	2.4981	2.4980	0.0000	-0.0075	0.0010
Cooling to 20°C[$]	2.4985	2.4960	0.0004	-0.0020	0.0025

[@] Negative values refer to a tensile stress in the MFI layer
[#] In comparison with calcination up to 450°C:
    l_{MFI}=2.4941 cm; l_{Clay}=2.5067 cm; Δl= -0.0126 cm
    At 20°C the MFI layer will be under a tensile stress (Δl = -0.0015 cm)
[$] Due to the orthorhombic-to-monoclinic phase transition at 77°C (cf. Chapter 4, Table 3)

The imposed stresses within the MFI layer are qualitatively shown in Figure 7 for calcination at 400°C. When the calcination is performed at 450°C, the imposed tensile stresses on the MFI layer at high temperature are substantially higher. It may be noted that the empty (template-free) zeolite reaches a zero-stress point upon cooling to ca. 100°C.
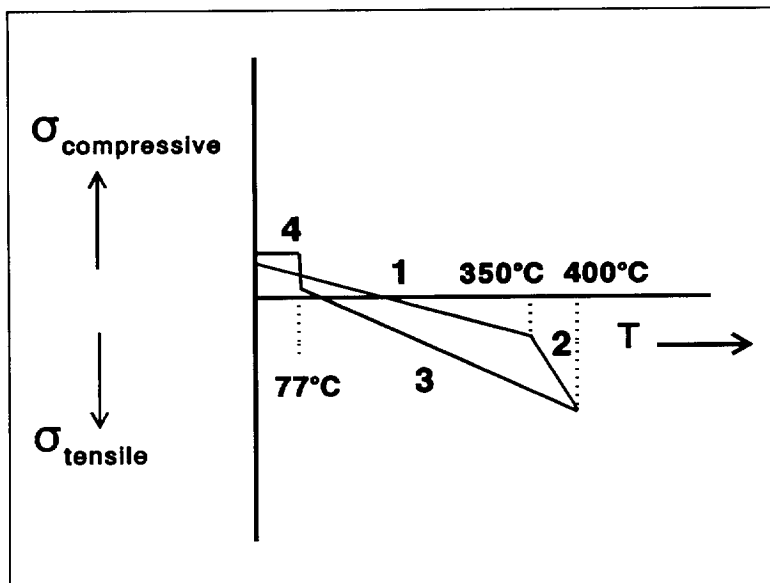
Figure 7   Qualitative evaluation of the developing stresses within a clay-supported, polycrystalline MFI layer upon calcination at 400°C: 1) heating cooling TPA-MFI up to 350°C, 2) removal of TPA degradation products up to 400°C, 3) shrinkage of clay support upon cooling, 4) orthorhombic-to-monoclinic phase transition of MFI

Inspection of in situ grown MFI layers on clay substrates after calcination in air at 400 and 450°C (Figure 8) indicates that the behaviour of the MFI/clay system agrees with the expected tensile stress within the MFI phase at high temperature. Upon calcination at 400°C (heating rate 1°C/min, dwell time over 10 hours), no cracks are observed by visible light microscopy and the morphology of the layer is preserved (Figure 8a). When the calcination is performed in a similar way at 450°C, the top section of the MFI layer has partly disappeared (Figure 8b). According to SEM, however, the clay substrate is still fully covered by MFI material. Apparently, the tensile stresses within the MFI layer at 400°C are still below the tensile strength of the material. At 450°C, however, the stresses within the MFI layer exceed the tensile strength, which may limit the high-temperature applications to ca. 400°C. As the cracks develop within the MFI phase, rather than on the MFI/clay interface it is concluded that the bonding to the clay phase is strong, and survives the thermal treatment.

(a) _____ (b)

10 µm
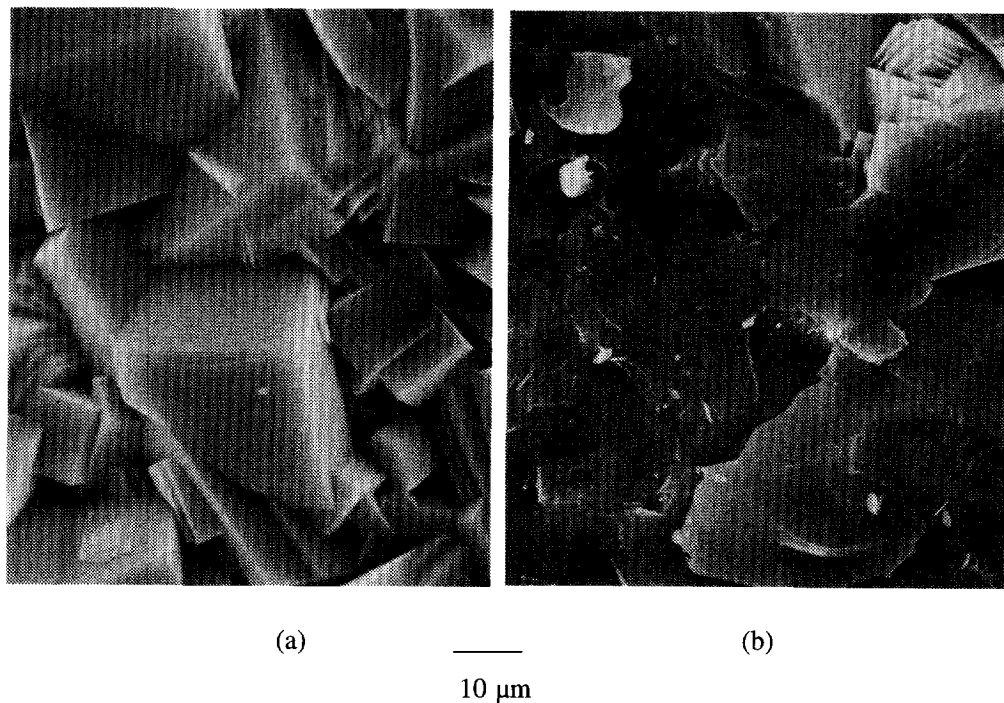
Figure 8   SEM-picture of the MFI layer on top of an optimized clay support after calcination: (a) at 400°C, and (b) at 450°C

For the stainless steel supported MFI layers the same calcination procedure has been applied. Despite the higher thermal expansion of stainless steel (cf. Table 4), the MFI layers remain intact after calcination at 400°C (cf. Chapter 7). The thermomechanical properties may, nevertheless, vary from the clay supported MFI layers, because a different synthesis mixture has been applied for the growth on stainless steel.

The MFI lattice remains quite stable under both compressive and tensile stresses. From a thermomechanical point of view, the high stability of the MFI material may be related to a high strength (high critical compressive and tensile stress) and a low Young's modulus. The lattice is indeed quite flexible, as even large guest molecules, such as p-xylene, are

accommodated within the MFI pore system with substantial geometrical changes of the lattice (cf. Chapter 4, Table 3). Another factor may be the flexibility of the porous support and/or the elasticity of the support material (especially stainless steel). The presence of pores within the substrate may lead to the accumulation of stress over only a limited length, thus reducing the stress as compared to a dense substrate.

As has been mentioned earlier, the at 400°C activated MFI layer is under a compressive stress by the strong bonding to the clay substrate under ambient conditions. The powder X-ray diffraction pattern of a carefully polished clay supported MFI layer after calcination at 400°C reveals that the normally present doublets[13] at $2\Theta = 24°$ and $2\Theta = 28.5°$ are single (Figure 9).
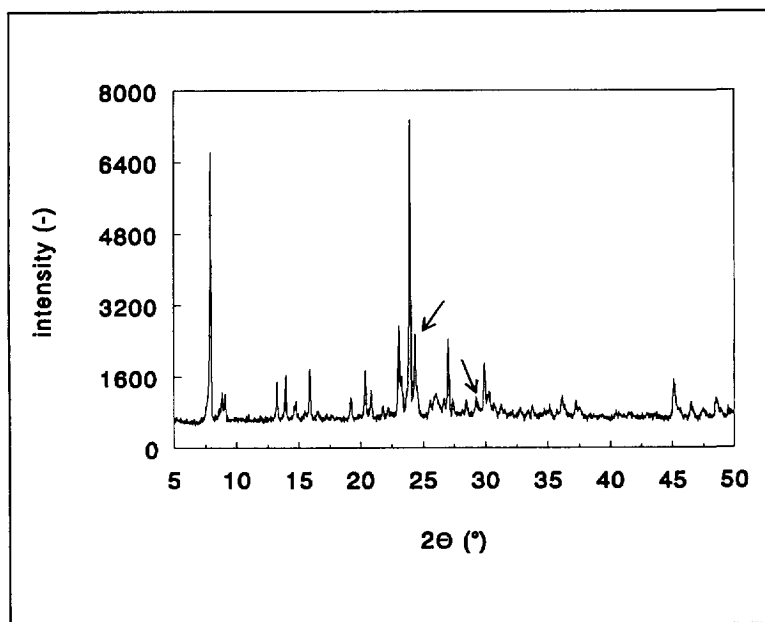
Figure 9   X-ray powder diffraction pattern of a polished, clay-supported MFI layer after calcination at 400°C; the single peaks that are doublets for unsupported silicalite are marked with an arrow

As has been discussed previously in Chapter 4, the occurrence of doublets is attributed to the fact that the calcined lattice is built up out of monoclinic twin domains. It is possible

to reduce the population of the twin domains by applying a uniaxial mechanical compressive stress, after which process the doublets are single.[14] The imposed compression of the MFI layer by the clay substrate may lead to the same reduction of the population of twin domains.

5.5 Literature

1. L. Stuckert, *Die Emailfabrikation*, Springer-Verlag, Berlin, 1941, 34-49.
2. H. Scholze, *Die physikalischen und chemischen Grundlagen der Keramik*, Springer-Verlag, Berlin-Heidelberg, 1968, 72-82.
3. A. Petzold, H. Pöschmann, *Email und Emailliertechnik*, Springer-Verlag, Berlin-Heidelberg, 1987, 58-76.
4. S. Stefanov, S. Batschwarov, *Keramik-Glasuren/Ceramic Glazes*, Bauverlag, Wiesbaden-Berlin, 1988, 39.
5. C.L. Bijl, *Chem.Weekbl.*, 48 (1952) 998.
6. R.W. Jones, *Fundamental Principles of Sol-Gel Technology*, The Institute of Metals, London, 1989, 97-98.
7. H. Schmidt, G. Rinn, R. Nasz, and D. Sporn, in: *Better Ceramics Through Chemistry III*, C.J. Brinker, D.E. Clark, D.R. Ulrich (Eds), Mat.Res.Soc.Symp.Proc. Vol 121, MRS, Pittsburgh, 1988, 743-754.
8. L.L. Hench, G. Orcel, J.L. Nogues, in: *Better Ceramics Through Chemistry III*, C.J. Brinker, D.E. Clark, D.R. Ulrich (Eds), Mat.Res.Soc.Symp.Proc. Vol 73, MRS, Pittsburgh, 1986, 35-47.
9. T.M. Shaw, in: *Better Ceramics Through Chemistry III*, C.J. Brinker, D.E. Clark, D.R. Ulrich (Eds), Mat.Res.Soc.Symp.Proc. Vol 73, MRS, Pittsburgh, 1986, 215-223.
10. C.J. Brinker, G.W. Scherer, *Sol-Gel Science, The Physics and Chemistry of Sol-Gel Processing*, Academic Press, London, 1990, 453.
11. A. Mulder, F. van Looij, P.A. Dekker, E.R. Geus, J.W. Geus, in: *Inorganic Membranes*, A.J. Burggraaf, J. Charpin, L. Cot (Eds), Proc. ICIM$_2$-91, Trans.Tech.Publ.Ltd, Zürich, 1991, 411-414.
12. W. van Noort, Ferro B.V. Rotterdam, private communication, September 1991.
13. H. van Koningsveld, J.C. Jansen, and H. van Bekkum, in: R. von Ballmoos, and J.B. Higgins (Eds), *Zeolites*, 10 (1990) 442s.
14. H. van Koningsveld, F. Tuinstra, J.C. Jansen, and H. van Bekkum, *Zeolites*, 9 (1989) 253.

6. Sorption and Diffusion Studies on Large MFI-Type Crystals by FTIR-Spectroscopy

A new technique has been developed to study sorption and diffusion within large zeolite crystals by microscope FTIR-spectroscopy. Different IR absorption bands of the adsorbed molecules can be used for data evaluation, but here the aliphatic C-H stretching bands around 2900 cm^{-1} have been taken predominantly. Quantitative adsorption measurements have been performed on various small hydrocarbons (n-butane, isobutane, 1-butene, and neopentane), using calibration data provided by gravimetry and Si-O framework bands as internal standards. It is demonstrated that diffusional data can be obtained from uptake measurements, applying commonly accepted diffusion models. The FTIR technique also allows measurement of the self-diffusion of tracer molecules, such as deuterated species (D$_2$O). The range in which diffusivity data can be obtained is limited by the crystal size and the frequency with which spectra can be taken with respect to the time interval for each measurement. Selective sealing of crystal faces leads to confined desorption of aromatics (4-methylpyridine) from the anisotropic MFI framework.

6.1 Introduction

Adsorption and diffusion processes play an important part in the separation of mixtures and in catalytic conversions by means of zeolites and other crystalline molecular sieve materials. For this reason, adsorption and diffusion are major topics in the field of zeolite science, which have been studied extensively using various methods.[1-3] The laws governing diffusion in zeolite crystals or extrudates equally apply to the molecular flow through the zeolite membranes under consideration in this work. Profound knowledge of the fundamentals of molecular migration within zeolite micropores may therefore assist in understanding the observed membrane permeation behaviour (cf. Chapter 7).

As far as adsorption data are concerned, there is generally good agreement between the results obtained using different techniques (mainly gravimetry and volumetry), and even between data obtained on samples of different origin. With diffusional data, however, the situation is less favourable. Since the late seventies it has been noted that a large discrepancy exists between intracrystalline self-diffusion coefficients in zeolites, essentially determined by NMR methods or neutron scattering (microscopic), and transport diffusivities, based on transient sorption rate measurements (macroscopic).[4,5] Direct information on the molecular mobility of adsorbed species is obtained from the pulsed field gradient (pfg) NMR technique,[6,7] which, combined with diffusional data from NMR tracer uptake measurements,[8] may provide additional data on the existence and intensity of transport resistances at the surface of the zeolite crystals.[9,10] Prior to the introduction of the above NMR technique, diffusional data (transport diffusivities) were generally derived from uptake measurements employing experimental set-ups that were also used to measure adsorption isotherms. Comparison between the thus obtained (macroscopic) transport diffusivities and the intracrystalline diffusivities determined according to the NMR method led to a critical examination of the former (macroscopic) measuring techniques, in which the effects of external heat and mass transfer resistances were sometimes underestimated.[10] Several new techniques to measure transport diffusivities have, subsequently, been developed, such as frequency response techniques (FR)[11-14] and zero length column

chromatography (ZLC).[15-18] Using results obtained with the newly developed techniques it has been tried to reconcile the macroscopic data with the microscopic NMR data. So far, it seems that the FR technique, operating under near equilibrium conditions, has been more successful than the ZLC method. Other techniques to measure transport diffusivities have been reported, such as membrane permeation,[19,20] and diffusion limited (or controlled) catalytic conversions.[21,22]

In this chapter the application of microscope FTIR-spectroscopy to study sorption and diffusion in a large zeolite single crystal is dealt with. In a preliminary publication the desorption of 4-methylpyridine (cf. section 6.3.2 and 6.4.4) from a single silicalite crystal has been studied.[23] *In situ* FTIR spectroscopy on several zeolite crystals has been applied previously to study chemical reactions[24], or the template (TPA) decomposition within fluoride-synthesized MFI.[25] Recently, Karge et al.[26] have reported the determination of the uptake rate of benzene and ethylbenzene into ZSM-5 crystallites, compressed in the form of self-supported wafers by FTIR spectroscopy.

In the present work, large, cube-shaped silicalite single crystals are involved, hence the presence of larger pores within the sorbent is avoided. Diffusion measurements on one zeolite crystal have only been performed previously by Tiselius on the adsorption of water in heulandite (HEU),[27] and ammonia into analcime (ANA),[28] using polarized (visible) light to study the adsorption in large crystals by birefringence changes.

6.2 FTIR-Technique: Experimental Set-Up

Transmission IR spectra of one single crystal can be taken by means of a light microscope FTIR Spectrometer (Bruker IFS 66), provided a sufficiently large crystal is used. Therefore silicalite cubes have been chosen of typical dimensions of 100 x 40 x 200 μm, which remain crack-free upon calcination (cf. Chapter 4). The crystals are attached to a silicon wafer (5x5 mm^2) by a ceramic kit (Royal Delft Ware Manufactory, Delft, The Netherlands)

with the ac-plane parallel to the wafer (Figure 1). The silicon wafer is installed in a stainless steel wafer holder, to control the orientation of the crystal in the IR beam. Moreover, the position of the crystal is thus easily maintained within the gas stream during adsorption/desorption measurements.

25 μm
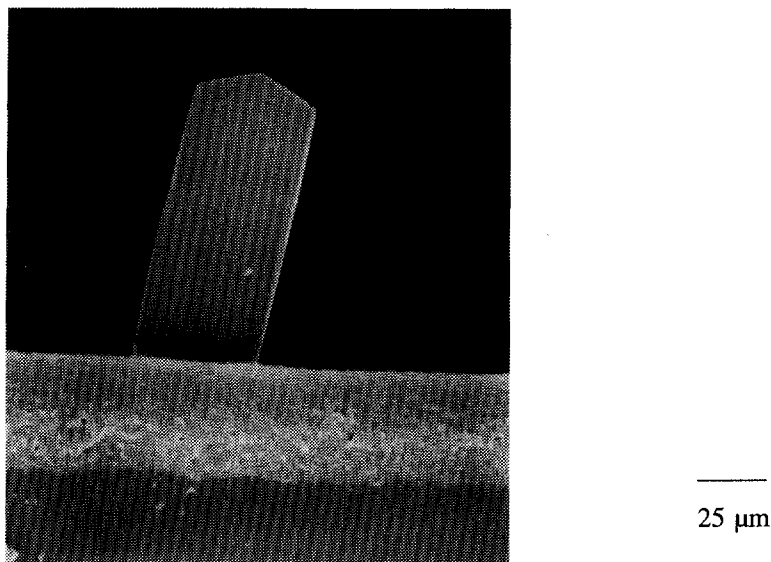
Figure 1   SEM image of a silicalite single crystal attached to a silicon wafer by a ceramic kit in the ac-plane

The wafer holder, together with the silicon wafer and an attached silicalite crystal, is installed in ambient air near a thermocouple into a specially designed stainless steel flow-cell (Figure 2). The flow-cell is positioned underneath an IR/VIS-light microscope (total magnification 150x). The calcination experiments of Chapter 4 have been carried out using the same configuration. The crystal under investigation can thus be activated in air (temperatures up to 450°C), and cooled down in a water-free nitrogen atmosphere (under atmospheric pressure). The cell is provided with IR transparent windows (BaF_2 or NaCl) within tight-fitting metal inlays (also shown in Figure 2). As some leakage into and out of

the flow-cell may occur, a purge gas flow (> 20 ml/min) is applied. Generally nitrogen (99.999%; Air Products) serves as the inert carrier gas. The nitrogen flow is mixed with either another gas stream (small hydrocarbons) or with vapours (e.g. aromatics). The standard flow rate of the purge gas amounts to 550 ml/min, unless stated otherwise.
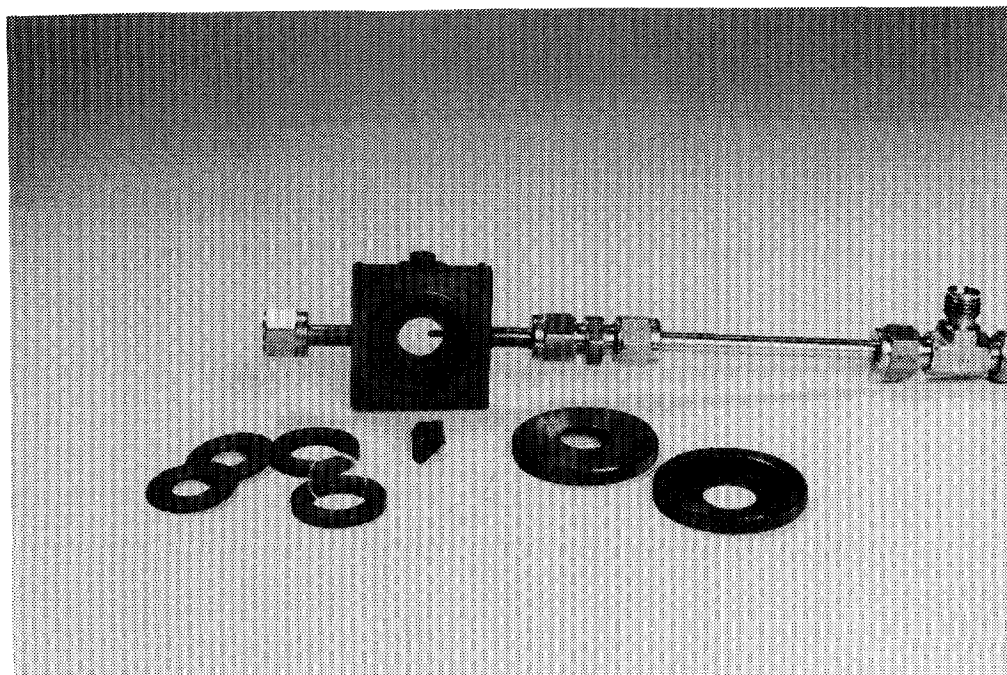
Figure 2   FTIR flow-cell, also showing the IR transparent (BaF_2) windows, the tight-fitting stainless steel inlays, and the silicon wafer holder

Though the IR beam can be focused on the centre of the crystal by visible light microscopy, still a significant part of the IR beam by-passes the crystal. Therefore, a sufficiently small aperture is chosen to make sure that only that part of the IR beam that is actually transmitted through the crystal is detected. Single beam spectra are taken; the sample and reference single beam spectra (focusing besides the zeolite crystal) have therefore to be taken consecutively. The IR spectra are determined from a sample and a reference single

beam spectrum. Some heating of the zeolite crystal by the IR beam (the intensity on the crystal amounts to 500 mW/cm^2) may be considered, although it is expected that the temperature increase of the crystal is at most about 5°C.[29]

The single beam spectra may be taken within 4 to 10 seconds (10 to 25 scans; spectral resolution 8 cm^{-1}), preserving the required accuracy of the measurement. The quality of the spectrum does depend on the orientation of the crystal within the IR beam, as significant reflection losses may occur if the crystal orientation deviates too strongly from the orientation parallel to the silicon wafer. Therefore measurements along the c-direction of silicalite cubes may only be possible after polishing the crystal to obtain flat and parallel ab-faces. The minimum spot size on the crystal has been found to be approximately 40 μm. After the initial data collection the further processing can be postponed, which is essential to be able to monitor transient processes, such as desorption (*vide infra*). With the present system it is possible to obtain spectra at a rate of ca. 10 min^{-1}. With a more sophisticated spectrometer, the frequency with which spectra are taken may be increased, whereas the time interval required for reliable data acquisition may be reduced as well.

Owing to the height of the flow-cell (ca. 1 cm), accurate measurement of the gas phase is feasible. The partial pressure of molecules of some adsorbate within the purge gas flow may be varied between 1 and 100 kPa, depending on the absorbance of the species involved. Hence, the equilibrium between the gas phase and the adsorbate phase can be studied to obtain adsorption isotherms (cf. section 6.3). The maximal absorbance may, however, be exceeded during the sample measurement (measuring through both the *crystal* and the *gas* phase), in which case a thinner silicalite crystal must be used to reduce the path length through the adsorbate phase. Obviously, a flow-cell of a shorter path length may be used (> 1 mm), in which case the absorbance of the gas phase is negligible.

6.3 Adsorption

6.3.1 Adsorption of Aliphatic Hydrocarbons

The IR spectrum of a calcined and dehydrated silicalite crystal is shown in Figure 3.
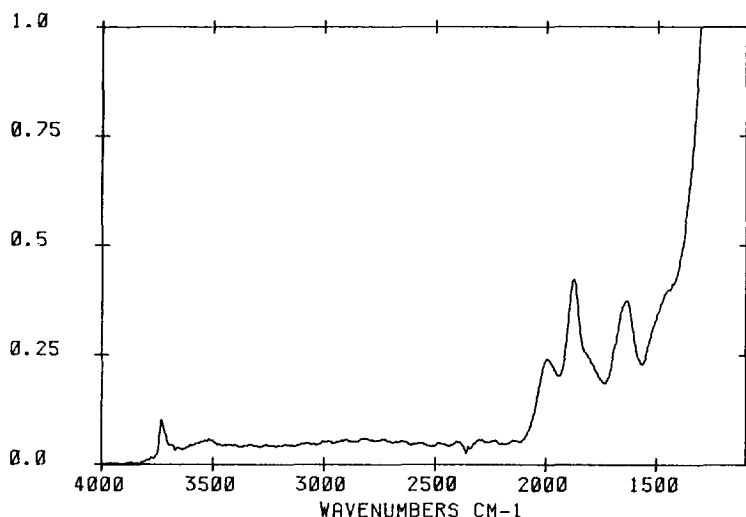
Figure 3 IR-spectrum of a calcined silicalite crystal, fully dehydrated in nitrogen atmosphere

Even at room temperature it is possible to obtain a fully dehydrated crystal by flushing with nitrogen, which illustrates the hydrophobic character of silicalite. Gases studied include n-butane, isobutane (2-methylpropane), and 1-butene (>99.5%; Messer Griesheim, Germany) as sorbate molecules, because the gases can be easily introduced into the flow-cell by mixing with an inert gas stream. Moreover, the position of several typical C-H absorption bands in the IR spectrum (3100-2800 cm^{-1}; cf. Table 1)[30] does not coincide with that of the absorption bands of the silicalite framework.

Quantitative measurements are favourably performed in the high frequency area for the *aliphatic* hydrocarbon absorption bands (3100-2800 cm^{-1}) because of the high extinction coefficients and the absence of other absorption bands.

Table 1   IR stretching (ν) and bending (δ) vibrations of C-H bands of hydrocarbons[30]

Group		Band (cm^{-1})	Intensity	Assignment
Alkanes	-CH$_3$	2960	strong	ν_{as} CH$_3$
		2870	medium	ν_s CH$_3$
		1460	medium	δ_{as} CH$_3$
		1380	strong	δ_s CH$_3$
	-CH$_2$-	2925	strong	ν_{as} CH$_2$
		2850	strong	ν_s CH$_2$
	-CH-	1470	medium	CH$_2$ scissor
Alkenes	=CH$_2$	3080	medium	ν_{as} CH$_2$
		2975	medium	ν_s CH$_2$
	=CH-	3020	medium	ν CH$_2$

(a)   (b)
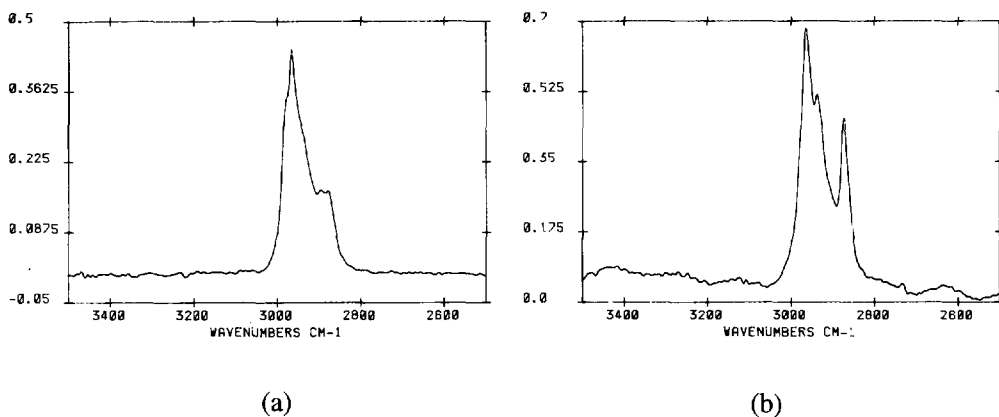
Figure 4   IR-spectra of n-butane (a) in the gas phase, and (b) adsorbed within a silicalite crystal at room temperature

(a)

(b)
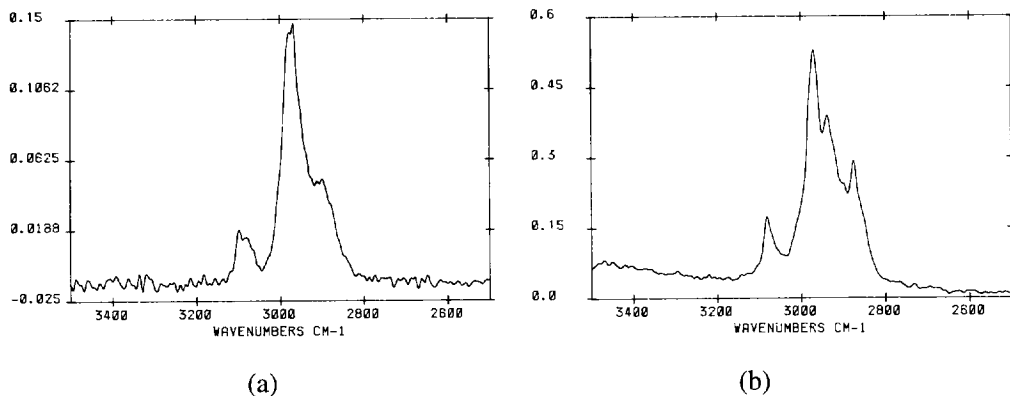
Figure 5   IR-spectra of 1-butene (a) in the gas phase, and (b) adsorbed within a silicalite crystal at room temperature

The above hydrocarbons are strongly adsorbed within the hydrophobic silicalite framework. Partial pressures of about 5-10% suffice for near saturation adsorption at room temperature. In Figure 4 (n-butane) and 5 (1-butene), the notably different IR spectra of the gas and the adsorbate phase are presented. A typical IR absorption band at about 2873 cm^{-1} is pronouncedly present in all adsorbate spectra. Apparently, the molecular movements (rotation) in the adsorbed phase are limited as compared to within the gas phase. The absorption band at about 2873 cm^{-1} may therefore be attributed to a typical C-H bond, interacting with the silicalite framework.

The sorbate concentration within the silicalite crystal and the gas phase concentration within the flow-cell may be related to the C-H absorbance according to the Lambert-Beer law:

$$\log \frac{I}{I_0} = - \varepsilon \cdot c_{a,g} \cdot l_{c,f} \tag{1}$$

with ε the extinction coefficient (m^2/mol), $c_{a,g}$ the sorbate concentration (mol/m^3) in the crystal and gas phase, respectively, and $l_{c,f}$ the path length (m) through the crystal and the flow-cell, respectively.

According to this procedure, it is possible to measure adsorption isotherms, provided sufficiently thin crystals are used (*vide supra*). This is shown for n-butane and isobutane in Figure 6. The aliphatic hydrocarbon absorbances have been integrated (range 3039-2792 cm^{-1}) and plotted versus the partial pressure in the gas phase. The substantially lower absorbance of isobutane as compared to n-butane is not due to a difference in extinction coefficient, as within the gas phase the extinction coefficient of isobutane is even slightly higher than that of n-butane. Apparently, there is a notable difference in adsorption capacity between the butane isomers under the conditions applied here, in agreement with gravimetric adsorption measurements on similar silicalite material under the same conditions (*vide infra*):[31] the adsorption capacity of isobutane at 95°C (0.54 mmol/g) is only half the adsorption capacity of n-butane (1.13 mmol/g). It is expected that the packing of isobutane within the MFI lattice is less efficient than that of n-butane.
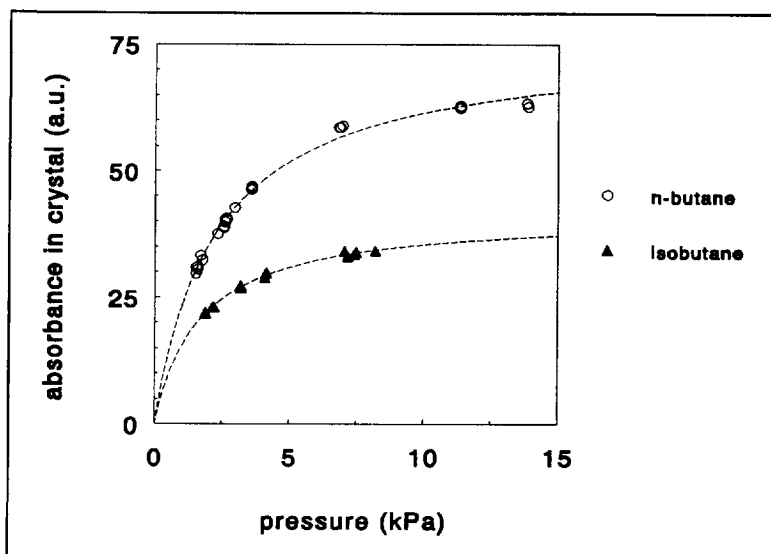
Figure 6   Adsorption isotherms for n-butane and isobutane at 95°C on a silicalite single crystal (thickness 35 µm), according to the FTIR-spectroscopic technique; the integrated absorbances of the adsorbed hydrocarbons (3039-2792 cm^{-1}) are represented in arbitrary units (cf. text)

In Figure 7 the gas phase and adsorbate spectra are shown for neopentane (2,2-dimethylpropane). Apparently, neopentane may also enter the silicalite framework, which is surprising in view of the kinetic diameter of neopentane (6.2 Å).[32] The IR absorption bands of neopentane remain present, even after flushing with pure nitrogen for more than 1 hour (cf. section 6.4). In addition, the typical 2873 cm^{-1} absorption band is exhibited in the adsorbate spectrum (Figure 7b), also suggesting that neopentane is adsorbed within the MFI framework.

(a)   (b)
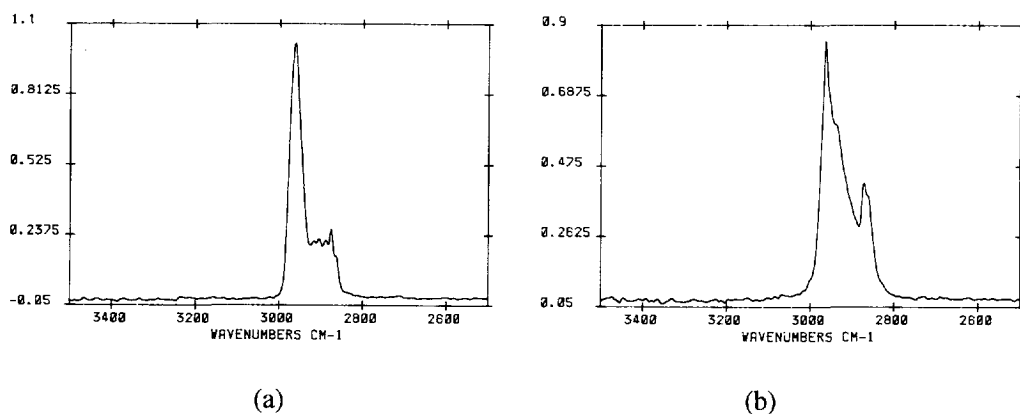
Figure 7   IR-spectra of neopentane (2,2-dimethylpropane) (a) in the gas phase, and (b) adsorbed within a silicalite crystal at 57°C and subsequently cooled to room temperature

Nevertheless, it requires some special manipulation to achieve adsorption of neopentane into silicalite. The applied neopentane (95%; Air Products) is contaminated with cis-2-butene (5 vol%), which is readily adsorbed at room temperature and seems to hinder the adsorption of neopentane. Even after removal of the contaminant by selective adsorption into zeolite CaA (LTA), no neopentane adsorption has been observed at room temperature. Only after heating the zeolite crystal to 57°C, subsequently introducing purified neopentane (10 vol%), and finally cooling down to room temperature, the IR spectrum in Figure 7b could be measured.

The accessibility of the MFI framework for neopentane has been reported in the literature,

but the adsorption capacity is as yet unknown. Flanigen et al.[33] report an adsorption capacity of 1.4 molecules per unit cell (0.24 mmol/g) at room temperature. Dessau merely mentions that neopentane does adsorb from the liquid phase at room temperature, similarly to, for instance, o-xylene and 2,2-dimethylbutane.[34] It seems that the adsorption of neopentane within the MFI framework requires a slightly elevated temperature.

An estimate of the extent of the neopentane adsorption may be provided according to the here presented FTIR-spectroscopic technique. The extinction coefficients of the hydrocarbon absorption bands in the gas phase are expected to be slightly different from those in the adsorbate phase, because different absorption bands are observed as well. Hence, a calibration method is required to relate the IR absorbances of adsorbed molecules to the actual concentrations within the framework. In this particular case, n-butane and isobutane have been taken as the two calibration gases for three reasons, viz. (i) both gases adsorb readily in silicalite, (ii) n-butane contains similar functional groups as 1-butene ($-CH_2-$ and $-CH_3$), and (iii) isobutane contains similar groups as neopentane (i.e. the strongly absorbing $-CH_3$). The other prerequisite is an internal standard to which the IR absorbances of the adsorbed molecules can be related. For the here studied silicalite cubes, the Si-O overtones at 2000 and 1880 cm^{-1} have been chosen, similar to Mirth et al.[35] The Si-O absorbance remains constant, irrespective of the nature and concentration of the sorbate. At a fixed temperature, the ratio of the aliphatic C-H absorbance of the adsorbed hydrocarbon and the Si-O overtones varies within approximately 10% for different crystals.

The adsorption capacities of n-butane (1.59 mmol/g) and isobutane (0.81 mmol/g) under ambient conditions have also been measured gravimetrically for similar silicalite crystals at a sorbate partial pressure of 0.37 bar in helium (1 bar total pressure).[31] The observed adsorption capacity being higher for n-butane than for isobutane is also in qualitative agreement with data by Zheng et al. for volumetric measurements on again similar silicalite material.[36] The observed adsorption capacity of n-butane is in good agreement with data reported in the literature (about 1.6 mmol/g).[14,37] In an earlier study, however, Jacobs et al. reported an essentially equal adsorption capacity for n-butane, viz. 1.89 mmol/g (0°C), but a much higher capacity of 1.92 mmol/g for isobutane (20°C).[38]

The values according to the above gravimetric measurements of the butane isomers have been taken to estimate the sorption capacities of 1-butene and neopentane. The observed ratios of the aliphatic C-H absorbance and the intensities of the Si-O overtone absorption bands are listed in Table 2 for atmospheric adsorption at room temperature (10% in nitrogen). The nature and number of functional groups for each hydrocarbon are also listed in Table 2, from which the relative extinction coefficients (n-butane/1-butene and isobutane/neopentane) are obtained. Accordingly, the estimated adsorption capacity of 1-butene amounts to 1.66 mmol/g. As expected, the difference in adsorption capacity between n-butane and 1-butene is negligible, in agreement with adsorption data on n-butane and 2-butyne.[14] The adsorption capacity of neopentane amounts to 0.66 mmol/g, or 3.80 molecules per unit cell (containing 4 intersections). This seems to suggest a specific adsorption site for neopentane within the MFI framework, which may be located at the intersections in view of the bulky character of the sorbate molecule.

Table 2   Ratio of the aliphatic hydrocarbon IR-absorbances over the absorbance of the Si-O overtones at 2000 and 1880 cm^{-1} for n-butane, 1-butene, isobutane, and neopentane adsorption in silicalite. Conditions: flow about 10 vol% of the hydrocarbon in nitrogen at room temperature (total pressure 1 bar)

hydrocarbon	n-butane	1-butene	isobutane	neopentane
C-H over Si-O absorbance	4.29	2.26	2.51	2.71
number of functional groups $\quad$ -CH$_3$ $\quad$ -CH$_2$	2 2	1 1	3 -	4 -

6.3.2 Adsorption of Aromatics

The adsorption of some aromatics has been pursued: (i) to validate this newly developed technique, (ii) to study the accessibility of the MFI framework, and (iii) to prepare silicalite single crystals saturated with a selected species for X-ray single crystal structure analysis,

similar to silicalite saturated with p-xylene.[39] In the latter study, a full loading of p-xylene (8 molecules per unit cell) has been achieved by rapidly cooling down from 200 to 20°C in a p-xylene atmosphere, as at the latter temperature the p-xylene molecules are virtually frozen within the MFI framework. Basically the same procedure has been followed for the adsorption of aromatics, such as trifluorotoluene ($PhCF_3$), benzoic acid, and 4-methylpyridine (γ-picoline), and in fact, also of neopentane. The adsorption of several well-known aromatics (such as benzene, toluene, ethylbenzene, and the xylene isomers) using various techniques has already been reported on in the literature.[26,40-44]

The adsorption of γ-picoline into silicalite cubes (Figure 8) has been carried out in exactly the same way as the above mentioned p-xylene adsorption.[39] Some water adsorption has taken place, which adsorption process is rather slow in the presence of γ-picoline. The adsorption of γ-picoline does not lead to a sorbate induced phase transformation of the MFI framework as for p-xylene, which has been established by X-ray diffractometry (cf. Chapter 4, section 4.3).
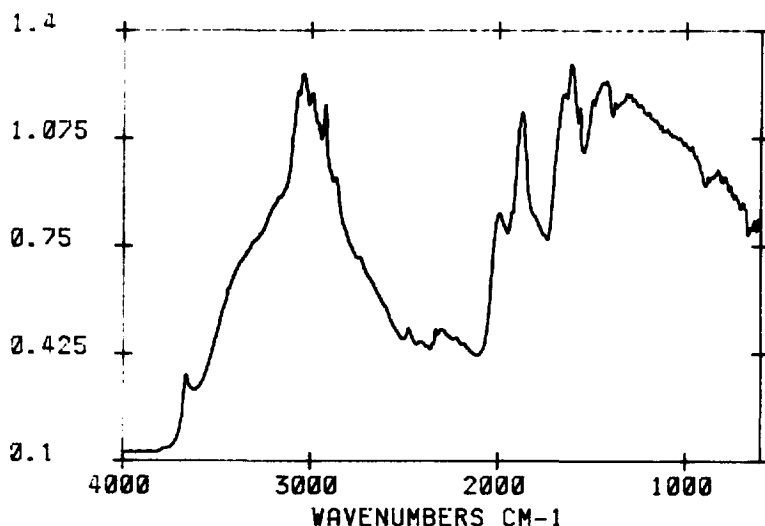
Figure 8   IR-spectrum of γ-picoline (4-methyl pyridine) adsorbed within a silicalite crystal by cooling from 200°C to ambient temperature in γ-picoline vapour

The crystals loaded with γ-picoline have further been used for desorption experiments, in which also the adsorption by selectively sealed silicalite cubes has been included (cf. section 6.4.4). As a sealing material an epoxide resin (bisphenol A glycidyl ether/polyamine; Araldit, Ciba-Geigy) is applied. In this way, molecular transport is confined exclusively to either the straight (sealing the ab and bc faces), or the sinusoidal channels (sealing the ab and ac faces). The absorption bands of γ-picoline at 3000 cm^{-1} are again related to the Si-O overtone bands at 2000 and 1880 cm^{-1}, resulting in a constant ratio, irrespective of the faces sealed. It can therefore be assumed that the crystals are fully loaded with γ-picoline.

The adsorption of trifluorotoluene has been studied in situ by FTIR spectroscopy. Nitrogen is used as a carrier gas to transport trifluorotoluene vapour from a saturator at room temperature into the flow-cell. In Figure 9a the gas phase spectrum of trifluorotoluene is represented.

(a)   (b)
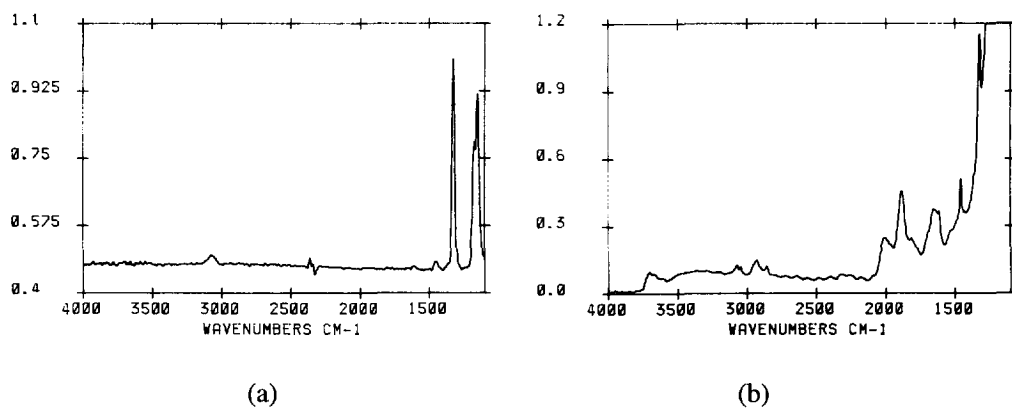
Figure 9   IR-spectra of trifluorotoluene (a) in the gas phase, and (b) adsorbed within a silicalite crystal by cooling down in a trifluorotoluene vapour in nitrogen from 150°C to 60°C

The C-F bands are visible at 1327, 1174, and 1151 cm^{-1}, in accordance with the C-F stretching vibration area (1400-1000 cm^{-1}).[45] No significant adsorption has been observed at room temperature. Upon heating, the first adsorption takes place at approximately 150°C. While cooling down, the sorbate concentration increases, and reaches its maximum at

approximately 60°C as shown in Figure 9b, in which only two C-F vibrations bands are visible (1456 and 1323 cm^{-1}). The aromatic C-H vibrational bands are slightly visible, together with some aliphatic C-H absorption bands, of which the origin is uncertain. Similarly to the adsorption experiment with γ-picoline, some water adsorption is observed under ambient conditions, but the C-F absorption bands remain constant. A thus prepared silicalite cube, saturated with trifluorotoluene, has also been analyzed by X-ray diffractometry, but again no change in the monoclinic symmetry is observed.

Finally, the adsorption of benzoic acid within silicalite crystals has been investigated. In this case, some calcined crystals are heated in the presence of benzoic acid to 150°C (melting point benzoic acid is 122.4°C), and cooled to room temperature in benzoic acid vapour. As a reference a solution of benzoic acid in tetrachloromethane (CCl$_4$) is poured over a KCl crystal and left to dry. The IR spectrum (Figure 10a) is in good agreement with the spectrum of benzoic acid in a KBr pellet.[46] The IR spectrum of benzoic acid in silicalite is shown in Figure 10b.

(a)   (b)
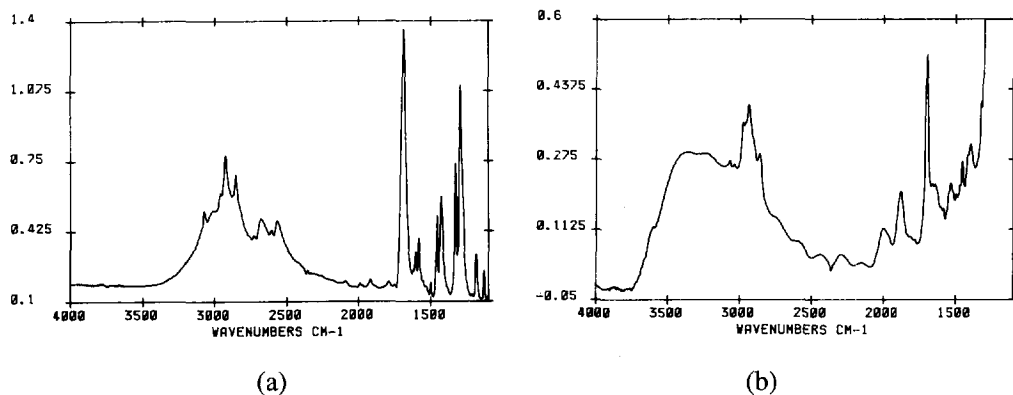
Figure 10   IR-spectra of benzoic acid (a) as a thin solid film on a KCl crystal, and (b) adsorbed within a silicalite crystal by cooling down benzoic acid vapour from 150°C to room temperature under ambient conditions

Again some water adsorption can be observed. The benzoic acid adsorbed on the external surface of the silicalite crystal is removed by immersion of the loaded crystal into CCl$_4$ at

room temperature. After 30 seconds, the crystal is removed from the liquid and left to dry under ambient conditions, which procedure is repeated three times. After the treatment with CCl_4, the benzoic acid absorption bands are still exhibited, and, hence, benzoic acid is still present within the silicalite framework. X-ray diffractometry indicates that the silicalite cube loaded with benzoic acid has changed its symmetry. This symmetry will be further investigated by X-ray diffraction to elucidate the crystallographic structure.

6.4 Diffusion

6.4.1 Desorption of Hydrocarbons from a Single Crystal

The desorption process from a silicalite crystal has been monitored as a function of time by taking IR spectra within suitable time intervals (cf. section 6.2). Adsorption of hydrocarbons (n-butane, 1-butene, isobutane, and neopentane) is achieved from a sorbate gas flow (10 vol% in nitrogen), after which desorption is initiated by changing to a pure nitrogen flow (purge gas flow rate 550 ml/min). Within a few seconds the gas phase concentration is reduced to about 5% of the original concentration, and after 30 seconds, the gas phase concentration is too low to be accurately quantified. In this way, the technique resembles the earlier mentioned ZLC method, developed by Ruthven and coworkers.[15-18] In contrast to the ZLC method, however, the amount of sorbate molecules remaining in the framework is measured.

In Figure 11 the desorption of isobutane at 43°C is shown as a stack-plot of subsequently taken IR spectra of the silicalite crystal. The desorption progress can be plotted as a function of time, either as the relative intensity (simply by dividing by the initial IR absorbance), or as the fractional coverage of the micropores, based on the adsorption isotherm. The reproducibility of the procedure is demonstrated for the desorption of n-butane at different temperatures (Figure 12). The effect of the nature of the purge gas is checked by comparison with desorption into helium, with which no significant differences in the desorption rates are observed.
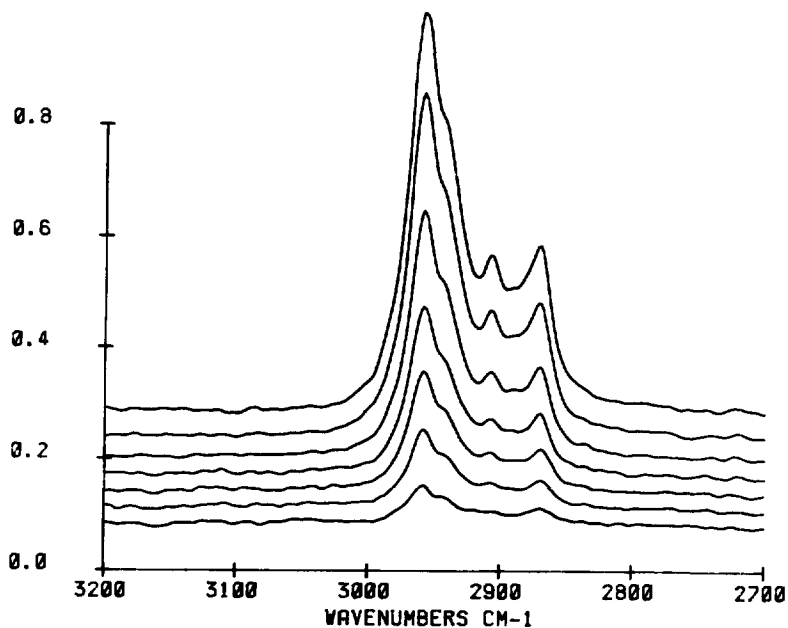
Figure 11   Stack-plot of 7 IR spectra of a silicalite crystal from which isobutane desorbs
at 43°C at different times
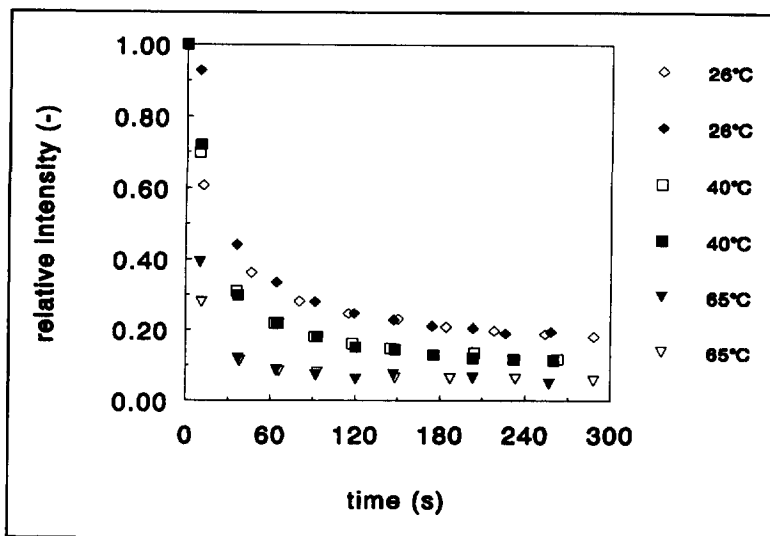
Figure 12   Desorption progress of n-butane from a large silicalite crystal at 26, 40, and
65°C (purge gas flow rate 550 ml/min); two independent series are
represented at each of the above mentioned temperatures

The desorption proves, however, to be dependent on the purge gas flow rate, which is not expected if desorption is fully determined by intracrystalline diffusion. The dependence on the flow rate of the purge gas is a rather difficult point in the ZLC method, as the desorption is expected to depend on the purge gas flow rate anyway. Apparently, the desorption from the silicalite crystal is to some extent governed by the removal of sorbate molecules from the gas phase surrounding the silicalite crystal (cf. section 6.4.2). Nevertheless, significant differences in the rate of desorption have been observed under equal conditions between 1-butene and n-butane, on the one, and isobutane, on the other hand (Figure 13). In Figure 14 the desorption of neopentane at 27°C is shown (purge gas flow rate 780 ml/min). These observations form the basis for the discussion on diffusion modelling in the next section.
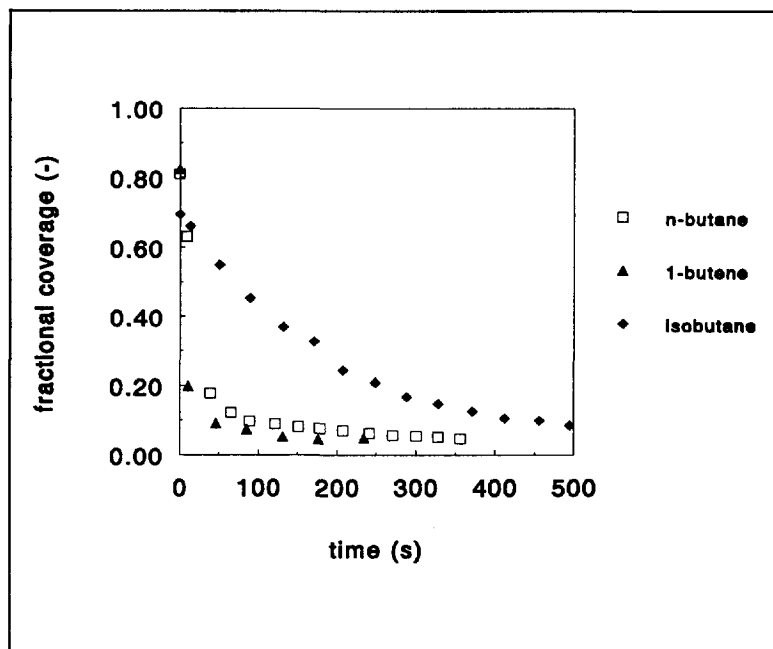
Figure 13   Comparison of the desorption of n-butane, 1-butene, and isobutane from a silicalite crystal (40 μm thickness) at 53°C (purge gas flow rate 550 ml/min)
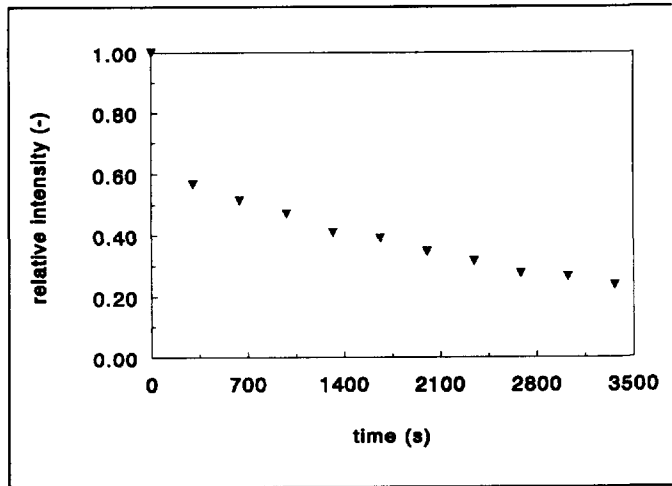
Figure 14   Desorption of neopentane from a silicalite single crystal (40 μm thickness) at 27°C (purge gas flow rate 780 ml/min)

6.4.2 Modelling of Desorption from a Silicalite Single Crystal

In all desorption experiments measurements are performed along the b-direction. As opposed to the adsorption experiments, where equation (1) holds, the sorbate concentration varies over the crystal, leading to:

$$\log \frac{I}{I_0} = -\varepsilon \cdot \frac{1}{L} \int_0^L q(x) \, dx \qquad (2)$$

with L the crystal thickness (m), and q (formerly c_a) the sorbate concentration (mol/m³). Provided that the absorbance does not change as a function of the concentration, the average sorbate concentration is obtained.

Considering pure intracrystalline diffusion, the desorption data may be evaluated from the appropriate solution of Fick's second law of diffusion. Cranck has provided various solutions in which different boundary conditions for the surrounding gas phase (step, exponential, or linear) have been imposed.[47] For the here applied silicalite cubes, the

desorption process is expected to proceed predominantly in the b-direction, because the crystal dimensions in the a and c-direction are substantially larger. The equation for a slab is then appropriate (step change to effectively zero concentration):

$$\frac{q(t)}{q(0)} = \frac{8}{\pi^2} \sum_{n=0}^{\infty} \frac{1}{(2n+1)^2} \cdot \exp \left[\frac{-D \cdot (2n+1)^2 \cdot \pi^2 \cdot t}{L^2} \right] \tag{3}$$

with q(0) the initial sorbate concentration (mol/m^3), D the apparent diffusivity (m^2/s), and t the time after switching to a pure nitrogen flow (s). The corrected (or intrinsic) diffusivity D_0 is related to D according to:

$$D = D_0 \cdot \frac{d \ln p}{d \ln q} \tag{4}$$

with p the gas phase pressure (Pa) in equilibrium with the sorbate concentration (q). Equation (4) resembles the familiar Darken equation,[48] which has been derived for the interdiffusion of two alloys. Within the Henry region the Darken factor (d ln p/d ln q) equals unity, but the factor strongly increases for sorbate concentrations near saturation. Equation (4) is therefore to be used in the present case, because of the high sorbate concentrations (adsorption near saturation conditions). When, on the other hand, larger (thicker in the b-direction) crystals are used, the diffusion may be studied within the Henry region.

It should be noted that the present expressions relate to a diffusion model in which the intrinsic diffusivity (D_0) is considered to be constant (independent on the sorbate concentration). In Chapter 7 (section 7.2.2) a concentration-dependent intrinsic diffusivity $D_0(q)$ has been used for the modelling of methane and n-butane permeation through MFI type membranes. In that case, however, available data on the self-diffusivity based on separately performed (pfg NMR) experiments have been correlated to the diffusion model. The desorption curves are poorly fitted by equations (3) and (4). The poor fit is mainly due to the fact that the decrease in concentration within the gas phase is not a step to an effectively zero concentration as assumed in the model. In Figure 15 the different situations are schematically shown. If the sorbate molecules are not sufficiently fast removed from the

gas phase within the flow-cell, the desorption process may even be fully controlled by the gas phase concentration (Figure 15a). The mobility of the sorbate molecules within the crystal is such that the sorbate concentration does not vary over the crystal. In fact, the adsorption isotherm may be obtained, provided the partial pressure within the flow cell is accurately known in time. The desired condition is represented in Figure 15c, in which the sorbate concentration in the outer rim of the crystal is in equilibrium with an effectively zero concentration in the gas phase.
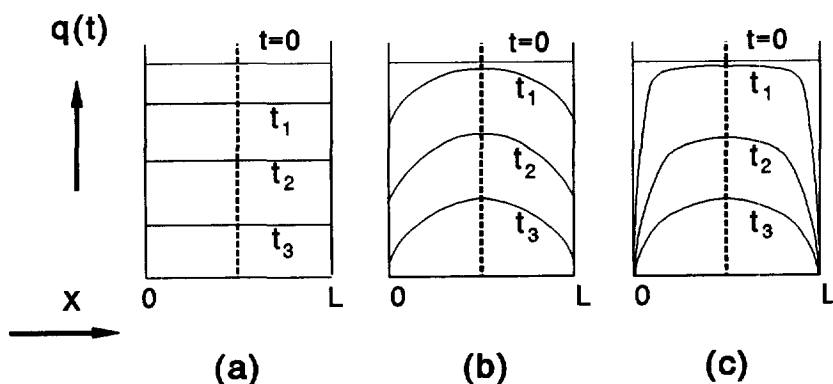
Figure 15   Schematic view of the desorption process governed by (a) the partial pressure decrease in the gas phase, (b) intracrystalline diffusion and the gas phase partial pressure decrease, and (c) intracrystalline diffusion

From the above considerations the desorption model has been revised by introducing a step to a non-zero sorbate concentration, and an exponentially decreasing gas phase concentration. The 'fit' with the desorption data remains, however, unsatisfactory. For 1-butene and n-butane (Figure 13), it is expected that the desorption is fully determined by the gas phase concentration around the crystal according to Figure 15a, and only minimum diffusivities are found (of the order 10^{-11} m^2/s at room temperature). Some diffusivity data on n-butane in MFI (either intrinsic (D_0), or self-diffusivities (D_s)) may be compared: pfg NMR in the order of 10^{-9} m^2/s (extrapolated self-diffusivity),[6] frequency response technique

$8.7*10^{-11}$ m^2/s,[14] and membrane method $3.7*10^{-12}$ m^2/s (at 60°C).[19]

For isobutane the desorption process may be governed by both the gas phase concentration and intracrystalline diffusion (cf. Figure 15b), leading to a lower diffusivity (of the order 10^{-12} m^2/s). Only for neopentane the desorption data (Figure 14) lead to a reasonably accurate fit with the original diffusional model (D = $2*10^{-14}$ m^2/s). For comparison, the diffusivity of benzene and ethylbenzene in self-supported ZSM-5 wafers measured as mentioned previously by FTIR spectroscopy has been found to be of the order of 10^{-14} m^2/s).[26]

6.4.3 Tracer Exchange of Deuterated Species

Instead of transport diffusivities by uptake measurements, it is also possible to study the self-diffusivity based on the exchange of isotopically labelled species by FTIR-spectroscopy. The self-diffusivity (D_s) may be related to the amount of exchanged tracer molecules as a function of time ($\gamma(t)$), according to:[8]

$$\int_0^\infty [1 - \gamma(t)] \, dt = \frac{R^2}{15 \, D_s} \tag{5}$$

with R the equivalent sphere diameter of the zeolite crystal (m).

In the present case the use of perdeuterated species is possible, which is demonstrated in Figure 16 for the H$_2$O/D$_2$O exchange at 150°C in a large silicalite crystal, containing a few cracks (R = 222 µm).

From these experiments using equation (5) the self-diffusivity of water has been calculated to be of the order of 10^{-11} m^2/s. According to Caro et al.,[49] the self-diffusivity of water in silicalite/ZSM-5 samples at 23°C is of the order of 10^{-9} m^2/s (pfg NMR). It should be noted that apart from molecular diffusion of water, also a proton/deuteron exchange may take place, which is expected to be a much faster process. From the low value for D_s obtained in the present FTIR experiments, however, such an ion exchange process is not very likely. The large difference in self-diffusivity between tracer exchange uptake experiments and the pfg NMR technique again suggests the occurrence of transport resistances at the outer surface of the zeolite crystals.[9,10]
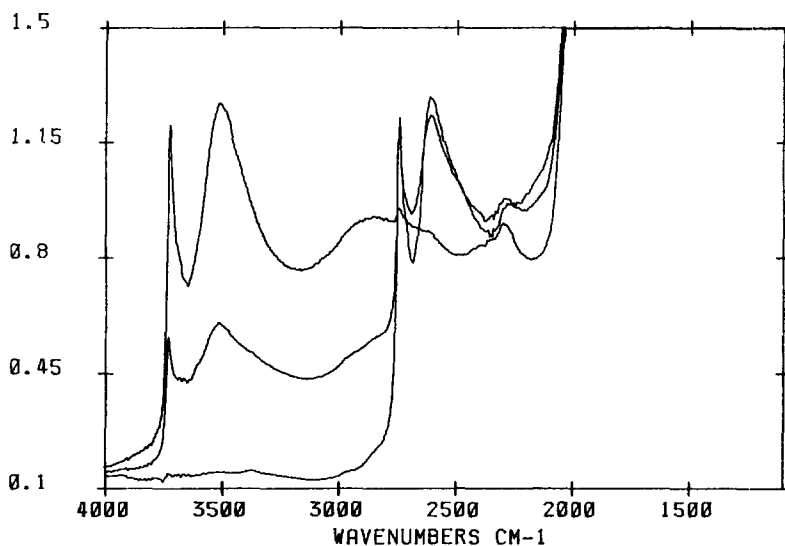
Figure 16   Three IR-spectra of a large silicalite crystal taken during the H_2O/D_2O tracer exchange at 150°C; the strong O-H absorption band at 3500 cm^{-1} disappears, while the O-D absorption band appears at ca. 2600 cm^{-1}

Self-diffusion experiments may also be performed using deuterated or perdeuterated hydrocarbons. In principle, only the disappearance of the aliphatic C-H absorption bands is essential to acquire data on the self-diffusivity of the adsorbed species. Based on the shift in position of the O-D absorbance in comparison with the O-H band it is, however, expected that the high-frequency aliphatic C-D stretching vibrations may be measured quantitatively as well.

A great advantage of the FTIR spectroscopy tracer exchange method as compared with the desorption (transport diffusivities) measurements is based on the boundary conditions that can be established more easily. As discussed in the previous section the relatively strong adsorption of hydrocarbons within the silicalite micropores gives rise to still high sorbate concentrations, although the partial pressure within the gas phase is even too low to be detected. With the tracer exchange measurements it suffices to change from the deuterated to the undeuterated species and vice versa, which does not involve any experimental

difficulty (except for being rather expensive experiments). It should further be noted that these experiments may be carried out in a range of sorbate concentrations, thus allowing the acquisition of concentration-dependent self-diffusivities.

6.4.4 Channel-Related Desorption of γ-Picoline

Based on the reported hysteresis loop in the p-xylene adsorption isotherm,[40,43,50] the presence of two different adsorption sites has been proposed within the MFI framework.[51] The first four p-xylene molecules are expected to adsorb on the intersections and/or in the straight channels. Only at a sufficiently high p-xylene partial pressure, the further adsorption of another four p-xylene molecules takes place, which may be considered as a nucleation process from the rapid increase in the sorbate concentration.[52] This is also in accordance with the temperature interval in which the hysteresis is observed (30-70°C), as at lower temperature the tendency for p-xylene to move into the sinusoidal channels seems to be no longer the limiting factor.

Based on the single crystal structure elucidation of a silicalite cube fully adsorbed with eight p-xylene molecules per unit cell, van Koningsveld et al. suggest that the diffusion process is controlled by the shape of the double ten-membered rings.[39] Above the monoclinic-to-orthorhombic phase transition at about 77°C[53,54] (cf. Chapter 4), the maximum adsorption capacity amounts to only four p-xylene molecules per unit cell,[40] in which case the sinusoidal channels are inaccessible to the p-xylene molecule (orthorhombic symmetry). For the straight channels, on the other hand, both symmetries provide sufficient space for p-xylene to enter and to migrate.

Still referring to the single crystal structure elucidation of p-xylene in MFI,[39] it has been noticed that there is a substantial larger number of sorbate-sorbent interactions of the aromatic ring with the double ten-membered ring of the sinusoidal channel as compared with the intersection. This suggests a slower diffusion process for desorption, once the sinusoidal channel sites of the MFI framework are filled with aromatic species. As to check the occurrence of different adsorption sites, the desorption of γ-picoline as a model-aromatic including a basic group has been studied. Selectively sealed crystals (cf. section 6.3.2) have been used, giving rise to effective transport through either exclusively the sinusoidal, or the straight channels.
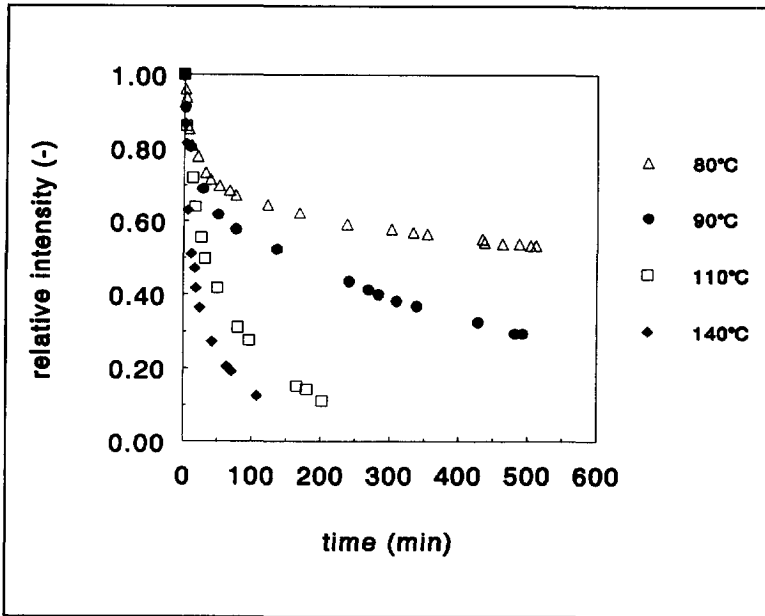
Figure 17a   Desorption isotherms of γ-picoline from an unsealed silicalite cube at different temperatures

Prior to the desorption from selectively sealed crystals, however, the desorption of unsealed silicalite cubes, fully loaded with γ-picoline, has been monitored using the absorption band at 3000 cm^{-1} (Figure 17a). The desorption of γ-picoline at moderate temperatures (80-140°C) is quite slow, but as compared to the crystals used in the experiments on hydrocarbons (*vide supra*), the silicalite crystal has a considerably larger b-axis (150x140x200 µm^3). An estimate of the diffusivity has been made from a solution of Fick's second law of diffusion (sphere), applicable only for long times:[55]

$$\frac{q(t)}{q(0)} = \frac{6}{\pi^2} \cdot \exp\left[- \frac{D \cdot \pi^2 \cdot t}{R_0^2} \right] \tag{6}$$

The curve fitting is demonstrated in Figure 17b for the desorption of γ-picoline at 90 and 110°C. The results for all desorption isotherms are presented in Table 3.
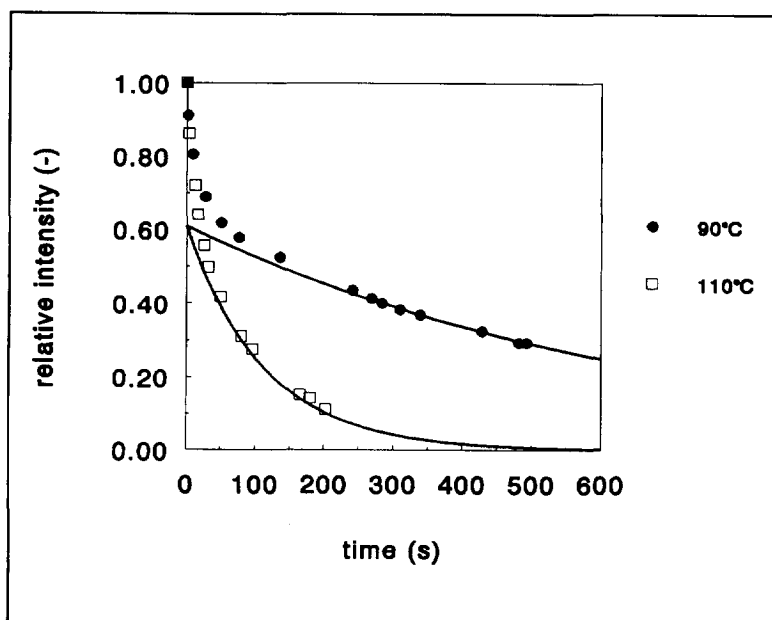
Figure 17b   Presentation of the desorption modelling of γ-picoline at 90 and 110°C, fitted for long times according to equation (6)

Table 3   Diffusion coefficients for γ-picoline in silicalite based on the desorption isotherms of Figure 17a, with $r_0 = 100$ μm (equation (6))

temperature (°C)	80	90	110	140
D (m²/s)	$5*10^{-15}$	$2.5*10^{-14}$	$1.5*10^{-13}$	$3.0*10^{-13}$

In Figure 18a and b the desorption of γ-picoline is compared for an unsealed and a sealed crystal, allowing transport in the b and a-direction, respectively. The simultaneous desorption from two equally large crystals (sealed versus unsealed) is thus demonstrated. At 90°C, the desorption through both sealed crystals is hindered as compared with the unsealed crystals. For the sinusoidal channels (a-direction), however, the hindrance is much

stronger than for the straight channels (b-direction). Only at 140°C a significant desorption of γ-picoline through the a-direction takes place. The difference between the two sealed crystals seems to be indicative for the adsorption strength of aromatics within the straight and sinusoidal channels of MFI.
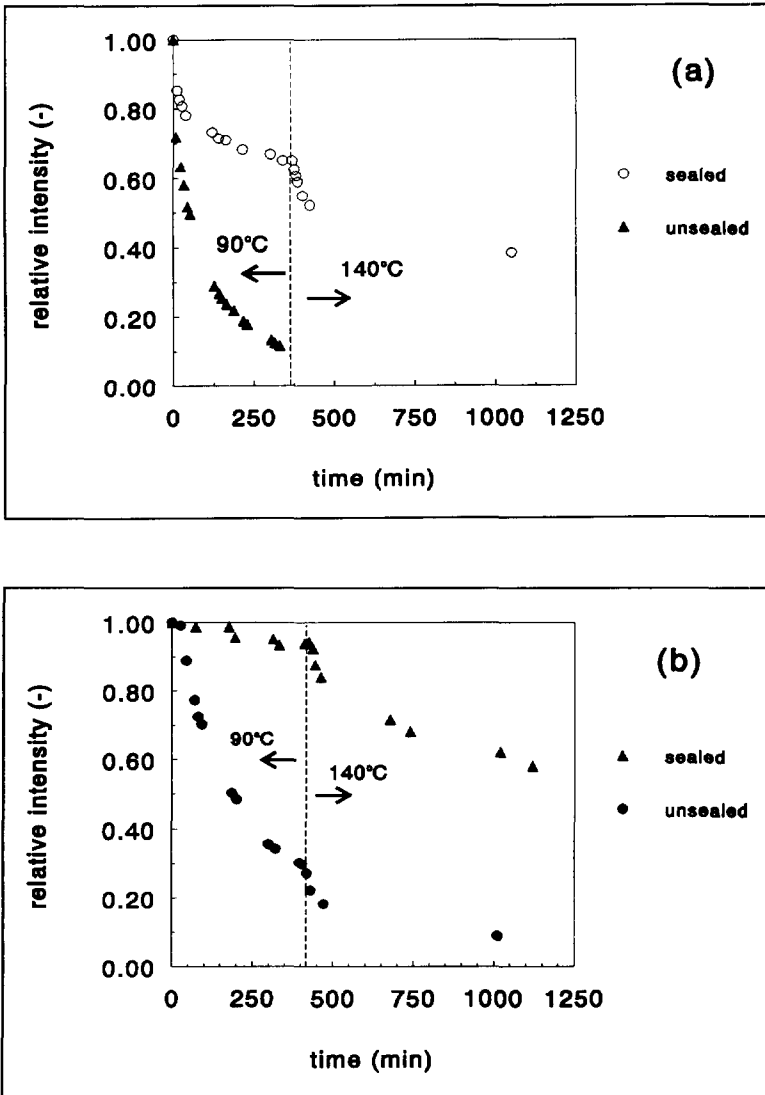
Figure 18   Desorption progress for γ-picoline from a sealed silicalite cube along (a) the b-direction (straight channels), and (b) the a-direction (sinusoidal channels)

Anisotropic diffusional behaviour has been clearly demonstrated for methane within aligned silicalite prisms, as the diffusion coefficient in the c-direction has been found to be notably smaller than that in the a- and b-direction.[56] In that case the anisotropy is, however, expected to be related to the tortuosity of the framework in the c-direction.[57] In the present case for the aromatics in MFI, the anisotropy is related mainly to the difference in adsorption strength for different adsorption sites, leading to a lower diffusivity in the sinusoidal channels.

6.5 Concluding Remarks

It has been shown that the physical processes within a zeolite single crystal can be studied in detail by microscope FTIR-spectroscopy (similarly to the chemical processes in Chapter 4). Adsorption and diffusion experiments are favourably performed on well-defined, crack-free zeolite single crystals, although care should be taken with the definition of single crystals (section 4.5). In many cases the source and/or pretreatment of the zeolite sample has been found to lead to unreliable and inconsistent results on diffusion.

As opposed to other techniques in which the changes in the surrounding gas phase or the weight of the sample are monitored, the measurements are directly related to the processes occurring within the zeolite phase. Despite the fact that quite accurate data can be obtained, calibration of the method with respect to the sorbate concentration and adsorption capacity is required. Furthermore, the technique is limited to flat-shaped crystals and a rather narrow region of crystal sizes, mainly affecting the working area for diffusion (r^2/D). Thus far, it seems that only relatively slow systems ($D < 10^{-14}$ m^2/s) can be studied by the present technique.

Nevertheless, the FTIR-spectroscopic technique offers some new procedures to measure . intracrystalline diffusion. First, the sealing of one or more crystal faces to confine the adsorption/diffusion processes seems to be an excellent tool to study diffusional anisotropy, and may compete with membrane permeation experiments on oriented zeolite single

crystals. When properly calibrated, the sorbate concentration within the crystal can be measured directly, as opposed to the assumed boundary conditions for the sorbate concentration on either side of the zeolite membrane (cf. Chapter 7). With both techniques, however, relatively simple diffusional models can be applied, and some variation of the crystal shape and size is allowed. Furthermore, the tracer exchange experiments enable one to compare the self-diffusivities (tracer exchange) and the transport (uptake) diffusivities. Finally, it is possible to study diffusion of multicomponent systems, which has, in fact, already been performed by the use of a purge gas (nitrogen or helium). These permanent gases are, however, not strongly adsorbed within the silicalite micropores. With other gases (e.g. carbon dioxide, sulfur hexafluoride), or by preadsorption of other sorbate molecules, it is possible to improve the knowledge on counterdiffusion.

Further improvement of, in particular, the diffusional part of the technique may be achieved by optimizing the design of the flow-cell. Secondly, the frequency with which spectra can be taken, and thus the time interval required to collect the data for each spectrum, now being of the order of seconds, may be shortened substantially.

6.6 Literature

1. R.M. Barrer, *Zeolites and Clay Minerals as Sorbents and Molecular Sieves*, Academic Press, London, 1978.
2. D.M. Ruthven, *Principles of Adsorption and Adsorption Processes*, Wiley-Interscience, New York, 1984.
3. M.F.M. Post, in: *Introduction to Zeolite Science and Practice*, H. van Bekkum, E.M. Flanigen, and J.C. Jansen (Eds), Stud.Surf.Sci.Catal. Vol. 58, Elsevier, Amsterdam, 1991, 391.
4. J. Kärger, and D.M. Ruthven, *J.Chem.Soc. Faraday Trans.*, 77 (1981) 1485.
5. J. Kärger, and D.M. Ruthven, *Zeolites*, 9 (1989) 267.
6. J. Caro, M. Bülow, W. Schirmer, J. Kärger, W. Heink, H. Pfeifer, and S.P. Zdanov, *J.Chem.Soc. Faraday Trans.*, 81 (1985) 2541.
7. J. Kärger, H. Pfeifer, D. Freude, J. Caro, M. Bülow, and G. Ohlmann, in: *Proc. 7th IZC Tokyo*, Y. Murakami, A. Iijima, J.W. Ward (Eds), Elsevier, Amsterdam, 1987, 633.
8. C. Förste, J. Kärger, and H. Pfeifer, in: *Zeolites: Facts, Figures, Future*, P.A. Jacobs, and R.A. van Santen (Eds), Stud.Surf.Sci.Catal. Vol. 49, Elsevier, Amsterdam, 1989,

907.

9. J. Kärger, H. Pfeifer, and W. Heink, in: *Proc. 6th Int.Zeol.Conf.*, D. Olson, and A. Bisio (Eds), Butterworths, London, 1984, 184.

10. J. Kärger, and H. Pfeifer, *Zeolites*, 7 (1987) 90.

11. Y. Yasuda, *J.Phys.Chem.*, 86 (1982) 1913.

12. N.G. van-den-Begin, and L.V.C. Rees, in: *Zeolites: Facts, Figures, Future*, P.A. Jacobs, and R.A. van Santen (Eds), Stud.Surf.Sci.Catal. Vol. 49, Elsevier, Amsterdam, 1989, 915.

13. D. Shen, L.V.C. Rees, J. Caro, M. Bülow, B. Zibrowius, and H. Jobic, *J.Chem.Soc. Faraday Trans.*, 86 (1990) 3943.

14. D. Shen, and L.V.C. Rees, *Zeolites*, 11 (1991) 684.

15. M. Eic, and D.M. Ruthven, *Zeolites*, 8 (1988) 40.

16. M. Eic, and D.M. Ruthven, in: *Zeolites: Facts, Figures, Future*, P.A. Jacobs, and R.A. van Santen (Eds), Stud.Surf.Sci.Catal. Vol. 49, Elsevier, Amsterdam, 1989, 897.

17. D.M. Ruthven, M. Eic, and Z. Xu, in: *Catalysis and Adsorption by Zeolites*, G. Öhlmann, H. Pfeifer, and R. Fricke (Eds), Stud.Surf.Sci.Catal. Vol. 65, Elsevier, Amsterdam, 1991, 233.

18. D.M. Ruthven, M. Eic, and E. Richard, *Zeolites*, 11 (1991) 647.

19. (a) A.R. Paravar, and D.T. Hayhurst, in: *Proc. 6th Int.Zeol.Conf.*, D. Olson, and A. Bisio (Eds), Butterworths, London, 1984, 217; (b) D.T. Hayhurst, and A.R. Paravar, *Zeolites*, 8 (1988) 27.

20. D.L. Wernick, E.J. Osterhuber, in: *Proc. 6th Int.Zeol.Conf.*, D. Olson, and A. Bisio (Eds), Butterworths, London, 1984, 122.

21. M.F.M. Post, J. van Amstel, and H.W. Kouwenhoven, in: *Proc. 6th Int.Zeol.Conf.*, D. Olson, and A. Bisio (Eds), Butterworths, London, 1984, 517.

22. J. Wei, *J.Catal.*, 76 (1982) 433.

23. E.R. Geus, J.C. Jansen, and H. van Bekkum, in: *Zeolites for the Nineties*, J.C. Jansen, L. Moscou, and M.F.M. Post (Eds.), Recent Research Reports 8th Int.Zeol.Conf., 1989, 293.

24. G. Mirth, and J.A. Lercher, *J.Catal.*, 132 (1991) 244.

25. M. Nowotny, J.A. Lercher, and H. Kessler, *Zeolites*, 11 (1991) 454.

26. H.G. Karge, and W. Niessen, *Catal. Today*, 8 (1991) 451.

27. A. Tiselius, *Z.phys.Chem.*, A169 (1934) 425.

28. A. Tiselius, *Z.phys.Chem.*, A174 (1935) 401.

29. G. Zachmann, Bruker Spectrospin, Germany, private communication, August 1991.

30. K. Nakanishi, *Infrared Absorption Spectroscopy*, Holden-Day, Inc., San Francisco, Nankodo Company Ltd., Tokyo, 1962, 17.

31. J.C.M. Muller, and E.R. Geus, unpublished results, July 1992.

32. D.W. Breck, *Zeolite Molecular Sieves; Structure, Chemistry, and Use*, Wiley-Interscience, New York, 1974, 636.

33. E.M. Flanigen, J.M. Bennett, R.W. Grose, J.P. Cohen, R.L. Patton, R.M. Kirchner, and J.V. Smith, *Nature*, 271 (1978) 512.

34. R.M. Dessau, in: *Adsorption and Ion Exchange with Synthetic Zeolites, Principles and*

Practice, W.H. Flank (Ed.), ACS, Washington, D.C., 1980, 123.

35. G. Mirth, J.A. Lercher, M.W. Anderson, and J. Klinowski, *J.Chem.Soc. Faraday Trans.*, 86 (1990) 3039.
36. R.E. Richards, and L.V.C. Rees, *Langmuir*, 3 (1987) 335.
37. W.J.W. Bakker, G. Zheng, F. Kapteijn, M. Makkee, J.A. Moulijn, E.R. Geus, and H. van Bekkum, in: *Precision Process Technology: Perspectives for Pollution Prevention*, M.P.C. Weijnen, and A.A.H. Drinkenburg (Eds), Kluwer Academic Publ., Dordrecht, The Netherlands, 425-436.
38. P.A. Jacobs, H.K. Beyer, and J. Valyon, *Zeolites*, 1 (1981) 161.
39. H. van Koningsveld, F. Tuinstra, J.C. Jansen, and H. van Bekkum, *Acta Cryst.*, B45 (1989) 423.
40. D.H. Olson, G.T. Kokotailo, S.L. Lawton, and W.M. Meier, *J.Phys.Chem.*, 85 (1981) 2238.
41. H. Thamm, *J.Phys.Chem.*, 91 (1987) 8.
42. D.B. Shah, D.T. Hayhurst, G. Evanina, and C.J. Guo, *AIChE J.*, 34 (1988) 1713.
43. R.E. Richards, and L.V.C. Rees, *Zeolites*, 8 (1988) 35.
44. C.G. Pope, *J.Phys.Chem.*, 90 (1986) 835.
45. M. Avram, and G.D. Mateescu, *Infrared Spectroscopy; Applications in Organic Chemistry*, Wiley-Interscience, New York, 1972, 235.
46. R.T. Conley, *Infrared Spectroscopy*, Allyn and Bacon, Inc., Boston, 1966, 149.
47. J. Cranck, *Mathematics of Diffusion*, Clarendon Press, Oxford, 1975.
48. L.S. Darken, *Trans. AIME*, 175 (1948) 184.
49. J. Caro, S. Hdcevar, J. Kärger, and L. Riekert, *Zeolites*, 6 (1986) 213.
50. K. Beschmann, G.T. Kokotailo, and L. Riekert, *Chem.Eng.Process.*, 22 (1987) 223.
51. P.T. Reischman, K.D. Schmitt, and D.H. Olson, *J.Phys.Chem.*, 92 (1988) 5165.
52. R.M. Barrer, private communication, January 1990.
53. D.G. Hay, H. Jäger, and G.W. West, *J.Phys.Chem.*, 89 (1985) 1070.
54. H. van Koningsveld, J.C. Jansen, and H. van Bekkum, *Zeolites*, 7 (1987) 564.
55. R.M. Barrer, in: *Zeolite Science and Technology*, F. Ramoa Ribeiro, A.E. Rodrigues, L.D. Rollmann, and C. Naccache (Eds), Martinus Nijhoff Publishers, 1984, 263.
56. U. Hong, J. Kärger, R. Kramer, H. Pfeifer, G. Seiffert, U. Müller, K.K. Unger, H.B. Lück, and T. Ito, *Zeolites*, 11 (1991) 816.
57. J. Kärger, and H. Pfeifer, in *Proc. 9th Int.Zeol.Conf.*, J.B. Higgins, R. von Ballmoos, and M.M.J. Treacy (Eds), Butterworth-Heinemann, 1993, in press.

7. Permeation through MFI-Type Membranes[1]

The permeation through MFI-type membranes is dealt with both theoretically and experimentally using silicalite single crystal membranes and supported, in situ grown MFI-type layers. A step-wise permeation model, involving adsorption onto the outer zeolite surface, transfer to the zeolite adsorption sites, intracrystalline diffusion, and desorption from the micropores of the zeolite to the gas phase, is proposed, partly in view of the difference between uptake (transport) and pfg NMR (intracrystalline) self-diffusivities. The permeation through some prototype membranes is discussed, as to demonstrate the constraints of a reliable study of the permeation through zeolite membranes. The stainless steel supported MFI layers within a high-temperature module (Chapter 3) reveal typical cryogenic permeation behaviour at room temperature, which is demonstrated by weakly (methane and neon) and strongly (n-butane and isobutane) adsorbed probe molecules. Permeation experiments up to 350°C have been performed, from which it is concluded that the MFI/stainless steel membranes remain uncracked upon use at high temperatures. The highest selectivities are, however, observed at low temperatures. It is exemplified by methane/butane binary mixtures that the adsorption strength rather than the individual diffusivities governs the selectivity.

7.1 Introduction

The interest in permeation through zeolite membranes is characterized by (i) the desire to obtain accurate data on intracrystalline diffusion through zeolites (for instance, in order to improve the understanding of their catalytic action), and (ii) the assessment of the separative potential of this new type of membrane for industrial applications. The first measurements on zeolite membranes were reported by two different groups on the 6th International Conference on Zeolites in 1983. Each study was devoted to one of the above goals. Paravar and Hayhurst[1] studied the transient permeation through a twinned silicalite crystal, oriented in the c-direction to obtain the intrinsic diffusivity according to the time lag method. Wernick and Osterhuber performed steady-state measurements on a NaX single crystal to investigate the separative potential.[2] Considering each purpose, however, one might argue that it would have been more appropriate when the research groups had exchanged their membranes, since well-defined membranes are essential for reliable diffusivity data, whereas a zeolite membrane based on single crystals is not a prerequisite for industrial membranes. For long these early studies remained the only published results in the field,[3,4] although some theoretical studies on the permeation through zeolite membranes were recently published by Barrer.[5,6]

This chapter serves to describe the characterization of the various membrane systems as described in Chapter 2 and 3 by means of permeation experiments. The first purpose is, however, to demonstrate that true zeolite membranes have been prepared. It has been argued thus far that the successful preparation of a zeolite membrane can only be proven by the molecular sieving effect.[1,3] There are, however, other properties of zeolite membranes that may, perhaps not as definite as for the true molecular sieve effect, demonstrate their microporous nature. Such properties may be equally desirable for industrial applications, and involve a difference in affinity for adsorption within the micropores (e.g. hydrophilic/hydrophobic framework),[7] or shape selectivity in general, which is reflected in the difference in mobility of the adsorbed species. In addition, the well-known cryogenic

effects of mesoporous membranes[8,9] as a result of enhanced transport of heavier molecules via surface diffusion,[10-12] or the reduced flow of highly mobile species in the presence of larger and more strongly adsorbed molecules by capillary condensation[13] may well serve to demonstrate the successful preparation of a zeolite membrane.

The permeation through microporous materials is first discussed in a qualitative way. Next, a mathematical model for intracrystalline diffusion is proposed to which the experimentally observed flow rates have been compared. The different experimental set-ups are briefly discussed. In view of the permeation through so-called 'prototype' membranes, the detrimental effect of cracked zeolite crystals[14] and other larger pores within the membrane layer[15] is discussed. Furthermore, the moderating effect of low-porosity supports (clay-supported MFI layer; Chapter 3) on the membrane performance is demonstrated.[16,17] Finally, the performance of stainless steel-supported, continuous MFI layers within high-temperature membrane modules is presented.[18,19]

7.2 Theoretical Model for Flow

7.2.1 Description of Permeation by Separate Steps

In the description of a steady molecular flow through a zeolite membrane with a gaseous feed and permeate several consecutively occurring processes are to be considered:

1) Adsorption from the gas phase onto the external zeolite surface
2) Entry into the zeolite micropores
3) Intracrystalline transport through the micropores
4) Exit from the zeolite micropores to the external zeolite surface
5) Desorption from the external adsorbate phase to the gas phase

A schematic representation of the model is given in Figure 1, in which each step may contribute to the (single component) permeation rate. It should be emphasized that only the

steps directly involved with sorption and diffusion within the zeolite micropores are taken into account, assuming that no other barriers (e.g. macroporous support) are present (cf. section 7.2.2).
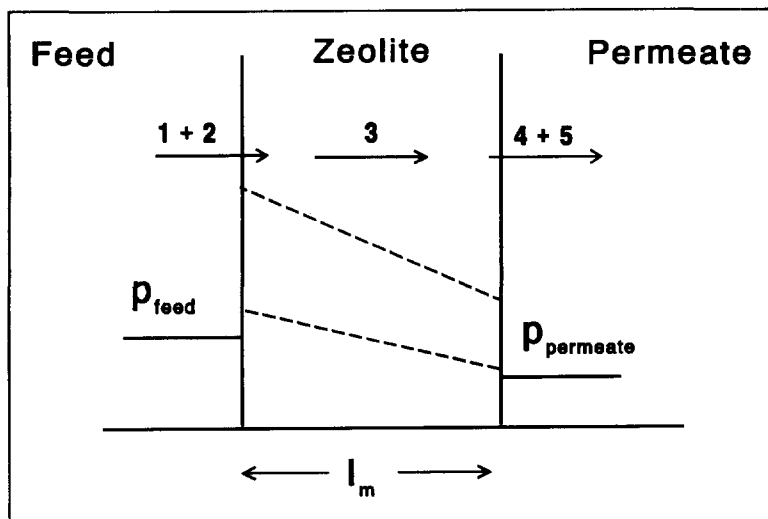
Figure 1   Schematic view of the permeation through a zeolite membrane; the two dashed lines refer to species of different adsorption strengths (cf. text for steps)

The presence of an externally adsorbed layer is expected to depend upon the nature of the sorbate molecule and the conditions (pressure, temperature) under which permeation takes place. Weakly adsorbed species may pass directly from the gas phase to the intracrystalline adsorption sites, provided the window of the zeolite pore is sufficiently wide.[5]

In this respect the reported higher intracrystalline (microscopic, pfg NMR) diffusivities as compared with the transport (macroscopic, uptake) diffusivities may be considered (cf. Chapter 6).[20,21] The basic difference is that the microscopic techniques, in which self-diffusivities are measured, only account for the mobility of molecules within the zeolite framework (except for tracer exchange techniques), whereas in macroscopic measurements the extracrystalline sorption processes into or out of the zeolite micropores are involved as

well, and are therefore referred to as apparent diffusivities. Kärger et al.[22] have argued that according to the Darken equation[23] (cf. Chapter 6), the self-diffusivity is lower than or equal to the apparent diffusivity, which may be rationalized from the absence of a concentration gradient as a driving force in the self-diffusion experiments.

Obviously, the contribution of extracrystalline processes of whatever nature to the uptake rate can be reduced by increasing the crystal size. For methane in Chabazite (CHA) Kärger and Caro have demonstrated the contribution of the extracrystalline processes,[24] thus showing that the self-diffusivity is independent of the crystal size, whereas the apparent diffusivity increases with larger crystal sizes. From a comparison of different systems in an extensive review on intracrystalline diffusion, Kärger and Ruthven[21] have noted that good agreement generally exists when the intracrystalline mobility is relatively low. Nevertheless, they consider several other explanations for the observed discrepancy (e.g. boundary conditions in the uptake measurement, origin of the sample, surface barriers, *vide infra*). Their conclusion that as yet no conclusive evidence has been generated for the observed discrepancies is shared by Post in another recent review.[25]

Although some doubt has been raised on the contribution of extracrystalline processes to the uptake rate, there is no obvious reason to object to the step-wise permeation model of Figure 1. Based on heats of desorption and activation energies for intracrystalline diffusion according to Kärger et al.,[22] Barrer has suggested that molecules leaving the crystal experience an evaporation barrier.[26] The occurrence of surface resistances surrounding the crystals has also been considered to have a moderating effect on the uptake process, and has been demonstrated for the diffusion of ethane into CaNaA zeolite.[27] However, the occurrence of an evaporation barrier has been put under some doubt by Kärger.[28]

Barrer has evaluated the above step-wise permeation model by the concept of activated transport,[5,6] which was earlier suggested for the mass transfer resistance at the surface of zeolite crystals in general.[29] This is visualized in Figure 2, in which the concept of an evaporation barrier is directly related to the adsorption enthalpy (ΔH_{vap}) and the activation energy for intracrystalline diffusion (E_1) as mentioned above. Furthermore, an external adsorbate layer has been introduced on either side of the membrane, owing to which the

sorption processes may take place in two steps. The adsorption on the feed side is thus governed by the activation energy E_s for the transfer from the external adsorbate phase to the first intracrystalline adsorption site, and even some surface barrier (E_s^*) may be included.[29] The adsorption energy onto the external zeolite surface (ΔE_s) may also be considered an adsorption enthalpy (ΔH_s). For desorption from the micropores to the external sorbate phase a much higher activation energy (E_d) applies, but owing to the external adsorbate layer, the activation energy is assumed to be lower than the evaporation enthalpy (ΔH_{vap}).[6]
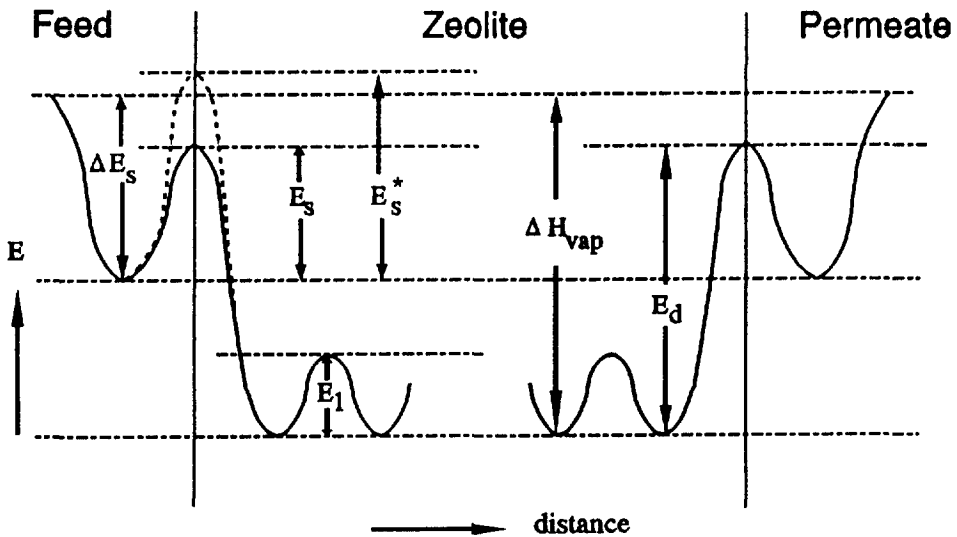
Figure 2   Energy-distance curves according to the step-wise permeation through a zeolite membrane, with E_1 the activation energy for intracrystalline diffusion, ΔH_{vap} the evaporation enthalpy, E_s the activation energy for adsorption into the zeolite micropores, E_{s^*} the activation energy for a surface barrier present, and E_d the activation energy of desorption[5,29]

7.2.2 Permeation through Zeolite Membranes: Mathematical Approach

In the previous section only steady-state flow through a zeolite membrane has been considered. Membrane characterization by permeation experiments can, however, be

performed under steady-state or under transient conditions. The transient experiments may be favourably used for new types of membrane, as it may reveal typical aspects of the permeation behaviour. Therefore, the discussion is started for single component transient experiments.

Transient Permeation

For relatively thick zeolite layers (100 μm) and at room temperature, sorption into and out of the zeolite micropore system may be considered to be fast as compared to intracrystalline diffusion.[6] Consequently, thermodynamical equilibrium exists on either side of the membrane. Fick's second law of diffusion applies:

$$\frac{\partial q}{\partial t} = D \frac{\partial^2 q}{\partial x^2} \tag{1}$$

with q the sorbate concentration (mol/m^3), t the time (s), D the apparent intracrystalline diffusivity (m^2/s), and x the distance in the zeolite layer (m).

Equation (1) has been analytically solved for flow through a microporous membrane by Barrer.[30] The cumulative number of molecules flowing through a membrane surface area A_m into a permeate volume V_p can be calculated from the appropriate solution (q(x,t)) of equation (1):

$$N_t = - \int_0^t D \cdot A_m \cdot \left(\frac{\partial q}{\partial x}\right)_{x=l_m} dt \tag{2}$$

with l_m the layer thickness (m).

According to the ideal gas law, N_t is equal to the permeate pressure increase actually measured. Upon linearization of equation (2), the time lag can be defined as $t_l = l_m^2/6.D$, from which D can be calculated. Provided adsorption takes place within Henry's region, the apparent diffusivity obtained via the time lag procedure is equal to the intrinsic diffusivity D_0 (cf. section 6.4.2). This is a well-accepted procedure for (organic) polymer membranes,[31] and has also been applied on one crystal in a membrane configuration at low

feed pressures.[1,3] The pressure increase on the permeate side should be small to maintain a constant driving force, and long times are required for accurate measurement of the time lag ($> 10*t_l$). The time lag is supposed to be independent of the applied feed pressure. The occurrence of a time lag in transient experiments is, however, not exclusively based on diffusion. As the sorbate concentration within the zeolite micropores is higher for more strongly adsorbed species under similar conditions, the linearized, quasi-steady-state flow is related to the time to reach the quasi-steady-state. Thus, the time lag procedure provides only a rough estimate of the diffusivity, even when the above prerequisites are met. Instead of the time lag method it is possible to relate the delay time to reach the steady-state to the pore filling of the membrane, based on the observed steady-state permeation rate.[19]

The diffusivity may also be directly calculated from the quasi-steady-state pressure increase, provided the adsorption characteristics of the membrane material are known from independent measurements.[16] For sorption within Henry's region, Fick's first law of diffusion applies to define the quasi-steady-state permeate flow:

$$\phi_{mol}^{s-s} = D^{s-s} \cdot K \cdot \frac{A_m}{l_m} \cdot \Delta p \tag{3}$$

with D^{s-s} the quasi-steady-state diffusivity (m^2/s) and K the Henry coefficient ($mol/m^3.Pa$). Only within Henry's region, however, D^{s-s} may be compared with the (concentration-independent) intrinsic diffusivity D_0.

Steady-State Permeation

Equation (3) also holds for steady-state permeation, and shows that the maximum driving force for single component flow through a zeolite membrane is given by $K*\Delta p$. The earlier mentioned extracrystalline surface effects can be visualized according to Figure 3, in which the equilibrium and steady-state sorbate concentrations are schematically indicated, together with the fluxes due to adsorption and desorption. The permeation process gives rise to a reduced driving force for intracrystalline diffusion. As there is no equilibrium, the adsorption and desorption rates on each side of the membrane are not equal, and the true driving force for permeation is lower than defined under equilibrium conditions.
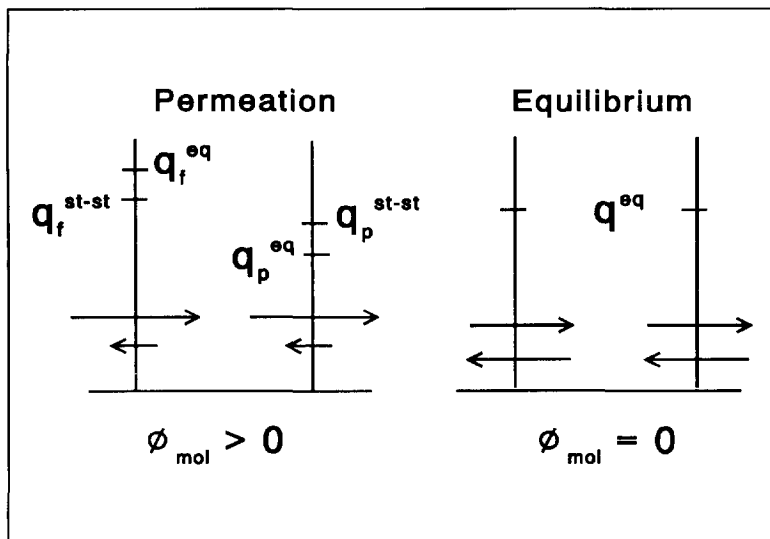
Figure 3   Schematic view of the concentration profile during (quasi)-steady-state permeation and under thermodynamical equilibrium

A convenient way to define the (quasi)-steady-state permeation rate through a membrane is to use the permeability. Similar to polymer membranes, the permeability is defined as P = D*K.[12] The Henry coefficient (K) can be considered as the enrichment factor within the zeolite phase, similar to the solubility with polymer membranes. For very weakly adsorbed species (helium and hydrogen) or at very high temperature, the adsorbate concentration equals the gas phase concentration, thus K = 1/RT.

Outside Henry's region, the diffusivity cannot be considered to be constant, and it is more appropriate to take the gradient of the chemical potential ($\partial\mu/\partial x$) into account, which is the true driving force for permeation. The apparent or Fickian diffusivity D(q) is related to the intrinsic diffusivity $D_0(q)$ via a Darken type equation:[25]

$$D(q) = D_0(q) \cdot \frac{d \ln p}{d \ln q} \tag{4}$$

In contrast to section 6.4.2 the intrinsic diffusivity is here considered to be dependent of the sorbate concentration within the zeolite micropores (*vide infra*).

173

The factor (d ln p/d ln q), generally referred to as the Darken factor, can be directly obtained from the adsorption isotherm. The Fickian diffusivity strongly depends on the Darken factor, which is related to the adsorption model chosen. Generally the Langmuir adsorption model is applied, in which case the Darken factor equals $1/(1-\theta)$, with θ the relative surface coverage.

From Fick's first law of diffusion, still assuming that the adsorption to and the desorption from the zeolite micropores proceed relatively fast as compared to intracrystalline diffusion, the permeation through the zeolite membrane may be calculated from:[17]

$$\phi_{mol} = - A_m \cdot D(q) \cdot \frac{\partial q(x)}{\partial x} \tag{5}$$

In order to evaluate the permeation outside Henry's region, the concentration dependence of $D(q)$ must be known. The self-diffusivity data from the pfg NMR technique may serve to formulate a concentration-dependent intracrystalline diffusivity. This is, however, only true if the cross coefficients (as defined in irreversible thermodynamics) can be neglected.[25,32,33] It has been argued by Barrer[26] that for Langmuir's isotherm the decrease of the self-diffusivity $D_s(q)$ is proportional to the sorbate concentration, so $D_s(q=0)*(1-\theta)$. As for Langmuir's isotherm the Darken correction equals $1/(1-\theta)$, a constant apparent diffusivity would be expected. It was, nevertheless, established by the pfg NMR technique that for high sorbate concentrations (near saturation conditions) the decrease of $D_s(q)$ is overruled by the Darken factor.[34] From a theoretical point of view, however, Langmuir's adsorption isotherm is not valid under near saturation conditions: for instance, the constraint of a constant adsorption enthalpy is not met.

Based on self-diffusivity data for methane, ethane, and propane in silicalite, Caro et al.[35] proposed a modified free volume theory, relating the molecular mean jump length ($<l^2>$) to $D_s(q)$:

$$D_s(q) = \frac{<l^2>}{6 \cdot \tau} = A \cdot v_f^{2/3} \cdot \Gamma(\frac{5}{3}, \frac{B}{v_f}) \tag{6}$$

in which τ is the mean residence time between two succeeding jumps (s), A and B are

constants, v_f is the mean free volume (m^3), and Γ denotes the incomplete gamma function. Since for near zero sorbate concentrations very large values for $D_s(q)$ are calculated, a modified model has been derived, only taking the first term of the Taylor development of the incomplete gamma function into account:[17]

$$D_s(q) = D_{s,0} \cdot \exp(-\frac{\gamma \cdot q}{q_c - q})$$

(7)

where the parameter $D_{s,0}$ may be referred to as the intrinsic self-diffusivity (m^2/s), and γ (-) and q_c (mol/m^3) are fit parameters, although related to the model in equation (6). This model approximates equation (6) for high sorbate concentrations, and has a linear dependence at low concentrations.

The permeation model for a steady-state flow through a zeolite layer may then be calculated:

$$\int_0^{l_m} \phi_{mol} \cdot dx = - A_m \int_{q_F}^{q_P} D_s(q) \cdot \frac{d \ln p}{d \ln q} \, dq$$

(8)

with q_F and q_P the sorbate concentrations (mol/m^3) on feed and permeate side, respectively. The theoretical concentration profile over the membrane can be calculated as well.

In Figure 4 the permeate flow for methane (adsorption within Henry's region) and n-butane (adsorption under near saturation conditions) have been calculated at room temperature as a function of the feed pressure. Up to high (1000 Pa) permeate pressures, the methane permeation remains linear with the feed pressure, in accordance with theory (linear concentration profile). For n-butane permeation, a strongly non-linear behaviour is shown with a maximal flow rate, which depends on the permeate pressure. The non-linear behaviour is attributed to the fact that the concentration profile over the zeolite layer is non-linear, and changes with the Darken factor according to Langmuir's isotherm. As has been pointed out earlier, the Langmuir adsorption model is in principle not valid for near saturation adsorption conditions. From the shape of most adsorption isotherms (type I, according to the Brunauer classification), on the other hand, it is not likely that other

adsorption models will lead to a very different thermodynamical correction (Darken factor) for diffusion. From these considerations the permeation model described by equation (8) has been used to relate the theoretical permeation rates of pure gases to the experimentally observed rates.
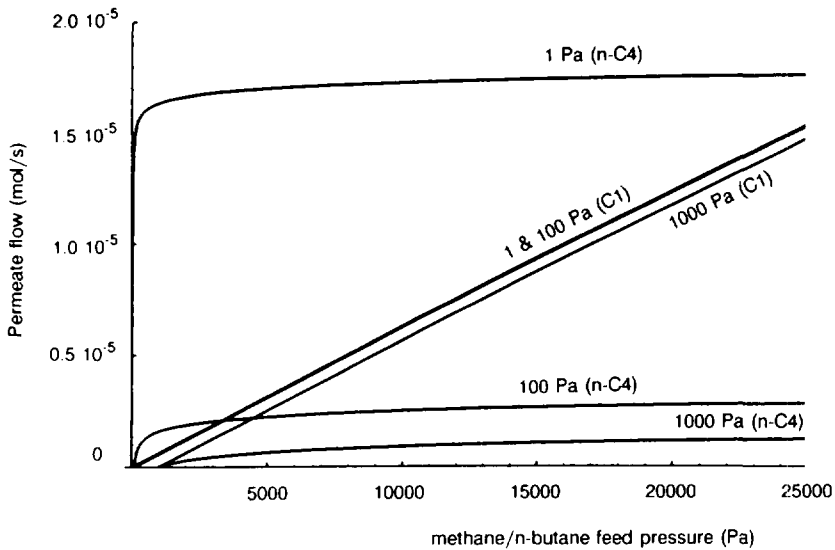
Figure 4   Theoretical single component flows for methane (C1) and n-butane (n-C4) as a function of the feed pressure for the different permeate pressures indicated in Figure (A_m=1.5 cm^2; l_m=50 μm)[17]

The presence of a *macroporous support* has not yet been taken into account. A porous support, attached to the membrane layer, introduces an additional resistance to mass flow. A second effect on the mass flow is due to the bonding of the zeolite layer to the porous support. When the zeolite/porous support interface is gas-tight, application of the zeolite layer onto the porous support will lead to many dead-end pores, which reduces the effective membrane surface area. The effect of the interface between the zeolite and the porous support may also be referred to as introducing a higher tortuosity factor for the combination of the zeolite layer and the interface with the porous substrate.

For the above effects, the location of the support phase, which can be on either the feed or

the permeate side, is not expected to lead to large differences. On the permeate side (low pressure) the flow regime may be changed from, for instance, molecular diffusion to Knudsen flow.[36-38] Figure 4 demonstrates, however, that for strongly adsorbed species the flow due to intracrystalline diffusion is reduced significantly for different permeate pressures at the same feed pressure. A support with a relatively low porosity on the permeate side will give rise to a higher permeate pressure near the zeolite surface, and, hence, the permeability may be lower than when the support is present on the feed side.

7.3 Permeation Equipment and Experiments on Prototype Membranes

7.3.1 Experimental Aspects

Preliminary permeation experiments have been performed on several prototype membranes (cf. section 7.3.2). These generally disk-shaped membranes are attached to larger perforated metal disks using a gas-tight epoxy resin (Araldite; Ciba-Geigy) as a sealant. In the membrane cell two Viton O-rings (Eriks, The Netherlands) are pressed on both sides of the metal disk. The installation into the membrane cell thus does not require the application of a high mechanical stress onto the membrane itself, and allows for testing in different permeation equipment. The membrane layer always faces the high pressure or feed side, unless stated otherwise.

Three different experimental set-ups have been used:

System I   Single component permeation (pressure difference as the driving force)

System II   Multicomponent permeation (pressure difference)

System III   Single and multicomponent permeation (concentration difference by applying helium as a carrier gas on either side of the membrane; Wicke-Kallenbach concept)[39,40]

Transient, single component experiments have been performed on permeation equipment (*System I*) in which the pressure increase on the permeate side is monitored for temperatures

up to 250°C (courtesy TNO Environmental and Energy Research, Zeist, The Netherlands). Prior to the experiments, the cell is evacuated to ca. 1 Pa, generally overnight. Measurements are performed by first evacuating to 1 to 5 Pa, and then raising the pressure on the feed side instantaneously to 1 to 4 bar. Both the quasi-steady-state permeation rate and the time lag are obtained. The measuring time depends on the pressure increase, and may be varied from 6 seconds to several minutes. Several high-purity gases (generally >99.9%) have been used as probe molecules (hydrogen, methane, nitrogen, oxygen, carbon dioxide, dichlorodifluoromethane (CFC-12), ethane, and n-butane).

Some steady-state experiments have been performed on permeation equipment in which again a pressure difference is applied over the membrane (*System II*; courtesy Shell Research, Amsterdam, The Netherlands). The pressure on the permeate side remains atmospheric (the air present is replaced by the permeate), and the feed pressure may be over 10 bar. Both permeate and feed are analyzed by gas chromatography. The permeate flow is measured by a flow meter.

Transient and steady-state experiments have been performed on permeation equipment in which either a pressure difference or a pure concentration difference can be applied over the membrane (*System III*; courtesy of the Department of Chemical Technology, Delft University, The Netherlands).[19] The experiments are generally performed according to the Wicke-Kallenbach concept (concentration gradient as the driving force),[39,40] with helium as a purge gas. Unless stated otherwise, gas flows of 100 ml (STP)/min are applied on either side of the membrane (total pressure 1 bar). For transient measurements, the concentration on the feed side is nearly step-wise raised by the introduction of a premixed gas flow, metered with mass flow controllers. The permeate side is continuously flushed with helium and analyzed by mass spectrometry (Leybold-Heraeus). High-purity gases have been applied in all experiments (Intermart: helium (99.996%), methane (99.5%), neon, n-butane, and isobutane (99.95%)).

7.3.2 Experiments on Prototype Membranes

Apart from the stainless steel supported MFI layers within the high-temperature membrane module, several other (prototype) membranes have been prepared and characterized. In this section some permeation experiments on (i) large silicalite single crystals embedded in

epoxy resin,[14] (ii) silicalite crystals on a macroporous support in a glaze matrix (cf. Chapter 2),[15] and (iii) in situ grown MFI layers on a clay support (Chapter 3) are discussed.[16,17] The presented results mainly serve to demonstrate pitfalls in the construction of and permeation through zeolite membranes.

Silicalite Single Crystals in Epoxy Resin

The permeability of large silicalite cubes, embedded in epoxy resin (Araldite), has been studied by transient, single component experiments (*System I*). A thin copper platelet (thickness 50 μm) is provided with 10 holes (diameter 150 μm). The mixed epoxy resin is carefully spread around each hole and the silicalite cubes (200x100x350 μm^3) are positioned on each hole. Thus, a zeolite membrane consisting of 10 silicalite single crystals, oriented in the b-direction, is prepared (membrane surface A_m=1.36*10^{-7} m^2). It should, however, be noted that all crystals are partly cracked, which can only be observed by light microscopy (cf. Chapter 4). After some experiments the membrane is inspected by light microscopy, revealing that two crystals are severely cracked and according to FTIR-spectroscopy contain some hydrocarbons. The membrane is repaired by covering these two cracked crystals with epoxy resin, and again permeation experiments are performed (A_m=1.10*10^{-7} m^2). In these experiments the permeate pressure never exceeds 100 Pa, except for hydrogen (< 250 Pa).

The results are shown in Table 1. After the initial repair a decrease in permeability of two orders of magnitude is observed; the earlier observed high flux is therefore attributed to the observed cracks within the two silicalite crystals. At 30°C (first series after repair) the permeability of n-butane is even higher than that of hydrogen. At a higher temperature (130°C) all permeabilities increase, except for n-butane, but after cooling to 30°C (second series) much higher flow rates are observed. It seems that further cracking occurs within the large silicalite crystals as a result of the imposed pressure difference over the membrane. For this reason only the data at 30°C of the first series after repair (8 crystals) are expected to be reliable. The theoretical permeabilities under similar conditions according to the earlier proposed model in equation (8) amount to 2*10^{-10} mol.m.m^{-2}.s^{-1}.Pa^{-1} for methane (higher than observed) and 6*10^{-12} mol.m.m^{-2}. s^{-1}.Pa^{-1} for n-butane (slightly lower than observed).

Table 1   Permeabilities for permanent gases and alkanes through silicalite-epoxy resin composites (Δp=1.6 bar)

Membrane	Permeability (10^{-12} mol.m.m^{-2}.s^{-1}.Pa^{-1})			
	10 crystals	8 crystals (after repair)		
Temperature (°C)	30	30	130	30
Gas				
H_2	690	9.5	23.4	43.0
N_2	240	4.6	5.8	13.4
O_2	330	-	5.7	12.0
CO_2	200	-	5.2	-
CH_4	320	3.7	8.2	18.2
C_2H_6	370	2.7	6.5	15.8
n-C_4H_{10}	420	14.5	5.6	-

Composite Membrane of Silicalite Crystals in a Glaze Matrix

The permeability of untreated clay supports, thick glaze layers (> 100 μm) on top of clay supports, and silicalite prisms, embedded in thin glaze layers on top of γ-alumina supports (cf. Chapter 2) has been measured on *System I* for some gases (hydrogen, nitrogen, methane, and CFC-12). The permeation through the glaze layer is mainly governed by Knudsen selectivity (H_2/CFC-12=6; theoretical ratio being 7.5 for pure Knudsen diffusion). In Figure 5 the results for methane permeation are plotted as a function of the applied pressure difference. Only small differences in permeability are observed for a glaze layer facing either the feed or the permeate side (Glaze1 versus Glaze2, respectively).

The methane permeability of the composite membrane (silicalite prisms within a dip-coated glaze layer) is lower than the above-mentioned theoretical value of $2*10^{-10}$ mol.m.m^{-2}.s^{-1}.Pa^{-1}, and slightly higher than the permeability of the large silicalite single crystals ($3.7*10^{-12}$ mol.m.m^{-2}.s^{-1}.Pa^{-1}; cf. Table 1). According to SEM some small pores are still

present within the glaze matrix. The permeability of a macro- or mesoporous support can thus be reduced substantially by a thin glaze layer. The permeability of the glaze matrix (for small alkanes and permanent gases) is over two orders of magnitude lower than that of silicalite.
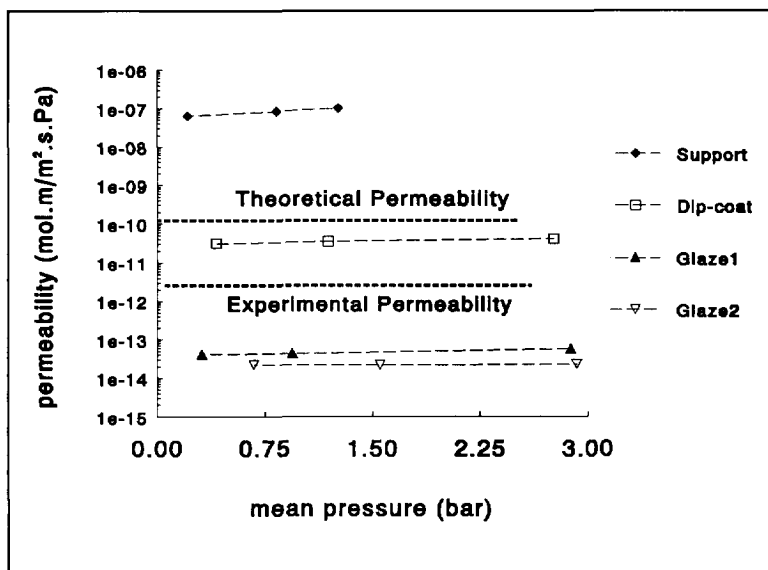
Figure 5 CH_4-permeability as a function of the mean pressure; comparison of untreated clay substrates (support), thick lead-boron silicate layers (glaze1 and glaze2) on clay (cf. text), and thin, dip-coated glaze layers with silicalite prisms (dip-coat); the theoretical (Figure 4) and observed (Table 1) permeability for silicalite are shown for comparison

It is emphasized that under similar conditions and within Henry's region the permeability may be considered as a material property. Therefore, the data presented in Figure 5 can be used to predict the flow rates through a composite membrane systems of silicalite crystals within a glaze layer, if the surface areas and average thicknesses of each phase are known. For sufficiently high silicalite crystal coverages the permeation will be governed mainly by the zeolite phase. The glaze material may also be used as a gas-tight sealant in general, but the surface area to be sealed should be minimized and thick layers have to be applied.

MFI Layers on Ceramic (Clay) Supports

The in situ grown MFI layers on clay supports (Chapter 3) have been studied by both single component and multicomponent permeation experiments. As-synthesized (template-containing) MFI layers are gas-tight for all gases. The single component permeation results measured at 21 and 145°C (as performed on *System I*) for an MFI/clay membrane calcined at 400°C are summarized in Table 2 (hydrogen, nitrogen, methane, carbon dioxide, and CFC-12). Significant and reproducible time lags are found at both temperatures for all gases, which vary slightly at different feed pressures. At 145°C all permeabilities are lower except that of hydrogen.

Table 2   Pure gas permeation results (*System I*) on an MFI/clay membrane

Gas	Permeability (P) (mol.m/m^2.s.Pa)	Time lag (t$_l$) (s)	Diffusivity D(TL) (m^2/s)	D^{s-s} (m^2/s)	Henry coef. (K) (mol/m^3.Pa)
Temp. = 21°C; Feed pressure = 2 bar; Initial permeate pressure = 2 Pa					
H$_2$	$8.2*10^{-12}$	0.4	$4.2*10^{-9}$	$2.0*10^{-8}$	0.0004
N$_2$	$2.7*10^{-12}$	11	$1.5*10^{-10}$	$4.0*10^{-10}$	0.0068
CH$_4$	$3.8*10^{-12}$	18	$9.3*10^{-11}$	$2.2*10^{-10}$	0.0174
CO$_2$	$3.2*10^{-12}$	60	$2.8*10^{-11}$	$5.0*10^{-11}$	0.0643
CF$_2$Cl$_2$	$9.0*10^{-13}$	118	$1.4*10^{-11}$	-	-
Temp. = 145°C; Feed pressure = 2 bar; Initial permeate pressure = 15 Pa					
H$_2$	$9.4*10^{-12}$	0.1	$1.7*10^{-8}$	$3.3*10^{-8}$	0.0003
N$_2$	$2.1*10^{-12}$	4.7	$3.5*10^{-10}$	$7.4*10^{-10}$	0.0029
CH$_4$	$2.5*10^{-12}$	4.5	$3.7*10^{-10}$	$8.3*10^{-10}$	0.0030
CO$_2$	$2.7*10^{-12}$	42	$4.0*10^{-11}$	$6.5*10^{-10}$	0.0042
CF$_2$Cl$_2$	$6.0*10^{-13}$	57	$2.9*10^{-11}$	-	-

Prior to reactivation the MFI/clay composite is treated with methanol to remove the epoxy resin with which the membrane is attached to the metal disk (section 7.3.1). The reactivation is performed by calcination at 400°C in air for 10 hours (twice). The permeabilities after reactivation (in $mol.m.m^{-2}.s^{-1}.Pa^{-1}$) at room temperature for hydrogen $(6.1*10^{-12})$, nitrogen $(2.0*10^{-12})$, and methane $(2.8*10^{-12})$ are in good agreement with the data of Table 2. It is concluded that the MFI/clay membrane withstands treatment with methanol and water, and repeated reactivation at 400°C.

Intracrystalline diffusivities have been calculated from the data in Table 2 via both the time lag and the quasi-steady-state permeation procedure according to equation (3), assuming a membrane thickness of 100 μm. Adsorption data for methane, nitrogen, and carbon dioxide have been taken from Rees.[41] For 145°C the available data have been subjected to extrapolation by an Arrhenius type equation. For hydrogen a very small time lag is found; the adsorption is therefore assumed to be negligible (K=1/RT). For freons (e.g. CFC-12)[19] and trifluorochloromethane type I isotherms are reported, the latter, however, at 0°C and up to 15 kPa.[42] As Henry's law is not obeyed, D^{s-s} has not been calculated for CFC-12. For carbon dioxide at 21°C also some deviation from Henry's law arises for pressures higher than 0.5 bar.[43]

Some binary mixtures have been tested for the MFI/clay membrane (*System II*). For hydrogen/methane mixtures some selectivity has been observed (Table 3). The selectivity is found to depend on both the feed pressure and the feed composition. For the binary mixture hardly any selectivity is observed, which is in qualitative agreement with the data in Table 2, as the ratio of the pure gas permeabilities at 21°C amounts to 2.2 only. As both species obey to Henry's law (up to at least 2 bar), the observed permeation behaviour is not expected to be caused by hindered diffusion by either sorbate molecule.

The highest selectivity is achieved for the 87/13 hydrogen/methane mixture, which is rationalized from the fact that the driving force for methane permeation is reduced by the low feed partial pressure. The maximal pressure difference for methane amounts to 0.2 bar, whereas for hydrogen a minimal pressure difference of about 0.5 bar applies. On the other hand, enrichment of methane for a 10/90 hydrogen/methane mixture (especially at the high feed pressure of approximately 5 bar) does not occur, which might be attributed to the presence of the clay support on the permeate side (back-diffusion).[13]

Table 3   Permeation results for hydrogen/methane mixtures (*System II*) on an MFI/clay membrane (Temperature = 21°C; Permeate pressure = 1 bar)

Feed pressure (bar) (H$_2$/CH$_4$)	Feed composition (H$_2$/CH$_4$)	Permeability (mol.m.m^{-2}.s^{-1}.Pa^{-1})		Permeability ratio (H$_2$/CH$_4$) (-)
		H$_2$	CH$_4$	
5.3	14/86	$9.3*10^{-13}$	$7.0*10^{-13}$	1.3
2.4	50/50	$6.9*10^{-13}$	$4.8*10^{-13}$	1.4
3.0	77/23	$6.4*10^{-13}$	$4.8*10^{-13}$	1.3
2.0	77/23	$5.8*10^{-13}$	$5.8*10^{-13}$	1.0
2.5	87/13	$7.8*10^{-13}$	$2.4*10^{-13}$	3.3
2.0	87/13	$9.0*10^{-13}$	$0.8*10^{-13}$	11.3
1.7	87/13	$9.3*10^{-13}$	$0.6*10^{-13}$	15.5

For a binary mixture of propane/propene at room temperature and a feed pressure of 2 bar no selectivity is obtained ($3.1*10^{-12}$ mol.m.m^{-2}.s^{-1}.Pa^{-1} for both gases). For a binary mixture of the butane isomers at room temperature and a feed pressure of 2 bar the MFI/clay membrane reveals an initial selectivity for n-butane. Under steady-state conditions after 1 hour on stream, however, the selectivity is negligible (n-butane: $1.4*10^{-12}$ and isobutane $1.3*10^{-12}$ mol.m.m^{-2}.s^{-1}.Pa^{-1}). At 150°C a slight increase of selectivity is found, whereas the permeability decreases.

The long delay time for the butane isomer mixture to reach steady-state has also been observed in pure gas permeation experiments for both butane isomers in a Wicke-Kallenbach configuration (*System III*). The transient permeation behaviour of the MFI/clay system for single components (15% in helium, corresponding to a partial pressure of 0.25 bar) at room temperature is shown in Figure 6. Weakly adsorbed gases (methane, neon)

reach steady-state within 7 to 9 minutes, whereas heavier molecules are only detected after 4 to 5 minutes and reach steady-state after one hour. The steady-state flow of n-butane is substantially higher than that of isobutane, in accordance with the difference in molecular shape between the two isomers. The steady-state permeabilities (in $mol.m.m^{-2}.s^{-1}.Pa^{-1}$) for methane ($1.7*10^{-12}$), neon ($1.1*10^{-12}$), n-butane ($8.1*10^{-13}$), and isobutane ($3.6*10^{-13}$) are of the same order of magnitude as in Table 2.
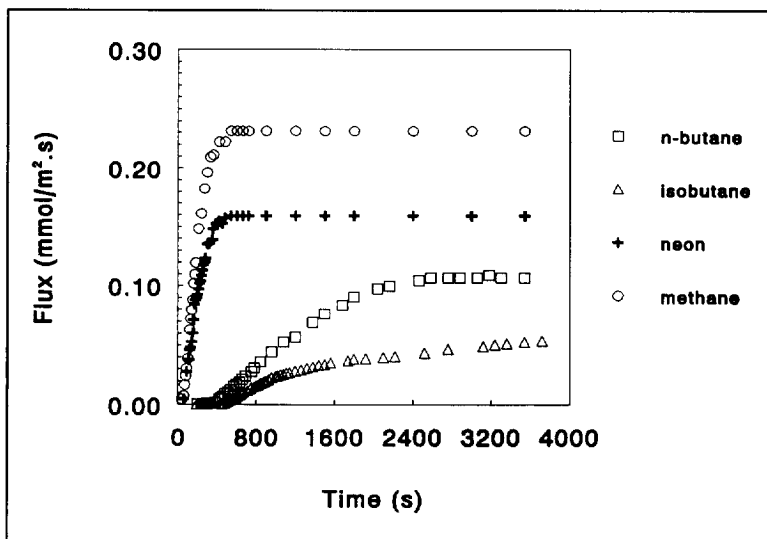
Figure 6   Transient, single component permeation through an MFI/clay membrane (A_m=1.5 cm^2, l_m=100 μm) at room temperature for 0.25 bar partial pressure in helium (*System III*)

In Figure 7 the permeation behaviour (*System III*) of an equimolar binary mixture of methane and isobutane (0.25 bar/0.25 bar) is represented. Permeation of methane initially proceeds similarly to the pure gas measurement, but deviates after 2 to 3 minutes to reach a temporary maximum (a helium purge gas flow is applied on the permeate side). Thereafter the methane flow decreases to reach a steady-state permeation rate that is substantially lower than the 'pure' gas value. The presence of methane has no noticeable effect on the isobutane permeation. At steady-state the observed separation factor is only

1.3 (nearly non-selective), whereas the ideal separation factor (based on pure gas permeabilities) under similar conditions is equal to 3. Apparently, isobutane, being far more abundant in the zeolite framework, reduces the methane mobility. Thus, some molecular sieve effect seems to be observed for the MFI/clay membrane.
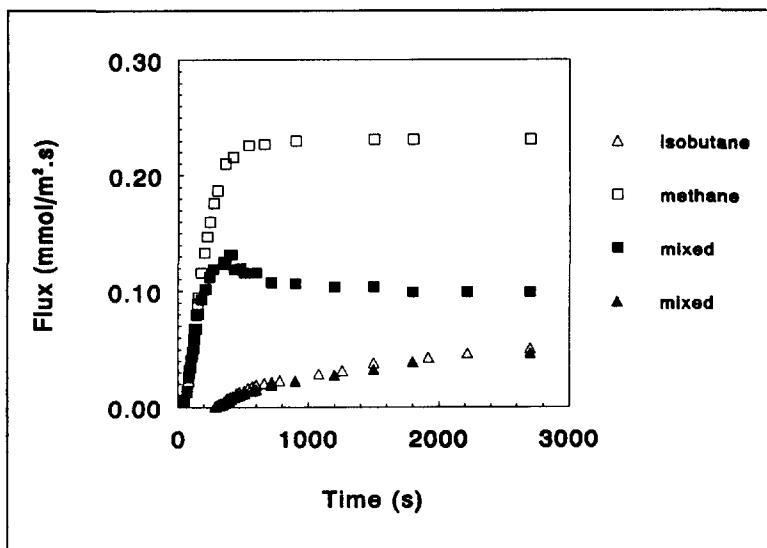
Figure 7   Transient permeation through the MFI/clay membrane of Figure 6 for a mixture of methane (0.25 bar) and isobutane (0.25 bar) in helium at room temperature, and the single component transient permeation for comparison

For methane the obtained diffusivities mentioned in Table 2 are over two orders of magnitude lower than according to the pfg NMR method.[35] The low diffusivity experimentally observed is attributed to the presence of the clay support with a relatively low porosity on one side of the membrane (cf. section 7.2.2). It has already been mentioned in Chapter 3 that the clay support does not remain inert under the hydrothermal conditions, and seems to be denser after crystallization. Neither the time lag nor the quasi-steady-state data therefore relate to genuine intracrystalline diffusion. The membrane permeability may be improved by applying a more porous support, as it is also expected that the low-porosity support obscures the true molecular sieve properties of the MFI-type membrane.

7.4 Permeation through Stainless Steel MFI-Type Membranes

The permeation of single components and (binary) mixtures through the stainless steel supported MFI (in situ grown) membranes described in Chapter 3 is dealt with in this section. The high-temperature membrane module, provided with a freshly prepared MFI layer, is installed in the permeation equipment using similar flange connections as for the hydrothermal synthesis. Instead of Teflon, commercially available high-temperature resistant copper sealing rings are used (cf. Figure 8).
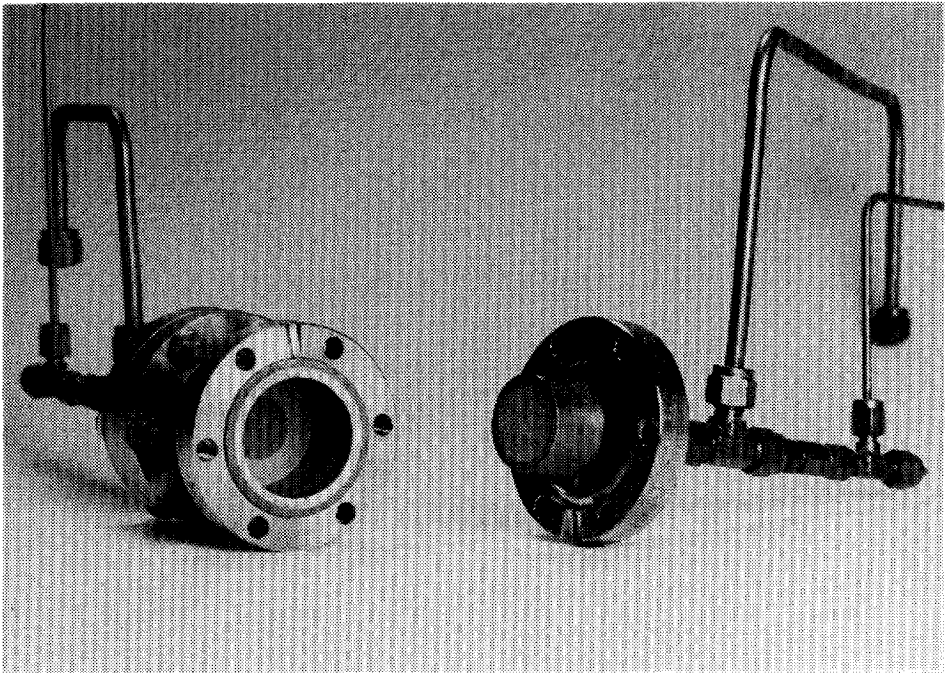
Figure 8   Picture of the stainless steel (AISI-316) high-temperature membrane module

All permeation experiments have been performed according to the Wicke-Kallenbach concept (*System III*), using helium as a purge gas (total pressure 1 bar). The zeolite layer is exposed to the feed side, because the inner surface of this compartment is fully covered

with MFI material. On the permeate side this additional MFI material may influence the transient permeation results due to readsorption. Although some other gases have been used as well,[19] the discussion is mainly limited to methane, neon, n-butane, and isobutane.

7.4.1 Molecular Sieve Behaviour of Stainless Steel Supported MFI Layers

The TPA-containing, as-synthesized MFI layer is impermeable for a pure neon feed (flow $< 7.4*10^{-12}$ mol/s; P $< 4.1*10^{-17}$ mol.m.m^{-2}.s^{-1}.Pa^{-1}). Next, the MFI layer is calcined at 400°C (heating rate 1°C/min; dwell time 16 hours) in air (100 ml/min through both compartments). In section 7.4.3 the permeability for krypton during the calcination process is discussed. Prior to the measurements the membrane module is flushed with pure helium until no other species are apparent by mass spectrometry (<5 ppm; 0.5 Pa).

Single Component Measurements

The transient permeation behaviour of methane, neon, and the butane isomers at room temperature is shown in Figure 9.
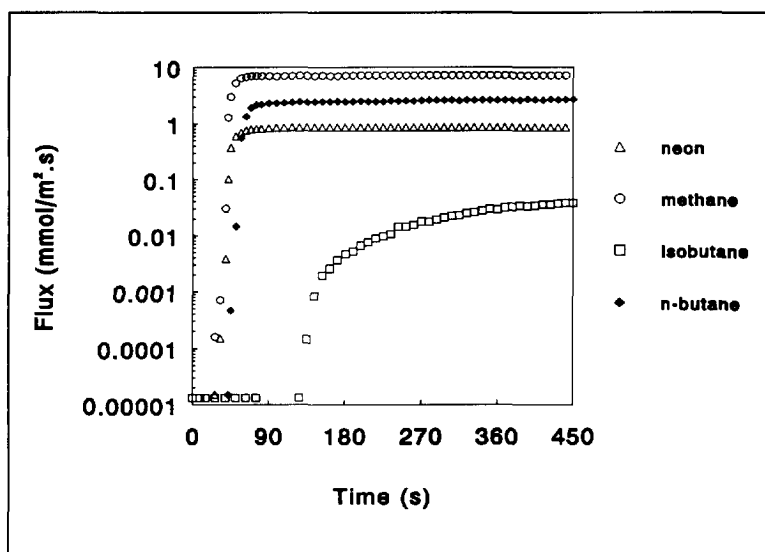
Figure 9   Transient permeation behaviour through the MFI/stainless steel membrane (A_m=3 cm^2, l_m=50 μm) of methane, neon, n-butane, and isobutane at 25°C (feed 0.3 bar)

The time to detect methane (34 s) and neon (38 s) is slightly longer than the delay time of the experimental set-up (module without any zeolite material inside: 26 s). The detection of the onset of the fluxes of the two butane isomers depends strongly on the isomer: n-butane after 42 s, and isobutane after about 2 min. For methane, neon, and n-butane the steady-state fluxes are reached within 1 to 2 min. In the case of isobutane it takes over 10 min to reach the steady-state, and the permeation rate is 1 to 2 orders of magnitude lower. Under the applied conditions, the steady-state permeabilities (in $mol.m.m^{-2}.s^{-1}.Pa^{-1}$) amount to $1.2*10^{-11}$ (methane), $1.5*10^{-12}$ (neon), $4.5*10^{-12}$ (n-butane), and $7.0*10^{-14}$ (isobutane). In Figure 10a the steady-state flux for each component is plotted as a function of the feed partial pressure. The weakly adsorbed gases (methane and neon) reveal a linear relationship with the feed pressure. The rise in permeability for the at room temperature strongly adsorbed butane isomers levels off at rather low pressures (< 10 kPa; compare Figure 4). At 350°C all fluxes are linear with the feed pressure (Figure 10b).

The significant difference in permeation rate between the two butane isomers under near saturation conditions (pure gas permeation ratio of over 60) cannot be simply attributed to the lower isobutane adsorption capacity of MFI (cf. Chapter 6). According to permeation measurements on a twinned silicalite crystal at 24°C,[1] the intrinsic diffusivity of isobutane is slightly lower (factor 3) than that of n-butane (measurements performed within Henry's region). In Chapter 6, on the other hand, it has been observed that the desorption of isobutane out of a near-to-saturated silicalite crystal is substantially slower (over one order of magnitude) than that of n-butane. Hence, the low permeation rate of isobutane as compared with that of n-butane may be attributed to the bulkiness of isobutane, perhaps especially under near saturation conditions leading to substantially lower apparent diffusivities.
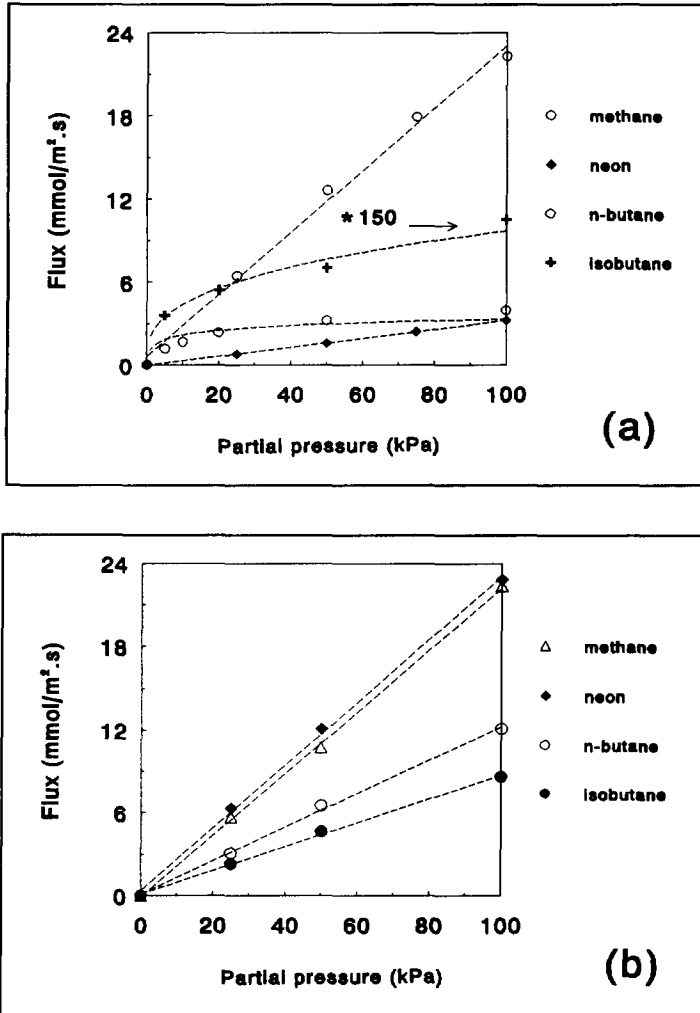
Figure 10   Steady-state flux and permeate partial pressure of methane, neon, n-butane, and isobutane as a function of the feed partial pressure at (a) 25°C (note: isobutane flux * 150), and (b) 350°C

Multicomponent Measurements

Figure 11 shows the transient permeation behaviour of a binary neon/methane mixture at room temperature. The two weakly adsorbed components do not affect each other, and the steady-state permeation values are equal to the single component values (cf. Figure 9). It

should be noted that for high feed concentrations a considerable driving force exists for counterdiffusion of helium from the permeate to the feed side, which is negligible for low feed concentrations. The influence on the results presented here is, however, expected to be limited.
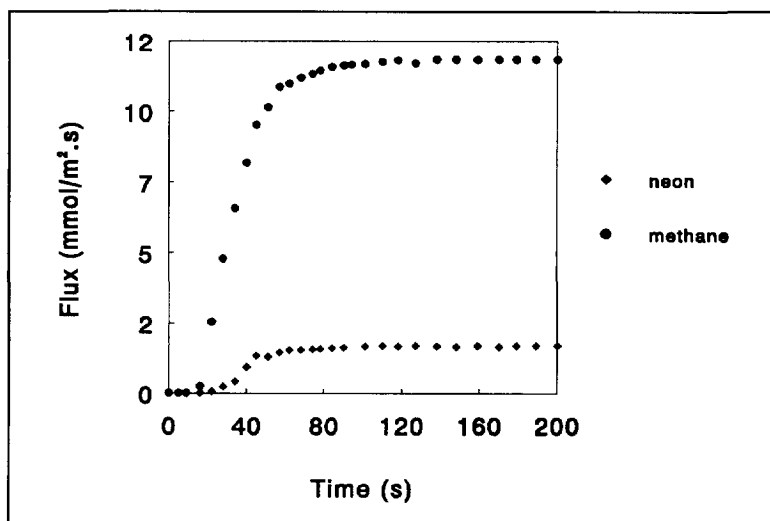
Figure 11   Transient permeation behaviour of a binary (0.50 bar/0.50 bar) methane/neon mixture (total pressure 1 bar) through a stainless steel supported MFI-type membrane at 25°C

The selectivity (α) is generally defined as the enrichment factor of one component in the permeate as compared to the feed composition ratio:

$$\alpha = \frac{x_F \cdot y_P}{x_P \cdot y_F} \tag{9}$$

with x the mol fraction of the first, and y that of the second component, while the subscripts F and P denote the feed and the permeate side, respectively. The selectivity of a binary mixture is not a constant, and may vary with the applied conditions on both the feed and the permeate side of the membrane (cf. Table 3). For the here studied neon/methane mixture a selectivity of 7 is obtained.

191

Typical and at first sight unexpected transient permeation behaviour is observed for a binary methane/n-butane mixture (Figure 12). The methane flux starts out similarly to the pure gas measurement, but levels off after a few seconds to reach a temporary maximum. The permeation behaviour of n-butane is hardly affected by the presence of methane in stead of helium on the feed side. Steady-state is reached within 2 minutes, similarly to the pure gas permeation experiment for n-butane. The selectivity (α), however, amounts to approximately 50 in favour of n-butane, whereas the ideal separation factor, based on pure gas permeabilities, is in favour of methane. This transient behaviour of a mixture of a weakly and a strongly adsorbed component is similar to the results for the MFI/clay membrane, but here the effect is much more dramatic.
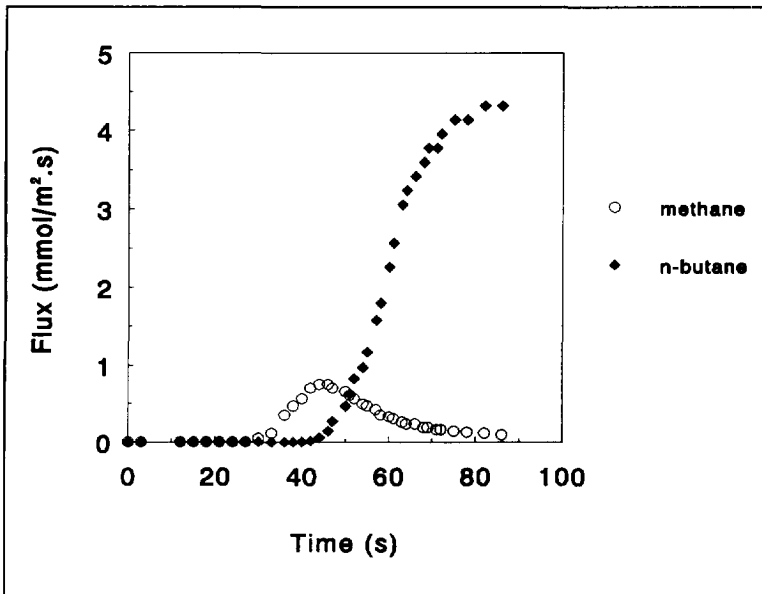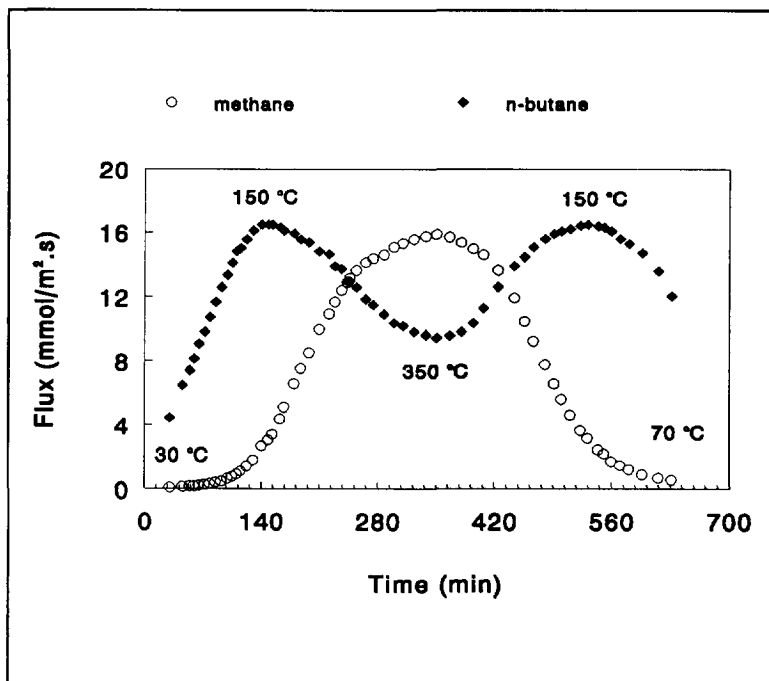

Figure 12   Transient permeation behaviour of a binary (0.50 bar/0.50 bar) methane/n-butane (total pressure 1 bar) mixture through a stainless steel supported MFI-type membrane at 25°C

The methane permeation is equally reduced in the presence of isobutane. Figure 13 shows the permeation behaviour of methane after addition of either n-butane or isobutane to the

initially pure methane feed (70% in helium). Again, the time required to reach steady-state depends on the butane isomer. The major drop in methane permeation, however, results directly after the feed gas has been switched to either butane isomer. It appears that the zeolite micropores on the feed side are effectively blocked by the strongly adsorbed butane molecules, and the separation is apparently governed by a difference in adsorption strength. In addition, it is to be expected that the mobility of methane within the zeolite micropores is substantially reduced in the presence of larger, strongly adsorbed and more slowly moving molecules. Accordingly, it may be mentioned that it has been established by the pfg NMR method that in the presence of virtually immobile benzene molecules (2 per unit cell), the methane diffusivity within the MFI framework is reduced by approximately two orders of magnitude.[44,45]
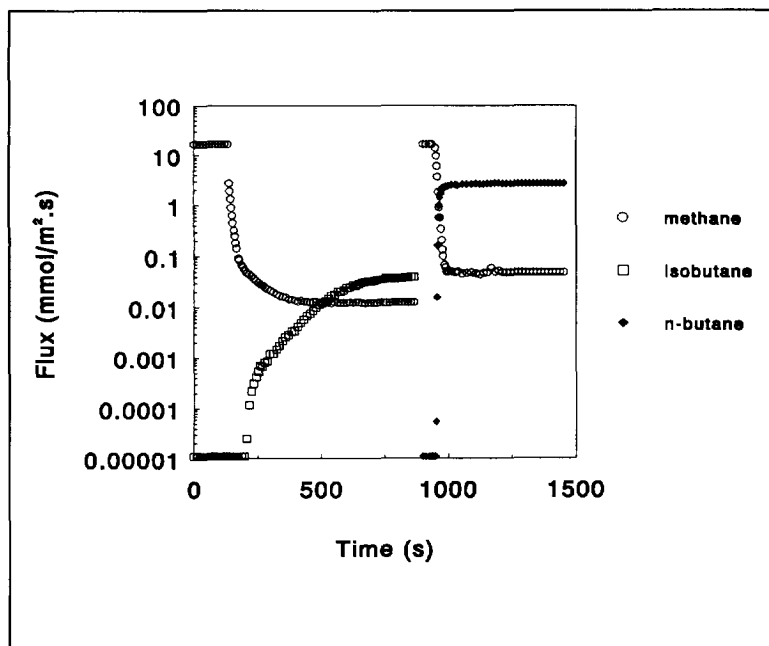
Figure 13   Transient permeation behaviour for a methane feed (0.7 bar in helium) to which either n-butane or isobutane (0.3 bar) is added through a stainless steel supported MFI-type membrane at 25°C (total pressure 1 bar)

193

The drop in methane permeation is of the same order of magnitude for both butane isomers. Based on the previously mentioned difference in sorption capacity, however, the methane sorbate concentration on the feed side may be higher in the presence of isobutane than with n-butane being present. Hence, a higher driving force for methane permeation is expected in the presence of isobutane, in principle leading to a higher methane permeation rate. As compared to isobutane, however, the methane permeation in the presence of n-butane is even slightly higher, which suggests that the higher driving force for methane permeation is cancelled by the presence of slowly moving isobutane molecules. In the case of n-butane, all the methane molecules that enter the zeolite framework are dragged through the micropores by the relatively fast moving n-butane molecules. With both butane isomers being present at room temperature the high intrinsic mobility of methane is overruled.

The steady-state permeation behaviour of a binary methane/n-butane mixture as a function of temperature is shown in Figure 14. A steady increase of the n-butane flux with rising temperature is observed (up to approximately 160°C). The methane permeation rate remains low up to approximately 140°C, and the selectivity is in favour of n-butane. At higher temperatures the methane flow becomes substantial and even exceeds the decreasing n-butane flow at approximately 230°C. At still higher temperatures (up to 350°C) the rise in methane permeation levels off. The same permeation behaviour for both gases is observed upon cooling, and has been found to be reproducible for several cycles, *inter alea* proving that the MFI/stainless steel membrane remains thermomechanically stable up to at least 350°C.

All the observed features of Figure 14 may be related to the fact that both diffusion and adsorption are temperature dependent. For the n-butane permeation rate, the initial increase with temperature may arise from the higher intrinsic diffusivity, as diffusion is an activated process. Concurrently, however, the n-butane adsorption shifts out of the saturation area, first on the permeate side, which increases the driving force for n-butane permeation as well. For still higher temperatures, the driving force for n-butane decreases, as the adsorbate concentration on the feed side is no longer under near saturation conditions.

Figure 14   Steady-state permeation rates of a binary (0.50 bar/0.50 bar) methane/n-butane mixture (total pressure 1 bar) through a stainless steel supported MFI-type membrane as a function of temperature (heating rate 1°C/min; cooling rate 1.5°C/min)

As pointed out earlier, the methane permeation rate at low temperatures is governed by the n-butane adsorbate concentration. The initial rise in the methane permeation rate at low temperature may therefore be attributed to the increasing n-butane flow. At higher temperatures the competition with the n-butane molecules diminishes, and both the driving force for methane permeation and the methane mobility strongly increase. At sufficiently high temperatures, the selectivity is based on the permeability ratio of the pure gas components (adsorption obeying Henry's law for both components). This is further demonstrated for the transient permeation of binary mixtures of methane/n-butane (Figure 15a) and methane/isobutane (Figure 15b) at 350°C. Under these conditions the transient methane permeation is not affected by the presence of either butane isomer, as the

195

adsorption obeys Henry's law for all components.

By applying higher n-butane (partial) feed pressures still higher n-butane permeation rates may be reached. For other than the here applied feed conditions (1 bar, 50/50 mixture), the permeation behaviour as a function of temperature may vary, although the trend is expected to be similar to that of Figure 14.
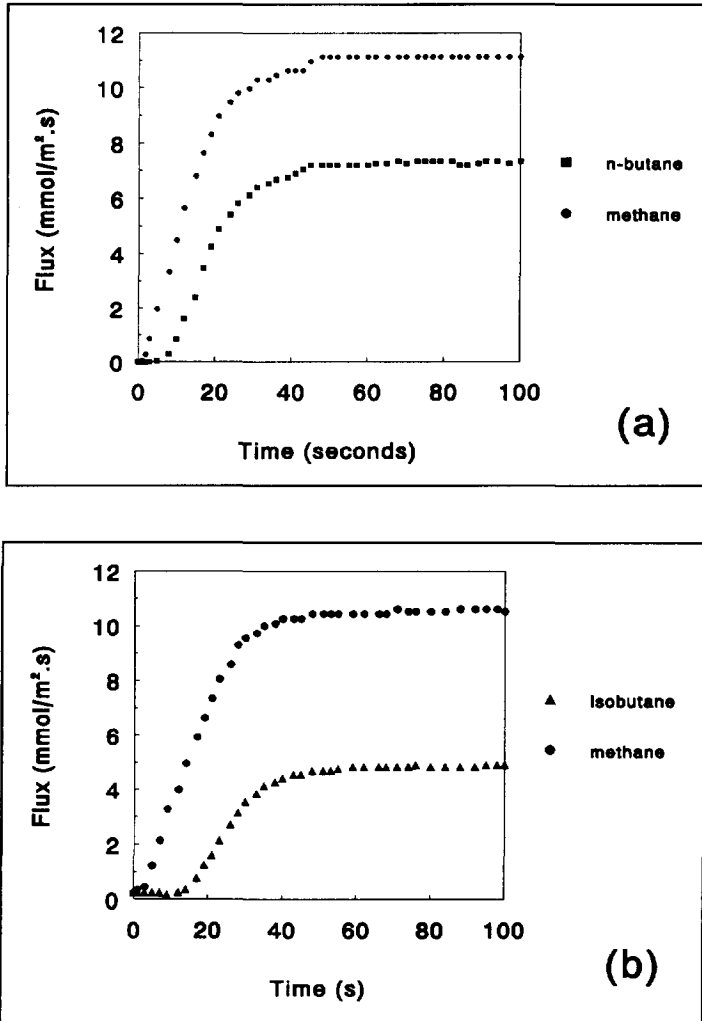
Figure 15   Transient permeation behaviour at 350°C of a binary mixture (0.50 bar/0.50 bar) of (a) methane/n-butane, and (b) methane/isobutane

7.4.2 Comparison of Theoretical and Observed Flow Rates

Aiming at the measurement of true intracrystalline diffusivities, the effect of the macroporous stainless steel support on the steady-state permeation rates of methane and neon has been studied. Upon variation of the purge gas flow rate on the permeate side it is observed that the steady-state permeation rates for methane and neon are not dependent on the helium flow rate on the permeate side (variation 50 to 500 ml/min).[19] Hence, it is concluded that the overall permeation rate is not affected by the diffusion through the macroporous support. This has only been checked for the weakly adsorbed species. For near saturation adsorption the flow as a result of intracrystalline diffusion is expected to depend on the partial pressure on the permeate side (cf. section 7.2.2, Figure 4). In fact, an intrinsic problem of the Wicke-Kallenbach approach is encountered here, because the partial pressure of the permeate and the flow rate through the membrane are interrelated. When a higher purge gas flow rate is applied, the permeate partial pressure is reduced and thus a higher flow rate is to be expected.

In Table 4, the observed steady-state flow rates for methane and n-butane are compared with the theoretical steady-state permeation rates, according to the permeation model of equation (8) in section 7.2.2. The observed flow rate for n-butane is of the same order of magnitude as the theoretical value (factor of 3 lower), whereas for methane the experimental flow is more than one order of magnitude lower than the value calculated according to theory. It should be noted that the here applied permeation model is basically more reliable for methane, for which species Henry's law is obeyed, than for n-butane.

Although the macroporous support itself does not seem to give rise to an additional resistance to mass flow, care should be taken while comparing the observed flow rates with the theoretical values. The earlier mentioned effect of the zeolite layer/macroporous support interface porosity (section 7.2.2) may give rise to a significant labyrinth or tortuosity factor. Moreover, the flow rate can be reduced if some plugging of the stainless steel top layer by deposited MFI material has occurred, as the plugging is not expected to be remedied by increasing the purge gas flow rate. Slightly lower experimental permeation rates are to be expected for these polycrystalline layers anyway, based on the random orientation of the

197

MFI crystals. For only a few crystals within the layer the permeation proceeds exclusively via the straight or sinusoidal channels. Due to the diffusional anisotropy,[47,48] the average diffusivity through the MFI layer will therefore be lower than the maximum level. As the crystals within the MFI layer are expected to be grown separately *next to*, and not *on top* of each other (cf. Chapter 3), it seems unlikely that an additional resistance to mass flow does occur from crystal interfaces.

Table 4   Comparison of methane and n-butane steady-state permeation rates with the permeation model according to equation (8), for a 0.3 bar feed (partial pressure) in helium at 25°C

Model	Gas	
	methane	n-butane
Diffusion D_0[@] (m^2/s) q_c $(mol.m^{-3})$ γ	$1.1*10^{-8}$ $3.25*10^4$ 11.1	$5.9*10^{-9}$ $8.97*10^3$ 11.1
Adsorption k[$] (Pa^{-1}) q_0[$] $(mol.m^{-3})$ K[#] $(mol.m^{-3}.Pa^{-1})$	- - 0.0174	0.031 2750 -
p_{feed} (kPa)	30	30
$p_{permeate}$ (kPa)	2.9	1.1
Φ_{mol} experimental $(mol.s^{-1})$	$2.2*10^{-6}$	$8.1*10^{-7}$
Φ_{mol} theoretical $(mol.s^{-1})$	$3.3*10^{-5}$	$2.5*10^{-6}$

[@]   intrinsic diffusivity, parameter in the diffusion model,[17] according to pfg NMR self-diffusion data from Caro et al.[35]
[$]   Langmuir isotherm parameters, fitted for adsorption data from Richards and Rees[46]
[#]   Henry coefficient taken from Rees[41]

It is striking that agreement is best for the more strongly adsorbed n-butane as compared to the weakly adsorbed methane. In fact, the same has been observed with the permeation measurements on the silicalite single crystals embedded in epoxy resin (section 7.3.2).[14] One way to account for the good agreement between the observed and the theoretical permeation ratios for strongly adsorbed species, such as n-butane, at room temperature is by the earlier mentioned external surface contributions on the entry and exit side of the membrane. Strongly adsorbed species may give rise to an adsorbate phase on the external zeolite surface, and the entry to the zeolite micropores by surface migration may thus proceed sufficiently fast to establish a sorbate concentration near to the thermodynamical equilibrium. Weakly adsorbed species, on the other hand, must be directly adsorbed within the zeolite micropores, because the tendency to form an adsorbate phase on the external zeolite surface is much weaker. These considerations hold for the feed, but also for the permeate side, and in either case the driving force for intracrystalline diffusion decreases. The occurrence of the above assumed extracrystalline contributions to mass transport has been found to be in accordance with the comparison of the observed and the expected delay times to achieve the steady-state. The adsorption capacity of the membrane layer (l_m=50 μm; A_m=3 cm^2), assuming equilibrium under the applied conditions on the feed and the permeate side, and the observed steady-state permeation rate may be combined to estimate the delay time to reach the steady-state. Surprisingly, for methane and neon the estimates amount to only a few seconds, which is substantially lower than the actually required times. For n-butane, the estimated value is only slightly lower (about 1 min), whereas for isobutane the required delay time is substantially shorter than the estimated value (over 2000 s). Apparently, the transient permeation behaviour depends strongly on the permeating species. The comparison of expected and observed delay times (actually the time to fill the zeolite micropores to the average concentration under the applied steady-state conditions) has been performed on several weakly and strongly adsorbed molecules at room temperature, from which a general trend has been observed:[19] substantially lower expected time delays for methane, argon, krypton, and ethane than actually were observed, and small differences for n-butane, isobutane, and CFC-12. The phenomenon that weakly adsorbed

199

molecules cannot or can only with difficulty enter the sorbent micropores has also been observed for nitrogen adsorption onto active carbon at liquid nitrogen temperature and low pressures. The tendency to adsorb on the outer sorbent surface is low, and as the chance to enter directly through the narrow window of the sorbent pores is small, the thermodynamical equilibrium is reached only after very long times.[49]

7.4.3 Nature of the MFI Layer/Stainless Steel Support Membrane

It has been mentioned in Chapter 3 (section 3.4) that owing to the growth on the stainless steel support, the resulting zeolite layer consists of a polycrystalline layer of randomly oriented MFI crystals *next to*, and not *on top* of each other. Therefore, the permeation through the MFI/stainless steel membrane is thought to proceed mainly through each crystal separately, without the need to pass extra intercrystalline interfaces. Even within silicalite single crystals, however, the occurrence of crystal interfaces cannot be completely ruled out (cf. section 4.5).[50]

The strong blocking effect of n-butane and isobutane on the methane permeation under the here applied conditions (ambient conditions, p/p_0 of approximately 0.14) points out that the membraneous layer indeed consists of micropores. These experiments do, however, not exclude the presence of larger pores, by which the separative potential of the membrane may be reduced. The presence of larger pores can be established by the occurrence of hysteresis in the adsorption on the membrane material, for instance for nitrogen adsorption at -196°C. However, the occurrence of hysteresis in the nitrogen isotherm at -196°C for separate MFI crystals, prepared in alkaline medium, has been observed consistently, and is attributed to liquid-to-solid transition of the adsorbate phase by Müller and Unger.[51] Axon and Klinowski,[52] on the other hand, report that for fluoride-synthesized MFI no hysteresis is observed, which deviating adsorption behaviour is said to be related to the more perfect, defect-free crystals formed in the fluoride medium. These ambiguous results may therefore not necessarily provide conclusive evidence on the presence of mesopores.

It is, however, unlikely that the nucleation and growth of the here discussed in situ grown MFI layer on stainless steel supports proceed in such a way that absolutely no larger pores

are present within the zeolite phase. In many cases growing crystals have to meet in order to produce a fully covered porous support. The occurrence of larger pores within the here considered stainless steel-supported MFI layers has been investigated by the permeation of krypton during the calcination process (cf. Figure 16). It is clear that the first permeation of krypton proceeds at about 260°C, at which temperature the template TPA is still present (Chapter 4; section 4.3). In fact, even up to approximately 320 to 330°C the TPA-decomposition has only proceeded to the formation of tripropylamine, hence the zeolite micropores are still expected to be nearly fully blocked. It appears from Figure 16 that only at ca. 350°C the zeolite micropores are indeed emptied. At the applied low heating rate the voids are completely emptied once the temperature has reached 400°C. The small permeation for krypton at the lower temperatures during the thermal treatment is therefore attributed to some larger pores present within the MFI layer.
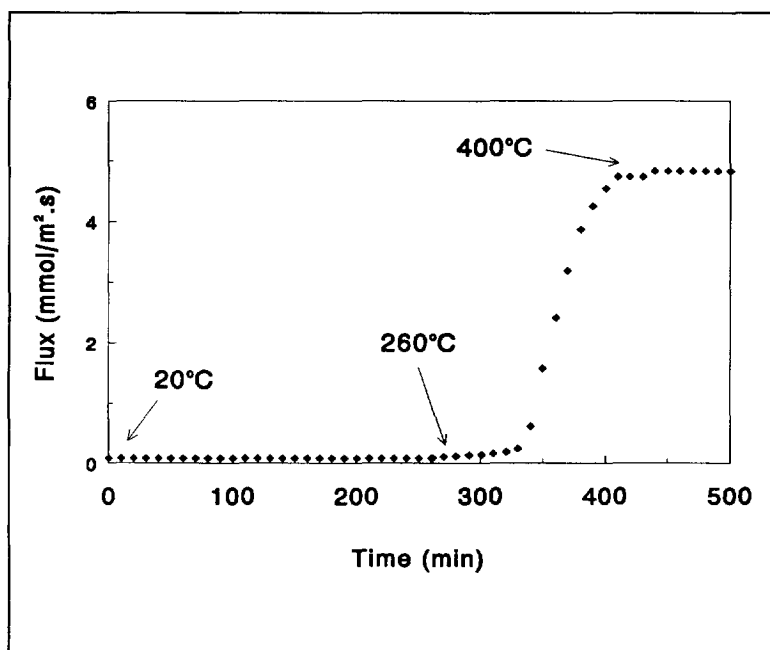
Figure 16   Permeation of krypton during the calcination in a nitrogen/oxygen ((80/20) flow of an as-synthesized, TPA-containing MFI layer within the high-temperature module (heating rate 1°C/min; p_{Kr}=20 kPa)

Further evidence for the presence of larger pores within the MFI layer is provided by the observation that at 50°C a small 2,2,4-trimethylpentane (iso-octane) flow is observed for the same MFI layer after calcination (cf. Figure 17). Since under these moderate conditions the bulky iso-octane molecule does not have access to the MFI micropores,[53,54] it is concluded that some larger pores are present within the MFI layer. Moreover, the permeation of methane is hardly hindered by the presence of iso-octane, whereas the introduction of n-butane leads to a similar drop in permeation for methane as described above. Apparently, the MFI layer comprises a two-pore system of MFI micropores and some larger pores. The presence of the larger pores is, however, not detrimental to the membrane performance. It is nevertheless possible that the membrane preparation can be further optimized to avoid the presence of such larger pores. Without wider pores an even better performance of the present composite system as a true molecular sieve membrane may be obtained.
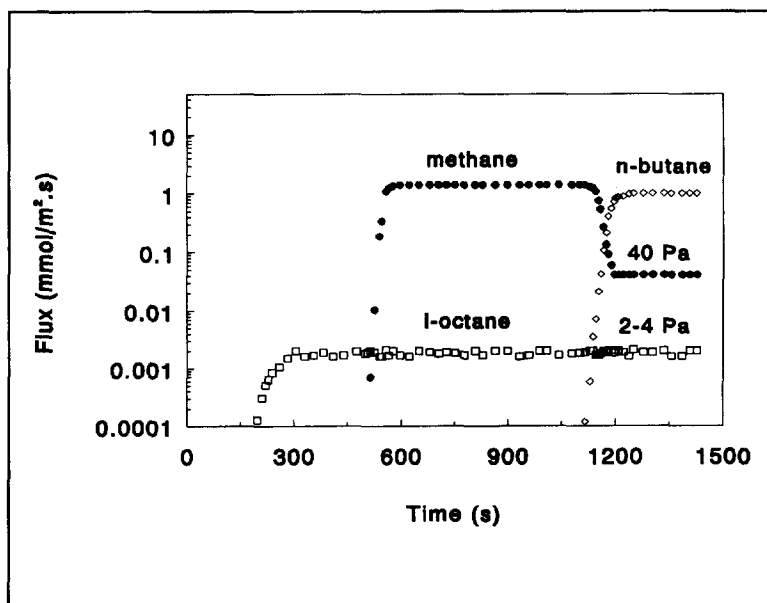
Figure 17   Permeation behaviour of a multicomponent feed, consisting of 5 kPa iso-octane, 25 kPa methane, and 25 kPa n-butane at 50°C; consecutive introduction of iso-octane at t=0 s, methane at t=500 s, and n-butane at t=1100 s

7.5 Concluding Remarks

The permeation data on MFI/stainless steel membranes presented here show reasonably good agreement with the developed (Fickian) permeation model, based on pfg NMR diffusivity data. Best agreement is, however, obtained for more strongly adsorbed species, such as n-butane, whereas the diffusivity for methane is found to be more than one order of magnitude lower. The considerable difference may be attributed to extracrystalline contributions to the mass transport through the zeolite membrane, as for weakly adsorbed species the entry to (and perhaps also the exit from) the zeolite micropores does not take place via an external adsorbate phase.

The permeation results dealt with here suggest that for mixtures consisting of weakly and strongly adsorbed molecules, the membrane is expected to be selective towards the more strongly adsorbed species, notwithstanding the generally lower intrinsic diffusivity. The high permeation rate for strongly adsorbed species can be attributed to the principle of surface diffusion. Enhanced transport of 'heavier' molecules under cryogenic conditions within mesoporous membranes has been reported previously, and is ascribed to surface diffusion.[10-12] The near-to-total blockage of weakly adsorbed species in the presence of more strongly adsorbed species offers high-efficiency membrane processes in, for instance the hydrocarbon recovery from diluted gas phases.

This type of membrane may also be of interest to separate molecules with a difference in polarity. For example, on the silicalite membranes described here the separation of water/ethanol mixtures may lead to a substantial enrichment of ethanol, because the affinity of the hydrophobic MFI lattice for ethanol is much higher than that for water.[55] The rather hydrophilic external zeolite surface silanol groups may, however, reduce the selectivity and/or the flux. Such effects may be reduced by some after-treatment of the membrane to provide a hydrophobic external surface area (e.g. reaction with trimethylchlorosilane). The large difference in pure gas permeabilities of n-butane and isobutane, on the other hand, may not lead to high selectivities, as the difference in adsorption strength is only small. In addition, separation at high temperatures does not necessarily lead to improved selectivities,

because both the differences in intrinsic diffusivity and in the adsorption strength seem to diminish at rising temperatures.

Finally, it will be interesting to further study the permeation under near saturation conditions, and to apply a pressure difference over the MFI/stainless steel membrane instead of the here described concentration difference. For the MFI/clay membrane quite high flow rates have been observed, although the concentration gradient over the membrane is negligible (feed pressure 2 bar and permeate pressure 1 bar), and the contribution of an additional driving force to mass flow (hydrostatic pressure difference) can thus be studied.[17]

7.6 Literature

1. A.R. Paravar, and D.T. Hayhurst, in: *Proc. 6th Int.Zeol.Conf.*, D. Olson, and A. Bisio (Eds), Butterworths, London, 1984, 217.
2. D.L. Wernick, and E.J. Osterhuber, in: *Proc. 6th Int.Zeol.Conf.*, D. Olson, and A. Bisio (Eds), Butterworths, London, 1984, 122.
3. D.T. Hayhurst, and A.R. Paravar, *Zeolites*, 8 (1988) 27.
4. D.L. Wernick, and E.J. Osterhuber, *J.Membrane Sci.*, 22 (1985) 137.
5. R.M. Barrer, in: *Catalysis and Adsorption by Zeolites*, G. Öhlmann, H. Pfeifer, and R. Fricke (Eds), Stud.Surf.Sci.Catal. Vol. 65, Elsevier, Amsterdam, 1991, 233.
6. R.M. Barrer, *J.Chem.Soc. Faraday Trans.*, 86 (1990) 1123.
7. S.A.I. Barri, G.J. Bratton, and T. de V. Naylor, European Patent Application 0 481 660 A1, (1991) to British Petroleum Company.
8. H.L. Fleming, in: *1986 Membrane Technology/Planning Conference Proceedings*, Business Communications Co., Cambridge, 1986.

9.   J.D. Way, and D.L. Roberts, *Separation Sci.Techn.*, 27 (1992), 29.

10.   K. Kammermeier, in: *Progress in Separation and Purification*, E.S. Perry (Ed.), Vol 1, Wiley-Interscience, New York, 1968, 356.

11.   R.W. Tock, and K. Kammermeier, *AIChE J.*, 15 (1969) 715.

12.   S.T. Hwang, and K. Kammermeier, *Membranes in Separations*, Techniques of Chemistry, Vol. 7, A. Weissberger (Ed.), Wiley-Interscience, 1975, 91.

13.   R.J.R. Uhlhorn, PhD Thesis, Twente University, The Netherlands, 1990.

14.   E.R. Geus, A.E. Jansen, J.C. Jansen, J. Schoonman, and H. van Bekkum, in G. Öhlmann, H. Pfeifer, R. Fricke (Eds.), *Catalysis and Adsorption by Zeolites*, Proc. ZEOCAT 90, Stud.Surf.Sci.Catal. Vol. 65, Elsevier, Amsterdam, 1991, 457.

15.   E.R. Geus, J. Schoonman, and H. van Bekkum, in: *Synthesis/Characterization and Novel Applications of Molecular Sieve Materials*, R.L. Bedard, T. Bein, M.E. Davis, J. Garces, V.A. Maroni, and G.D. Stucky (Eds), MRS Symp.Ser. Vol. 233, Materials Research Society, Pittsburgh, 1991, 231.

16.   E.R. Geus, M.J. den Exter, and H. van Bekkum, *J.Chem.Soc. Faraday Trans.*, (1992) 3101.

17.   E.R. Geus, W.J.W. Bakker, P.J.T. Verheijen, M.J. den Exter, J.A. Moulijn, and H. van Bekkum, in J.B. Higgins, R. von Ballmoos, and M.M.J. Treacy (Eds.), Proc.9th Int.Zeol.Conf., Butterworth-Heinemann, Stoneham, Massachusetts, 1992, in press.

18.   E.R. Geus, H. van Bekkum, W.J.W. Bakker, and J.A. Moulijn, *Microporous Materials*, (1993), in press.

19.   W.J.W. Bakker, G. Zheng, F. Kapteijn, M. Makkee, J.A. Moulijn, E.R. Geus, and H. van Bekkum, in: *Precision Process Technology: Perspectives for Pollution Prevention*, M.P.C. Weijnen, and A.A.H. Drinkenburg (Eds), Kluwer Academic Publ., Dordrecht, The Netherlands, 425-436.

20.   J. Kärger, and D.M. Ruthven, *J.Chem.Soc.Faraday Trans.*, 77 (1981) 1485.

21.   J. Kärger, and D.M. Ruthven, *Zeolites*, 9 (1989) 267.

22.   J. Kärger, H. Pfeifer, M. Rauscher, and A. Walter, *J.Chem.Soc. Faraday Trans.*, 76 (1980) 717.

23.   L.S. Darken, *Trans. AIME*, 175 (1948) 184.

24.   J. Kärger, and J. Caro, *J.Chem.Soc. Faraday Trans.*, 73 (1977) 1363.

25.   M.F.M. Post, in: *Introduction to Zeolite Science and Practice*, H. van Bekkum, E.M. Flanigen, and J.C. Jansen (Eds), Stud.Surf.Sci.Catal. Vol. 58, Elsevier, Amsterdam, 1991, 391.

26.   R.M. Barrer, *Langmuir*, 3 (1987) 309.

27.   J. Kärger, H. Pfeifer, R. Seidel, B. Staudte, and T. Gross, *Zeolites*, 7 (1987) 282.

28.   J. Kärger, *Langmuir*, 4 (1988) 1289.

29.   M. Kocirik, P. Struve, K. Fiedler, and M. Bülow, *J.Chem.Soc. Faraday Trans.*, 84 (1988), 3001.

30. R.M. Barrer, Diffusion in and through Solids, Cambridge University Press, 1941, 14.

31. D.R. Paul, and D.R. Kemp, *J.Polymer Sci.*, Symposium no. 41 (1973) 79.

32. R. Ash, and R.M. Barrer, *Surf.Sci.*, 8 (1967) 461.

33. J. Kärger, *Surf.Sci.*, 36 (1973) 797.

34. J. Kärger, S.P. Shdanov, and A. Walter, *J.Chem.Soc. Faraday Trans.*, 256 (1975) 319.

35. J. Caro, M. Bülow, W. Schirmer, J. Kärger, W. Heink, H. Pfeifer, and S.P. Zdanov, *J.Chem.Soc. Faraday Trans.*, 81 (1985) 2541.

36. R.E. Cunningham, and R.J.J. Williams, *Diffusion in Gases and Porous Media*, Plenum Press, New York, 1980, 19.

37. J.M. Coulson, and J.F. Richardson, *Chemical Engineering*, Vol. 3, Pergamon Press, Oxford, 1979, 110.

38. M. Suzuki, *Adsorption Engineering*, Kodansha, Tokyo, and Elsevier, Amsterdam, 1990, 63.

39. E. Wicke, Kolloid Z., 93 (1940) 9.

40. E. Wicke, and R. Kallenbach, Kolloid Z., 97 (1941) 135.

41. L.V.C. Rees, in: *Catalysis and Adsorption by Zeolites*, G. Öhlmann, H. Pfeifer, and R. Fricke (Eds), Proc. ZEOCAT 90, Stud.Surf.Sci.Catal. Vol. 65, Elsevier, Amsterdam, 1991, 61.

42. P.J.M. Carrott, and K.S.W. Sing, *Adsorp.Sci.Technol.*, 6 (1989) 136.

43. P. Graham, A.D. Hughes, and L.V.C. Rees, *Gas Sep.Purif.*, 3 (1989) 56.

44. J. Kärger, H. Pfeifer, D. Freude, J. Caro, M. Bülow, and G. Ohlmann, in: *Proc. 7 IZC Tokyo*, Y. Murakami, A. Iijima, and J.W. Ward (Eds), Elsevier, Amsterdam, 1987, 633.

45. C. Förste, A. Germanus, J. Kärger, H. Pfeifer, J. Caro, W. Pilz, and A. Zikanova, *J.Chem.Soc.Faraday Trans.*, 83 (1987) 2301.

46. R.E. Richards, and L.V.C. Rees, *Langmuir*, 3 (1987) 335.

47. U. Hong, J. Kärger, R. Kramer, H. Pfeifer, G. Seiffert, U. Müller, K.K. Unger, H.B. Lück, and T. Ito, *Zeolites*, 11 (1991) 816.

48. B. Zibrowius, J. Caro, and J. Kärger, *Z.phys.Chemie (Leipzig)*, 269 (1988) 1101.

49. J.W. Geus, Utrecht University, The Netherlands, private communication.

50. E.R. Geus, J.C. Jansen, and H. van Bekkum, *Zeolites*, submitted.

51. U. Müller, and K.K. Unger, in: *Characterization of Porous Solids*, K.K. Unger (Ed.), Stud.Surf.Sci.Catal., Vol. 39, Elsevier, Amsterdam, 1988, 101.

52. S.A. Axon, and J. Klinowski, *Appl.Catal.*, 81 (1992) 27.

53. G. Zheng, unpublished adsorption results by volumetry at 20°C

54. V.R. Choudhary, and D.B. Akolekar, *J.Catal.*, 117 (1989) 542.

55. W.-D. Einicke, M. Heuchel, M. v.Szombathely, P. Bräuer, R. Schöllner, and O. Rademacher, *J.Chem.Soc.,Faraday Trans.*, 85 (1989) 4277.

Summary

Zeolites and other crystalline molecular sieves are commonly utilized as ion exchangers, adsorbents, and catalysts. In catalysis, the high selectivities achieved are often attributed to either the fact that some molecules do not have access to the zeolite micropores and others do (reactant selectivity), or that the reaction is confined to a limited volume within the framework (transition state selectivity), or that a difference in mobility of the different products exists (product selectivity). If some molecules cannot enter into the zeolite micropores, or if different molecules exhibit a different mobility within the zeolite, application of zeolites in a membrane configuration would fulfill the desire to make optimal use of the molecular sieve properties. In addition, the development of inorganic zeolite membranes would generate the possibility to combine catalytic reaction and separation within one unit operation.

Several other materials and approaches have been suggested for the preparation of high-temperature gas separation membranes. Therefore, the advantages of zeolites as a membrane component are discussed in **Chapter 1**. Furthermore, the two basically different approaches to the preparation of inorganic zeolite membranes as discussed in this thesis are presented, viz. (i) a monolayer of oriented zeolite (single) crystals in a gas-tight matrix on a porous support, and (ii) a continuous, polycrystalline zeolite layer, grown on top of a porous substrate.

Chapter 2 describes the preparation of zeolite membranes according to the monolayer approach, which is based on the availability of separately synthesized, large silicalite (Si-rich ZSM-5; MFI-type) crystals of up to 500 μm. From the literature several synthesis procedures are known to prepare batches of sufficiently large silicalite crystals of a uniform size. An array of the silicalite crystals is oriented on a porous support, preferably embedded within a thin porous interlayer to facilitate the next preparative step (matrix deposition). The open spaces in between the zeolite crystals are subsequently closed by the deposition of a gas-tight matrix. Different matrix deposition procedures, such as sol-gel, chemical vapour deposition, and glazing techniques, have been investigated to achieve selective deposition in between the zeolite crystals. Thus, the removal of matrix material deposited on top of the zeolite crystals, obstructing the passage through the zeolite micropores, can be avoided. Dip-coating of glazes from dilute suspensions leads to the controlled deposition of matrix precursor material, and, as glazes of relatively low melting temperatures are utilized, allows one to achieve a homogeneous matrix at about 500°C. The size of the zeolite crystals and the thickness of the matrix layer deposited need to be minimized to avoid crack-formation (generally within the gas-tight matrix).

Chapter 3 presents the direct growth of polycrystalline zeolite layers on top of porous, inorganic substrates. Besides the fact that relatively large crystals can be grown, the choice of MFI as the zeolite type for the in situ growth approach is also based on the observation

that intergrowth takes place frequently. Different inorganic porous supports, such as alumina, zirconia, aluminosilicates (clay), and stainless steel (AISI-316), have been used. For high pH levels of the synthesis mixture the crystallization product may not be MFI. The failure to grow MFI has been attributed to the reactivity of support materials (alumina and clay), from which metal ions such as aluminium are leached. The chemical composition of the synthesis mixture is thus changed and other (crystalline) phases result. More inert materials, such as zirconia and stainless steel, are hardly affected by alkaline treatment. On both reactive (clay), and inert porous supports (stainless steel), the growth of continuous, polycrystalline layers of MFI has been achieved. As compared to ceramic substrates, stainless steel has favourable mechanical properties for the construction of high-temperature membrane modules. Porous and non-porous parts can be easily combined, and attached to the generally stainless steel module housing. By directing the growth of the zeolite layer over both porous and non-porous parts, the use of gas-tight sealants can be made redundant.

Chapter 4 deals with the calcination or activation of as-synthesized, template (TPA; tetrapropyl ammonium) containing MFI-type zeolites. Activation is required to render the zeolite framework accessible. Especially with relatively large zeolite crystals (> 100 μm), however, calcination often leads to cracked crystals. The use of cracked crystals in the preparation of zeolite single crystal membranes will lead to inaccurate or erroneous data on the separation potential of this new type of membrane. The development of cracks upon removal of TPA from the in situ grown MFI layers is for the same reason unacceptable. By means of microscope FTIR-spectroscopy it has been found that the development of cracks depends on the preparation procedure of TPA-containing MFI-type zeolites. In addition, temperature-programmed X-ray powder diffraction has improved the knowledge on the thermal expansion/contraction behaviour of both as-synthesized, TPA-containing MFI upon calcination, and activated MFI when subjected to thermal cycling. A 'safe' calcination procedure has been formulated from the in **Chapter 4** described observations, which is further elaborated in **Chapter 5** for the clay supported MFI layer. The 'safe' calcination procedure has been confirmed by permeation experiments with krypton on as-synthesized, in situ grown MFI layers within a high-temperature membrane module during calcination (**Chapter 7**).

The thermomechanical stability of both types of MFI-based zeolite membranes is addressed in **Chapter 5**. First, the thermomechanical compatibility of multilayer systems is treated in general. The principle of the bonding temperature, at which temperature no mechanical stresses occur within the composite (zero-stress), is dealt with. The material compatibility is particularly relevant to the matrix deposition techniques applied in **Chapter 2**, as at least three different materials are involved. The calcination temperature required to remove TPA from the as-synthesized MFI framework, and the thermomechanical properties of MFI during calcination are similarly related. The fact that the supported, in situ grown MFI layers of **Chapter 3** do not crack upon calcination at 400°C has been explained by the expected stabilizing effect of the strong bonding of the zeolite layer to the substrate, and the flexibility of the MFI lattice.

Microscope FTIR-spectroscopy, also applied in **Chapter 4** to study the calcination of TPA-templated MFI, has been developed as a new technique to investigate the sorption and diffusion processes within one, carefully selected zeolite (silicalite) single crystal under well-defined conditions (**Chapter 6**). Quantitative adsorption measurements are performed on

various small hydrocarbons (n-butane, isobutane, 1-butene, and neopentane), using gravimetric calibration data and zeolite Si-O vibrational bands as an internal standard. Diffusional data have been obtained successfully for relatively slow moving species, viz. aromatics ($D < 10^{-13}$ m^2/s). For the more mobile small hydrocarbons the FTIR-technique is expected to be in principle appropriate, but requires improvement of the present experimental set-up. The microscope FTIR-spectroscopic technique also enables one to measure the self-diffusivity of tracer molecules, for instance deuterated species (D_2O). The selective sealing of crystal faces demonstrated the difference in adsorption sites of aromatics (4-methyl pyridine) in MFI, related to the typical anisotropic channel structure.

Chapter 7 is dedicated to the permeation through zeolite-based membranes. A theoretical multistep permeation model has been presented to account for the significant deviation between uptake (macroscopic) diffusivities, on the one, and the (microscopic) self-diffusivities as obtained by the pfg NMR technique, on the other hand. Furthermore, a quantitative permeation model has been developed for small hydrocarbons (methane, ethane, propane, and n-butane), based on pfg NMR self-diffusivity data. The permeation through some prepared prototype membranes (**Chapter 2** and **Chapter 3**) is described, demonstrating the effect of leaks or cracks within the zeolite crystals and of the presence of a mesoporous support on the permeation (clay supported MFI layer). With the stainless steel supported MFI layer within the high-temperature membrane module (**Chapter 3**) permeation experiments up to 350°C have been performed.

The following table demonstrates the difference in flow rate through different MFI membranes. The differences are presented as the surface areas required for the permeation of 1000 kg methane per day at 20°C (membrane thickness 50 µm; feed pressure 1 bar; permeate pressure 0 bar).

Membrane Type	Required Membrane Surface Area (m^2)
MFI supported on clay	400
MFI supported on stainless steel	29
Based on intracrystalline diffusion	1.8

Moreover, typical cryogenic permeation behaviour has been observed at room temperature for the stainless steel supported MFI membranes of **Chapter 3** (e.g. permeation of weakly adsorbed methane being strongly reduced by the presence of n-butane). These results prove that the prepared MFI membranes have molecular sieve properties, but the highest selectivities are observed at low temperature. The adsorption strength, rather than the individual diffusivities, seems to govern the selectivity. The stainless steel supported membranes remain stable during thermal cycling up to at least 350°C.

Samenvatting

Kristallijne moleculaire zeven zoals zeolieten worden industrieel toegepast als ionwisselaars, adsorbentia en als katalysator. In de katalyse worden de gerealiseerde hoge selectiviteiten vaak toegeschreven aan het feit dat sommige moleculen geen toegang tot de zeolietporiën hebben terwijl andere moleculen dat juist wel kunnen (reactant-selectiviteit), of dat de reactie binnen de zeolietporiën een zekere transitietoestand niet toelaat (transitie-selectiviteit), of dat er een verschil in mobiliteit tussen verschillende producten bestaat (product-selectiviteit). Indien sommige moleculen veel trager door het zeolietrooster heen bewegen of zelfs helemaal geen toegang hebben tot de microporiën, kan de toepassing van zeolieten in een membraan-configuratie tot een echt moleculaire-zeefmembraan leiden. Bovendien bieden anorganische zeolietmembranen de mogelijkheid tot het combineren van een katalytische reactie met een scheidingsproces in één processtap.

Voor de bereiding van hoge-temperatuur gasscheidingsmembranen zijn verschillende materialen en werkwijzen gesuggereerd. In **Hoofdstuk 1** worden derhalve de voordelen van zeolieten als het scheidende medium behandeld. Daarnaast worden de twee benaderingswijzen voor de bereiding van zeolietmembranen zoals besproken in dit proefschrift gepresenteerd: (i) een monolaag van georiënteerde zeolietkristallen in een gasdichte matrix op een poreuze onderlaag, en (ii) een aaneengesloten, polykristallijne zeolietlaag, gegroeid op een poreus substraat.

Hoofdstuk 2 beschrijft de bereiding van zeolietmembranen volgens de monolaag van zeolietkristallen. Silikaliet (Si-rijk ZSM-5; MFI-type) kan gegroeid worden tot relatief zeer grote kristallen (> 500 μm lengte). Uit de literatuur zijn verschillende procedures bekend voor de 'batch'-gewijze synthese van voldoende grote silikalietkristallen met een uniforme grootte. Een aantal silikalietkristallen wordt op een poreuze onderlaag aangebracht, bij voorkeur verankerd met behulp van een poreuze tussenlaag. Dit vereenvoudigt de volgende processtap, de depositie van de gas-dichte matrix. De lege ruimtes tussen de zeolietkristallen worden vervolgens gedicht (gevoegd). Verschillende depositietechnieken (sol-gel, 'chemical vapour deposition' en glazuurtechnieken) zijn onderzocht, waarbij selectieve depositie beoogd wordt. Hiermee wordt voorkomen dat na depositie het matrixmateriaal dat op de zeolietkristallen is gedeponeerd weer verwijderd moet worden om transport door de zeolietkristallen mogelijk te maken. Met name het zogenaamde 'dippen' van verdunde glazuursuspensies blijkt tot de gewenste selectieve depositie te leiden, terwijl het gebruik van al bij lage temperatuur smeltende glazuren de vorming van een homogene laag realiseert na een temperatuur-behandeling van 500°C. Grote zeolietkristallen en dikke glazuurlagen blijken echter de vorming van scheuren in de glazuurlaag in de hand te werken.

Hoofdstuk 3 behandelt de vorming van continue, polykristallijne zeolietlagen op poreuze onderlagen via directe synthese. Als zeoliet is ook hier silikaliet gekozen. Ten eerste omdat relatief grote kristallen gegroeid kunnen worden, maar ook omdat vaak vergroeide kristal-

diffusie in een zeolietéénkristal gepresenteerd. Kwantitatieve adsorptiemetingen zijn uitgevoerd aan verschillende koolwaterstoffen zoals n-butaan, isobutaan, 1-buteen en neopentaan in silikaliet, gecalibreerd aan de hand van gravimetrische gegevens. Si-O IR-vibratiebanden zijn als interne standaard gebruikt. Diffusiegegevens zijn verkregen voor relatief trage systemen, zoals aromaten in silikaliet (D < 10^{-13} m^2/s). Voor snellere systemen dient de apparatuur aangepast te worden. Het is ook mogelijk om de zelf-diffusie van 'tracer'-componenten te bestuderen met behulp van gedeutereerde moleculen (bijvoorbeeld D$_2$O). Door middel van het selectief afsluiten van kristalvlakken is aangetoond dat er voor aromaten (4-methylpyridine) in MFI twee verschillende adsorptieplaatsen zijn, hetgeen overeenstemt met de anisotrope poriestructuur.

Hoofdstuk 7 is gewijd aan de permeatie door zeolietmembranen. Een theoretisch meerstaps-permeatiemodel wordt gesuggereerd, hetgeen in verband wordt gebracht met de systematische verschillen tussen macroscopische ('uptake') en microscopische (zelf-)diffusiecoëfficiënten, gemeten via de pfg NMR techniek. Daarnaast is een kwantitatief permeatiemodel opgesteld, waarmee de permeatie van kleine koolwaterstoffen (methaan, ethaan, propaan en n-butaan) op basis van pfg NMR meetgegevens berekend kan worden. De permeatie door enkele prototype membranen (**Hoofdstukken 2 en 3**) wordt gepresenteerd, waarbij het effect van lekken of scheuren in de zeolietkristallen wordt aangegeven. Bovendien wordt aangetoond dat een niet voldoende poreuze onderlaag de scheidende eigenschappen van zeolietmembranen sterk nadelig beïnvloedt (MFI-lagen op aardewerk). Met de op roestvast staal gegroeide MFI-lagen in een hoge-temperatuur membraanmodule (**Hoofdstuk 3**) zijn permeatiemetingen tot 350°C verricht (thermische cycleerbaarheid is mogelijk).

De volgende tabel geeft de verschillen in permeatie aan tussen verschillende zeoliet-membranen. De verschillen zijn weergegeven als het benodigde oppervlak voor de permeatie van 1000 kg methaan per dag bij 20°C (membraandikte 50 μm; voedingsdruk 1 bar; permeaatdruk 0 bar):

Membraan	Benodigd Membraanoppervlak (m^2)
MFI-laag op aardewerk	400
MFI-laag op roestvast staal	29
Uitsluitend intrakrystallijne diffusie	1.8

Bovendien is met de roestvast staal gedragen MFI-lagen typisch cryogeen gedrag waargenomen bij kamertemperatuur (reductie in permeatie van zwak-adsorberend methaan in aanwezigheid van sterk-adsorberend n-butaan), hetgeen de moleculaire-zeefeigenschappen van de bereide zeolietmembranen aantoont. De hoogste selectiviteiten zijn echter gerealiseerd bij lage temperatuur. De adsorptie is kennelijk meer bepalend dan de mobiliteit van de verschillende moleculen.

Dankwoord

213

voor het verrichten van enkele oriënterende CVD-experimenten.

Marjan Versluys (RUU) wil ik hartelijk danken voor de uitleg en gebruik van de densitometer voor het Röntgendiffractiewerk, waarvoor de heren N.M. van der Pers en J.F. van Lent op uitstekende wijze de metingen hebben verricht. Bovendien heb ik de instructie van de heer van der Pers aangaande de interpretatie van de meetgegevens zeer op prijs gesteld. De fotografen Piet Dullaart en in het bijzonder Fred Hammers (waar is de maandbon?) hebben onwaarschijnlijke hoeveelheden foto's, dia's en posters verzorgd, die vaak binnen een record-tijd gereed moesten zijn. Wim Jongeleen heeft enkele lastige figuren voor mij getekend. De heer Molenkamp van de glasblazerij en de heren van den Berg en Verbooij van de instrumentmakerij hebben zeer veel verschillende werkstukken afgeleverd. De technische assistentie van Ernst Wurtz en Ben Meester bij de meest uiteenlopende klussen is onontbeerlijk geweest. Over de chemische analyses van de heren Padmos en Koot was ik altijd zeer te spreken.

Hans van der Schaaf dank ik hartelijk voor het beheren van de zogenaamde 'middelen', waardoor het project soepel liep. Mieke van der Kooij ben ik uitermate dankbaar voor haar steun en met name haar geduld tijdens de telefoongesprekken in de slotfase.

Alette Mulder (ook al bijna dr.) van de RUU dank ik voor de prettige samenwerking en het gezamelijk bijwonen van de congressen in Montpellier. In het bijzonder wil ik Peter Verheijen danken voor zijn uitstekende assistentie bij het interpreteren van opvallende meetgegevens omtrent diffusie en permeatie in zeolieten die nooit vreemd waren. Guhong Zheng (TU Delft) is thanked for his assistence in the sorption and permeation experiments.

Met Daniella Vischjager heb ik met veel vreugde samengewerkt op het gebied van de EVD. Paul van der Put heeft er voor gezorgd dat ik op gezette tijden enkele practicanten tot mijn beschikking had, hetgeen overigens niet altijd uitkwam. Hanneke Becht heeft mij veel geholpen met de operatie van de SEM, waarbij ik ook enkele onorthodoxe trucjes heb geleerd om de apparatuur weer aan de gang te brengen.

Koos Jansen bedank ik voor de zeer afwisselende maar overwegend doeltreffende begeleiding en, daarenboven, voor de toevoeging van enkele kernachtige uitspraken aan mijn kennis van de Nederlandse Taal. Met Marcel den Exter heb ik een korte doch uiterst productieve samenwerking op het gebied van de in situ groei van zeolietmembranen gehad. Op de oio-rots "Het Ghulden Schilt" zijn vele avonduren verslonden door geanimeerde discussies met Marcello Rigutto. De Aula-lunches met Nelleke van der Puil mogen ook zeker niet onvermeld blijven. And I thank Ahmed Arafat for the way he prepared the coffee, and for teaching me this one arabic sentence (on request).

De afstudeerders Marcel Velterop, Jolanda van Doesburg, Peter Dekker, theoriemans Diederik Jaspers en praktijkmans Rob van Gemert, Wridzer Bakker, de surfende Rick van der Vaart en Anneke Muller bedank ik hartelijk voor de intensieve en prettige samenwerking. Daarnaast dank ik de vele studenten die één of meerdere scripties in het kader van het zeolietmembranenproject geschreven hebben.

Mijn ouders bedank ik voor het zondagochtendgevoel en alle andere zeer welkome ondersteuningen. And I thank Marie who, although more often than not being far away, always managed to remain close to me.

Curriculum Vitae

Eduard Rudolf Geus werd geboren op 9 juli 1965 te Sittard. In 1983 behaalde hij het VWO diploma op Het Nieuwe Lyceum te Bilthoven. De studie Scheikundige Technologie aan de Technische Universiteit Delft werd aangevangen in augustus 1983. In maart 1988 werd de ingenieurstitel behaald op het onderwerp Laser Chemical Vapour Deposition van siliciumnitride poeders bij prof. dr J. Schoonman. Aan dezelfde universiteit begon hij in april 1988 met de ontwikkeling van anorganische zeolietmembranen, het promotie-onderzoek waarover dit boekwerkje verslag uitbrengt. Sinds januari 1993 is hij in dienst bij Shell Internationale Petroleum Maatschappij te Den Haag.

Het Noorderlicht roept.